Metal-organic and porous covalent networks for Fe^{3+} detection and CO_2/CH_4 separation

Inaugural-Dissertation

zur Erlangung des Doktorgrades
der Mathematisch-Naturwissenschaftlichen Fakultät

der Heinrich-Heine-Universität Düsseldorf

vorgelegt von

Hanibal Othman

aus Izraa

Düsseldorf

aus dem Institut für nanoporöse und nanoskalierte Materialien ACI

der Heinrich-Heine-Universität Düsseldorf

Gedruckt mit der Genehmigung der
Mathematisch-Naturwissenschaftlichen Fakultät der

Heinrich-Heine-Universität Düsseldorf

Berichterstatter:

1. Prof. Dr. Christoph Janiak

2. Prof. Dr. Christian Ganter

Tag der mündlichen Prüfung:

16.12.2025

Eidesstattliche Erklärung

Eidesstattliche Erklärung Ich versichere an Eides statt, dass die vorliegende Dissertation von mir selbstständig und ohne unzulässige fremde Hilfe unter Beachtung der „Grundsätze zur Sicherung guter wissenschaftlicher Praxis“ an der Heinrich-Heine-Universität Düsseldorf erstellt worden ist. Die aus fremden Quellen direkt oder indirekt übernommenen Gedanken sind als solche kenntlich gemacht. Die Arbeit wurde bisher weder im Inland noch im Ausland in gleicher oder ähnlicher Form einer anderen Prüfungsbehörde vorgelegt. Es wurden keine früheren erfolglosen Promotionsversuche unternommen.

Düsseldorf, 06.11.2025	Hanibal Othman
Ort, Datum	Unterschrift

Danksagung

Ich möchte mich herzlich bei Herrn Prof. Dr. Christoph Janiak für die Möglichkeit zur Promotion in seinem Arbeitskreis bedanken. Vielen lieben Dank dafür, dass ich meine eigene Forschung frei entdecken und verfolgen konnte sowie für die stets konstruktiven Diskussionen. Ich danke Ihnen für Ihre Geduld und Unterstützung und für die Gelegenheit, gemeinsam Symposien zu besuchen.

Herrn Prof. Dr. Christian Ganter danke ich herzlich für die Übernahme des Koreferats sowie für seine stete Ansprechbarkeit und Bereitschaft, meine Aufregungen anzuhören.

Ich möchte mich außerdem bei Herrn Prof. Dr. Suta bedanken. Vielen Dank für die Bereitstellung der Arbeitsmöglichkeiten und die zahlreichen hilfreichen Tipps.

Vielen Dank an alle Co-Autoren, die durch ihre produktive Mitarbeit an den jeweiligen Manuskripten mitgewirkt haben. Frau Vivan Küll danke ich für ihre wiederholten CO_2-Messungen und die stets freundliche Zusammenarbeit. Der NMR-Abteilung CeMSA@HHU danke ich für die zahlreichen NMR-Messungen. Für die IR- und AAS-Messungen bedanke ich mich herzlich bei Frau Birgit Tommes und Frau Annette Ricken.

Ein großes Dankeschön geht an den gesamten Arbeitskreis für die gute Zusammenarbeit und die freundliche Atmosphäre.

Herrn Dr. István Boldog möchte ich für die zahlreichen Fachgespräche, seine Hilfsbereitschaft, die Mitarbeit am Paper sowie für die fortwährende Unterstützung während meiner gesamten Promotion danken.

Den festangestellten Mitarbeiterinnen und Mitarbeitern, Frau Jutta Bourgeois und Herrn Marcell Demandt, gilt ebenfalls ein großer Dank für ihre stetige Ansprechbarkeit.

Für die Unterstützung im AC1-Praktikum und die freundliche Büroatmosphäre, die ich in diesen drei Jahren erleben durfte, bedanke ich mich sehr herzlich bei Frau Birgit Tommes, Frau Annette Ricken und Herrn Tim Müller.

Ich danke meinen Bachelorstudentinnen Frau Beyza Bildirici und Frau Layla Almolsi sowie meiner Masterstudentin Frau Vivan Küll für ihre engagierte und produktive Mitarbeit.

Bei Herrn Nabil Assahub, Marcus Fetzer, Abdulrahman Mohabbat, Julia Michalski, Annette Vollrath, Sven Hößel, Aysenur Limon, Lukas Eisenhuth, David Geller, Brenda Flore Kenyim, Robert Oestreich, Philipp Seiffert und Takin Haj Hassani Sohi bedanke ich mich für die hervorragende Arbeitsatmosphäre.

Auch sehr herzlich danke ich Sarah Salloum, Imene Ziani-Cherif und Max Vieten für die schönen Zeiten und die vielen angenehmen Unterhaltungen.

Ich möchte meinen Eltern und meinen Brüdern für ihre Unterstützung und ihr grenzenloses Vertrauen danken, dass ich die Ziele erreichen kann, die ich mir für mein Leben gesetzt habe. Für ihre unerschütterliche Liebe und Wertschätzung, die es mir ermöglicht haben, weiterzumachen, selbst wenn alle Chancen gegen mich standen. Ich möchte auch den Menschen danken, die mein Leben mit Liebe und Freude erfüllt haben.

Für meine Eltern

For the LORD gives wisdom; from his mouth come knowledge and understanding.

Proverbs 2:

I. Abstract:

In this work we present the wide scope in which porous materials can be used in ranging from iron (III) ions sensing Metal Organic frameworks (first part) to covalent triazine frameworks that can separate CO_2/CH_4 mixtures (second part) and be used in industrial settings to reduce air pollution. In the first part the work aims to introduce a novel Metal-organic framework (MOF) derived from the well-established 2-amino-[1,1'-biphenyl]-4,4'-dicarboxylic acid MOF by modifying the constitution of the organic linker thus changing structure of the MOF to enhance its properties and applications. The luminescent 2-naphthyl moiety was attached to the amino group of the linker via the Buchwald-Hartwig reaction to form the new luminescent Al-based MOF Al-BP-Naph with a surface area of 456 $m^2\ g^{-1}$ and a pore volume of 0.55 $cm^3\ g^{-1}$. Al-BP-Naph showed high selectivity towards Fe^{3+} ions due to the overlapping absorption and excitation spectra of both Fe^{3+} and MOF. The MOF demonstrated a detection limit of approximately $6 \cdot 10^{-6}$ mol L^{-1} with a limit of quantification of about $19 \cdot 10^{-6}$ mol L^{-1} and a very fast response time (less than 10 seconds). The Stern–Volmer constant was approximately $0.09 \cdot 10^5$ L mol^{-1}. The second part presents the monomer 4,4′-(phenazine-5,10-diyl)dibenzonitrile (pBN), new pBN-CTFs were synthesized using the ionothermal method with varying temperatures (400 and 550 °C) and the $ZnCl_2$-to-monomer ratio (10 and 20). N_2 adsorption yielded BET surface areas up to 1460 m^2g^{-1}. The pBN-CTFs are promising CO_2 adsorbents and are comparable to other benchmark CTFs such as CTF-1 with a CO_2 uptake of pBN-CTF-10-550 at 293 K of up to 54 $cm^3\ g^{-1}$ or 96 mg g^{-1}, with a CO_2/CH_4 IAST selectivity of 22 for a 50% mixture of CO_2/CH_4. pBN-CTF-10-400 has a very high heat of adsorption of 79 kJ mol^{-1} for CO_2 near zero coverage in comparison to other CTFs, and it also stays well above the liquefaction heat of CO_2 due to its high microporosity of 50% of the total pore volume.

In the last part of this work (unpublished works) we present an unfinished work that contains the initial evidence of manganese (II) induced phosphorescence in Metal Organic frameworks. ($Mg_2(dhtp)(H_2O)_2$]), was synthesized via solvothermal methods, The structural integrity and crystallinity of the modified MOFs was retained, nitrogen adsorption measurements concluded that the modified MOF has a lower surface area than the pristine MOF with a surface area of 331 $m^2\ g^{-1}$. A key finding of this study was the discovery of Mn-induced luminescence with just 1 wt% Mn addition, a phenomenon not observed in other MOFs when adding other paramagnetic metals. Time-resolved measurements provided further insight into the luminescent lifetime, Additionally, we investigated the thermal dependence of the luminescence, observing significant variations in intensity and lifetime with temperature changes ranging between 2 and 9 μs and a thermal quenching efficiency of 100 % at room temperature

II. Publication list:

Hanibal Othman, István Boldog, Christoph Janiak:

"**Synthesis of a Luminescent Aluminum-Based MOF for Selective Iron(III) Ion Sensing"**

Molecules **2025**, *30*(20), 4146**;** https://doi.org/10.3390/molecules30204146

Hanibal Othman, Robert Oestreich, Vivian Küll, Marcus N. A. Fetzer and Christoph Janiak:

"**Synthesis and Characterization of Covalent Triazine Frameworks Based on 4,4′-(Phenazine-5,10-diyl)dibenzonitrile and Its Application in CO_2/CH_4 Separation**"

Molecules. **2025**; *30(15)*:3110. https://doi.org/10.3390/molecules30153110

Idriss Kamdem Taquieteu, Hermann Dzoujo Tamaguelon, Victor Shikuku, Sylvain Tome, Donald Kamdem Njouond, Manelle Fouetfack Dongmo, Hanibal Othman, Annette Vollrath, Abdulrahman Mohabbat, Christoph Janiak, Charles Banenzouéa and David Joh Daniel Dina:

"Synthesis and characterization of lignin-modified geopolymer composites for aqueous phase sequestration of methyl orange dye in a fixed-bed column"

*Mater. Adv. **2025**,6, 5074-5088*, DOI: 10.1039/D5MA00248F

Jacques Madiba Mboka, Hermann Dzoujo Tamaguelon, Victor Shikuku, Sylvain Tome, Valery Franck Deugueu, Hanibal Othman, Christoph Janiak, Marchand Manga Dika, Marie Annie Etoh & David Joh Daniel Dina.

"**Novel Superadsorbent from Pozzolan-Charcoal based Geopolymer Composite for the Efficient Removal of Aqueous Crystal Violet"**

Water Air Soil Pollut: **2024** *235,430.* Doi*: https://doi.org/10.1007/s11270-024-07257-4*

Table of contents:

I. Abstract I

II. Publication list II

III. Table of contents III

IV. List of abbreviations IV

1.Introduction 1

1.1 Metal–organic frameworks 1

1.1.1 Metal–organic frameworks characteristics and properties 3

1.1.2 Metal–organic frameworks applications 5

1.1.3 Metal –organic frameworks and luminescence 6

1.1.3.1 Mechanisms of optical sensing in MOFs 9

1.1.4 Phsophorescence 11

1.1.4.1 Mechanism of phosphorescence 12

1.1.4.2 Design principles for efficient RTP 13

1.1.4.3 Classes of phosphorescent materials 13

1.1.4.4 Applications of RTP materials 13

1.2 Porous organic polymers 14

1.2.1 Covalnet triazine frameworks 14

1.2.2 Advantages of covalent triazine frameworks (CTFs) 14

1.2.3 Disadvantages of covalent triazine frameworks 15

1.2.4 Applications of covalent triazine frameworks (CTFs) 15

1.2.5 Synthesis methods for covalent triazine frameworks (CTFs) 16

2. Dissertation goal and scope 17

3. Cumulative Part 19

3.1 Synthesis of a luminescent Aluminum-based MOF for selective Iron(III) ion sensing 19

3.2 Synthesis and characterization of covalent triazine frameworks Based on 4,4′-(Phenazine-5,10-diyl)dibenzonitrile and Its application in CO_2/CH_4 Separation 56

3.3 Contribution in other publication 97

3.4 Unpublished works 99

4. Conclusion 126

5. References 127

IV. List of abbreviations:

acac: Acetylacetone

BET: Brunauer–Emmett–Teller

bpdc: 4,4′-biphenyl dicarboxylate

bpe: 1,2-bis(4-pyridyl)ethylene

bpim: Bipyrimidine

COF: Covalent Organic Framework

COP: Covalent Organic Polymer

CTF: Covalent Triazine Framework

DFT: Density Functional Theory

DMF: Dimethylformamide

DMSO: Dimethyl sulfoxide

DUT: Dresden University of Technology

EDX: Energy Dispersive X-ray

FRET: Förster Resonance Energy Transfer

IAST: Ideal Adsorbed Solution Theory

ICT: Intermolecular Charge Transfer

IRMOF: Isoreticular Metal–Organic Framework

ISC: Intersystem Crossing

K_{nr}: Non-radiative decay rate constant

K_q: Quenching rate constant

K_r: Radiative decay rate constant

LMOF: Luminescent Metal–Organic Framework

LOD: Limit of Detection

LOQ: Limit of quantification

MIL: Matériaux de l´Institut Lavoisier

MLCT: Metal-to-Ligand Charge Transfer

MOF: Metal–Organic Framework

MTV-MOF: Multivariate Metal–Organic Framework

NL-DFT: Non-Local Density Functional Theory

NMR: Nuclear Magnetic Resonance

PET: Photo-Induced Electron Transfer

POP: Porous Organic Polymer

PSA: Pressure Swing Adsorption

PXRD: Powder X-ray Diffraction

RTP: Room-Temperature Phosphorescence

SBU: Secondary Building Unit

SEM: Scanning Electron Microscopy

SOC: Spin–Orbit Coupling

S_0, S_1, Sn: Singlet ground and excited states

TGA: Thermogravimetric Analysis

TSA: Temperature Swing Adsorption

UIO: Universitetet i Oslo

VOC: Volatile Organic Compound

wt%: Weight percent

1. Introduction:

1.1 Metal–organic frameworks:

Porous materials constitute a versatile class of substances distinguished by their intricate network of void spaces, commonly referred to as pores, embedded within their solid structure. These pores, which vary in size, play a crucial role in defining the physical, chemical, and functional properties of the materials.[1,2] Based on their dimensions, pores are categorized into three types: micropores (diameter < 2 nm), mesopores (2-50 nm), and macropores (diameter > 50 nm).[3] The presence of these pores grants porous materials a vast internal surface area, which strongly influences their interactions with external substances. As a result, porous materials have garnered immense interest in both scientific research and industrial applications, driving innovations in fields as diverse as catalysis, gas storage, sensing, energy conversion, and environmental remediation.[4] The ability to fine-tune porosity, surface chemistry, and structural morphology at the nanoscale has led to ground-breaking discoveries and has significantly enhanced the performance of these materials across multiple domains.[5,6,7,8,9,10,11,12,13,14] Among the most extensively studied porous materials are metal-organic frameworks (MOFs), which represent a unique class of crystalline coordination polymers (CPs) composed of metal ions or clusters called secondary building units (SBUs) and are linked together by organic ligands usually carboxylic acid ligands or nitrogen ligands. Representative SBUs and ligands are shown in Figure 1.[15,16,17] MOFs exhibit a modular architecture that enables precise control over their pore size, shape, and chemical environment.[18,19,20] By selecting appropriate metal nodes and organic linkers. This structural customization has positioned MOFs at the forefront of porous material research, leading to notable advancements in adsorption, and gas storage.[21,22]

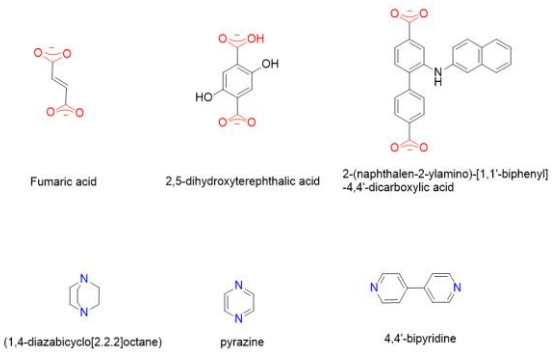

Figure 1: Representative organic linkers used in MOF synthesis. The upper row shows carboxylate-based linkers, and the lower row shows nitrogen-containing heteroaromatic linkers.

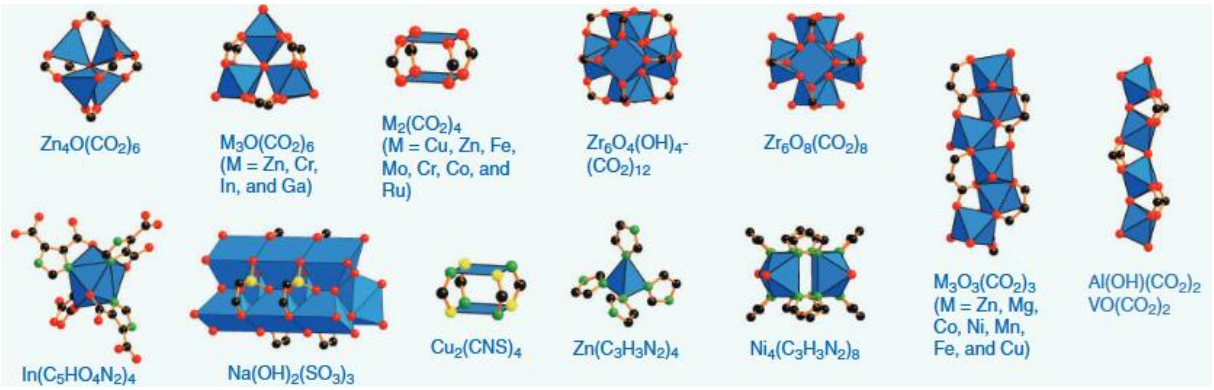

Figure 2: Representative secondary building units and metal clusters used in the production of MOFs and coordination polymers. The figure was permissioned and approved by the American Association for the Advancement of Science, © 2013.[23]

Several prominent examples illustrate the versatility of MOFs. Aluminium fumarate (AlFum), for instance, has shown considerable promise in adsorptive heat transformation due to its characteristic S-shaped water adsorption isotherm.[24,25] Notably, AlFum can be synthesized via environmentally green chemistry approaches using water as a solvent, making it an attractive material for sustainable applications. Similarly, the IRMOF family exemplifies the concept of isoreticular synthesis, where maintaining a consistent framework topology while varying pore size and functional groups allows for the creation of materials with extraordinary properties that can be used in a plethora of applications, including high methane storage capacity and ultralow density.[26,27] Additionally, functionalized MOFs such as MIL-53(Al)-NH_2 are being investigated for fluorescent sensing applications, with their ability to detect small molecules demonstrating their potential in analytical and biomedical fields.[28,29] The synthesis of aluminum-based MOFs (Al-MOFs) has gained significant attention due to the inherent properties of aluminum, including its natural abundance, low cost, low toxicity, and strong hydrothermal stability. These characteristics make Al-MOFs highly attractive for industrial and environmental applications.[30] Beyond MOFs, other porous materials such as zeolites, activated carbon, mesoporous silica, and metal oxides have played crucial roles in advancing scientific research and industrial processes.[31,32,33,34] Zeolites, characterized by their well-defined microporous structures, are extensively utilized in catalysis, ion exchange, and molecular sieving applications.[35,36,37] Activated carbon, known for its exceptionally high surface area, serves as an effective medium for adsorption-based purification and separation techniques, widely employed in water treatment and air filtration.[38] Silica-based porous materials, including xerogels and aerogels, stand out for their ultra-high porosity and lightweight nature, making them ideal for insulation, drug delivery, and advanced optical applications.[39] Additionally, metal oxides such as alumina demonstrate remarkable efficacy in specialized applications, such as fluoride removal from water, due to their strong adsorption properties and structural robustness.[40]

1.1.1 Metal–organic frameworks characteristics and properties:

The scientific importance of porous materials can be attributed to several key characteristics that define their functionality:

1. High surface area and porosity:

   One of the defining characteristics of MOFs is their ultra-high surface area and porosity, which are crucial for gas adsorption. The extensive internal voids provide a large number of adsorption sites, enhancing the material's capacity for gas uptake. As shown in the studies by Férey, Zhou and Kitagawa, MOFs can exhibit high surface areas exceeding 7000 m²/g, significantly surpassing traditional natural adsorbents such as zeolites or even activated carbons.[41,42] The large internal surface area of porous materials significantly enhances their ability to interact with guest molecules. This property is critical for adsorption, catalysis, and sensing applications. For example, the high surface area of AlFum contributes to its effectiveness in heat transformation, while MOFs with extensive porosity facilitate substantial fluoride adsorption.

   The isotherms measured in this work can be described using the IUPAC report published in 2015 by Thommes *et al*. in which the isotherms can be categorized into 6 types of different shapes, each representing a distinct sorption mechanism as illustrated in Figure 3.

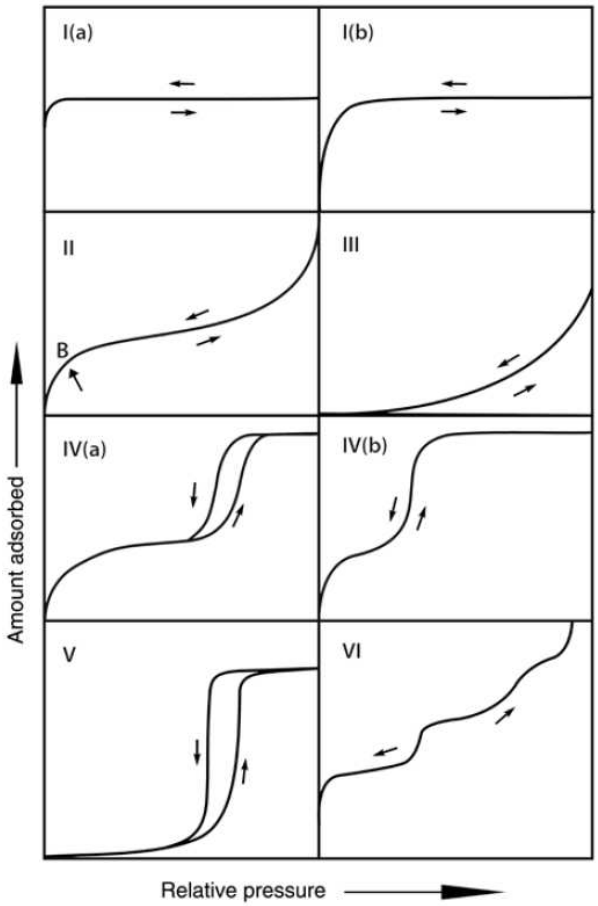

Figure 3: Classification of the idealized isotherms for microporous (Type I), nonporous or macroporous (Types II, III, and VI), and mesoporous materials (Types IV and V) according to IUPAC. Figure reproduced with permission from Ref. 3. © Copyright 2015, De Gruyter, IUPAC.

Type I isotherms correspond to microporous materials with a relatively small external surface area. Micropores are filled at low relative pressure and then reach a plateau at medium and high relative pressure due to the saturation of adsorption sites that can be accessed. Type I(a) is also found in microporous materials but have a very narrow pore size distributions, whereas Type I(b) possess a wider range of pores reaching up to 2.5 nm. Type II isotherms describe non-porous or macroporous materials, where the characteristic shape arises a result of the unrestricted monolayer-multilayer adsorption up to high relative pressure. In Type III isotherms there is no point B which represent the end of the monolayer sorption and therefore no described monolayer adsorption.

Type IV isotherms are characteristic of mesoporous materials, for which the adsorption behaviour is governed by adsorbate adsorbent relation and interaction. Type V is mainly observed in water vapour adsorption on hydrophobic microporous and mesoporous adsorbates, while Type VI is representative of layer-by-layer adsorption on highly uniform nonporous surfaces.[3]

2. Tuneable pore size and chemical functionality: The ability to precisely manipulate pore dimensions and surface chemistry allows for selective interactions with target molecules based on size, shape, and chemical affinity. This feature is essential in gas separation (CO_2/N_2, CO_2/CH_4), size-selective catalysis, and targeted drug delivery. Functionalization of pore walls with specific chemical groups further enhances selectivity and catalytic activity.

3. Structural stability: Many porous materials, including MOFs like CAU-10-H, exhibit remarkable thermal and hydrothermal stability, ensuring their long-term performance under harsh conditions.[43] This stability is crucial for industrial applications that require repeated adsorption-desorption cycles without significant degradation. Another important aspect of stability is the reusability of MOFs under their application-specific conditions. A key advantage of these materials is their relatively high thermal stability and resistance to pressure and any pollutants present in the operating environment. Materials such as MIL-101 and ZIF-8 have been shown to retain their structural integrity after repeated use, as highlighted by Davis and Jeremias et al. This feature is particularly beneficial for applications in carbon capture and natural gas storage, where materials must endure long-term operational stability.[44,45]

4. Versatile synthesis techniques: Advances in synthesis methods, including solvothermal, hydrothermal, sol-gel controlling, and environmentally friendly approaches, have enabled the fabrication of porous materials with controlled morphology, particle size, and defect engineering.[46] Ultrasonic synthesis techniques have been shown to improve the properties of materials like MIL-53(Al), enhancing their practical utility.

1.1.2 Metal–organic frameworks applications:

The significance of porous materials is further underscored by their wide range of applications, spanning multiple disciplines and sectors:

1. Adsorption and separation: Porous materials are extensively employed in selective adsorption and separation of gases, liquids, and pollutants.

   MOFs can be tailored for specific gas adsorption applications by modifying their pore sizes, functional groups, and metal centers. Studies conducted by Li et al. and Sumida et al. highlight the role of functionalization in improving CO_2 selectivity. For instance, MOFs containing open metal sites, such as HKUST-1 and Mg-MOF-74, have been shown to exhibit strong interactions with CO_2, leading to enhanced adsorption capacities even under low-pressure conditions.[47] Their ability to capture water,

methane, carbon dioxide, fluoride, dyes, and volatile organic compounds makes them invaluable for environmental remediation and industrial gas purification.[48,49,50,51]

2. Catalysis: The high surface area and the ability to control of the environments of the voids render MOFs highly effective as catalysts for numerous chemical reactions, including Friedel-Crafts reaction, and hydrocarbon separation.[52,53,54]

3. Energy storage and conversion: MOFs and other porous frameworks are actively investigated for their potential in energy storage applications, such as hydrogen and methane storage, thermal energy storage, and even mechanical energy retention.[55,56,57,58,59]

4. Sensing and detection: Functionalized porous materials, particularly luminescent MOFs, are being developed as highly sensitive and selective sensors for detecting metal ions, organic molecules, explosives, toxic gases, and environmental changes such as humidity and pH fluctuations.[60,61,62,63]

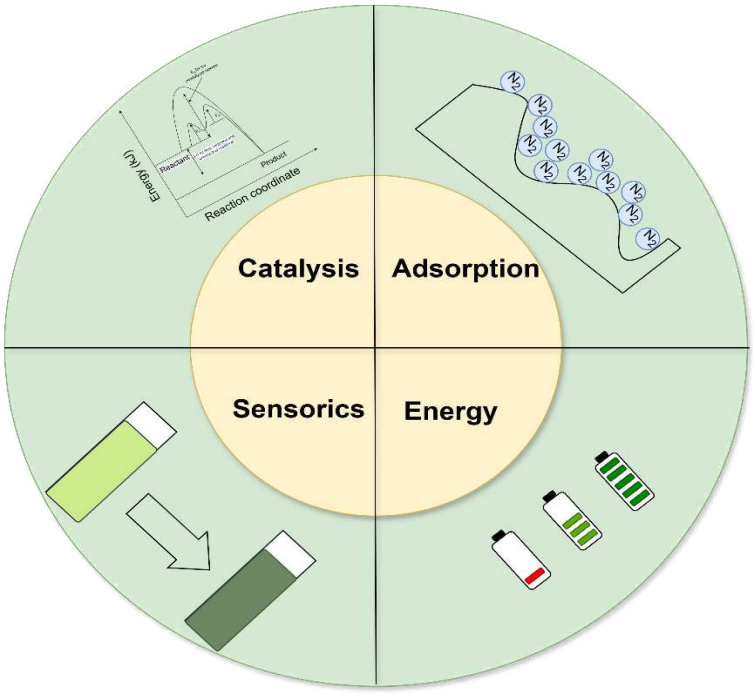

Figure 4: Application scope of metal–organic frameworks.

1.1.3 Metal–organic frameworks and luminescence:

As the results of the structural composition of metal–organic frameworks they possess highly versatile properties and can be counted as an interesting class of materials to explore the interplay between their luminescent properties and inherent porosity. This relationship is not merely coincidental; rather, it underpins a wealth of unique functionalities and applications that

distinguish MOFs from traditional luminescent non-porous materials and non-luminescent porous materials with regard to structural predictability, in addition to the well-defined environments for lumiphores in crystalline form.[64] The combination of a structurally well-defined and tunable porous architecture leads to tuneable photoluminescent properties.[65,66,67]

A central aspect of the importance of crystallinity in luminescent MOFs lies in its ability to modify and enhance the luminescence itself.[68] The rigid framework structure can isolate and organize luminescent components in ways not achievable in solution or conventional solid-state materials. This isolation can minimize inter-luminophore interactions such as π - π stacking, which often lead to broadened and red-shifted emission, as well as quenching in bulk solid ligands.[69] In open, low-density MOF structures, the linkers can exhibit more "solution-like" emission with well-resolved vibrational fine structure due to increased rigidity.[68] Furthermore, the constrained environment within the pores can reduce non-radiative decay pathways, leading to increased fluorescence intensity, longer lifetimes, and higher quantum yields of the organic linkers.[68,70] The presence of pores also enables the introduction of guest molecules into the vicinity of luminescent centers, creating entirely new luminescence pathways. This guest inclusion can lead to plethora of phenomena such as, Adsorbate-based emission and sensitization where a non-emissive/slightly emissive MOFs can be made luminescent by trapping luminescent guest molecules within their pores. Conversely, the presence of guest molecules can sensitize the luminescence of metal ions within the framework through antenna effects.[71] Other possibilities includes excimer and exciplex formation: The close proximity of linkers or linkers and guest molecules within the confined space of the pores can facilitate the formation of excited-state dimers (excimers) or heterodimers (exciplexes), resulting in broad, featureless emission at red-shifted wavelengths.[72,73] The MOF structure provides a platform to systematically study and control the orientation and distance of these interacting species. Guest-induced modulation of luminescence is another phenomenon that can occur in luminescent MOF where the adsorption of guest molecules can alter the electronic environment, coordination sphere of metal ions, or the relative arrangement of linkers, leading to changes in the MOF's emission wavelength, intensity, or lifetime. This sensitivity forms the basis for many sensing applications. [74-75]

The intimate relationship between luminescence and porosity is particularly evident in the application of MOFs as chemical sensors. The high surface areas and structural tunability of porous MOFs enable them to efficiently interact with analyte molecules. When these frameworks also possess luminescent properties, the binding or interaction with an analyte can be translated into a detectable optical signal. Various sensing mechanisms leverage this interplay, where for example fluorescence quenching where adsorption of an analyte within the pores can quench the MOF's luminescence through electron or energy transfer or other

mechanisms such as competitive energy absorption. The magnitude of quenching can be related to the concentration of the analyte and thus being a tool to assay the amount of analyte in a known volume.[76] Another mechanism that can be emphasised is solvatochromic shifting polarity of adsorbed guests perturbs the emission spectrum, producing wavelength shifts suitable for detection.[77] A third mechanism is the guest-induced emission, wherein the presence of specific guest molecules can induce or enhance luminescence through sensitization or formation emissive species within the pores.[78]

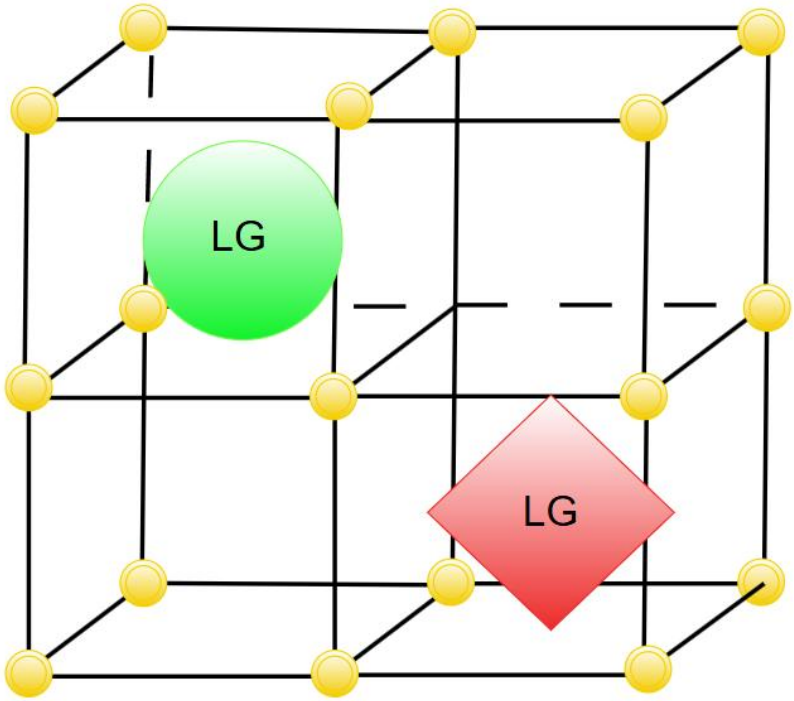

Figure 5: Integration of luminescent guests into the structure of metal–organic framework.

The sensing process generally involves the selective adsorption of targeted molecules, for which several factors that play a vital role in sensing can be highlighted. Functionalization of organic ligands allows systematic tuning of the MOF aperture modulation of emission properties (intensity, wavelength and sensitivity) leading to desired properties.[79,80,81] Another strategy involves the use of multivariate (MTV)-MOFs, which combine multiple species of organic linkers in one framework, can create a more complex electronic environment with better sensing performance.[82] Defects in MOFs, (e.g., missing nodes/linkers) can also be exploited to alter the interaction between the analyte and the framework of the MOF yielding in either a turn-off or a turn-on response that can be detected and sued for sensing. [83]

1.1.3.1 Mechanisms of optical sensing in MOFs:

MOF-based optical sensors utilize light–matter interaction such as light absorption, emission, reflection, refraction, scattering, or transmission. A typical optical sensing setup consists of a light source, a MOF sensing medium that interacts with analytes, and a detector. Detectable parameters can include refractive indices, scattering, absorbance, and luminescence, which are often dependent on guest molecules.

Colorimetric Sensing**:** In colorimetric sensing, exposure to analytes induces a visible color change. Chromism originates from interactions between a responsive center in the MOF and a triggering analyte, ranging from weak van der Waals interactions to bond formation and ligand coordination. A key mechanism involves coordination-driven chromism, where the analyte coordinates to a metal node (or to a metal dopant within the framework), and perturbs the transition-metal coordination geometry and thereby alters the colour. For example the coordination of acetylene on the platinum Pt-doped MOF was doped with. This coordination and interaction caused a certain polymerization that changed the colour of the MOF.[84] Another mechanism is the ligand-based charge transfer, where interaction between guest molecules and ligands triggers charge transfer processes, changing the perceived colour. For instance, a Cu(I)-MOF shows naked-eye chromic detection of polar aliphatic VOCs such as alcohols, ketones and halocarbons, due to intermolecular electron transfer between the ligand and encapsulated guests.[85] MOFs with redox-active ligands like tetrazine derivatives, and naphthalenediimides and diimides also show potential in colorimetric sensing through charge transfer processes upon interaction with electron-rich molecules.[86-90]

Functional MOF–composite colorimetric sensing: In this approach optically active guests such as organic dyes, metal nanoclusters are loaded within the host to achieve visual detection of analytes. These guests can be grafted onto metal oxoclusters or loaded into pores. For example, DTNB loaded in NU-1000 or grafted onto MOF-808 enables visual detection of the nerve agent VX through a colour change resulting from DTNB's reaction with degradation products.[91]

Luminescent Sensing: Luminescent sensing relies on analyte-induced changes in emission intensity, wavelength, or lifetime. Luminescence in MOFs may originate from the metal of the MOF for example lanthanide and d^{10} transition metal ions, where lanthanide ions, in particular, display sharp emission spectra, or from ligands with extended π-conjugation where the two main phenomena are fluorescence and phosphorescence.[92,93,94,95,96,97]

Charge-transfer (CT) based luminescence, including metal-to-metal (MMCT), ligand-to-ligand(LLCT), metal-to-ligand (MLCT), and ligand-to-metal charge transfer (LMCT).[98]

Another route to optical signaling is the guest-induced emission achieved by encapsulating luminescent guests such as lanthanide ions, quantum dots, or organic dyes in the MOF pores. In luminescent metal organic frameworks (LMOFs) common sensing mechanisms include photo-induced electron transfer (PET), intermolecular charge transfer (ICT), and Förster energy transfer (FRET). Guest-induced luminescence enhancement has also been reported wherein VOC adsorption supresses molecular vibrations inside the MOF, resulting in increased luminescence intensity.[99,100]

1.1.4 Phosphorescence

Phosphorescence is a photophysical process in which an excited molecule or solid returns from a triplet excited state (T_n) to the singlet ground state (S_0) via radiative decay. Unlike fluorescence, which occurs on the nanosecond timescale, phosphorescence persists for microseconds to hours depending on the host environment and nature of the emitter. The long-lived afterglow arises because the transition from the triplet (T1) to singlet (S0) state is spin-forbidden and therefore intrinsically slow.

In recent years have seen tremendous advances in room-temperature phosphorescence (RTP) including purely organic molecules, metal–organic frameworks (MOFs), and hybrid systems, spurred by applications in sensing, anti-counterfeiting, information storage, and bioimaging.[101]

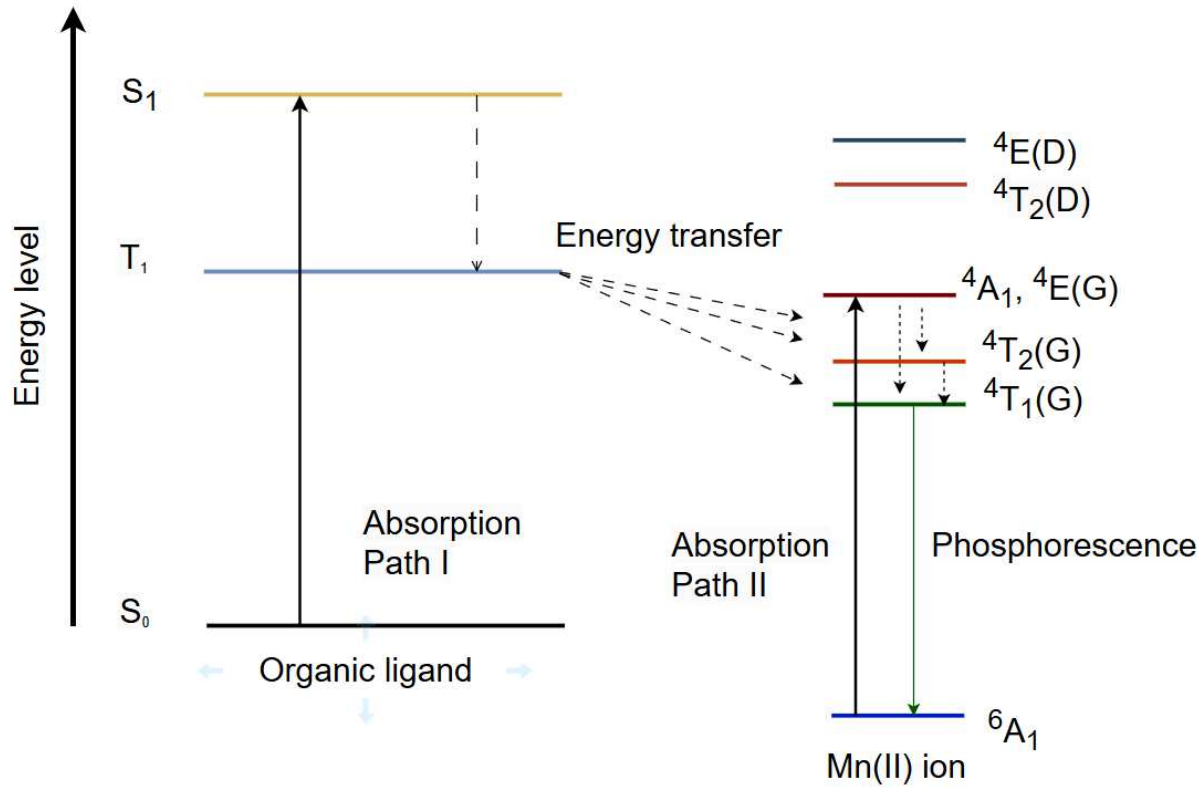

Figure 6: Jablonski diagram illustrating the electronic transitions and emission pathways.

1.1.4.1 Mechanism of phosphorescence:

When a material absorbs photons, electrons are promoted from the singlet ground state S_0 to higher singlet states S_n. Internal conversion (IC) relaxes these excited states to the first singlet excited state (S_1). A fraction of excitons undergoes intersystem crossing (ISC) to triplet states T_n, facilitated by spin–orbit coupling (SOC). Through internal conversion, excitons relax to the lowest triplet T_1, which then decays radiatively to S_0, producing phosphorescence.[101]

The efficiency of phosphorescence (T_r)depends on the competition between radiative K_r and non-radiative (K_{nr}) decay, as well as quenching by molecular oxygen K_q. The phosphorescence lifetime can be expressed as:

$$T_r = 1/K_r + K_{nr} + K_q \quad (1)$$

Thus, design strategies focus on enhancing ISC to increase K_r and suppressing non-radiative decay pathways.[101]

1.1.4.2 Design principles for efficient RTP:

Enhancing intersystem crossing (ISC) by introducing heavy atom/paramagnetic metals such as Ir, Pt, Br, I or heteroatoms with lone pairs (N, O, S) that enhances SOC (spin orbit coupling), thereby promoting ISC according to El-Sayed's rule where:

Intersystem crossing (ISC) is most efficient when the transition between the singlet and triplet states involves a change in the type of molecular orbital occupied (for example, from a π π state to an nπ state, or vice versa). ISC is much less efficient when both states have the same orbital configuration (π π* → π π* or n π* → n π*).[101,102]

Suppressing non-radiative decay using the rigidification, which is critical to restrict molecular motions that deactivate triplet states. Embedding emitters into crystalline matrices, MOFs, or polymer films effectively reduces vibrations and rotations.[103]

Host–guest and supramolecular approaches by embedding phosphors into polymer matrices or host–guest systems improve RTP by isolating luminophores and reducing quenching. In one example, a host crystal of 4,4′-dibromobiphenyl doped with 1% guest molecules yielded a phosphorescence quantum yield of 17% under ambient conditions.[101]

Defect engineering and hybridization is another way for improving the efficiency of room temperature phosphorescence where inorganic frameworks provide rigidity and stability but often lack tunability. Recent work shows that doping organic chromophores such as tetrafluoroterephthalic acid (TFTPA) into $CdCO_3$ yields hybrid systems with excitation-

dependent, multicolor persistent luminescence. The heavy atom Cd further enhances SOC, boosting RTP efficiency.[104]

1.1.4.3 Classes of phosphorescent materials

1- Purely organic RTP materials: Although spin-forbidden transitions limit efficiency, progress has been made with carbazole, phenothiazine, and phenazine derivatives. Carbazole systems are particularly important but require careful purification, since even 0.5% of isomeric impurities significantly alter RTP lifetimes.[101]

2- MOFs and coordination polymers: MOFs provide rigid environments and permanent porosity, ideal for stabilizing triplet states. Phosphorescence in such systems arises from metal-centered and MLCT transitions. For example, Mn(II)-based MOFs display long-lived phosphorescence due to the combined contribution of metal- and ligand-centered states.[105]

3- Organic–inorganic hybrids: hybrid perovskites and organic-doped inorganic frameworks merge rigidity with tunability. Perovskites can produce efficient RTP from common organic fluorophores under ambient conditions, while organic–inorganic composites exhibit excitation-dependent multicolor afterglow.[104]

4- Defect-engineered inorganic phosphors: defects act as traps for charge carriers, prolonging afterglow and enabling mechanoluminescence and persistent phosphorescence. For instance, in $SrAl_2O_4$: Eu^{2+}, Dy^{3+}, defect sites govern the depth and density of traps, directly impacting duration and color of the afterglow.[106]

1.1.4.4 Applications of RTP materials

1- Sensing: phosphorescence quenching by oxygen makes RTP materials valuable in sensing. Porous MOFs doped with Ir complexes show reversible quenching, while polymer-protected carbon dots offer robust RTP for ion detection, including Fe^{3+} sensing with μM-level detection limits.[101]

2- Security and information storage: the long-lived afterglow of RTP allows applications in anti-counterfeiting and data encryption. Hybrid organic–inorganic systems with tunable, multicolor emissions enable multi-channel encryption and time-dependent data storage.[104]

3- Bioimaging: because RTP avoids short-lived background fluorescence, it is particularly attractive for bioimaging. The development of red and near-infrared RTP emitters is crucial for deep-tissue imaging due to better penetration and reduced scattering.[101]

1.2. Porous organic polymers:

1.2.1 Covalent triazine frameworks:

Covalent Triazine Frameworks (CTFs) are a class of porous organic polymers (POP) constructed by aromatic 1,3,5-triazine rings with planar π-conjugation properties.[107] These materials are characterized by their robust aromatic covalent bonds, which provide exceptional chemical and thermal stability.[108] Furthermore, the high nitrogen content, resulting from the incorporation of triazine units, enhances their adsorption properties and catalytic potential. Due to these unique characteristics, CTFs have attracted growing interest in various scientific and industrial applications, ranging from gas separation and catalysis to energy storage and sensing.[109]

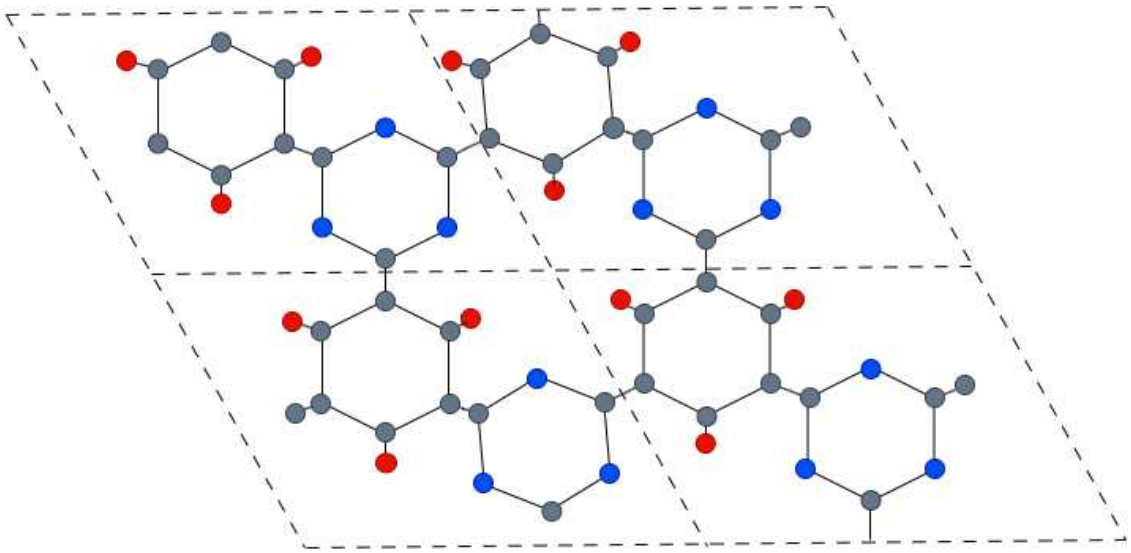

Figure7: Simplified illustration of the constitution of covalent triazine frameworks (blue circles: nitrogen, grey circles: carbon, red circles: different functional groups)

1.2.2 Advantages of covalent triazine frameworks (CTFs):

1- High thermal and chemical stability: due to their strong aromatic covalent bonds and the presence of triazine units, CTFs are resistant to harsh environments, including acidic and aqueous conditions. Many CTFs can endure temperatures exceeding 500 °C, making them suitable for high-temperature applications.[110]

2- High nitrogen content: The nitrogen atoms in the triazine rings contribute significantly to adsorption and catalytic activity. The interaction between nitrogen and CO_2,

facilitated by quadrupole-dipole interactions and Lewis-basic properties, improves CO_2 capture efficiency. Additionally, the heteroatom effect (HAE) plays a crucial role in enhancing catalytic performance.[111]

3- Tunable porosity and high surface area: Some CTFs have reported surface areas exceeding 2000 $m^2\ g^{-1}$, and their pore sizes can be precisely adjusted through the choice of monomers and synthetic conditions. This tunability allows for the development of materials optimized for specific adsorption and separation processes.[112]

4- Facile synthesis from readily available precursors: CTFs are typically synthesized from inexpensive organic nitriles, making them cost-effective. Various synthetic routes have been developed, offering flexibility in material design.[107]

5- Structural design versatility: By carefully selecting monomers and synthesis conditions, researchers can fine-tune the crystallinity, porosity, and electronic properties of CTFs, optimizing them for different applications such as photocatalysis, conductivity, and gas adsorption.

6- Hydrophobicity in some CTFs: Certain CTFs, such as those incorporating adamantane-based linkers, exhibit hydrophobic properties, which is beneficial for gas separation processes in humid environments.[113]

1.2.3 Disadvantages of covalent triazine frameworks (CTFs):

1- Limited crystallinity: Most CTFs are amorphous or semi-crystalline due to their strong covalent framework, which restricts structural ordering during polymerization. Achieving high crystallinity remains a challenge, although recent advances in synthetic methods are addressing this issue.[114]

2- Poor processability: The rigidity of CTFs makes them insoluble and infusible, limiting their ability to be processed into specific shapes or films. Conventional solution-based fabrication techniques are generally not applicable.

3- Potential carbonization: During high-temperature synthesis methods such as ionothermal polymerization and aromatic amide condensation, partial carbonization may occur, negatively affecting the optical and structural properties of the material.[107]

1.2.4 Applications of covalent triazine frameworks (CTFs):

- Gas storage and separation: CTFs demonstrate excellent potential for CO_2 capture and separation from other gases, such as N_2 and CH_4. Their tailored microporosity and nitrogen content make them highly selective for CO_2 adsorption.[110]

- Catalysis: CTFs serve as heterogeneous catalysts for various chemical transformations, including carbon dioxide fixation, photocatalytic water splitting, and heterogeneous catalysis. Their nitrogen-rich structure enables metal-free catalysis or efficient support for metal catalysts.[115,116,117]
- Pollutant adsorption: CTFs effectively remove organic dyes, heavy metal ions, and other pollutants from aqueous solutions, making them promising for water purification technologies.[118]
- Sensing applications: Some CTFs, particularly those with functionalized linkers, exhibit fluorescence quenching properties and can be used for detecting nitroaromatic explosives, metal ions, and other analytes.[119,120]
- Membrane applications: CTFs are being explored as gas separation membranes and as fillers in mixed matrix membranes (MMMs), where they enhance polymer membrane selectivity and permeability.[120]

1.2.5 Synthesis Methods for covalent triazine frameworks (CTFs):

CTFs are synthesized using methods that either construct triazine units in situ or incorporate preformed triazine-based monomers:

1- **Synthesis via triazine unit construction:**

- Ionothermal trimerization: High-temperature cyclotrimerization of nitriles in $ZnCl_2$ at 400-700 °C.[122,123]
- Superacid catalysis: Uses TFMS as a catalyst at milder temperatures, producing lower surface area materials but avoiding carbonization and metal contamination.[124]
- Amidine-aldehyde condensation: Yields non-carbonized CTFs through mild reactions of amidines and aldehydes.
- Aromatic amide condensation: Involves P_2O_5 as a catalyst at moderate temperatures, balancing surface area and stability.[125]
- Microwave-assisted synthesis: Enhances reaction speed and morphology control when combined with catalytic methods.[126]

2- **Synthesis via triazine-containing monomers:**

- Friedel-Crafts reaction: Cyanuric chloride reacts with aromatic monomers using Lewis acids (e.g., $AlCl_3$), though often yielding amorphous structures. [127,128]
- Coupling reactions: Includes Sonogashira, and Suzuki-Miyaura, reactions to link triazine-based monomers.[129,130]
- Schiff base reaction: Forms imine-linked triazine polymers.[131]

2. Dissertation Goal and Scope

The overarching goal of this dissertation is to advance the understanding of luminescence phenomena in porous materials, demonstrating their potential for applications in selective sensing, thermometry, and the integration of advanced emitters within covalent triazine frameworks (CTFs). This research seeks to build on the literature that researched the fields of photoluminescence and porosity, providing insights into the interplay between structural properties and optical behavior in metal-organic frameworks (MOFs) and CTFs.

This work explores the design, synthesis, and characterization of three distinct classes of luminescent porous materials, each tailored for specific applications:

1- Luminescent MOFs for Fe(III) Ion Sensing

Development of an Aluminium-based MOF (Al-BP-Naph) exhibiting selective fluorescence quenching in the presence of Fe^{3+} and investigating the interaction between Fe^{3+} ions and the MOF structure, leading to fluorescence quenching via competitive absorption or energy transfer mechanisms. The characterization of detection performance, including sensitivity, selectivity, and detection limits, using Stern-Volmer analysis and in the end a comparison with existing Fe^{3+} sensors to assess practical applicability and performance advantages.

2- CTFs Incorporating a Thermally Activated Delayed Fluorescence (TADF) Emitter

Synthesis and structural characterization of a novel CTF incorporating a TADF emitter, with a focus on achieving high porosity and surface area while investigating the effect of the synthesis method (the Ionothermal method) on the nature of the material and its influence on the CO_2/ CH_4 separation using adsorption and the focus on the isosteric heat of adsorption after which ideal adsorbed solution theory (IAST) selectivity to understand the behaviour of the adsorption in different atmospheres.

3- Manganese-Induced Phosphorescence in MOFs for Potential Thermometry

While this work stays unfinished and incomplete it tries to Examine the phosphorescence properties in Mg-CPO-27 induced by Mn doping, focusing on long-lived emission at low temperatures while evaluating the temperature dependence of phosphorescence, with emphasis on emission intensity and lifetime variation. In the work the role of ligand-to-metal charge transfer (LMCT) was observed and its influence on luminescence behaviour. The application of this work was the assessment of Mn-doped Mg-CPO-27's potential as a temperature-sensitive luminescent material, comparing its performance with MOFs doped with other paramagnetic metals.

By addressing these three research directions, this dissertation aims to provide a comprehensive understanding of the relationship between porous frameworks and

luminescent behaviour. The findings will contribute to the development of novel materials with tunable photophysical properties, expanding the possibilities for advanced sensing technologies, temperature-responsive materials, and optoelectronic applications.

3. Cumulative Part:

In the following two chapters, the results of the dissertation are presented, which were published as first-author articles in international journals. Each publication stands on its own with a separate numbering. The figures, tables, and schemes within the publications do not follow the main text. Likewise, the references used are listed in a separate bibliography at the end of each publication, which may result in some literature sources being cited twice. Published results with personal contributions as a co-author, as well as other unpublished results, are presented in Chapters 4.3 and 4.4

Each publication is introduced by its title, list of authors, journal name, and a short summary. Furthermore, the individual contributions of the authors to the publications are presented.

3.1 Synthesis of a luminescent Aluminum-based MOF for Selective iron(III) Ion sensing.

Hanibal Othman, István Boldog, Christoph Janiak:

Molecules **2025**, *30*(20), 4146**;** https://doi.org/10.3390/molecules30204146

Short summary:

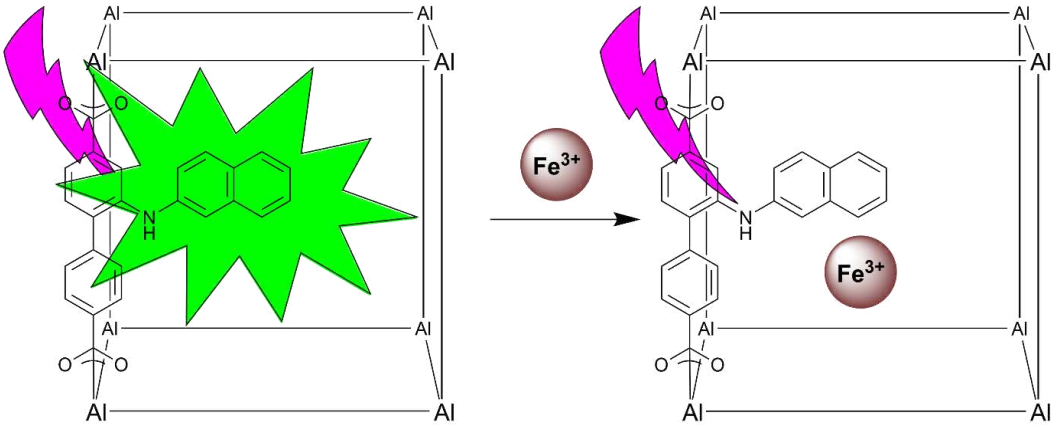

In the search for new materials to open up creative pathways for industry and research, modification is one of the best methods to implement. Developing materials with high sensitivity and selectivity for specific applications, such as ion sensing, remains a significant challenge. This work aims to introduce a novel metal-organic framework (MOF) derived from the well-established 2-amino-[1,1'-biphenyl]-4,4'-dicarboxylic acid MOF by modifying its structure to enhance its properties and applications. A luminescent 2-naphthyl moiety was attached to the amino group of the linker to form the new luminescent Al-based MOF Al-BP-Naph with a surface area of 456 $m^2\ g^{-1}$ and a pore volume of 0.55 $cm^3\ g^{-1}$. Al-BP-Naph showed high selectivity towards Fe^{3+} sensing due to the overlapping absorption and excitation spectra of both Fe^{3+} and MOF. The MOF demonstrated a detection limit of approximately $6 \cdot 10^{-6}$ mol L^{-1} with a limit of quantification of about $19 \cdot 10^{-6}$ mol L^{-1} and a very fast response time (less than 10 seconds). It also had a Stern–Volmer constant of approximately $0.09 \cdot 10^5$ L mol^{-1} , distinguishing it from other ions. Our work contributes to the expanding repertoire of functional materials with promising applications in sensing technologies, offering a novel MOF with superior properties for iron(III) ion detection.

Contribution to the publication:

- Hanibal Othman: Idea and concept development, synthesis and optimization of the reactions. N_2, CO_2 adsorption measurements and the calculation of the theoretical heat of adsorption. The measurement of spectral properties such as the excitation and emission spectra of the molecules. Assessment and interpretation of the results, writing and revision of the manuscripts.
- István Boldog: Structure solution using Le Bail fitting and description of the structure.

- Christoph Janiak: Assessment and interpretation of the results, writing and revision of the manuscripts.

molecules

MDPI

Article

Synthesis of a Luminescent Aluminum-Based MOF for Selective Iron(III) Ion Sensing

Hanibal Othman, István Boldog and Christoph Janiak *

Institut für Anorganische Chemie und Strukturchemie, Heinrich-Heine-Universität Düsseldorf, D-40204 Dusseldorf, Germany; hanibal.othman@hhu.de (H.O.); Istvan.Boldog@hhu.de (I.B.)
* Correspondence: janiak@uni-duesseldorf.de

Abstract

In the search for new materials to open up creative pathways for industry and research, modification is one of the best methods to implement. Developing materials with high sensitivity and selectivity for specific applications, such as ion sensing, remains a significant challenge. This work aims to introduce a novel metal–organic framework (MOF) derived from the well-established 2-amino-[1,1′-biphenyl]-4,4′-dicarboxylic acid MOF by modifying its structure to enhance its properties and applications. A luminescent 2-naphthyl moiety was attached to the amino group of the linker to form the new luminescent Al-based MOF Al-BP-Naph with a surface area of 456 $m^2 g^{-1}$ and a pore volume of 0.55 $cm^3 g^{-1}$. Al-BP-Naph showed high selectivity towards Fe^{3+} sensing due to the overlapping absorption and excitation spectra of both Fe^{3+} and MOF. The MOF demonstrated a detection limit of approximately 6×10^{-6} mol L^{-1} with a limit of quantification of about 19×10^{-6} mol L^{-1} and a very fast response time (less than 10 s). It also had a Stern–Volmer constant of approximately 0.09×10^5 L mol^{-1}, distinguishing it from other ions. Our work contributes to the expanding repertoire of functional materials with promising applications in sensing technologies, offering a novel MOF with superior properties for iron(III) ion detection.

Keywords: photoluminescence; metal–organic framework; limit of detection; iron sensing; Stern-Volmer equation

Academic Editor: Cheal Kim

Received: 11 September 2025
Revised: 10 October 2025
Accepted: 17 October 2025
Published: 21 October 2025

Citation: Othman, H.; Boldog, I.; Janiak, C. Synthesis of a Luminescent Aluminum-Based MOF for Selective Iron(III) Ion Sensing. *Molecules* **2025**, *30*, 4146. https://doi.org/10.3390/molecules30204146

1. Introduction

The development of sensors and materials that respond selectively to specific analytes is progressing for improved sensitivity, selectivity, and the range of detectable substances. These advancements are being driven by the need for more precise, reliable, and efficient analyte detection systems across various scientific and industrial fields. A particularly important area within the realm of sensing is photoluminescence sensing. The photoluminescent response can be classified as either positive or negative. In a positive response, known as photoluminescence enhancement or a "turn-on" reaction, the material's light emission increases when it encounters the analyte [1–4]. Conversely, in a negative response, referred to as photoluminescence quenching or a "turn-off" reaction, the material's emission is diminished or entirely suppressed in the presence of the analyte [5]. This dual capability makes photoluminescent sensors highly versatile and valuable in a wide range of applications, from environmental monitoring to biomedical diagnostics [6–10].

Iron is a critical element in both biological and industrial contexts and exemplifies the importance of precise analyte detection. In biological systems, iron plays a vital role

in various physiological processes, including oxygen transport, DNA synthesis, and electron transport within cells [11]. However, both iron deficiency and iron overload can lead to severe health complications, such as anemia in the case of deficiency or tissue damage and organ failure in cases of iron overload. Therefore, accurate quantification of iron in biological samples is crucial for effective medical diagnosis and treatment [12,13].

From industrial processes, large quantities of iron and other metals can be released into rivers, soil, and air, posing serious environmental and health risks. This necessitates stringent regulatory measures to monitor and limit the concentration of iron and other potentially harmful metals in the environment [14].

Metal–organic frameworks (MOFs) are emerging as powerful tools in the field of sensing. MOFs are porous structures formed through the coordination of metal ions with bridging organic linkers [15]. MOFs possess highly tunable properties, making them suitable for a wide array of applications, including photoluminescence sensing [16–19]. As photoluminescent sensors, MOFs have demonstrated exceptional sensitivity, capable of detecting a wide range of metal ions [20–22]. In this study, we introduce an aluminum metal–organic framework related to DUT-5 (Al(OH)(1,1′-biphenyl]-4,4′-dicarboxylate) [23], but synthesized using 2-(naphthalen-2-ylamino)-[1,1′-biphenyl]-4,4′-dicarboxylic acid (H_2BP-Naph), where we added the naphthylamino group to the biphenyl linker, achieving a strongly luminescent MOF (Scheme 1) [24]. The napthalene-2-ylamino luminophore group, and hence this newly developed MOF Al-BP-Naph, exhibits photoluminescent properties and experiences luminescence quenching in the presence of metal ions, most notably Fe^{3+}. We have investigated the quenching selectivity and concentration dependence for a potential sensing application of Al-BP-Naph. In line with related investigations in the literature, the MOF was applied as an N,N-dimethylformamide (DMF) dispersion because of the DMF properties with regard to polarity for metal-salt solubility and transparency in the UV-Vis region, due to its high refractive index (1.43), which minimizes the mismatch between the optical medium (quartz cuvettes) and the sample [25].

This work introduces Al-BP-Naph, a novel Al-based MOF that combines the stability of MIL-53-type frameworks with a naphthylamino-functionalized linker acting as an intrinsic luminophore. This MOF enables highly selective and rapid quenching by Fe^{3+} through spectral overlap, giving a low detection limit (5.6 μmol L^{-1}) and sub-10 s response time. These properties surpass many reported MOF sensors, highlighting the distinctiveness and novelty of Al-BP-Naph in luminescent iron sensing.

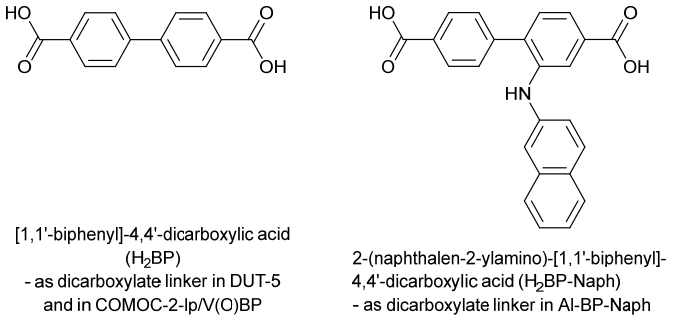

Scheme 1. Relevant linkers for the MOF structures in this work.

2. Results

The MOF compound Al-BP-Naph was synthesized from 2-(naphthalen-2-ylamino)-[1,1′-biphenyl]-4,4′-dicarboxylic acid [26] and aluminum nitrate nonahydrate in DMF. The structural analogy of the synthesized material Al-BP-Naph to the MOFs DUT-5 [23] and the related COMOC-2-lp/V(O)BP [27] was confirmed by powder X-ray powder diffraction

(PXRD) studies (Figure 1). The material is generally crystalline with a well-defined short-to-medium-range periodicity; however, there are also indications of compromised crystallinity, witnessed by a relatively high background. It is worth noting in this context that aluminum MOFs tend to form products with at least partially compromised crystallinity due to the low reversibility of the crystallization process. This is also the reason why Al-MOFs are often hard to obtain in single crystalline form for diffraction studies, which is also the case here.

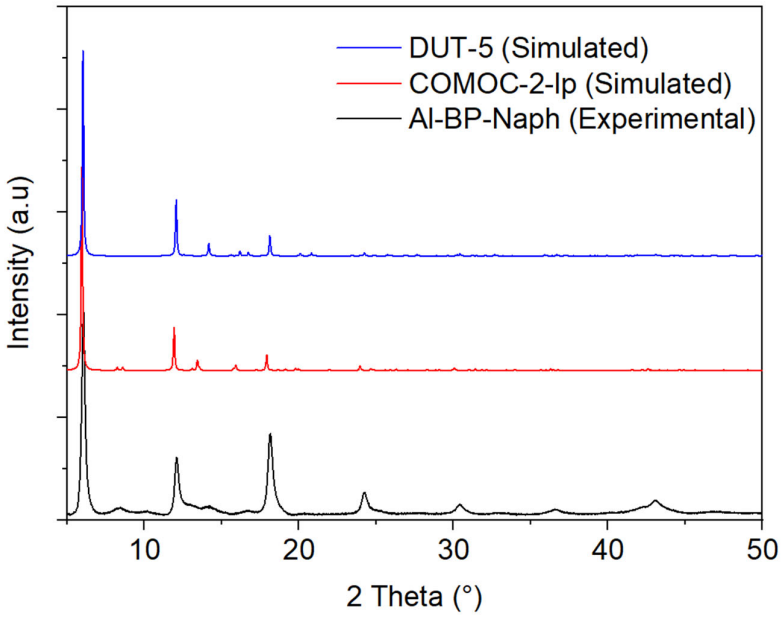

Figure 1. PXRD comparison between Al-BP-Naph dried at 70 °C for 24 h using a vacuum oven (1×10^{-3} bar), and the simulation for DUT-5 and COMOC-2-lp from the CCDC ref codes 691979 and 868306, respectively [23,27]. The background of the experimental pattern was removed (see the uncorrected pattern in Figure S4).

The indicators of somewhat lowered crystallinity are also expected as manifestations of structural flexibility. The latter is inherent in the "wine-rack" type MIL-53 structure (Figure 2), which can potentially adapt a continuous range of geometries within the Imma space group, which was assumed to be the same as in the case of COMOC-2-lp/V(O)BPDC and DUT-5 (see Figures S4–S9 and Table S1) [23,27].

The cell parameters vary slightly for the three compounds, which represent the open form of the MIL-53-type structure. Despite the same length of the ligand, the discussed slight flexibility of the framework, associated with the hinge-like movement of the ligands related to the secondary building unit (see Figure S6 for the cell overlap of Al-BP-Naph and COMOC-2-lp), can lead to a difference in the length of the a and c axis (cf. Figure 2; elongation of c when a becomes shorter and vice versa).

The low crystallinity can be further attributed to the disorder and amorphosity introduced into the lattice by the naphthylamino group attached to the side of the linker. The presence of this pendant group creates significant variability in the crystal structure because its orientation within the pore framework can occur on both sides of the linker (Figure 2). The significant disorder in this part of the structure restricted the refinement to the Le Bail method, as described in the Supplementary Materials [27].

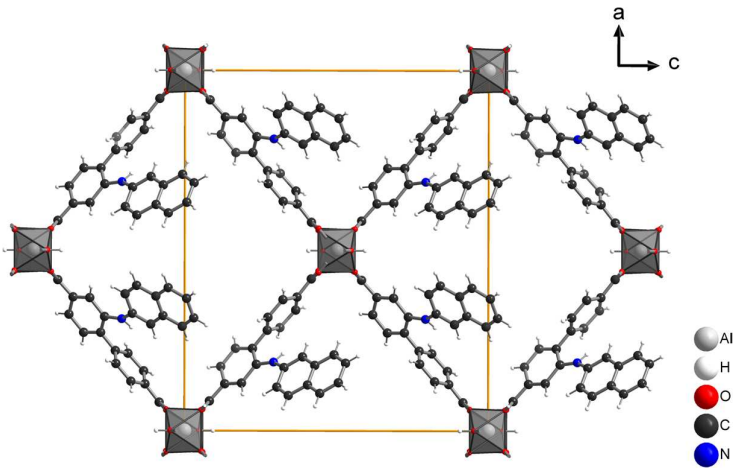

Figure 2. View along the b-axis for the structure of Al-BP-Naph with the "wine-rack" MIL-53 topology, demonstrating an approximate possible regular localization of the pendant naphthylamino group. The orange line is the unit cell outline.

Furthermore, the stability of the Al-BP-Naph material after being exposed to ambient air conditions at RT for 7 days and after activation for adsorption measurements was positively verified by PXRD (Figure S9), in line with the usual high stability of the MIL-53(Al)-type materials. Al-BP-Naph retained its crystallinity under these conditions, which is important for practical applications where prolonged exposure to ambient conditions is expected. However, its structural integrity was largely lost when heated to 90 °C for 24 h (Figure S9).

Thermogravimetric analysis (TGA) in Figure S11 of the dried MOF with the molecular formula [Al(OH)(BP-Naph)] = ($AlC_{24}H_{16}NO_5$) (revealed an initial mass loss of 10% between 60 °C and 160 °C, which is attributed to the release of residual ethanol and DMF solvents used during synthesis and trapped within the porous structure. Following this mass loss, a plateau is observed until approximately 400–500 °C, where a significant mass loss of 77% occurs, corresponding to the thermal decomposition of the organic linker (BP-Naph). When the contribution of the solvent loss is excluded and the mass at 225 °C is rescaled to 100%, the mass loss around 1000 °C becomes 88%, which matches the theoretical linker content (89.7%) of $C_{24}H_{15}NO_4$ in $AlC_{24}H_{16}NO_5$. The corrected residual mass at 1000 °C becomes 11.7% which agrees with the expected amount of Al_2O_3 (theor. 11.98% for 6.34 wt% of Al). Since the analysis was conducted under a synthetic air atmosphere, it is reasonable to assume that all aluminum present in the framework was fully converted to Al_2O_3.

IR spectroscopy in Figure S10 shows a shift in the C=O stretching mode between the linker and the MOF, indicating the coordination of the carboxylate group to the metal and also demonstrating the near absence of the non-deprotonated linker pore-filling impurity, which is typical for such compounds.

The surface area and porosity of Al-BP-Naph were analyzed through N_2 adsorption studies at 77 K. The adsorption isotherm of Al-BP-Naph is a combination of type I at lower and type II at higher relative pressures (Figure 3a). The steep uptake at low P/P_0 is indicative of a microporous material giving the type I isotherm. Type II isotherms stem from the physisorption on nonporous or macroporous adsorbents, here from the interparticle condensation. The composite type I and II isotherms often have an H4 hysteresis loop, which is also observed with aggregated crystals of zeolites, some mesoporous zeolites, and micro-mesoporous carbons [28]. From the adsorption branch, a BET surface area of approximately 456 $m^2\ g^{-1}$ was calculated (over a pressure range of P/P_0 = 0.04–0.1 with a correlation coefficient R^2 of 0.999 and a BET constant C of 183.9, Figure S13). The total pore volume was found to be 0.546 $cm^3\ g^{-1}$, with a micropore volume of 0.215 $cm^3\ g^{-1}$. For DUT-5, the surface area is 1413–1467 $m^2\ g^{-1}$, and the pore volume is ~0.71 $cm^3\ g^{-1}$ [29,30]. The

pore size distribution from NLDFT calculations indicates a fraction of 40% of micropores (<2 nm) and 60% mesopores (2–50 nm) (Figure 3b).

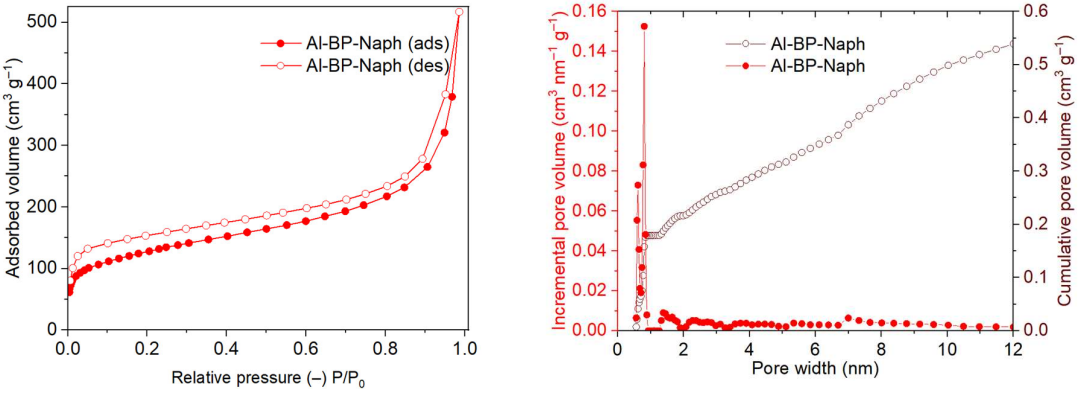

(**a**) (**b**)

Figure 3. (**a**) Al-BP-Naph N_2 sorption isotherm at 77 K (filled symbols: adsorption, empty symbols: desorption). (**b**) Pore size distribution using the slit pore, NLDFT equilibrium model.

CO_2 adsorption of Al-BP-Naph was examined at 273 K and 293 K with uptakes of 30.1 $cm^3\ g^{-1}$ and 29.4 $cm^3\ g^{-1}$, respectively. This CO_2 uptake is similar to the biphenyl-based MOFs of the same structure, such as DUT-5 (36.2 $cm^3\ g^{-1}$ at 298 K) [29] and COMOC-2 (19.0 $cm^3\ g^{-1}$) [31]. From the uptake at the two temperatures, the isosteric heat of adsorption near zero coverage was computed to 26 kJ mol^{-1} (Figure 4b), and this value drops with increasing uptake at 1 mmol g^{-1} to about 3.5 kJ mol^{-1}, which is below the heat of liquefaction of CO_2 [32] (see Section S6 for details). The heat of adsorption or the affinity for CO_2 diminishes with increasing uptake, as the higher-binding energy sites become increasingly occupied [33,34]. This isosteric heat of adsorption near zero coverage for CO_2 is similar to the values of UiO-67-$(NH_2)_2$- [35] and COMOC-2 [31] with around 30 kJ mol^{-1} and to other MOFs with a biphenyl linker (Table S3) [36–38].

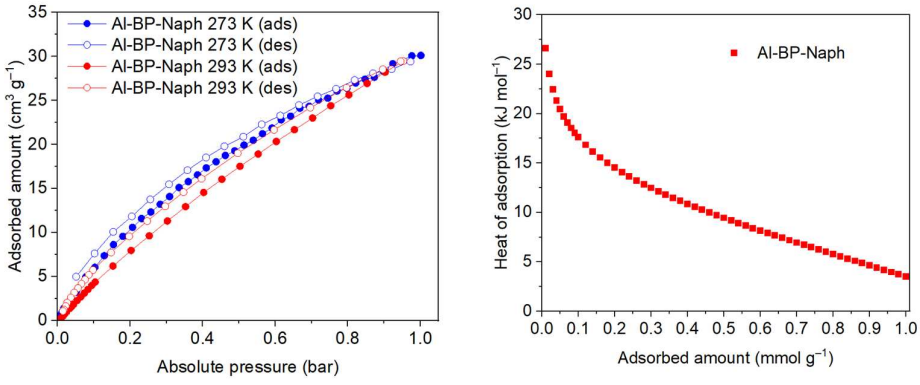

(**a**) (**b**)

Figure 4. (**a**) CO_2 sorption isotherms of Al-BP-Naph at 273 K and 293 K (filled symbols: adsorption, empty symbols: desorption). (**b**) Isosteric heat of CO_2 adsorption in Al-BP-Naph with increasing uptake.

The newly synthesized Al-based metal–organic framework (Al-BP-Naph) incorporates a naphthyl-substituted biphenyl linker bearing a naphthylamino functionality, which acts as a separate luminophore and enhances the framework's luminescence. Al-BP-Naph exhibits intrinsic photoluminescence, with an emission maximum observed in DMF suspension at 520 nm (Figure 5). A slight solvatochromic shift is noted compared to

the emission of the dry solid-state (510 nm), which is attributed to interactions between the naphthyl group in the MOF and the adsorbed solvent molecules that modulate the electronic environment and optical behavior, as it is also seen for the free linker H_2PB-Naph when comparing the solid-state and its DMF solution (Figure 5b).

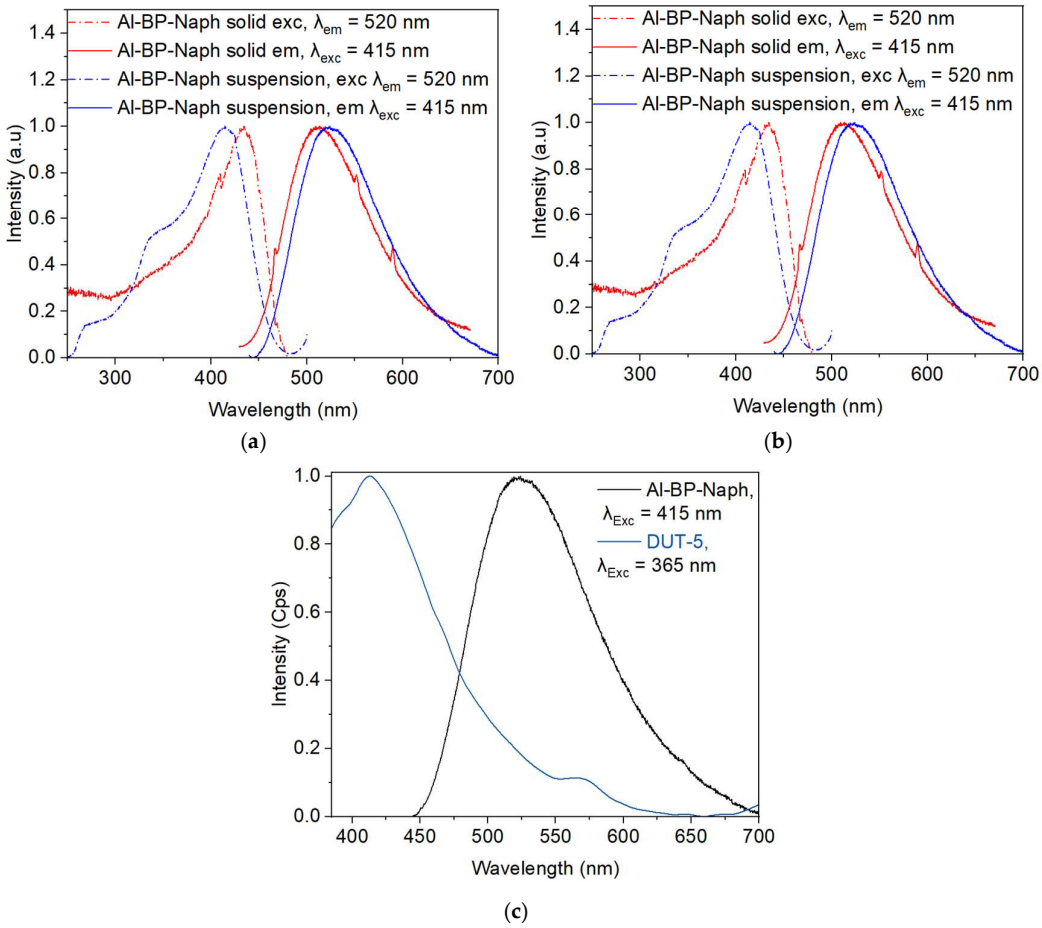

Figure 5. (**a**) Excitation (dashed lines) and steady-state photoluminescence spectra (solid lines) of Al-BP-Naph in solid form (red) and suspended (blue curves) in DMF. (**b**) H_2BP-Naph linker excitation and emission spectrum in DMF and the solid state. (**c**) Emission spectra of Al-BP-Naph and DUT-5, where Al-BP-Naph was excited at λ_{exc} = 415 nm and DUT-5 at λ_{exc} = 365 nm.

The emission of Al-BP-Naph was tested for the presence of metal ions in the DMF dispersion of the MOF and found to lead to various degrees of quenching of the emission intensity at 520 nm when the suspension was excited with 415 nm light. Fe^{3+} ions (c = 0.001 mol L^{-1}, added as $Fe(NO_3)_3$) result in strong emission quenching by about 75%. The metal ions Cr^{3+} and Zn^{2+} are quenched by only 22% and 13%, respectively, whereas the metal ions Mg^{2+}, Mn^{2+}, Co^{3+}, and Ni^{2+} leave the emission intensity unchanged, and, in contrast, the ions Ag^{+}, Al^{3+}, Pb^{2+}, Cd^{2+}, Ca^{2+} and Li^{+} even enhance the luminescence by about 10–20% (all at a concentration of 0.1 mol L^{-1}) (Figure 6).

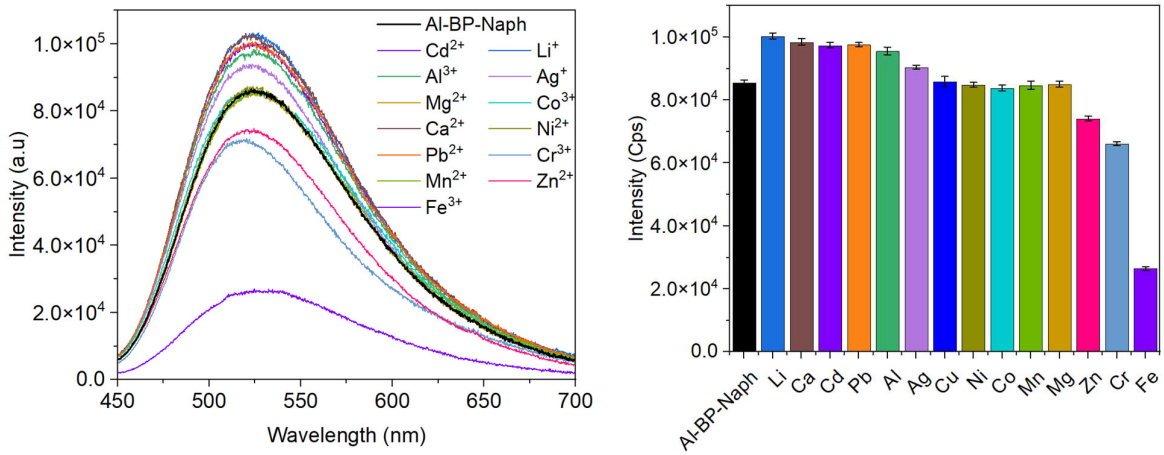

(**a**) (**b**)

Figure 6. (**a**) Emission spectra (λ_{exc} = 415 nm) of Al-BP-Naph (as DMF suspension of 1 g L^{-1}) in the presence of different metal ions at concentrations of 0.003 mol L^{-1}. (**b**) Luminescence intensity comparison of Al-BP-Naph for different metal ions with concentrations and ion charges as in (**a**). The intensity error was estimated to ±0.2 × 10^4.

As it was found that the emission of Al-BP-Naph is particularly quenched by Fe^{3+} ions (Figure 6), an increase in Fe^{3+} concentration led to a progressive quenching of the emission and was quantitatively analyzed using the Stern–Volmer Equation (1), which revealed a relatively high Stern-Volmer constant of 0.09 × 10^5 L mol^{-1} (Figure 7b). This high constant indicates that Fe^{3+} is an effective quencher of the luminescence of Al-BP-Naph.

$$I_0/I - 1 = K_{SV}\,Q \quad (1)$$

where

I_0: Luminescence intensity of pristine Al-BP-Naph in DMF suspension.
I: Luminescence intensity of Al-BP-Naph in the presence of Fe(III) ions in DMF
K_{SV}: Stern-Volmer constant
Q: Concentration of the quenching Fe^{3+} ions

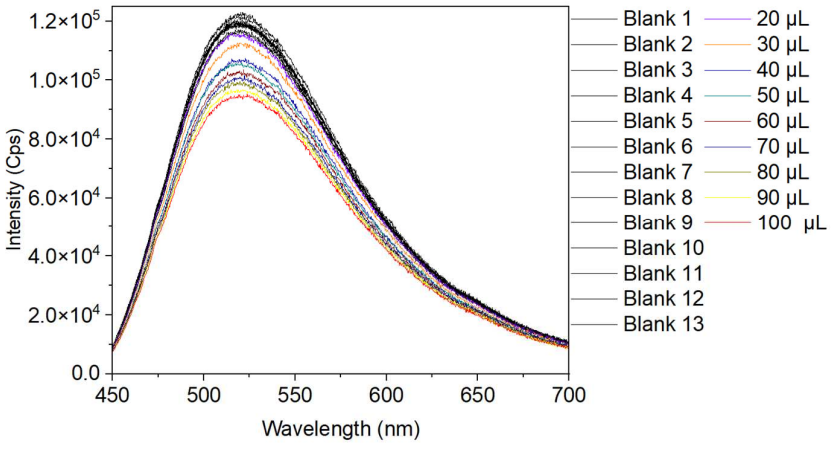

(**a**)

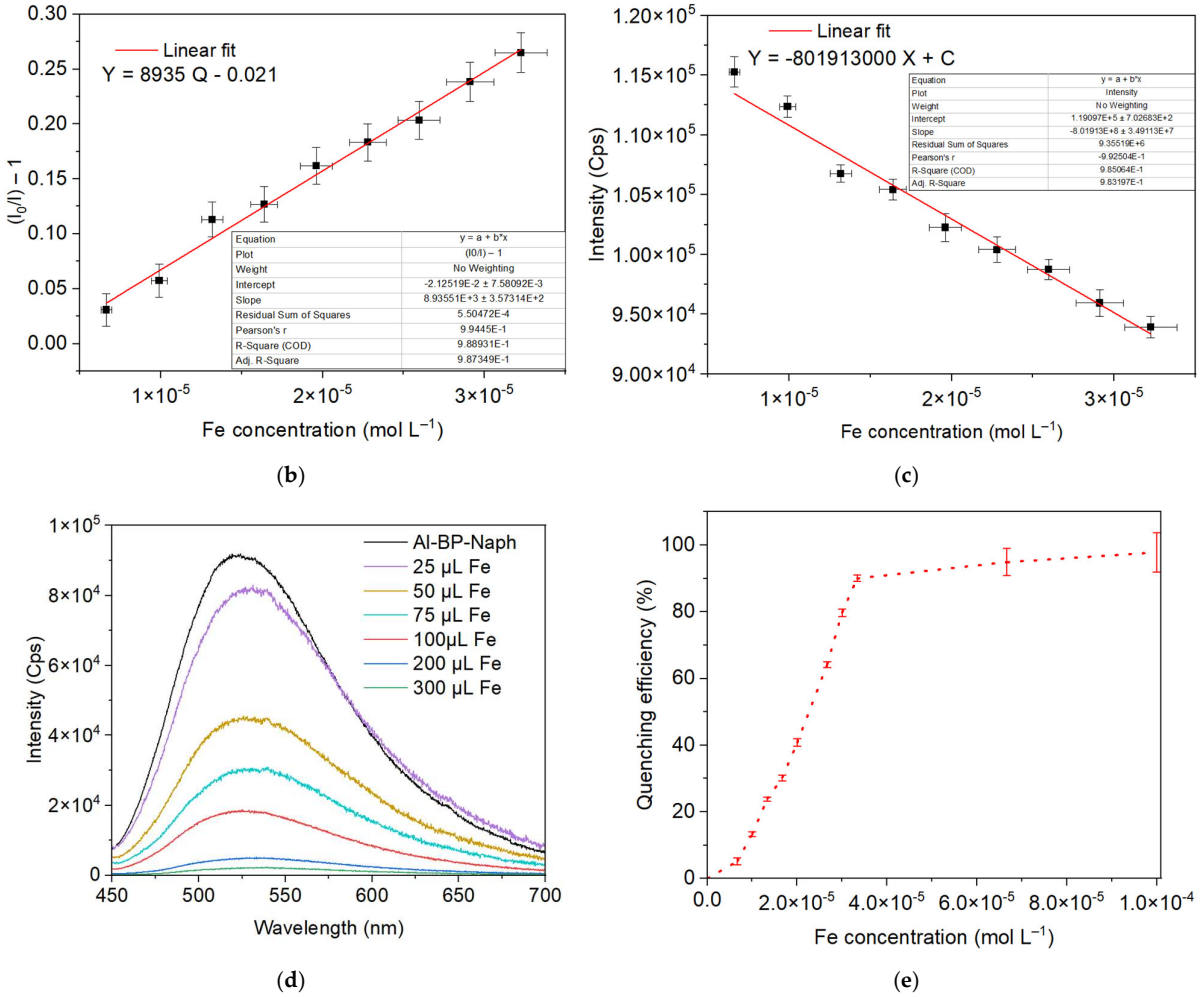

Figure 7. (**a**) Al-BP-Naph emission response (λ_{exc} = 415 nm) in DMF suspension (3.0 mL) to increasingly added volumes of a DMF Fe^{3+} solution (c = 0.001 mol L^{-1}) (thirteen measurements for the blank sample Al-BP-Naph), (**b**) Stern–Volmer plot for the fluorescence intensity of Al-BP-Naph to different concentrations of Fe^{3+}, (**c**) fit of the fluorescence intensity versus analyte ion concentration, (**d**) Al-BP-Naph response as DMF suspension to different amounts/concentrations of Fe^{3+} for the calculation of the quenching efficiency, (**e**) quenching efficiency to concentrations of Fe^{3+}. In (**b**) the error σ for $(I_0/I) - 1$ was derived from the general law of propagation of uncertainty $\sigma = (I_0/I)r\sqrt{2}$ and r = 1% from the relative error in the emission intensities. In (**c**) the intensity error was estimated to be ±0.2 × 10^4. The accuracy of the Fe^{3+} concentration was estimated with its dissolution and dilution procedures to ±5% and the error bars were added accordingly to (**b**,**c**) for the Fe-concentration axis. The error of the quenching efficiency in (**e**) was derived by calculating the relative error at each absorption maximum in (**d**) from the noise, divided by the absorption intensity, and adding this value as the error bar to the efficiency axis.

The proposed mechanism for the observed quenching effect is suggested to involve competitive absorption of the energy required for the excitation of the MOF. In this scenario, the energy intended to excite the MOF is instead absorbed by another species—in this case, the cation from the metal nitrate that is in direct contact with the MOF structure. The quenching effect observed in the presence of iron ions can be attributed to the overlap between the absorption spectrum of Fe^{3+} ions, which typically spans the wavelength range of 200 to 450 nm [34], and the excitation spectrum of Al-BP-Naph in DMF suspension (Figure S15). This spectral overlap results in a significant portion of the excitation energy

being absorbed by the iron ions rather than by the MOF itself. Consequently, this absorption by Fe^{3+} ions leads to a reduction in the energy available for exciting the MOF, which in turn causes a pronounced quenching of the emission in the suspension. In contrast, the absorption spectra of other metal nitrates, which were also tested, showed less overlap with the MOF excitation region (Figure S15), suggesting a reduced ability to interfere with the MOF's excitation process. These findings lend further credence to the idea that iron nitrate uniquely quenches the MOF's fluorescence via this competitive absorption mechanism.

We dismiss static quenching, that is, a complex formation between the naphthylamino fluorophore and Fe^{3+}, because among the tested metal ions, also Cr^{3+}, Mn^{2+}, Co^{2+}, Ni^{2+}, Cu^{2+}, and Cd^{2+} are known to readily form amine complexes. Dynamic quenching can occur when a quencher molecule collides with the excited fluorophore, transferring energy or electrons and returning the fluorophore to its ground state non-radiatively, which decreases fluorescence intensity but can also be excluded as the radius of high-spin Fe^{3+} is 0.78 Å, which is larger than for Al^{3+}, Co^{2+} and Cr^{3+} and smaller than for Mg^{2+}, Li^{+}, Pb^{2+}, Ni^{2+}, Mn^{2+}, Cd^{2+}, Ag^{+}, Ca^{2+}, Zn^{2+} and Cu^{2+} [39]. Thus, at least the ions Al^{3+}, Co^{2+} and Cr^{3+} (which are smaller than Fe^{3+}) could diffuse into the MOF similar to Fe^{3+} and result in dynamic quenching, which is, however, not seen.

The luminescence intensity at 520 nm displayed a negative linear correlation with Fe^{3+} concentration within the range of 6.6×10^{-6} to 3.2×10^{-5} mol L^{-1}, with a correlation coefficient (R^2) greater than 0.98, as illustrated in Figure 7b,c. This strong linear relationship allows for precise quantification of Fe^{3+} concentrations. The Stern-Volmer quenching constant (K_{SV}) calculated from these measurements reached a value of 0.09×10^5 L mol^{-1}, which underscores the high efficiency of iron ions in quenching the luminescence of the MOF. The quenching efficiency was calculated using the formula $(I_0/I - 1) \times 100\%$ where I_0 and I are the values of the luminescence intensity of pristine Al-BP-Naph- and Fe^{3+}-loaded Al-BP-Naph, respectively, indicating that Al-BP-Naph showed a high sensitivity in sensing fluorescence quenching. The quenching efficiency was close to 100% when the added volume of the Fe^{3+} solution reached 300 μL (giving an Fe^{3+} concentration of 10^{-4} mol L^{-1} in the Al-BP-Naph suspension) (Figure 7d,e).

Additionally, the limit of detection (LOD) for iron(III) nitrate was determined as low as about 6 μmol L^{-1}. This was calculated using the equation LOD = 3 σ/k, where σ represents the standard deviation of the 13 blank measurements (Table S4) and k denotes the slope of the fitting line of fluorescence intensity versus analyte ion concentration in Figure 7c. This low detection limit demonstrates the exceptional sensitivity of Al-BP-Naph and its capability for detecting very small concentrations of iron ions in solution. The limit of detection of Al-BP-Naph is lower than in many other MOFs in the field of iron detection, such as CdBPTC, Ni-MOF, Zn-MOF, and Cd-MOF with LODs of 17, 15, 28, and 57 μmol L^{-1}, respectively [16,40,41]. A detailed comparison can be seen in Table 1. The limit of quantification was also calculated with the equation LOQ = 10 σ/k with a value of 19 μmol L^{-1}. The MOF Al-BP-Naph presented in this work shows one of the best results when it comes to the limit of detection for Fe^{3+}.

The slight luminescence enhancement that is observed with Ag^{+}, Al^{3+}, Pb^{2+}, Cd^{2+}, Ca^{2+} and Li^{+} (Figure 6a) can be a result of the adsorption of these cations on the surface of Al-BP-Naph, perhaps through interaction between naphthyl-π system and the cations causing a slight change in the electronic properties of the naphthyl moiety, enhancing in turn the radiative relaxation pathways [42–44].

Table 1. Literature comparison for MOFs as Fe^{3+} sensors.

Sample	Solvent	LOD [μmol L^{-1}] [a]	LOD [μg mL^{-1}] [a]	K_{SV} [L mol^{-1}] [b]	Ref.
This work	DMF	5.6	0.31	0.09×10^5	This work
$Cu_{0.1}$/Zn-MOF	Water	833	46.51	0.27×10^5	[12]
EuBDC-OMe	Water	2.9	0.16	0.18×10^5	[13]
CdBPTC	Water	16.6	0.92	0.08×10^5	[17]
[Eu(BTPCA)(H_2O)]	DMF	10	0.55	-	[20]
Ni-MOF	EtOH	15	0.86	-	[40]
DMAC	DMAC	60	3.35	0.78×10^{-5}	[45]
EuOHBDC	Water	1.17	0.06	45.64	[46]
NNU-1	Water	200	11.2	-	[47]
Zn-MOF	Water	28	1.56	0.16×10^5	[41]
Cd-MOF	Water	57	3.18	0.10×10^5	[41]
[Eu(H_2O)$_2$(BTMIPA)]	Water	10	0.55	-	[48]
[Zn_2(L)$_2$(bpe)$_2$(H_2O)$_2$]	Water	25	1.39		[49]
MI-53-(Al)	Water	0.9	0.05	-	[50]
[Tb(HL)(DMF)(H_2O)$_2$] 3H_2O	Water	50	2.79	0.04×10^5	[51]
CALIX@UiO-66-NH_2	Water	6.7	0.37	0.02×10^5	[52]
Eu(L1)$_3$	Water	100	5.58	-	[53]
FJI-C8	DMF	23	1.30	0.08×10^5	[54]
[Eu_2(MFDA)$_2$(HCOO)$_2$(H_2O)$_6$ H_2O	DMF	0.33	0.018	-	[55]
Tb^{3+}@Cd-MOF	DMF	10	0.56	1.10×10^5	[56]

[a] LOD = limit of detection in two different units. [b] K_{SV} = Stern-Volmer constant.

3. Materials and Methods

Methyl-3-amino-4-bromobenzoate, 2-bromonaphthalene (98%), and (4-(methoxycarbonyl)phenyl)boronic acid (99.87%) were purchased from BLDpharm, and tetrakis(triphenylphosphine)palladium(0) (99%) and tri-tert-butyl phosphine (98%) from Sigma-Aldrich and used as received. Aluminum nitrate nonahydrate 98% was obtained from Roth. All solvents were bought from commercial suppliers with a minimum purity of 99.8% and used as received.

The ultrasonic device is a 2.8 L ultrasonic cleaner from Avantor (Avantor, Bruchsal, Germany). The oven used was a UNP 200–800 universal oven from Memmert (Memmert, Büchenbach, Germany). Fourier transform infrared spectroscopic measurements were performed using a Bruker Tensor 37 (Bruker AXS, Karlsruhe, Germany) with KBr pellets in the range between 4000 and 500 cm^{-1}. For the N_2 and CO_2 sorption analysis, a Quantachrome Autosorb-IQ-MP (Quantachrome, Boynton Beach, FL, USA) was used. The samples were degassed for 24 h at 170 °C before the gas sorption measurements. The N_2 sorption isotherms were collected at 77 K. The results were interpreted with the BET equation. The CO_2 sorption temperatures were 293 and 273 K. The temperatures were held by virtue of a thermostated water bath (293 and 283 K) or with a Dewar filled with liquid N_2 (77 K).

Thermogravimetric analysis was performed with a TG Tarsus 209 F3 (Netzsch, Selb, Germany). The samples were analyzed under synthetic air with a heating rate of 10 K/min from 25 to 1000 °C. Powder X-ray diffraction patterns were recorded using a Bruker D2 phaser benchtop diffractometer from Bruker (Bruker AXS, Karlsruhe, Germany) with Cu-Kα radiation, λ = 1.54182 Å at 300 W, 30 kV, and 10 mA. Nuclear magnetic resonance (^{1}H-NMR) spectra were collected with a Bruker Avance III-600-I (Bruker, Karlsruhe, Germany). The chemical shifts are given in ppm and referenced to the residual proton signal of the solvent versus TMS ($CDCl_3$: 7.26 ppm, DMSO-d6: 2.50 ppm). The excitation and photoluminescence spectra were measured with an FS5 spectrofluorometer from

Edinburgh Instruments (Edinburgh, Scotland) with a 150 W CW ozone-free xenon arc lamp as a light source.

3.1. Synthesis of Dimethyl-2-Amino-[1,1'-biphenyl]-4,4'-Dicarboxylate [26]

In a three-neck 250 mL round-bottom flask, (4-(methoxycarbonyl)phenyl)boronic acid (40 mmol, 7.20 g) was mixed with methyl-3-amino-4-bromobenzoate (40 mmol, 9.20 g), tetrakis(triphenylphosphine)palladium (0) (1.8 mmol, 2.1 g), and potassium carbonate (180 mmol, 25 g) in 1,4-dioxane (160 mL) and water (40 mL). A clear solution was obtained in the flask when the mixture was refluxed at 100 °C for 24 h. The reaction was monitored via thin layer chromatography (TLC), and after completion, the reaction mixture was allowed to cool to room temperature, and the contents of the flask were filtered, and the resulting phase was extracted with 3 × 30 mL ethyl acetate. After separation, the organic phase was dried over magnesium sulfate for 15 min. The salt was then filtered, and the organic phase was concentrated using a rotary evaporator. The resulting red solid was dried overnight using a high vacuum oven at 60 °C. The crude product was purified by column chromatography using n-hexane: ethyl acetate (2:1 v:v) as eluent, resulting in the formation of white needle-like crystals. Yield = 6.7 g, 58%. ^{1}H-NMR spectrum in Figure S1.

3.2. Synthesis of Dimethyl-2-(Naphthalen-2-ylamino)-[1,1'-biphenyl]-4,4'-Dicarboxylate

In a two-neck 100 mL round-bottom flask, 2-bromonaphthalene (3.8 mmol, 0.787 g, 1 eq) was dissolved in 40 mL of degassed dry toluene, and to this solution, 5 mol% each of palladium acetate (0.042 g) and tri-tert-butyl phosphine (0.05 mL) were added. This mixture was stirred under nitrogen for 10 min until the solution changed to a dark red color. After the color change, dimethyl-2-amino-[1,1'-biphenyl]-4,4'-dicarboxylate (4.5 mmol, 1.3 g, 1.2 eq) was further dissolved in 40 mL of toluene along with potassium carbonate (8 mmol, 1.1 g, 10 eq). The mixture was allowed to reflux at 111 °C for 24 h under thin-layer chromatography (TLC) monitoring. After cooling to room temperature, the contents were filtered, and the remaining solids were washed with ethyl acetate (3 × 50 mL). Afterwards, the ethyl acetate solution was washed with deionized water three times, with 50 mL each. After separation of the organic phase, consisting of toluene and ethyl acetate, it was dried over $MgSO_4$ for 15 min, then concentrated using a rotary evaporator. The crude product was purified using flash column chromatography on silica gel 40–63 μm—Silicycle with a (v:v) 2:1 or 3:1 eluent of cyclohexane/ethyl acetate. The yield of the isolated yellow powder was 0.78 g, 50%. IR spectrum, Figure S10, ^{1}H-NMR, Figure S2.

The up-scaled reaction of this compound was performed as follows: In a two-neck 1 L round-bottom flask, 2-bromonaphthalene (24.7 mmol, 5.116 g, 1 eq) was dissolved in 260 mL of degassed dry toluene. To this solution, 5 mol% each of palladium acetate (0.273 g) and tri-tert-butylphosphine (0.325 mL) were added. The mixture was stirred under nitrogen for 10 min until the solution turned dark red. After the color change, dimethyl-2-amino-[1,1'-biphenyl]-4,4'-dicarboxylate (29.25 mmol, 8.45 g, 1.2 eq) was dissolved in another 260 mL of toluene, along with potassium carbonate (52 mmol, 7.15 g, 10 eq). The reaction mixture was then refluxed at 111 °C for 24 h, under TLC monitoring. After cooling to room temperature, the contents were filtered, and the remaining solids were washed with ethyl acetate (3 × 100 mL). The combined organic phase was then washed with deionized water (3 × 100 mL). The organic layer (toluene + ethyl acetate) was dried over $MgSO_4$ for 15 min, then concentrated using a rotary evaporator. The crude product was purified by flash column chromatography on silica gel (40–63 μm, Silicycle), using a 2:1 or 3:1 v:v mixture of cyclohexane/ethyl acetate as eluent. The isolated product was obtained as a yellow powder. The yield was 5.3 g, 52%. The IR and ^{1}H-NMR spectra were identical to those in Figures S10 and S2.

3.3. Synthesis of 2-(Naphthalen-2-ylamino)-[1,1′-biphenyl]-4,4′-Dicarboxylic Acid

In a 100 mL round-bottom flask, dimethyl-2-(naphthalen-2-ylamino)-[1,1′-biphenyl]-4,4′-dicarboxylate (3.0 g, 7.2 mmol) was dissolved in 40 mL of THF. To this solution, 40 mL of NaOH (1 mol L^{-1}) solution was added and refluxed for 24 h at 100 °C. After cooling down to room temperature, THF was removed using a rotary evaporator. To the aqueous phase, 40 mL of a 0.1 mol L^{-1} HCl solution was added. The yellow solid was filtered and dried under vacuum at 80 °C. Yield = 2.49g, 90%. IR spectrum Figure S10, ^{1}H-NMR Figure S3.

3.4. Synthesis of the Al-BP-Naph

2-(Naphthalen-2-ylamino)-[1,1′-biphenyl]-4,4′-dicarboxylic acid (0.2 mmol, 0.076 g) and aluminum nitrate nonahydrate (0.2 mmol, 0.075 g) were dissolved in 6 mL of DMF with the assistance of the ultrasound device. The reaction mixture was heated to 110 °C over 1 h, held at this temperature for 24 h, and allowed to cool to room temperature within 1 h. The precipitated powder was separated by centrifugation and subsequently washed with 40 mL of DMF via a treatment at 80 °C for 24 h in a flask with occasional mild stirring to avoid mechanical deterioration of the product. The product was separated by centrifugation and dried at 70 °C for 24 h using a vacuum oven (1×10^{-3} bar). The yield after the washing and drying was 119 mg, 80%.

3.5. Quenching Experiments

To evaluate the quenching selectivity and sensitivity of Al-BP-Naph, suspensions were prepared in DMF at concentrations of 1 g L^{-1} for selectivity studies and 0.1 g L^{-1} for sensitivity measurements. In the selectivity experiments, various metal nitrate solutions (c = 0.1 mol L^{-1}) were employed from which 100 µL were added to the 3.0 mL of the Al-BP-Naph DMF suspension to give a metal ion concentration of 0.003 mol L^{-1}. In the sensitivity experiments, the concentration of the added iron(III) nitrate solution was 0.001 mol L^{-1}, from which 10 µL aliquots were added to the Al-BP-Naph suspension

For each measurement, 3.0 mL of the Al-BP-Naph suspension was transferred into a thoroughly cleaned quartz cuvette. The initial emission intensity of the suspension was recorded as a reference (blank) prior to the incremental addition of the analytes in steps of 10, 25 or more µL in the sensitivity experiments. All experiments were conducted under identical conditions to ensure maximum reproducibility and comparability of results.

4. Conclusions

In this work, we present a luminescence sensor based on a functionalized MOF with a MIL-53 or DUT-5 topology bearing a naphthylamino chromophore group on the linker. Al-BP-Naph exhibits a surface area of 465 m^2 g^{-1} and a total pore volume of 0.546 cm^3 g^{-1}, with a zero-coverage isosteric heat of CO_2 adsorption of 26 kJ mol^{-1}. Contrary to the solid MOF, the suspended MOF in DMF shows a slight red shift due to the solvatochromic effect. The MOF displays exceptional luminescence sensitivity for the detection of Fe^{3+} ions with a rapid turn-off response and a remarkably high Stern-Volmer constant of 9000 L mol^{-1} when we excited the MOF suspension at 415 nm and monitored the luminescence at 520 nm. Our findings indicate that Fe^{3+} in solution competes for the excitation energy required for the luminescence of Al-BP-Naph, effectively quenching the MOF's emission through a competitive energy absorption mechanism. This quenching effect is highly selective, as no significant response was observed for other metal ions. The fast response within 10 s to iron excludes the possibility of any complex formation causing static quenching. Similar ionic radii of other tested metal ions compared to Fe^{3+} exclude dynamic quenching.

Furthermore, the sensitivity of the MOF toward Fe^{3+} is seen with a concentration lower than 5.6×10^{-6} mol L^{-1}. The calculated limit of detection (LOD) of 5.6×10^{-6} mol L^{-1} (rounded to 6×10^{-6} mol L^{-1}) highlights its potential as a highly efficient iron nitrate sensor. These combined results establish Al-BP-Naph as a promising candidate for practical applications in luminescent Fe^{3+} sensing.

Supplementary Materials: The following supporting information can be downloaded at https://www.mdpi.com/article/10.3390/molecules30204146/s1: Section S1: Reaction schemes for ligand synthesis (Scheme S1–S3) and nuclear magnetic resonance spectra; Section S2: Structure determination and PXRD pattern; Section S3: Infrared spectroscopy; Section S4: Thermogravimetric analysis; Section S5: Digestion NMR analysis; Section S6: N_2 adsorption; Section S7: CO_2 adsorption and isosteric heat (enthalpy) of adsorption; Section S8: Photoluminescent properties; Section S9: References. Reference [57] is cited in the Supplementary Materials.

Author Contributions: Conceptualization, H.O.; methodology, H.O. and I.B.; software, H.O.; validation, C.J. and H.O.; formal analysis, H.O.; investigation, H.O.; resources, C.J.; data curation, H.O.; writing—original draft preparation, H.O.; writing—review and editing, H.O. and C.J.; visualization, H.O.; supervision, C.J.; project administration, C.J. All authors have read and agreed to the published version of the manuscript.

Funding: C. J. thanks the Deutsche Forschungsgemeinschaft (DFG, German Research Foundation) for grant 396890929/GRK 2482.

Institutional Review Board Statement: Not applicable.

Informed Consent Statement: Not applicable.

Data Availability Statement: The original contributions presented in this study are included in the article/Supplementary Material. Further inquiries can be directed to the corresponding author(s).

Acknowledgments: The authors would like to thank Birgit Tommes for providing the IR measurements. We also thank the Center for Molecular and Structural Analytics at Heinrich Heine University (CeMSA@HHU) for recording the mass spectrometric and NMR spectrometric data.

Conflicts of Interest: The authors declare no conflicts of interest.

References

1. Yu, C.; Luo, M.; Zeng, F.; Wu, S. A fast-responding fluorescent turn-on sensor for sensitive and selective detection of sulfite anions. *Anal. Methods* **2012**, *4*, 2638–2640. https://doi.org/10.1039/C2AY25496D.
2. Qiao, J.; Liu, X.; Zhang, L.; Eubank, J.F.; Liu, X.; Liu, Y. Unique Fluorescence Turn-On and Turn-Off–On Responses to Acids by a Carbazole-Based Metal–Organic Framework and Theoretical Studies. *J. Am. Chem. Soc.* **2022**, *144*, 17054–17063. https://doi.org/10.1021/jacs.2c06680.
3. Sun, S.; Liu, M.; Jin, X.-T.; Zhao, J.; Luo, Y.-H. Wavelength-Based Luminescence Sensing via Turn-On Responses for Acid Detection in Complex Environments. *Spectrochim. Acta A Mol. Biomol. Spectrosc.* **2025**, *326*, 125187. https://doi.org/10.1016/j.saa.2024.125187.
4. Luo, T.-Y.; Das, P.; White, D.L.; Liu, C.; Star, A.; Rosi, N.L. Luminescence "Turn-On" Detection of Gossypol Using Ln^{3+} -Based Metal–Organic Frameworks and Ln^{3+} Salts. *J. Am. Chem. Soc.* **2020**, *142*, 2897–2904. https://doi.org/10.1021/jacs.9b11429.
5. Ramírez Garza, R.E.; Rodríguez de Luna, S.L.; Padrón, G.H.; Gómez de la Fuente, I. A "turn-off" photoluminescent sensor for H_2O_2 detection based on a zinc oxide–graphene quantum dot (ZnO–GQD) nanocomposite and the role of amine in the development of GQD. *RSC Adv.* **2023**, *13*, 21808–21819. https://doi.org/10.1039/D3RA02355A.
6. Li, Y.; Tang, J.; He, L.; Liu, Y.; Liu, Y.; Chen, C.; Tang, Z. Core–Shell Upconversion Nanoparticle@Metal–Organic Framework Nanoprobes for Luminescent/Magnetic Dual-Mode Targeted Imaging. *Adv. Mater.* **2015**, *27*, 4075–4080. https://doi.org/10.1002/adma.201501779.
7. Du, P.-Y.; Gu, W.; Liu, X. A three-dimensional Nd(iii)-based metal–organic framework as a smart drug carrier. *New J. Chem.* **2016**, *40*, 9017–9020. https://doi.org/10.1039/C6NJ02221A.

8. Taokaenchan, N.; Tangkuaram, T.; Pookmanee, P.; Phaisansuthichol, S.; Kuimalee, S.; Satienperakul, S. Enhanced electrogenerated chemiluminescence of tris(2,2′-bipyridyl)ruthenium(II) system by l-cysteine-capped CdTe quantum dots and its application for the determination of nitrofuran antibiotics. *Biosens. Bioelectron.* **2015**, *66*, 231–237. https://doi.org/10.1016/j.bios.2014.11.030.
9. Zhang, F.; Yao, H.; Chu, T.; Zhang, G.; Wang, Y.; Yang, Y. A Lanthanide MOF Thin-Film Fixed with Co_3O_4 Nano-Anchors as a Highly Efficient Luminescent Sensor for Nitrofuran Antibiotics. *Chem. Eur. J.* **2017**, *23*, 10293–10300. https://doi.org/10.1002/chem.201701852.
10. Hao, J.-N.; Xu, X.-Y.; Lian, X.; Zhang, C.; Yan, B. A Luminescent 3d-4f-4d MOF Nanoprobe as a Diagnosis Platform for Human Occupational Exposure to Vinyl Chloride Carcinogen. *Inorg. Chem.* **2017**, *56*, 11176–11183. https://doi.org/10.1021/acs.inorgchem.7b01549.
11. Feng, A.; Smet, P.F. A Review of Mechanoluminescence in Inorganic Solids: Compounds, Mechanisms, Models and Applications. *Materials* **2018**, *11*, 484. https://doi.org/10.3390/ma11040484.
12. Jia, R.-Q.; Tan, G.; Chen, Y.-J.; Zuo, L.-Y.; Li, B.; Wang, L.-Y. CuII Ion Doping Enhances the Water Stability of Luminescent Metal–Organic Framework, Realizing the Detection of Fe^{3+} and Antibiotics in Aqueous Solutions. *Front. Chem.* **2022**, *10*, 860232. https://doi.org/10.3389/fchem.2022.860232.
13. Rozenberga, L.; Skinner, W.; Lancaster, D.G.; Bloch, W.M.; Blencowe, A.; Krasowska, M.; Beattie, D.A. A europium metal–organic framework for dual Fe^{3+} ion and pH sensing. *Sci. Rep.* **2022**, *12*, 11982. https://doi.org/10.1038/s41598-022-15663-z.
14. Gujja, C.S.; Pawar, S.D. Synthesis of Fluorescent Cu-MOF and Ni-MOF Sensors for Selective and Sensitive Detection of Arginine and Hydrogen Sulfide. *J. Inorg. Organomet. Polym. Mater.* **2023**, *33*, 2636–2646. https://doi.org/10.1007/s10904-023-02669-x.
15. Yusuf, V.F.; Malek, N.I.; Kailasa, S.K. Review on Metal–Organic Framework Classification, Synthetic Approaches, and Influencing Factors: Applications in Energy, Drug Delivery, and Wastewater Treatment. *ACS Omega* **2022**, *7*, 44507–44531. https://doi.org/10.1021/acsomega.2c05310.
16. Xu, L.-L.; Zhang, Q.-F.; Wang, D.; Wu, G.-W.; Cai, H. Construction of a Luminescent Cadmium-Based Metal–Organic Framework for Highly Selective Discrimination of Ferric Ions. *Molecules* **2021**, *26*, 6847. https://doi.org/10.3390/molecules26226847.
17. Chen, M.; Xu, W.-M.; Tian, J.-Y.; Cui, H.; Zhang, J.-X.; Liu, C.-S.; Du, M. A terbium(iii) lanthanide–organic framework as a platform for a recyclable multi-responsive luminescent sensor. *J. Mater. Chem. C* **2017**, *5*, 2015–2021. https://doi.org/10.1039/C6TC05615F.
18. Yu, Y.; Ma, J.-P.; Zhao, C.-W.; Yang, J.; Zhang, X.-M.; Liu, Q.-K.; Dong, Y.-B. Copper(I) Metal–Organic Framework: Visual Sensor for Detecting Small Polar Aliphatic Volatile Organic Compounds. *Inorg. Chem.* **2015**, *54*, 11590–11592. https://doi.org/10.1021/acs.inorgchem.5b02150.
19. Yang, N.-N.; Sun, W.; Xi, F.-G.; Sui, Q.; Chen, L.-J.; Gao, E.-Q. Postsynthetic N-methylation making a metal–organic framework responsive to alkylamines. *Chem. Commun.* **2017**, *53*, 1747–1750. https://doi.org/10.1039/C6CC10278F.
20. Tang, Q.; Liu, S.; Liu, Y.; Miao, J.; Li, S.; Zhang, L.; Shi, Z.; Zheng, Z. Cation Sensing by a Luminescent Metal–Organic Framework with Multiple Lewis Basic Sites. *Inorg. Chem.* **2013**, *52*, 2799–2801. https://doi.org/10.1021/ic400029p.
21. Xiao, Z.-Z.; Han, L.-J.; Wang, Z.-J.; Zheng, H.-G. Three Zn(ii)-based MOFs for luminescence sensing of Fe^{3+} and $Cr_2O_7^{2-}$ ions. *Dalton Trans.* **2018**, *47*, 3298–3302. https://doi.org/10.1039/C7DT04659F.
22. Liu, S.; Liu, M.; Guo, M.; Wang, Z.; Wang, X.; Cui, W.; Tian, Z. Development of Eu-based metal-organic frameworks (MOFs) for luminescence sensing and entrapping of arsenate ion. *J. Lumin.* **2021**, *236*, 118102. https://doi.org/10.1016/j.jlumin.2021.118102.
23. Senkovska, I.; Hoffmann, F.; Fröba, M.; Getzschmann, J.; Böhlmann, W.; Kaskel, S. New highly porous aluminium based metal-organic frameworks: Al(OH)(ndc) (ndc=2,6-naphthalene dicarboxylate) and Al(OH)(bpdc) (bpdc=4,4′-biphenyl dicarboxylate). *Microporous Mesoporous Mater.* **2009**, *122*, 93–98. https://doi.org/10.1016/j.micromeso.2009.02.020.
24. Gotthardt, M.A.; Grosjean, S.; Brunner, T.S.; Kotzel, J.; Gänzler, A.M.; Wolf, S.; Bräse, S.; Kleist, W. Synthesis and post-synthetic modification of amine-, alkyne-, azide- and nitro-functionalized metal–organic frameworks based on DUT-5. *Dalton Trans.* **2015**, *44*, 16802–16809. https://doi.org/10.1039/C5DT02276B.
25. Wang, T.; Zhu, L.; Yue, Y.; Asghari, M.R.; Samani, B.H.; Yamamoto, T.; Mukai, Y.; Kanda, H. N,N-dimethylformamide detection and refractive index sensing using an electrospun polymer/Ti_3C_2 MXene-TiO_2 modified optical fiber sensor. *Sens. Actuators B Chem.* **2024**, *417*, 136143. https://doi.org/10.1016/j.snb.2024.136143.
26. Cseri, L.; Hardian, R.; Anan, S.; Vovusha, H.; Schwingenschlögl, U.; Budd, P.M.; Sada, K.; Kokado, K.; Szekely, G. Bridging the interfacial gap in mixed-matrix membranes by nature-inspired design: Precise molecular sieving with polymer-grafted metal–organic frameworks. *J. Mater. Chem. A* **2021**, *9*, 23793–23801. https://doi.org/10.1039/D1TA06205K.

27. Liu, Y.-Y.; Couck, S.; Vandichel, M.; Grzywa, M.; Leus, K.; Biswas, S.; Volkmer, D.; Gascon, J.; Kapteijn, F.; Denayer, J.F.M.; et al. New VIV-Based Metal–Organic Framework Having Framework Flexibility and High CO_2 Adsorption Capacity. *Inorg. Chem.* **2013**, *52*, 113–120. https://doi.org/10.1021/ic301338a.
28. Thommes, M.; Kaneko, K.; Neimark, A.V.; Olivier, J.P.; Rodriguez-Reinoso, F.; Rouquerol, J.; Sing, K.S.W. Physisorption of gases, with special reference to the evaluation of surface area and pore size distribution (IUPAC Technical Report). *Pure Appl. Chem.* **2015**, *87*, 1051–1069. https://doi.org/10.1515/pac-2014-1117.
29. Raja, D.S.; Chang, I.H.; Jiang, Y.-C.; Chen, H.-T.; Lin, C.-H. Enhanced gas sorption properties of a new sulfone functionalized aluminum metal-organic framework: Synthesis, characterization, and DFT studies. *Microporous Mesoporous Mater.* **2015**, *216*, 20–26. https://doi.org/10.1016/j.micromeso.2015.02.023.
30. Lestari, W.W.; Afifah, E.N.; Mohammed, O.; Saraswati, T.E.; Al-Adawiyah, R.; Kadja, G.T.M.; Widiastuti, N. DUT-5 modified Pd metal-nanoparticles: Synthesis, chemical stability, and hydrogen sorption studies. *Mater. Res. Express* **2019**, *6*, 1250–1254. https://doi.org/10.1088/2053-1591/ab637c.
31. Wang, G.; Leus, K.; Couck, S.; Tack, P.; Depauw, H.; Liu, Y.-Y.; Vincze, L.; Denayer, J.F.M.; Van Der Voort, P. Enhanced gas sorption and breathing properties of the new sulfone functionalized COMOC-2 metal organic framework. *Dalton Trans.* **2016**, *45*, 9485–9491. https://doi.org/10.1039/C6DT01355D.
32. Nuhnen, A.; Janiak, C. A practical guide to calculate the isosteric heat/enthalpy of adsorption via adsorption isotherms in metal–organic frameworks, MOFs. *Dalton Trans*. **2020**, *49*, 10295–10307. https://doi.org/10.1039/D0DT01784A.
33. Llewellyn, P.L.; Maurin, G. Gas adsorption microcalorimetry and modelling to characterise zeolites and related materials. *Comptes Rendus Chim.* **2005**, *8*, 283–302. https://doi.org/10.1016/j.crci.2004.11.004.
34. Sutherland, T.I.; Sparks, C.J.; Joseph, J.M.; Wang, Z.; Whitaker, G.; Sham, T.K.; Wren, J.C. Effect of ferrous ion concentration on the kinetics of radiation-induced iron-oxide nanoparticle formation and growth. *Phys. Chem. Chem. Phys.* **2017**, *19*, 695–708. https://doi.org/10.1039/C6CP05456K.
35. Ko, N.; Hong, J.; Sung, S.; Cordova, K.E.; Park, H.J.; Yang, J.K.; Kim, J. A significant enhancement of water vapour uptake at low pressure by amine-functionalization of UiO-67. *Dalton Trans.* **2015**, *44*, 2047–2051. https://doi.org/10.1039/C4DT02582B.
36. Krap, C.P.; Newby, R.; Dhakshinamoorthy, A.; García, H.; Cebula, I.; Easun, T.L.; Savage, M.; Eyley, J.E.; Gao, S.; Blake, A.J.; et al. Enhancement of CO_2 Adsorption and Catalytic Properties by Fe-Doping of [$Ga_2(OH)_2(L)$] (H_4L = Biphenyl-3,3′,5,5′-tetracarboxylic Acid), MFM-300(Ga_2). *Inorg. Chem.* **2016**, *55*, 1076–1088. https://doi.org/10.1021/acs.inorgchem.5b02108.
37. Wang, B.; Zeng, J.; He, H. Enhancing CO_2 adsorption capacity and selectivity of UiO-67 through external ligand modification. *Sep. Purif. Technol.* **2025**, *354*, 128651. https://doi.org/10.1016/j.seppur.2024.128651.
38. Wang, B.; Huang, H.; Lv, X.-L.; Xie, Y.; Li, M.; Li, J.-R. Tuning CO_2 Selective Adsorption over N_2 and CH_4 in UiO-67 Analogues Through Ligand Functionalization. *Inorg. Chem*. **2014**, *53*, 9254–9259. https://doi.org/10.1021/ic5013473.
39. Shannon, R.D. Revised effective ionic radii and systematic studies of interatomic distances in halides and chalcogenides. *Acta Crystallogr. A* **1976**, *32*, 751–767. https://doi.org/10.1107/S0567739476001551.
40. Asiwal, E.P.; Shelar, D.S.; Gujja, C.S.; Manjare, S.T.; Pawar, S.D. A Ni-MOF based luminescent sensor for selective and rapid sensing of Fe(ii) and Fe(iii) ions. *New J. Chem*. **2022**, *46*, 12679–12685. https://doi.org/10.1039/D2NJ02263J.
41. Wang, F.; Zhang, F.; Zhao, Z.; Sun, Z.; Pu, Y.; Wang, Y.; Wang, X. Multifunctional MOF-based probes for efficient detection and discrimination of Pb^{2+}, Fe^{3+} and $Cr_2O_7^{2-}$/CrO_4^{2-}. *Dalton Trans*. **2021**, *50*, 12197–12207. https://doi.org/10.1039/D1DT01446C.
42. Wang, M.; Guo, L.; Cao, D. Metal-organic framework as luminescence turn-on sensor for selective detection of metal ions: Absorbance caused enhancement mechanism. *Sens. Actuators B Chem.* **2018**, *256*, 839–845. https://doi.org/10.1016/j.snb.2017.10.016.
43. Xiang, Z.; Fang, C.; Leng, S.; Cao, D. An amino group functionalized metal–organic framework as a luminescent probe for highly selective sensing of Fe^{3+} ions. *J. Mater. Chem. A* **2014**, *2*, 7662–7665. https://doi.org/10.1039/C4TA00313F.
44. Pal, T.K. Metal–organic framework (MOF)-based fluorescence "turn-on" sensors. *Mater. Chem. Front*. **2023**, *7*, 405–441. https://doi.org/10.1039/D2QM01070D.
45. Wang, L.; Yao, Z.-Q.; Ren, G.-J.; Han, S.-D.; Hu, T.-L.; Bu, X.-H. A luminescent metal–organic framework for selective sensing of Fe^{3+} with excellent recyclability. *Inorg. Chem. Commun*. **2016**, *65*, 9–12. https://doi.org/10.1016/j.inoche.2016.01.004.
46. Xu, H.; Dong, Y.; Wu, Y.; Ren, W.; Zhao, T.; Wang, S.; Gao, J. An -OH group functionalized MOF for ratiometric Fe^{3+} sensing. *J. Solid State Chem*. **2018**, *258*, 441–446. https://doi.org/10.1016/j.jssc.2017.11.013.
47. Hou, B.-L.; Tian, D.; Liu, J.; Dong, L.-Z.; Li, S.-L.; Li, D.-S.; Lan, Y.-Q. A Water-Stable Metal–Organic Framework for Highly Sensitive and Selective Sensing of Fe^{3+} Ion. *Inorg. Chem*. **2016**, *55*, 10580–10586. https://doi.org/10.1021/acs.inorgchem.6b01809.

48. Chen, Z.; Sun, Y.; Zhang, L.; Sun, D.; Liu, F.; Meng, Q.; Wang, R.; Sun, D. A tubular europium–organic framework exhibiting selective sensing of Fe^{3+} and Al^{3+} over mixed metal ions. *Chem. Commun*. **2013**, *49*, 11557–11559. https://doi.org/10.1039/C3CC46613B.
49. Hu, F.-L; Shi, Y.-X.; Chen, H.-H.; Lang, J.-P. A Zn(ii) coordination polymer and its photocycloaddition product: Syntheses, structures, selective luminescence sensing of iron(iii) ions and selective absorption of dyes. *Dalton Trans.* **2015**, *44*, 18795–18803. https://doi.org/10.1039/C5DT03094C.
50. Yang, C.-X.; Ren, H.-B.; Yan, X.-P. Fluorescent Metal–Organic Framework MIL-53(Al) for Highly Selective and Sensitive Detection of Fe^{3+} in Aqueous Solution. *Anal. Chem.* **2013**, *85*, 7441–7446. https://doi.org/10.1021/ac401387z.
51. Zhang, S.-T.; Yang, J.; Wu, H.; Liu, Y.-Y.; Ma, J.-F. Systematic Investigation of High-Sensitivity Luminescent Sensing for Polyoxometalates and Iron(III) by MOFs Assembled with a New Resorcin[4]arene-Functionalized Tetracarboxylate. *Chem. Eur. J.* **2015**, *21*, 15806–15819. https://doi.org/10.1002/chem.201501976.
52. Fonseca, J.; Costa, O.M.; Júnior, S.; Barros, B.; Kulesza, J. Photoluminescent Sensor for Fe^{3+} Based on Calix[4]arene-Derivative-Modified UiO-66-NH_2. *J. Braz. Chem. Soc.* **2024**, *36*, 20240146–20240147. https://doi.org/10.21577/0103-5053.20240146.
53. Zheng, M.; Tan, H.; Xie, Z.; Zhang, L.; Jing, X.; Sun, Z. Fast Response and High Sensitivity Europium Metal Organic Framework Fluorescent Probe with Chelating Terpyridine Sites for Fe^{3+}. *ACS Appl. Mater. Interfaces* **2013**, *5*, 1078–1083. https://doi.org/10.1021/am302862k.
54. Chen, C.-H.; Wang, X.-S.; Li, L.; Huang, Y.-B.; Cao, R. Highly selective sensing of Fe^{3+} by an anionic metal–organic framework containing uncoordinated nitrogen and carboxylate oxygen sites. *Dalton Trans.* **2018**, *47*, 3452–3458. https://doi.org/10.1039/C8DT00088C.
55. Zhang, C.; Yan, Y.; Pan, Q.; Sun, L.; He, H.; Liu, Y.; Liang, Z.; Li, J. A microporous lanthanum metal–organic framework as a bifunctional chemosensor for the detection of picric acid and Fe^{3+} ions. *Dalton Trans.* **2015**, *44*, 13340–13346. https://doi.org/10.1039/C5DT01065A.
56. Weng, H.; Yan, B. A flexible Tb(III) functionalized cadmium metal organic framework as fluorescent probe for highly selectively sensing ions and organic small molecules. *Sens. Actuators B Chem.* **2016**, *228*, 702–708. https://doi.org/10.1016/j.snb.2016.01.101.
57. Petříček, V.; Dušek, M.; Palatinus, L. Crystallographic Computing System JANA2006: General features. *Z. Für Krist.* **2014**, *229*, 345–352. https://doi.org/10.1515/zkri-2014-1737.

Synthesis of a Luminescent Aluminum-Based MOF for Selective Iron(III) Ion Sensing

Hanibal Othman, István Boldog and Christoph Janiak *

Institut für Anorganische Chemie und Strukturchemie, Heinrich-Heine-Universität Düsseldorf, D-40204 Dusseldorf, Germany
* Correspondence: janiak@uni-duesseldorf.de

Content

Section S1. Reaction schemes for ligand synthesis (Scheme 1-3) and nuclear magnetic resonance spectra **S2**

Section S2. Structure determination and PXRD pattern **S5**

Section S3. Infrared spectroscopy **S10**

Section S4. Thermogravimetric analysis **S11**

Section S5. Digestion NMR analysis **S12**

Section S6. N_2 adsorption **S13**

Section S7. CO_2 adsorption and isosteric heat (enthalpy) of adsorption **S14**

Section S8. Photoluminescent properties **S16**

Section S9. References **S18**

Section S1. Reaction schemes for ligand synthesis (Scheme 1-3) and nuclear magnetic resonance spectra

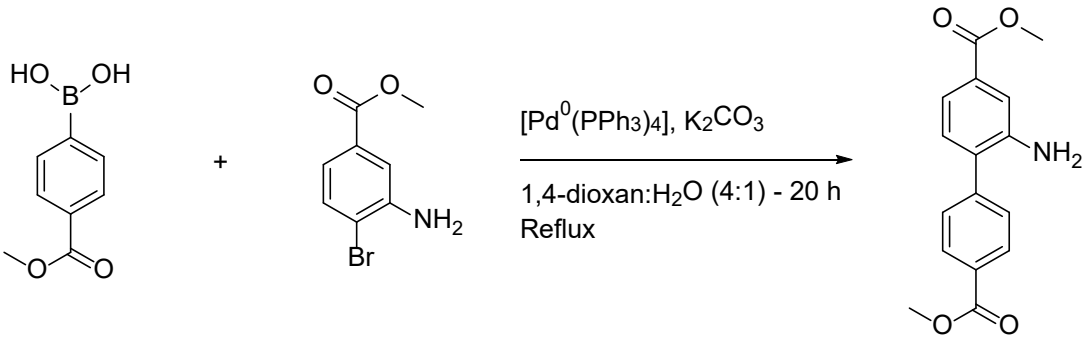

Scheme S1. Synthesis of dimethyl-2-amino-[1,1'-biphenyl]-4,4'-dicarboxylate [1].

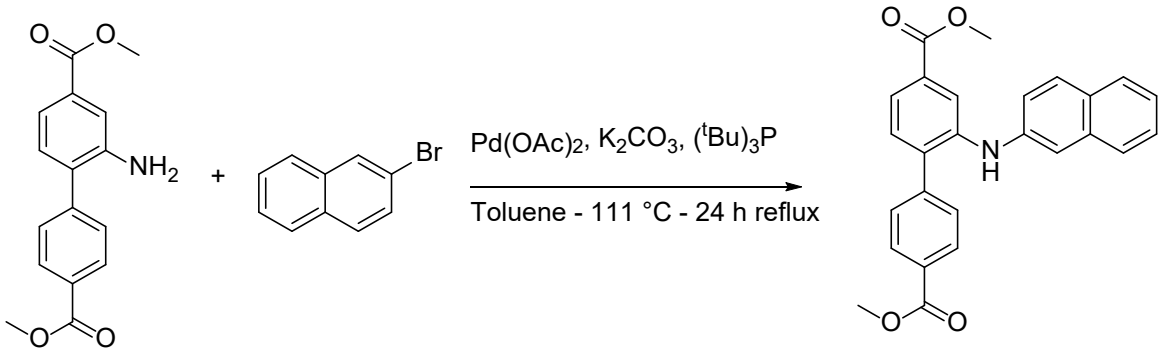

Scheme S2. Synthesis of dimethyl-2-(naphthalen-2-ylamino)-[1,1'-biphenyl]-4,4'-dicarboxylate.

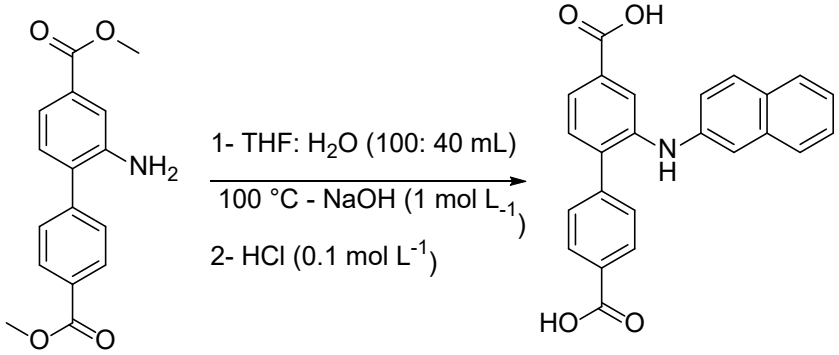

Scheme S3. Synthesis of 2-(naphthalen-2-ylamino)-[1,1'-biphenyl]-4,4'-dicarboxylic acid (H_2BP-Naph).

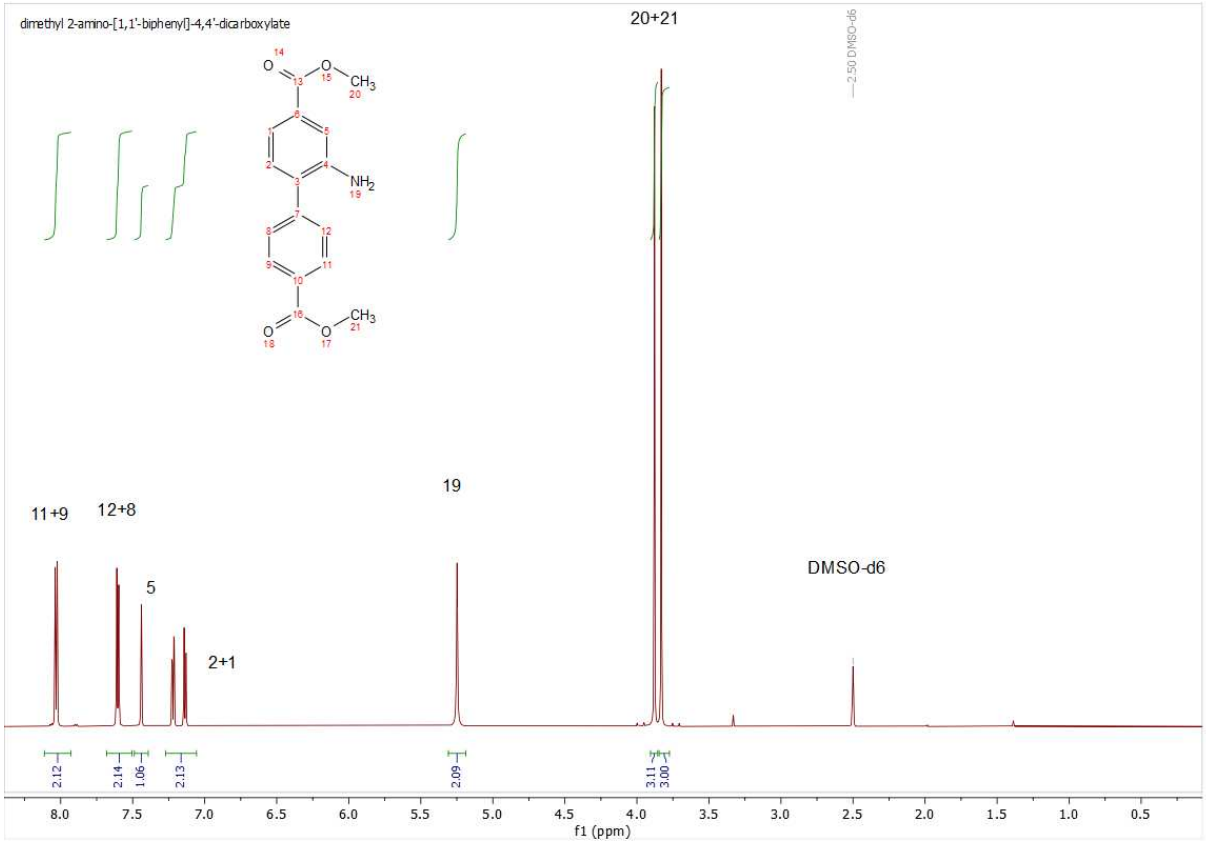

Figure S1. ^{1}H NMR spectrum (600 MHz, DMSO-d6) of dimethyl-2-amino-[1,1'-biphenyl]-4,4'-dicarboxylate.

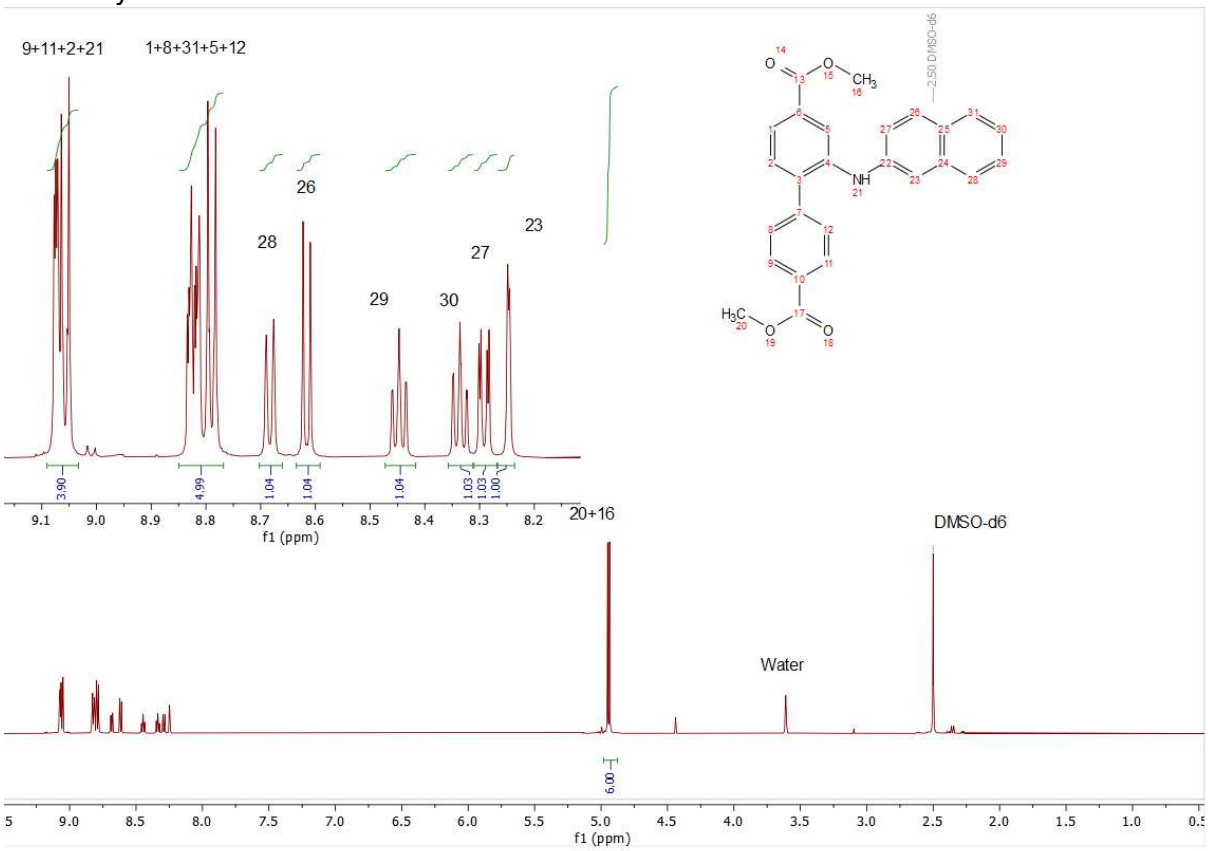

Figure S2. ^{1}H NMR spectrum (600 MHz, DMSO-d6) of dimethyl- 2-(naphthalen-2-ylamino)-[1,1'-biphenyl]-4,4'-dicarboxylate (Me_2BP-Naph).

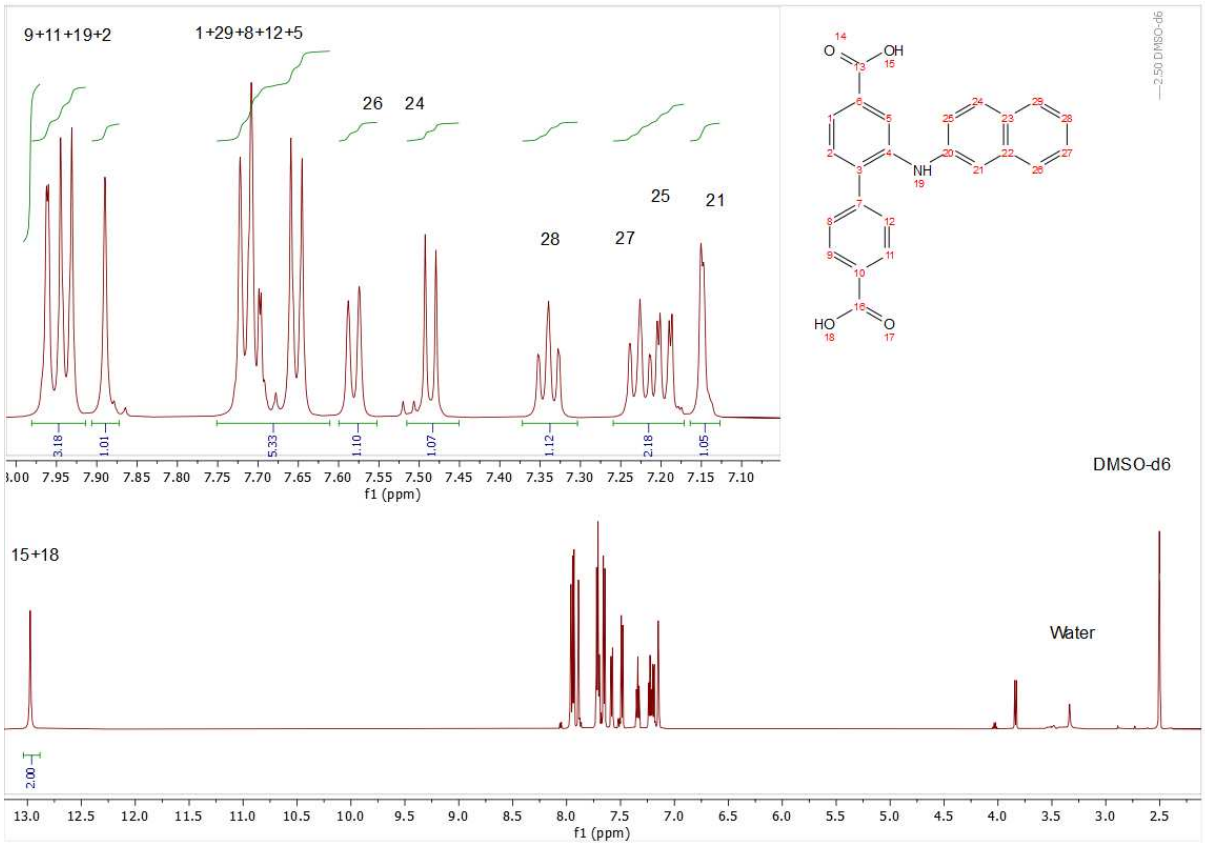

Figure S3. ^{1}H NMR (600 MHz, solvent DMSO-d6) NMR spectrum of 2-(naphthalen-2-ylamino)-[1,1'-biphenyl]-4,4'-dicarboxylic acid H_2BP-Naph.

Section S2. Structure determination and PXRD pattern

Le Bail fit*:*

The Powder X-ray diffraction (PXRD) data was Le Bail-fitted using the space group and the initial cell parameters for the published structure of [VO(BPDC)], where H_2BPDC = 4,4′-biphenyldicarboxylic acid, also known as COMOC-2-lp (lp stands for large pore) [2]. The Le Bail profile fitting yields excellent results (**Figure S1**, **Table S1**), however they are rather an indication of just moderate crystallinity (still excellent for such a case) and, hence, strong peak broadening, which allows precise fit, but provides little structural information.

Notably, the cell parameters of Al-BP-Naph significantly differ from those of COMOC-2-*lp*. While the cell volumes are nearly the same (~3% difference), the structure of Al-BP-Naph features as slight deflection from the nearly fully opened structure of COMOC-2-*lp*, which has nearly square shaped the lozenge pores running along the *b*-axis (*a/c* = 1.18 vs 1.04 respectively), while the fully closed structure is characterized by maximally elongated „narrow" lozenge pores.

It is presumed, that the naphthylaminyl substituent of the ligand in Al-BP-Naph is heavily disordered. As the ligand is essentially non-planar due to steric reasons, the possible and highly probable disorder on four positions (formally corresponding to 2,2',6,6' locants) is most probably complemented by the disorder due to the flexibility of the ligand, constituted of non-conjugated aromatic moieties. The moieties have a limited rotational degree of freedom, which could give several conformations with local energy minima, depending on the realized sets of intermolecular interactions with the neighboring „walls" of the framework and/or another naphthylaminyl subsituents. The latter interactions should be held responsible for the observed deflection of the cell parameters from the case of most opened structure. An attempt of a Rietveld refinement confirms the „smeared" electron densities at the ligands's localization, which precluded the possibility of a proper structural refinement.

The single naphthylaminyl substituent per ligand does not occupy the whole space of the pore leaving pores large enough to allow the adsorption of N_2 molecules (see Figure S5 for an arbitrarily chosen possible substituent localization).

The PXRD data for Al-BP-Naph was collected by a Rigaku Miniflex PXRD diffractometer using Cu-K$\alpha_{1,2}$ radiation in a Bragg-Brentano geometry on a flat sample employing a low-background silicon sample-holder with an indent. The sample was thoroughly homogenized, but no special grounding or sieving were used. The measurement was performed in air during 8.5h with 0.01° 2θ angular steps.

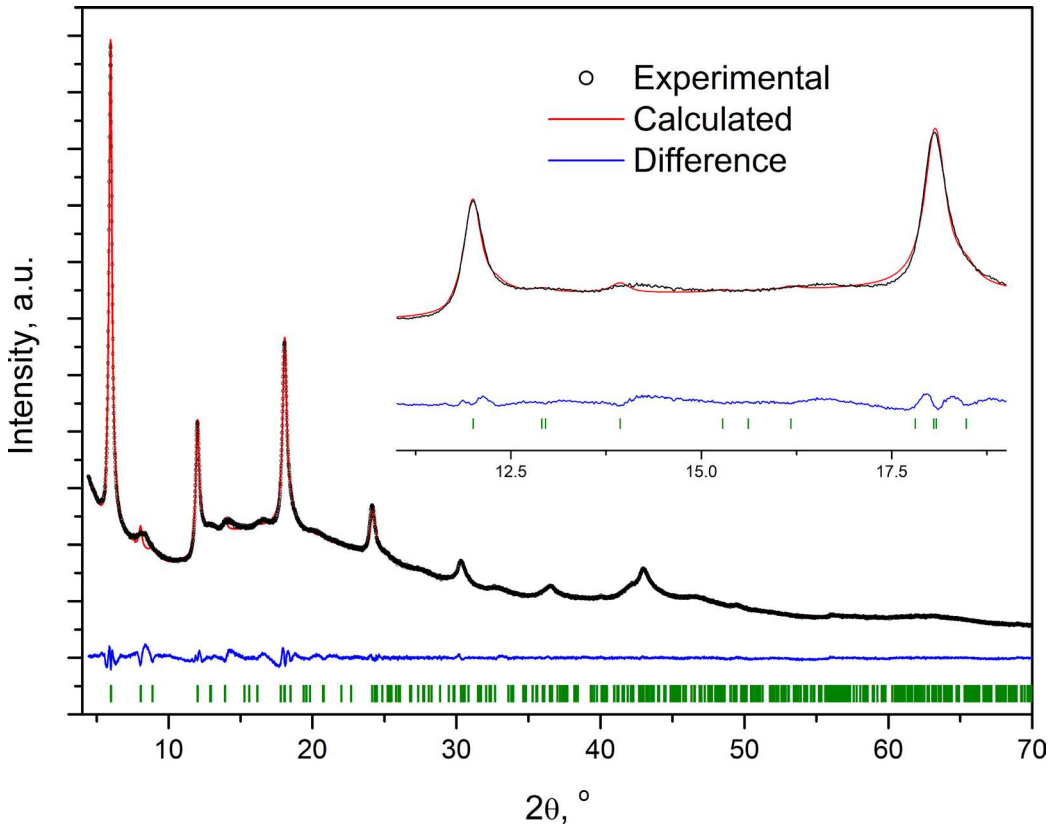

Figure S4. Le Bail fit of the PXRD data for Al-BP-Naph.

Table S1. Le Bail fitting results for Al-BP-Naph and its comparison with the reported crystal data and refinement details for the prototype structure COMOC-2-lp.

	COMOC-2-lp	**Al-BP-Naph**
Diffractometer	STOE STADI P	Rigaku Miniflex 600 (2019)
Temperature / K	293(2)	295(2)
Wavelength / Å [a)]	1.5418	1.54051, 1.54433 [a)]
Crystal system	Orthorombic	Orthorombic
Space group	*I*mma	*I*mma (disorder is implied)
***a* /Å**	21.443(3)	21.901(3)
***b* /Å**	6.957(4)	7.2686(13)
***c* /Å**	20.570(2)	18.5134(4)
***V* /Å^3**	3069(5)	3168.8(9)
***R*$_p$, *wR*$_p$**	0.035, 0.0507	0.0137, 0.0191
R, wR [I>3σ], Rietveld	0.0875, 0.0640	-
Goodness-of-fit, χ^2	n.d.	0.91

[a)] Cu K$\alpha_{1,2}$; I(Kα_2)/I(Kα_1) = 0.5

The Le Bail fit was performed using the Jana 2006 software [2] (note that the Le Bail fit, unlike the Rietveld fit, does not involve the information about the actual structure, but uses only the cell dimensions and space group. The Le Bail profile fit demonstrate the adequacy of the chosen space group and cell parameters combination for the given data). Manual background was used, while the three cell parameters for the assumed orthorhombic cell (*I*mma) symmetry in analogy with the published structure of COMOC-2-lp [3], two Lorenzian peak shape function parameters, the Simpson asymmetry correction parameter, and the sample shift were refined. The summary together with the comparable data for the COMOC-2-lp is given in **Table S1**.

It is worth noting that the disorder or the naphthylaminyl substituent precludes the precise determination of the space group. The *I*mma space group observed in COMOC-2-lp was retained, however even in the latter case, with structure solution and refinement based on powder data, the actual space group might be incorrect. Nevertheless, the primary objective of the PXRD data analysis was to confirm the structure of the framework, rather than attempt a Rietveld refinement of a seemingly strongly disordered structure using a data collected on a sample with just a moderate crystallinity (the strong disorder and compromised crystallinity are to a significant degree correlated). The difference Fourier maps for an attempted Rietveld refinement using COMOC-2-lp input with pre-refined cell parameters confirmed the placement of the metal atoms, however. the electronic density associated with the ligand was too smeared, making the pursue of the refinement unreasonable.

To demonstrate a possible localization of the naphthylaminyl pendant group a structural model was built manually, and the result, shown on **Figure S5**-Figure S7 should rather be viewed as a semi-artistic representation, even though the geometry of the cell and the molecular sizes are faithfully held to demonstrate the residual porosity. A lowered *I*m11 symmetry was chosen as one of the few possibilities; while it is not the highest apparent symmetry for a periodic structure with localized ligand's substituents, but it allows an easy demonstration of the residual porosity.

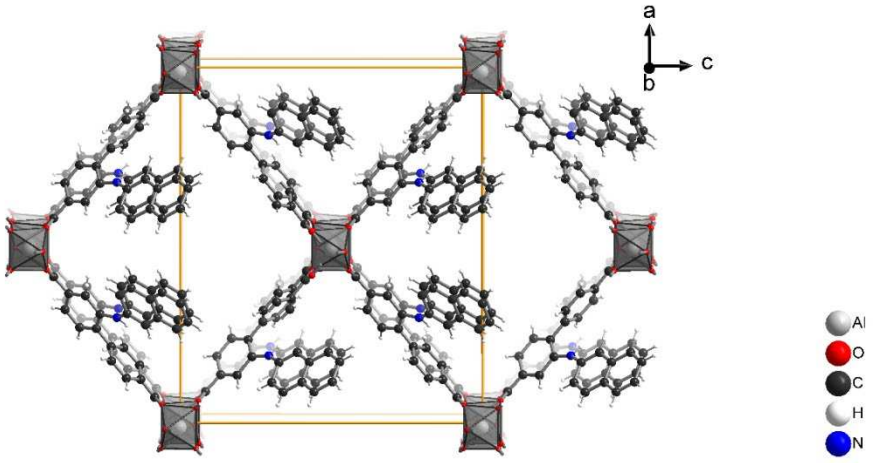

Figure S5. The approximate possible localization of the disordered naphthylamino pendant group in Al-BP-Naph (Im11 space group)

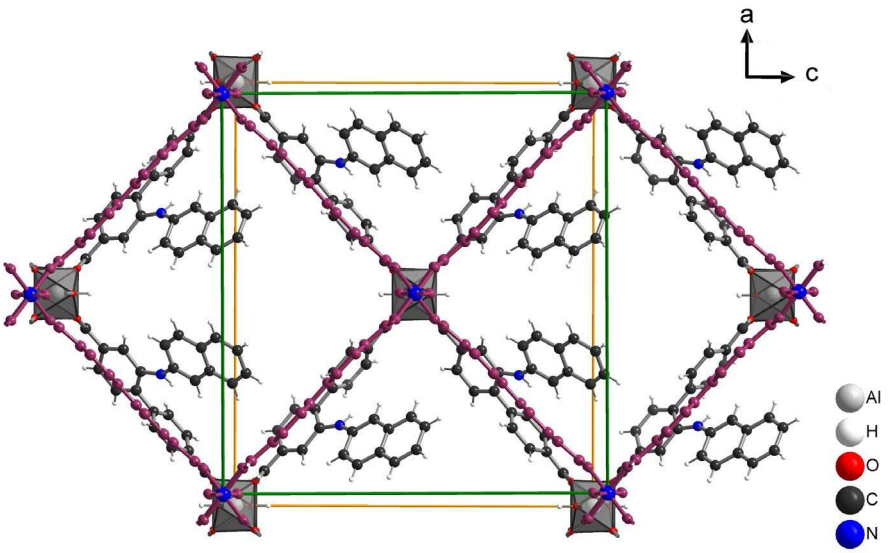

Figure S6. Overlap of the COMOC-2-lp cell and the model of Al-BP-Naph along the b axes with one of the possible localizations of the naphthylaminyl pendant group (Im11 space group).

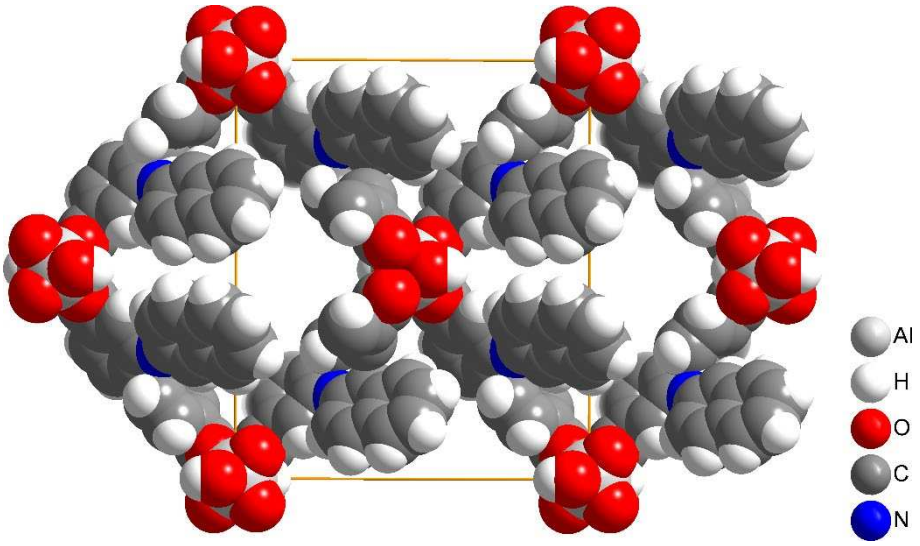

Figure S7. Space filling model for a structure representing a possible localization of the disordered naphthylamino pendant group in Al-BP-Naph (Im11 space group). Note the 4x4 $Å^2$ pore entrances, which appear barely accessible, but allow the adsorption of the N_2.

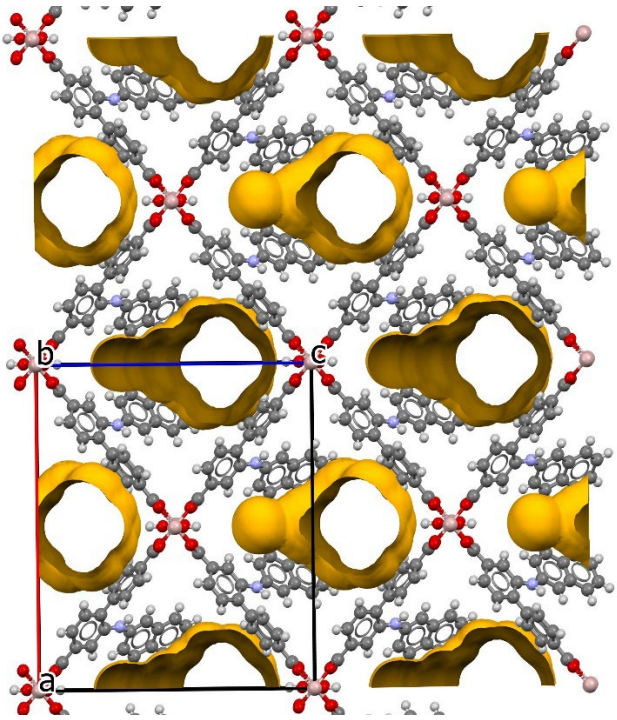

Figure S8. The model of the structure of S3, based on the comparison of PXRD with analogous COMOC-2-lp and DUT-5 structures with resolved naphthylamino-group disorder with one fixed position among the range of possible (the structure is given in lower-symmetry I).

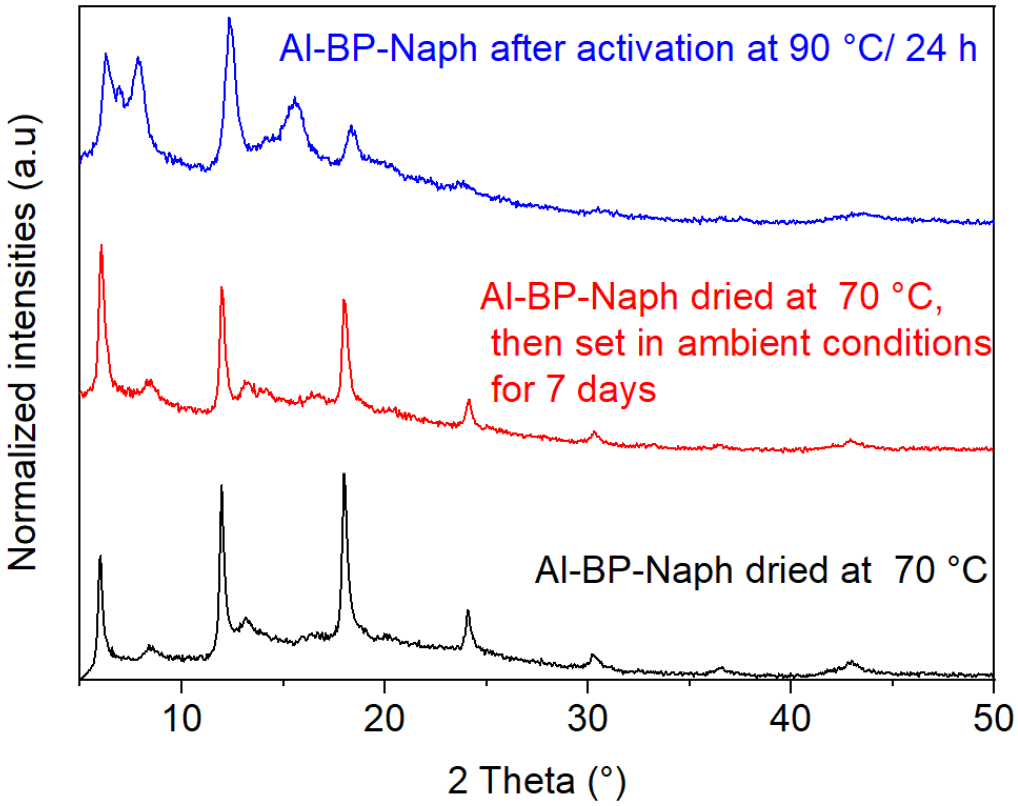

Figure S9. PXRD of dried Al-BP-Naph at 70 °C (black), dried Al-BP-Naph after 7 days in ambient conditions (red) and activated Al-BP-Naph (Blue).

Section S3. Infrared spectroscopy

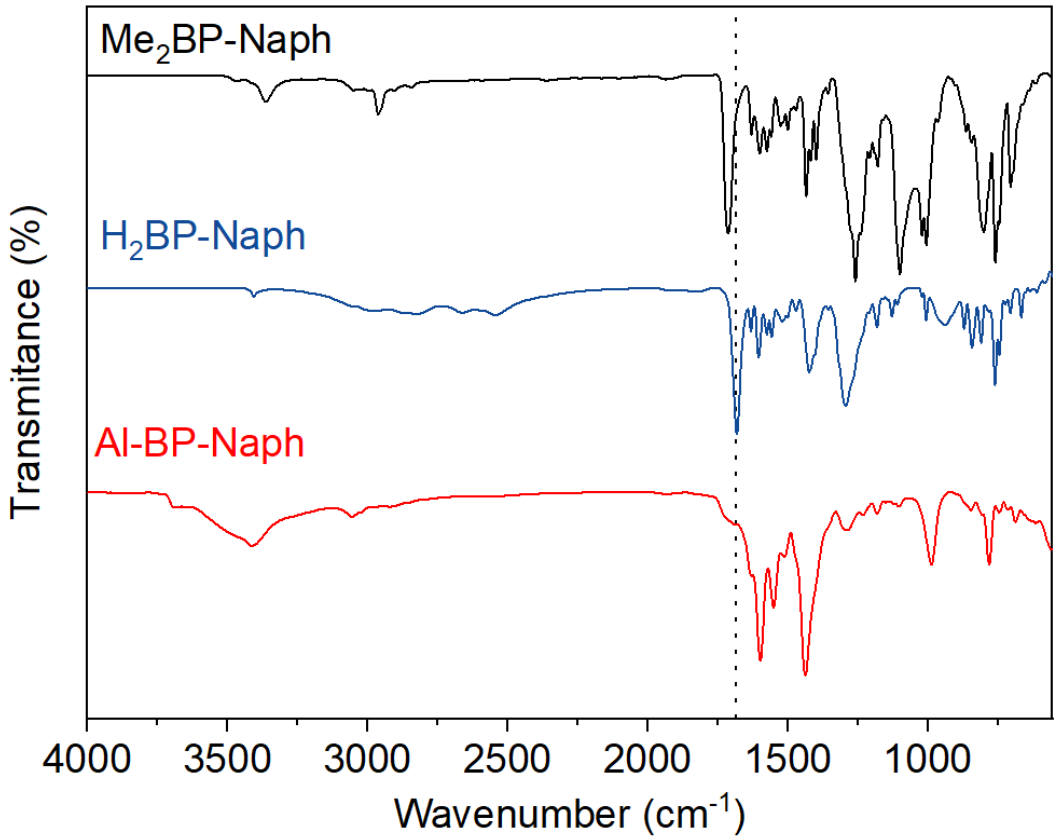

Figure S10. IR of Al-BP-Naph (red), free acid H_2BP-Nach linker (navy blue) and methylated linker Me_2BP-Naph (black) as KBr pellets.

Section S4. Thermogravimetric analysis

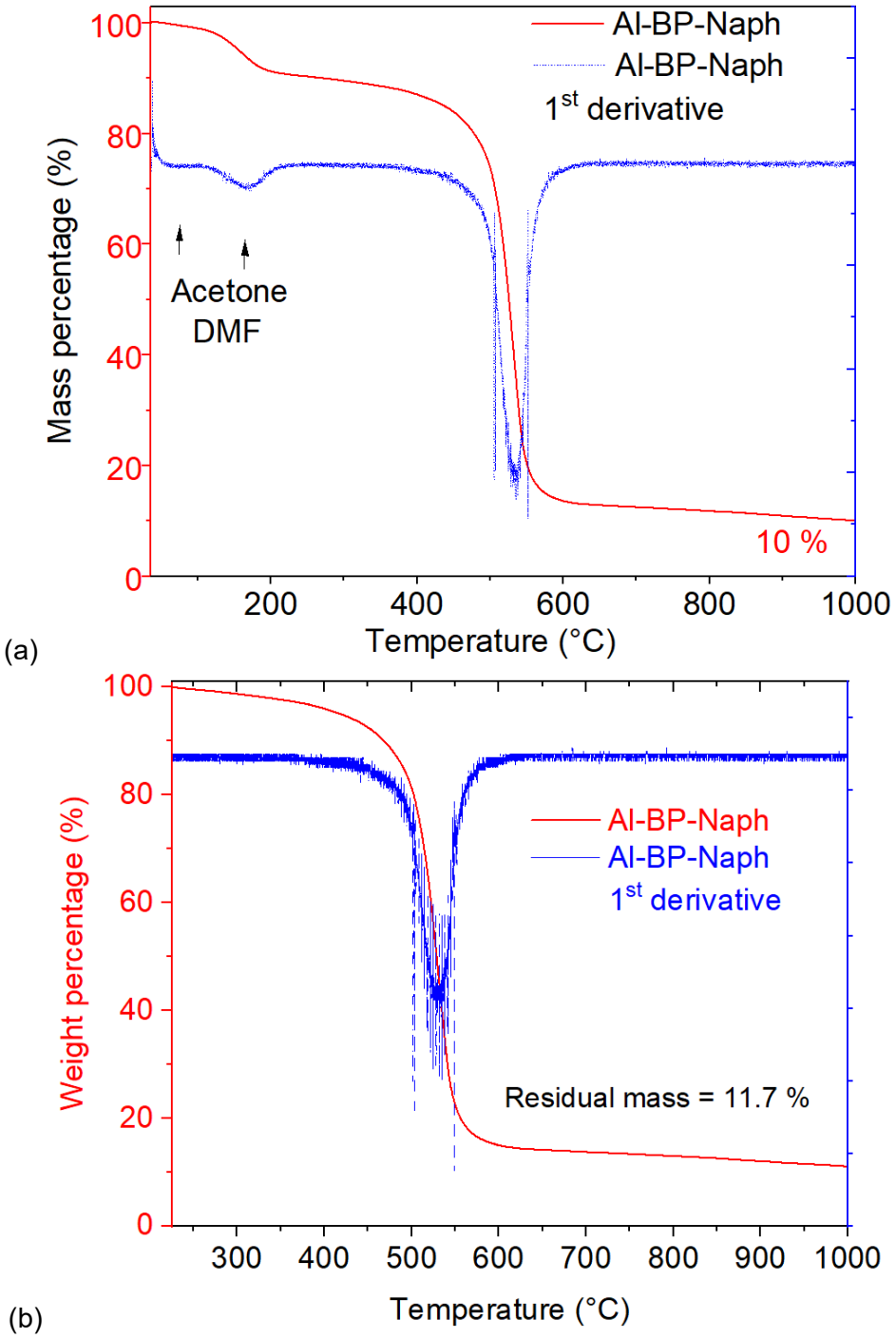

Figure S11. (a) TGA of Al-BP-Naph under synthetic air with a heating rate of 10 K min^{-1}. (b) Rescaled TGA plot after the solvent loss at 200 °C with the mass at 225 K set to 100%.
The thermogravimetric analysis was done with the NETZSCH TG 209 F3 Tarsus under synthetic air.

The theoretical mass loss of the BP-Naph linker from Al-BP-Naph is calculated to 89.7 wt% and the residual mass of Al_2O_3 to 11.98 wt%.

Al-BP-Naph has the molecular formula of [Al(OH)(BP-Naph)], $AlC_{24}H_{16}NO_5$.
$M_{Al\text{-}BP\text{-}Naph}$ = 425.38 g mol^{-1}
M_{Al} = 26.98 g mol^{-1}
$M_{BP\text{-}Naph}$ = 381.39 g mol^{-1}
1 mol of Al-BP-Naph gives 0.5 mol Al_2O_3 (1/2 M_{Al2O3} = 50.98 g mol^{-1})
50.98/425.38 × 100% = 11.98 % theoretical percentage of Al_2O_3 in Al-BP-Naph

Section S5. Digestion NMR analysis

TGA data already supports the composition of the ligand within Al-BP-Naph.
Yet, to confirm the integrity of the organic BP-Naph ligand within the MOF structure we have carried out a digestion NMR analysis.
In an NMR tube 10 mg of Al-BP-Naph was placed in 100 µL of NaOD/D_2O (1 mol/L) and shaken until a clear solution was obtained. Then 0.7 mL of DMSO-d_6 was added and the digestion NMR spectrum in Figure S12 showed all signals for the BP-Naph ligand (cf. Figure S3), albeit slightly shifted because of the deprotonation in the alkaline solution.

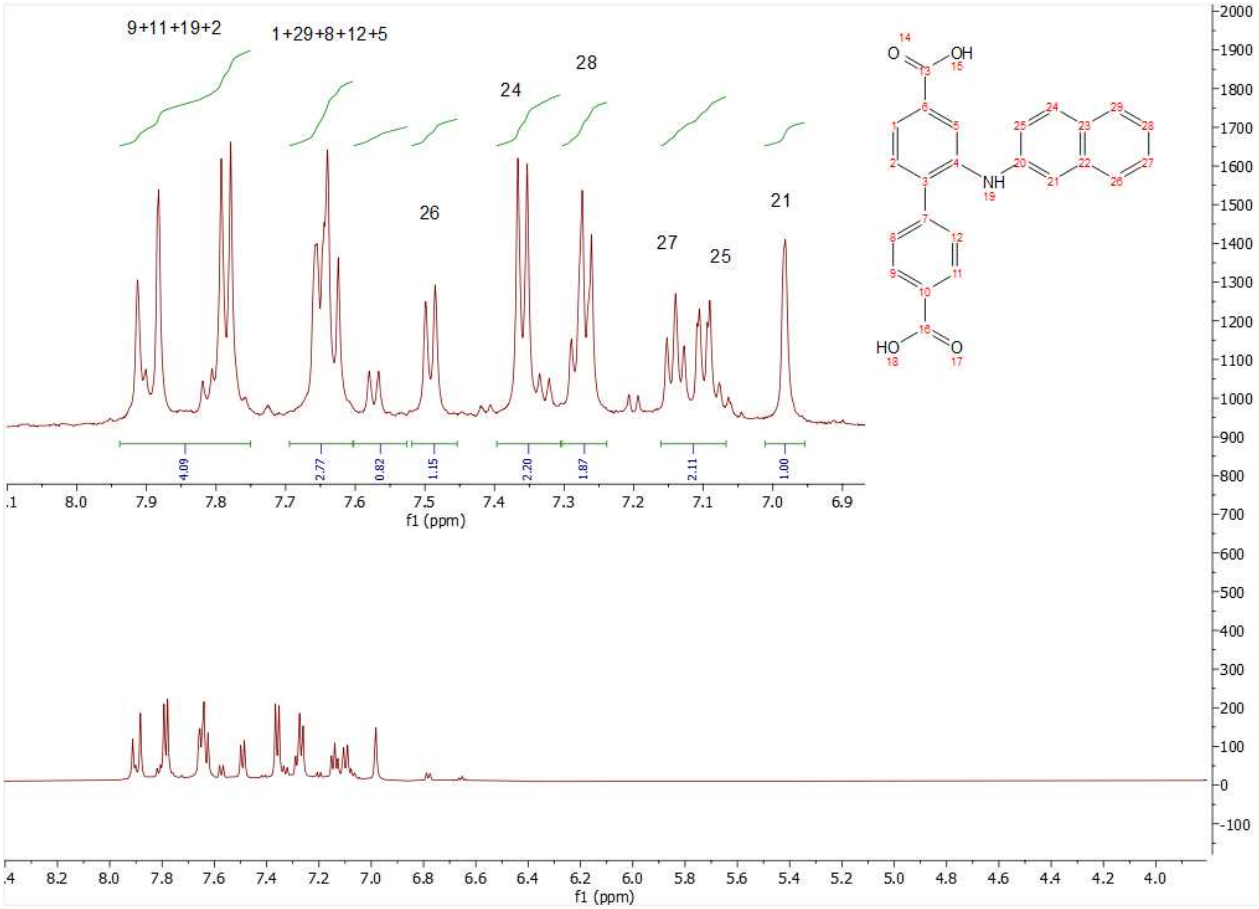

Figure S12. ("Digestion") ^{1}H NMR spectrum (600 MHz, solvent NaOD/D_2O/DMSO-d_6) of the solid Al-BP-Naph dissolved in NaOD/D_2O/DMSO-d_6 to verify the intact linker 2-(naphthalen-2-ylamino)-[1,1'-biphenyl]-4,4'-dicarboxylate. BP-Naph^{2-} (deprotonated in the alkaline medium).

Section S6. N_2 adsorption

The specific Brauner-Emmett-Teller surface area S_{BET} was calculated using the following equation (1)

$$S_{BET} = v_m \cdot N_A \cdot A_m / V_m \quad (1)$$

Where: S_{BET} = BET surface area $m^2\ g^{-1}$
v_m = Monolayer volume $cm^3\ g^{-1}$
N_A = Avogadro's number ($6.022 \cdot 10^{23}$ molecules mol^{-1})
A_m = Cross-sectional area of the adsorbate molecule (0.162 nm^2 for N_2)
V_m = Molar volume of ideal gas a STP = 22.414 L mol^{-1}

$$\frac{1}{V\left(\frac{P_0}{P}-1\right)} = \frac{C-1}{(V_m C)} \cdot \frac{P}{P_0} + \frac{1}{V_m C} \quad (2)$$

where:
V = Volume of gas adsorbed at pressure P ($cm^3\ g^{-1}$)
V_m = Monolayer capacity (volume of gas required to form a monolayer, cm^3/g)
P = Partial pressure of the adsorbate gas
P_0 = Saturation pressure of the adsorbate gas
C = BET constant, related to the energy of adsorption ($e^{\frac{E_1 - E_L}{RT}}$)
where:
E_1 = heat of adsorption for the first layer
E_L = heat of vaporization

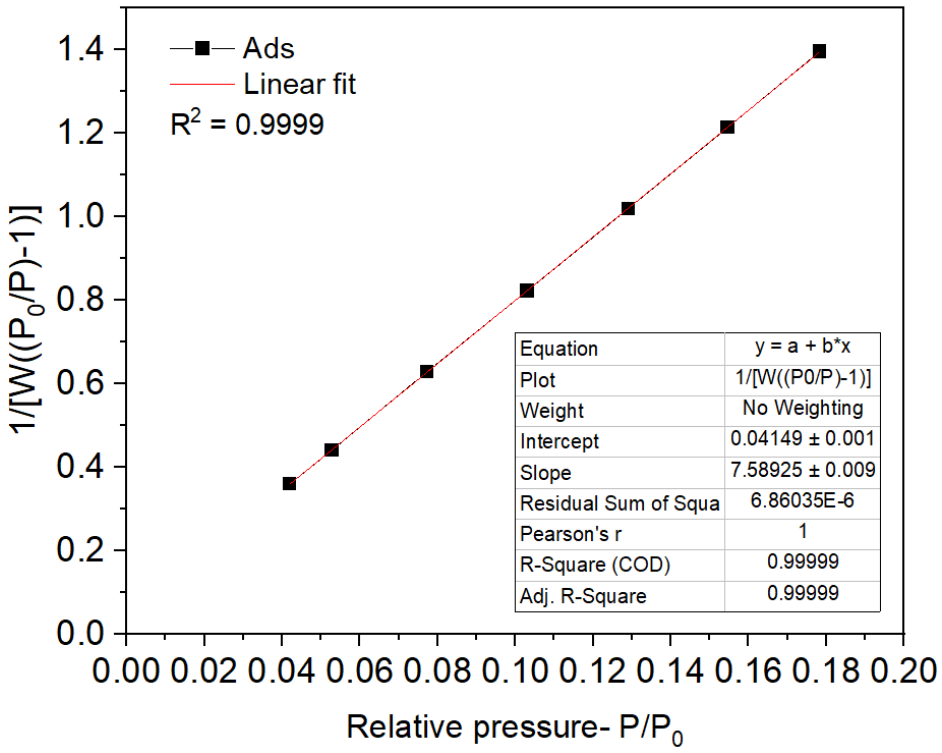

Figure S13. Derivation of the BET surface area from the 77 K nitrogen adsorption isotherms for Al-BP-Naph.

Section S7. CO_2 adsorption and isosteric heat (enthalpy) of adsorption

The isotherms were collected using a QUANTACHROME Autosorb-iQ-MP. The isosteric heat of adsorption was calculated using two different sets of isotherm data points at the different temperatures of 293 K and 273 K using the following Freundlich-Langmuir method with equation (2)

$$n = a \cdot b \cdot p^c / 1 + b \cdot p^c \qquad (2)$$

Where n: the adsorbed amount (mmol g^{-1}).
a: the maximal loading (mmol g^{-1})
b: the affinity constant
c: the heterogeneity exponent

The pressure at the given adsorbed amount can be calculated when rearranging the Freundlich-Langmuir equation to the following form, equation (3).

$$P(n) = c \cdot \sqrt{(n / a \cdot b - n \cdot b)} \qquad (3)$$

The parameters a, b and c were taken from the fitting equation.

The isosteric enthalpy of adsorption was then calculated via the Clausius-Clapeyron equation (4):

$$\Delta H_{(ads)} \cdot n = - R \cdot \ln(p_2/p_1) \cdot (T_1 \cdot T_2)/(T_2 - T_1) \qquad (4)$$

Where $\Delta H_{(ads)}$: the isosteric enthalpy of adsorption kJ mol^{-1}
T_1: absolute Temperature in K (here 273 K)
T_2: absolute Temperature in K (here 293 K)
R: the universal gas constant with the value 8.3145 J K^{-1} mol^{-1}.

According to Nuhnen et al. [4], when interpolating the loading n, the heat of adsorption Q_{st} is obtained as a function of a loading (equation (5)-(7)).

$$\Delta H_{(ads)} = - R \cdot m' \qquad (5)$$

$$m' = \ln(p_2/p_1) \cdot (T_1 \cdot T_2)/(T_2 - T_1) \qquad (6)$$

$$\Delta H_{(ads)} = - Q_{st} \qquad (7)$$

Table S2. Fitting constants of the Freundlich-Langmuir fit.

Measurement	A	B	C	R^2
Al-BP-Naph-273 K	3.7128	0.5688	0.8708	0.999
Al-BP-Naph-293 K	6.2964	0.2758	0.9646	0.999

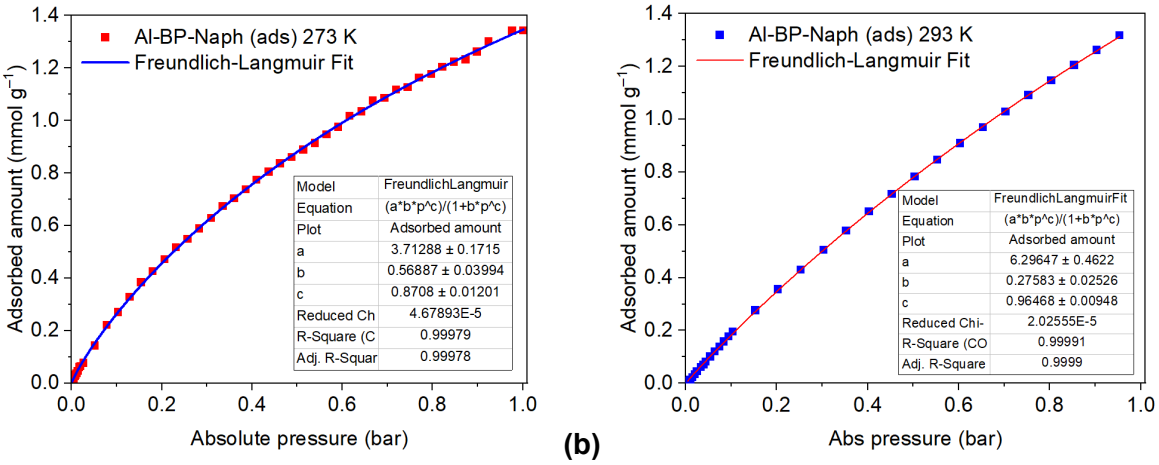

Figure S14. Adsorption of CO_2 at (**a**): 273 K and (**b**): 293 K, with the subsequent parameters of the Freundlich-Langmuir fit.

Table S3. Literature comparison between the CO_2 uptake and CO_2 heat of adsorption near zero coverage of Al-BP-Naph and other biphenyl-based MOFs.

	CO_2 uptake		CO_2 Q_{st}^0	
Sample	**293 K ($cm^3\ g^{-1}$)**	**273 K ($cm^3\ g^{-1}$)**	**(kJ mol^{-1})**	**Ref**
Al-BP-Naph	29.4	30.11	26	This work
DUT-5	36.2[a]	48.6	-[b]	5
COMOC-2	19.0	30.0	30	6
UiO-67(NH_2)$_2$	-[b]	-[b]	25	7
MFM-300(Ga_2)	52.6	56.2	34	8
MFM-300($Ga_{1.87}$ $Fe_{0.13}$)	57.5	85.6	31	8
UiO-67(1:2)	27.0	57.3	43	9
UiO-67-I(50)	45.0	86.5	51	9
BUT-10	50.6[a]	-[b]	22	10
BUT-11	53.5[a]	-[b]	26	10
UiO-67	22.9[a]	-[b]	17	10

[a]This measurement is done at 298 K.
[b] Not mentioned

Section S8. Photoluminescent properties

Selectivity: The photoluminescent (PL) properties of Al-BP-Naph in dimethylformamide (DMF) emulsion were investigated at room temperature. Metal ion quenching properties towards Al-BP-Naph were studied by introducing 3 mL of a 1 g L^{-1} suspension of Al-BP-Naph into the cuvette and then adding 100 µL of a 0.1 mol L^{-1} metal nitrate solution $M(NO_3)_x$ (M = Co^{2+}, Cu^{2+}, Mg^{2+}, Ni^{2+}, Cd^{2+}, Fe^{3+}, Ni^{3+}, Pb^{2+}, Zn^{2+}, Mn^{2+}, Li^{+}, Ca^{2+}, Ag^{+} and Cr^{3+}).

Sensitivity for LOD: The PL properties of Al-BP-Naph containing various concentration Fe^{3+} DMF solutions were also investigated using 3 mL of a 0.1 g L^{-1} MOF suspension and a 0.001 mol L^{-1} iron nitrate solution.

Table S4. Summary of the emission intensities from Figure 7a used to calculate the limit of detection (LOD).

Added volume of Fe^{3+} solution[(a)] (µL)	**Intensity I** (Cps)	Total volume (mL)	Final Fe^{3+} concentration (mol L^{-1})	$(I_0/I)-1$
Blank 1	119106	3	0	-
Blank 2	118903	3	0	-
Blank 3	117074	3	0	-
Blank 4	120194	3	0	-
Blank 5	119900	3	0	-
Blank 6	116524	3	0	-
Blank 7	118306	3	0	-
Blank 8	118597	3	0	-
Blank 9	119048	3	0	-
Blank 10	121846	3	0	-
Blank 11	120039	3	0	-
Blank 12	118425	3	0	-
Blank 13	116698	3	0	-
20	115271	3.020	6.623×10^{-6}	0.030788
30	112377	3.030	9.901×10^{-6}	0.057334
40	106763	3.040	1.316×10^{-5}	0.112932
50	105437	3.050	1.639×10^{-5}	0.126929
60	102261	3.060	1.961×10^{-5}	0.161929
70	100416	3.070	2.280×10^{-5}	0.183278
80	98738	3.080	2.597×10^{-5}	0.203387
90	95949	3.090	2.912×10^{-5}	0.238366
100	93932	3.100	3.226×10^{-5}	0.264958

[(a)] Concentration of Fe^{3+} solution: 0.001 mol L^{-1}.

Mean blank (I_0) = 118820

$\sigma_{Blank} = \sqrt{\frac{\sum(I-I_0)^2}{(N-1)}}$ = 1503 (N = 13)

Limit of detection (LOD) and limit of quantification (LOQ):

σ standard deviation of the blank measurements and k is the slope of fitting line of fluorescence intensity versus analyte ion concentration (Figure 7c in the main text)

LOD = 3σ/k = 3 × 1503/ (801913000 L mol^{-1}) = 5.6 µmol L^{-1}
LOQ = 10σ/k = 10 × 1503/ (801913000 L mol^{-1}) = 18.8 µmol L^{-1}

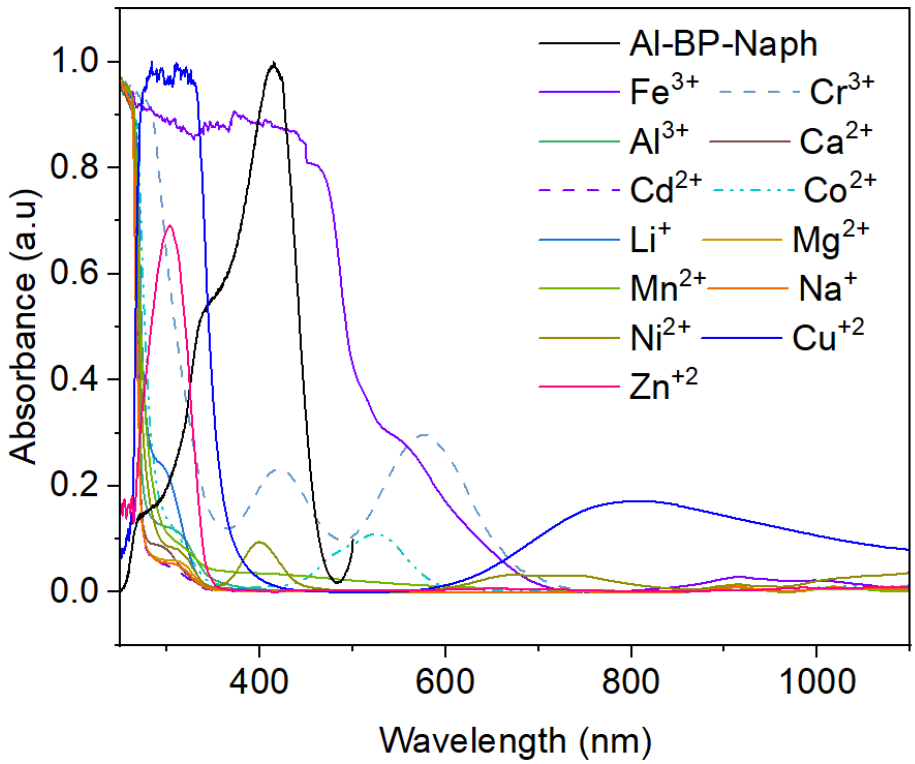

Figure S15. UV/Vis absorbance spectra of the different metal nitrate salts (0.1 mol L^{-1}) and the excitation spectrum of the Al-BP-Naph suspension in DMF (c = 1 g L^{-1}).

Co^{2+} has its absorption maximum at 525 nm with a range from 470 to 550 nm which is outside the main absorption of the Al-BP-Naph suspension.
Instead Cr^{3+} has an absorption at 415 nm with a range from 370 to 471 nm which explains why Cr^{3+} also slightly decreases the intensity of the MOF.
Also, Zn^{2+}has an absorption maximum at 370 nm with a range between 265 to 340 nm that overlaps with the high energy shoulder of the excitation spectrum of the MOF.
Thus, Cr^{3+} and Zn^{2+} can also compete with the MOF in absorbing electromagnetic energy and this translates to decreased emission intensity in Figure 6a and better represented in Figure 6b.
Cu^{2+} has its absorption maxima at 303 nm and 800 nm with ranges from 270 to 330 nm and 620 to 1000 nm. The first maximum at 300 nm overlaps only very slightly with the high-energy shoulder of the excitation spectrum of the Al-BP-Naph suspension but is otherwise largely outside the main absorption of the Al-BP-Naph suspension.

Section S9. References

1. Cseri, L.; Hardian, R.; Anan, S.; Vovusha, H.; Schwingenschlögl, U.; Budd, P. M.; Sada, K.; Kokado, K.; Szekely, G. Bridging the interfacial gap in mixed-matrix membranes by nature-inspired design: precise molecular sieving with polymer-grafted metal–organic frameworks. *J. Mater. Chem. A* **2021**, *9 (42)*, 23793-23801. DOI: 10.1039/D1TA06205K.

2. Petříček, V.; Dušek, M.; Palatinus, L. Crystallographic Computing System JANA2006: General features. *Z. Kristallogr.* **2014**, *229* (5), 345–352.DOI: 10.1515/zkri-2014-1737

3. Liu, Y.-Y.; Couck, S.; Vandichel, M.; Grzywa, M.; Leus, K.; Biswas, S.; Volkmer, D.; Gascon, J.; Kapteijn, F.; Denayer, J. F. M.; et al. New VIV-Based Metal–Organic Framework Having Framework Flexibility and High CO_2 Adsorption Capacity. *Inorg. Chem*. **2013**, *52 (1)*, 113-120. DOI: 10.1021/ic301338a.

4. Nuhnen, A.; Janiak, C. A practical guide to calculate the isosteric heat/enthalpy of adsorption via adsorption isotherms in metal–organic frameworks, MOFs. *Dalton Trans*. **2020**, *49 (30)*, 10295-10307. DOI: 10.1039/D0DT01784A.

5. Raja, D. S.; Chang, I.-H.; Jiang, Y.-C.; Chen, H.-T.; Lin, C.-H. Enhanced Gas Sorption Properties of a New Sulfone Functionalized Aluminum Metal-Organic Framework: Synthesis, Characterization, and DFT Studies. *Microporous Mesoporous Mater.* **2015**, *216*, 20–26. https://doi.org/10.1016/j.micromeso.2015.02.023.

6. Wang, G.; Leus, K.; Couck, S.; Tack, P.; Depauw, H.; Liu, Y.-Y.; Vincze, L.; Denayer, J. F. M.; Van Der Voort, P. Enhanced gas sorption and breathing properties of the new sulfone functionalized COMOC-2 metal organic framework. *Dalton Trans.* **2016**, *45 (23)*, 9485-9491, DOI: 10.1039/C6DT01355D.

7. Ko, N.; Hong, J.; Sung, S.; Cordova, K. E.; Park, H. J.; Yang, J. K.; Kim, J. A significant enhancement of water vapour uptake at low pressure by amine-functionalization of UiO-67. *Dalton Trans.* **2015**, *44 (5)*, 2047-2051, 10.1039/C4DT02582B. DOI: 10.1039/C4DT02582B

8. Krap, C. P.; Newby, R.; Dhakshinamoorthy, A.; García, H.; Cebula, I.; Easun, T. L.; Savage, M.; Eyley, J. E.; Gao, S.; Blake, A. J.; et al. Enhancement of CO_2 Adsorption and Catalytic Properties by Fe-Doping of $[Ga_2(OH)2(L)]$ (H_4L = Biphenyl-3,3′,5,5′-tetracarboxylic Acid), MFM-300(Ga_2). *Inorg. Chem.* **2016**, *55 (3)*, 1076-1088. DOI: 10.1021/acs.inorgchem.5b02108

9. Wang, B.; Zeng, J.; He, H. Enhancing CO_2 adsorption capacity and selectivity of UiO-67 through external ligand modification. *Sep. Purif. Technol.* **2025**, *354*, 128651. DOI: https://doi.org/10.1016/j.seppur.2024.128651.

10. Wang, B.; Huang, H.; Lv, X.-L.; Xie, Y.; Li, M.; Li, J.-R. Tuning CO_2 Selective Adsorption over N_2 and CH_4 in UiO-67 Analogues through Ligand Functionalization. *Inorg. Chem.* **2014**, *53* (17), 9254-9259. DOI: 10.1021/ic5013473.

11. Xu, H.; Dong, Y.; Wu, Y.; Ren, W.; Zhao, T.; Wang, S.; Gao, J. An -OH group functionalized MOF for ratiometric Fe^{3+} sensing. *J. Solid State Chem*. **2018**, *258*, 441-446. DOI: https://doi.org/10.1016/j.jssc.2017.11.013.

3.2 Synthesis and characterization of covalent triazine frameworks based on 4,4′-(Phenazine-5,10-diyl)dibenzonitrile and Its application in CO_2/CH_4 separation

This work was published in:

Othman, H.; Oestreich, R.; Küll, V.; Fetzer, M.N.A.; Janiak, C. Synthesis and Characterization of Covalent Triazine Frameworks Based on 4,4′-(Phenazine-5,10-diyl)dibenzonitrile and Its Application in CO_2/CH_4 Separation. Molecules 2025, 30, 3110. https://doi.org/10.3390/molecules30153110.

Short summary:

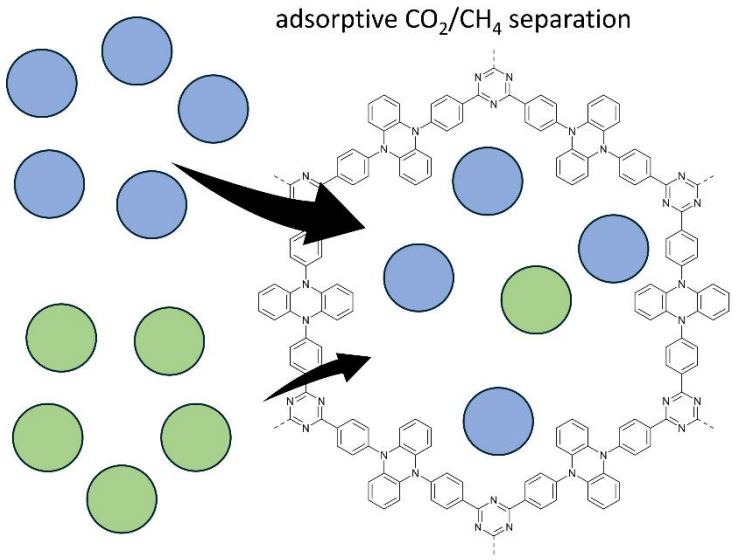

Covalent triazine frameworks (CTFs) have gained recognition as stable porous organic polymers, for example, for CO_2 separation. From the monomer 4,4′-(phenazine-5,10-diyl)dibenzonitrile (pBN), new pBN-CTFs were synthesized using the ionothermal method with a variation in temperature (400 and 550 °C) and the $ZnCl_2$-to-monomer ratio (10 and 20). N_2 adsorption yielded BET surface areas up to 1460 m^2g^{-1}. The pBN-CTFs are promising CO_2 adsorbents and are comparable to other benchmark CTFs such as CTF-1 with a CO_2 uptake of pBN-CTF-10-550 at 293 K of up to 54 $cm^3\ g^{-1}$ or 96 mg g^{-1}, with a CO_2/CH_4 IAST selectivity of 22 for a 50% mixture of CO_2/CH_4. pBN-CTF-10-400 has a very high heat of adsorption of 79 kJ mol^{-1} for CO_2 near zero coverage in comparison to other CTFs, and it also stays well above the liquefaction heat of CO_2 due to its high microporosity of 50% of the total pore volume.

Contribution to the publication:

Hanibal Othman: concept development. Synthesis of the organic monomer and the covalent triazine framework. Assessment and interpretation of the results. Writing and revision of the manuscripts.

Robert Oestreich: measurement of a few CO_2 adsorption.

Vivian Küll: measurement of a few CO_2 adsorption.

Markus N.A. Fetzer: Energy-dispersive X-ray spectroscopy measurements analysis and scanning electron microscopy photos.

Christoph Janiak: Idea and conceptualization. Assessment and interpretation of the results writing and revision of the manuscripts.

molecules

MDPI

Article

Synthesis and Characterization of Covalent Triazine Frameworks Based on 4,4′-(Phenazine-5,10-diyl)dibenzonitrile and Its Application in CO_2/CH_4 Separation

Hanibal Othman, Robert Oestreich, Vivian Küll, Marcus N. A. Fetzer and Christoph Janiak *

Institut für Anorganische Chemie und Strukturchemie, Heinrich-Heine-Universität Düsseldorf, 40204 Düsseldorf, Germany; hanibal.othman@hhu.de (H.O.); robert.oestreich@hhu.de (R.O.); vivian.kuell@hhu.de (V.K.); marcus.fetzer@hhu.de (M.N.A.F.)

* Correspondence: janiak@uni-duesseldorf.de

Abstract

Covalent triazine frameworks (CTFs) have gained recognition as stable porous organic polymers, for example, for CO_2 separation. From the monomer 4,4′-(phenazine-5,10-diyl)dibenzonitrile (pBN), new pBN-CTFs were synthesized using the ionothermal method with a variation in temperature (400 and 550 °C) and the $ZnCl_2$-to-monomer ratio (10 and 20). N_2 adsorption yielded BET surface areas up to 1460 m^2g^{-1}. The pBN-CTFs are promising CO_2 adsorbents and are comparable to other benchmark CTFs such as CTF-1 with a CO_2 uptake of pBN-CTF-10-550 at 293 K of up to 54 $cm^3\ g^{-1}$ or 96 mg g^{-1}, with a CO_2/CH_4 IAST selectivity of 22 for a 50% mixture of CO_2/CH_4. pBN-CTF-10-400 has a very high heat of adsorption of 79 kJ mol^{-1} for CO_2 near zero coverage in comparison to other CTFs, and it also stays well above the liquefaction heat of CO_2 due to its high microporosity of 50% of the total pore volume.

Keywords: covalent triazine frameworks; BET surface area; adsorption; carbon dioxide separation from methane; heat of adsorption

Academic Editor: Francis Verpoort

Received: 1 July 2025
Revised: 17 July 2025
Accepted: 22 July 2025
Published: 24 July 2025

Citation: Othman, H.; Oestreich, R.; Küll, V.; Fetzer, M.N.A.; Janiak, C. Synthesis and Characterization of Covalent Triazine Frameworks Based on 4,4′-(Phenazine-5,10-diyl)dibenzonitrile and Its Application in CO_2/CH_4 Separation. *Molecules* **2025**, *30*, 3110. https://doi.org/10.3390/molecules30153110

1. Introduction

Porous materials contain interconnected pores which can have different length scales from micro- (<2 nm) and meso- (2–50) nm to macropores (>50 nm) [1,2]. Covalent triazine frameworks (CTFs) are micro-mesoporous organic polymers that are constructed from 1,3,5-triazine rings joined with linkers to ideally give two-dimensional networks with hexagonal openings (Figure 1) [3–5].

The nitrogen content and the porosity of the CTFs together with their thermal stability make them interesting materials for gas adsorption, storage and separation, pollutant removal, catalysis, and sensing [6–13], including CO_2/N_2 and CO_2/CH_4 separation, both in the neat form [14–17] and as a filler for organic polymers in mixed-matrix membranes [18–20]. Since the inception of covalent triazine frameworks in 2008 [21], these materials have been investigated for their CO_2 adsorption [22–31].

One of the standard synthesis methods of CTFs is the ionothermal method, in which the nitrile monomer is heated with excess zinc chloride under vacuum or an inert atmosphere to a chosen temperature in the range between 400 and 900 °C [32]. In this reaction, the molten zinc chloride salt acts as a solvent, as a Lewis acid, and as a porogen [33].

The surface area is not necessarily the determining and main property of CTFs for CO_2 adsorption. A study showed an inverse relationship between BET surface area and the

uptake of CO_2 [16]. This correlation can be understood by the increase in the surface area with synthesis temperature and the concomitant decrease in the nitrogen content. When the CTFs are synthesized under relatively low temperatures (e.g., at 350 °C), the nitrogen loss is minimized but so is the surface area. Under higher synthesis temperatures (over 500 °C), significant nitrogen loss occurs, resulting in materials that transition towards high-surface-area carbon structures with some residual nitrogen content. Often, 400 °C is chosen as a compromise between good surface area and not too high nitrogen loss. For a high CO_2 uptake, a high nitrogen content is aimed for. The structural features and performance of CTFs are highly sensitive to the monomer structure and the salt-to-monomer ratio employed during synthesis. For instance, adjusting the $ZnCl_2$ ratio can influence the degree of polymerization, porosity, and degree of graphitization, all of which affect gas sorption behavior [21].

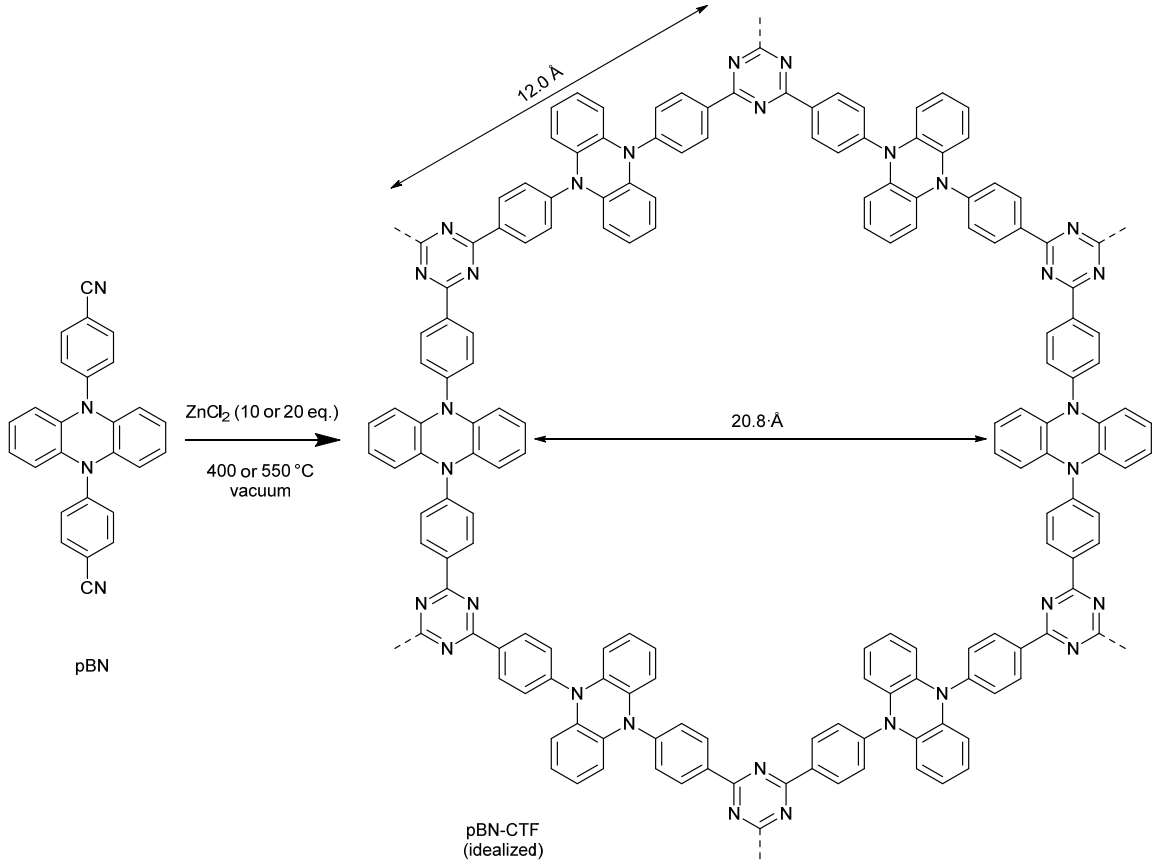

Figure 1. Synthesis of pBN-CTF from the monomer 4,4′-(phenazine-5,10-diyl)dibenzonitrile (pBN) with the CTF shown as an idealized hexagonal ring structure. The edge length and width of the ideal hexagon were determined graphically on the basis of the length of the C = C double with 1.34 Å.

Several studies have demonstrated the superior CO_2 adsorption capacity and selectivity of functionalized CTFs. Gu et al. reported CTFs with notable CO_2 uptake and selectivity, emphasizing the role that microporosity plays in enhancing gas affinity. Similarly, Buyukcakir et al. introduced charged CTFs, showing that ionic functionality can improve both CO_2 capture and catalytic conversion, underlining the synergy between framework charge and adsorption behavior [22,23].

The introduction of electron-withdrawing or polar functional groups such as fluorine or amines has also proven effective. Perfluorinated CTFs exhibit high CO_2 selectivity and water tolerance, while amine-modified frameworks display improved CO_2/CH_4 selectivity due to favorable acid–base interactions. These findings are consistent with those of Dawson

et al., who emphasized the role played by targeted chemical functionalization in enhancing CO_2 binding through dipole–quadrupole and hydrogen bonding interactions [24,26,27].

Together, these studies demonstrate that by carefully controlling synthesis parameters—including salt-to-monomer ratios—and integrating tailored functional groups, the adsorption performance of CTFs towards CO_2 can be significantly improved.

In this work, we use the dinitrile monomer 4,4′-(phenazine-5,10-diyl) dibenzonitrile (pBN) (Figure 1) to increase the nitrogen content for CO_2 adsorption and separation from CO_2/CH_4 mixtures. The CTFs from this monomer were synthesized with two ratios of $ZnCl_2$ to observe the impact of the salt ratio on the surface area and two temperatures to compare the effect of the temperature on the CO_2 and CH_4 adsorption.

2. Results and Discussion

New covalent triazine frameworks with the monomer 4,4′-(phenazine-5,10-diyl) dibenzonitrile (pBN) were synthesized via the ionothermal route with molten zinc chloride at two molar $ZnCl_2$/monomer ratios of 10:1 and 20:1 at three temperatures of 350 °C, 400 °C, and 550 °C, all at the reaction time of 48 h. The CTF samples are coded as pBN-CTF-xx-yyy by giving the molar $ZnCl_2$/monomer ratio (xx = 10 or 20), followed by the reaction temperature (yyy = 350, 400, or 550 °C). The pBN-CTF products were obtained as black monoliths, as typically observed for CTFs [34]. We tried to remove $ZnCl_2$ through washing with acidified water, as described in the literature for CTFs [34,35]. The product yields ranged from 68 to 92% (Table 1). The scanning electron microscopy images indicate the typical shard-like morphology of CTFs (Figure S1a–d, Supplementary Materials).

Table 1. Summary of the reaction parameters and yields for pBN-CTFs.

CTF Product [(a)]	Molar Ratio $ZnCl_2$/Monomer	Temperature (°C)	Yield (%)
pBN-CTF-10-350	10	350	79
pBN-CTF-20-350	20	350	78
pBN-CTF-10-400	10	400	68
pBN-CTF-20-400	20	400	92
pBN-CTF-10-550	10	550	84
pBN-CTF-20-550	20	550	40

[(a)] The first number in the product name after CTF gives the molar $ZnCl_2$/monomer ratio (10 or 20), followed by the reaction temperature (400 or 550 °C).

In the infrared spectra, the characteristic C-N stretching band of the triazine units was observed at 1384 and 1508 cm^{-1}, which slightly shifted from the C-N breathing and stretching mode of a molecular triazine unit (1363 and 1511 cm^{-1}, respectively), in agreement with the infrared spectra of other CTFs [3,36]. At the same time, the CN band of the monomer at 2227 cm^{-1} disappeared (Figure S2, Supplementary Materials), signaling that the monomer was consumed during polymerization.

The CHN elemental combustion analysis reveals the typical nitrogen loss which increases with a higher temperature (Table S1). Nitrogen loss is due to a partial aromatic nitrile decomposition into HCN, CN radicals, NH_3, and other species from the synthesis at temperatures of several hundred °C [3,5,35,37–42]. It can be seen that the C/N ratio is increased while the C/H ratio does not change much and stays close to the theoretical ratio, thereby indicating the primary loss of nitrogen-rich species. These results correlate with the general observation that an increase in temperature in ionothermal CTF synthesis leads to enhanced carbonization of the samples [5,12,39]. To avoid nitrogen loss, we also performed pBN-CTF formation at 350 °C. It became evident, however, that the surface area, porosity, and gas sorption of the samples at 350 °C varied greatly from batch to batch and

among different probes from the same batch (Section S4, Figures S5 and S6, Table S2). The surface area of the pBN-CTF-10-350, which is based on N_2 gas adsorption, ranged from 660 to 1027 m^2 g^{-1} across three batches (Figure S5a). CO_2 adsorption also showed variation across the three different batches and in addition across three probes from the same batches, with the uptake varying from 38 to 66 cm^3 g^{-1} (Figure S6).

Thus, the samples at 350 °C were inhomogeneous and could not be reproducibly synthesized. Therefore, the results from the reaction temperature at 350 °C were not included in the discussion here in the main text.

The remaining difference in the combined weight percentage of C, H, and N to 100% amounts to ~20% and is usually explained by residual $ZnCl_2$ or by the adsorption of water upon sample handling. In the literature, it is well known and frequently stated that the ionothermal $ZnCl_2$ route gives hard-to-remove $ZnCl_2$ metal impurities from the needed 5–10 times molar excess [8,21]. Energy-dispersive X-ray spectroscopy (EDX) gave a consistent amount of both Zn (~4.5 wt%) and Cl (7–10 wt%, Table S1). $ZnCl_2$, which is embedded in the pores of the CTFs, is difficult to remove even by extended washing, as some of the pores may no longer be accessible. The still remaining difference of ~5–15 wt% was shown to be due to the adsorption of moisture from air in the porous CTF. We have recently verified that CTFs are hygroscopic, with a water uptake of up to 0.12–0.20 g g^{-1} (equivalent to 11–17 wt%) at 50–60% air humidity (that is $P/P_0 \approx 0.5$–0.6) when handled or stored under ambient air [14,39,43].

Powder X-ray diffractograms (PXRDs) yield only broad reflexes without any clear signature of (001) reflections for parallel two-dimensional sheets in eclipsed stacking (Figure S3), which indicates a very amorphous structure because of defects in the idealized hexagonal sheets with possibly partial interpenetration or three-dimensional framework arrangements.

The nitrogen sorption isotherms of the CTFs in Figure 2 all show a pronounced adsorption step at $P/P_0 < 0.05$ corresponding to gas sorption in the micropores (pores < 2 nm, Figure 3, see Figure S5b for the 350 °C samples). The adsorption isotherms at 400 °C are largely of type Ib, indicative of materials with micropore size distributions over a broader range and narrow mesopores (pores > 2 nm, Figure 3a,b, Table 2) [1]. There is an H4 hysteresis, where the hysteresis loop closes only at very low relative pressure P/P_0. Such H4 loops are found among others with micro-mesoporous carbons [1,2]. For 550 °C, the adsorption isotherm of the 10–550 sample appears to be a Type I and IV combination. The adsorption branch has a "knee" at $P/P_0 \sim 0.4$ and the saturation plateau, which is a typical feature of Type IV isotherms, is then reached at high P/P_0. Type IV isotherms are given by largely mesoporous adsorbents (Figure 3c,d, Table 2). The isotherm at 550 °C has a hysteresis loop of Type H2b, which is associated with pore blocking in a wide range of pore neck widths. The N_2 adsorption isotherm of the sample 20–550 can be assigned as a mixture of Type I and Type II isotherms. The nitrogen uptake does not saturate towards $P/P_0 = 1$, which is due to a Type II branch. Type II indicates macropores (pores > 50 nm), which can also be caused by the voids between the particles. The isotherm has an H3 hysteresis loop that correlates with macropores that are not filled with pore condensate [1,2].

The specific surface areas were obtained from the Brunauer–Emmett–Teller (BET) model over the pressure range of $P/P_0 \approx 0.01$–0.07. Generally, the surface areas are higher for the 10:1 than for the 20:1 $ZnCl_2$/monomer ratios, giving 809–1460 m^2 g^{-1} for the former and only 348–950 m^2 g^{-1} for the latter (Table 2).

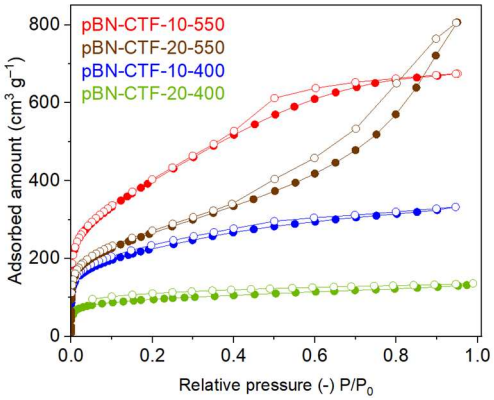

Figure 2. N_2 isotherms (at 77 K) of pBN-CTFs (filled symbols adsorption, empty symbols desorption).

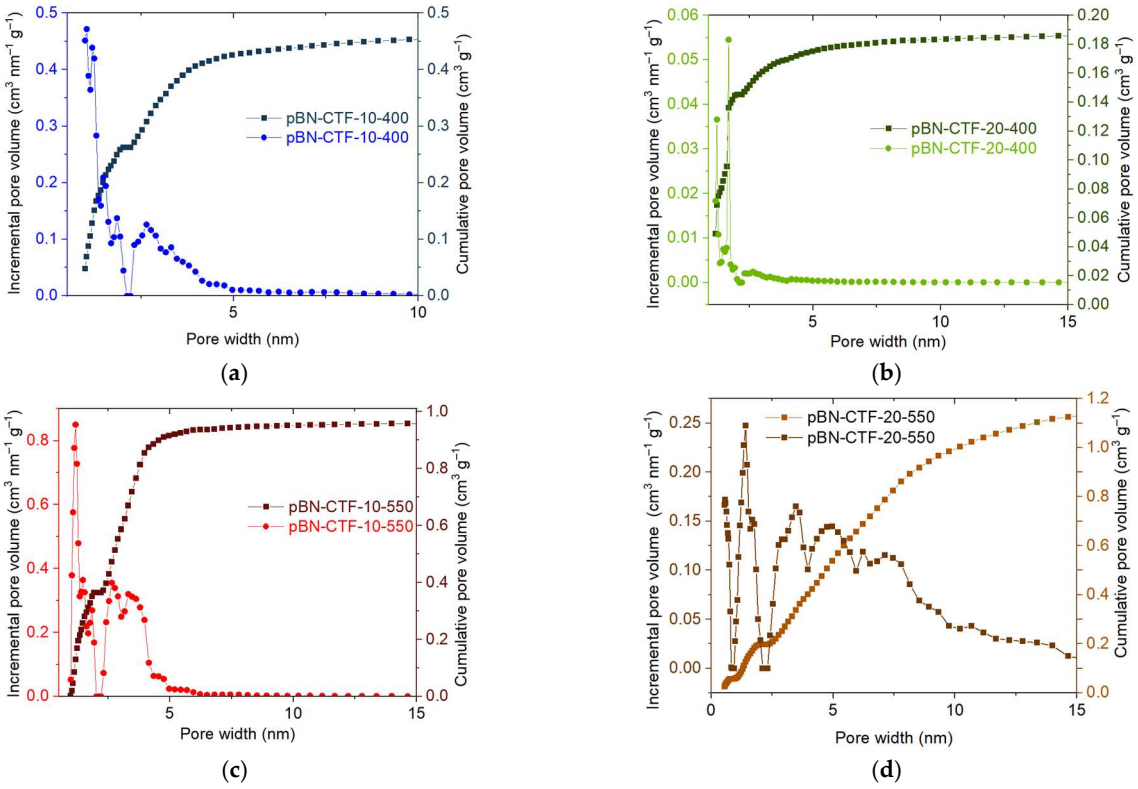

Figure 3. NLDFT pore size distribution (PSD) curves showing the cumulative pore volume (right y axes) and the incremental pore volume (left y axes) of pBN-CTF from N_2 adsorption using the "N_2 at 77 K on carbon slit pore, NLDFT equilibrium model" for (**a**) pBN-CTF-10-400, (**b**) pBN-CTF-20-400, (**c**) pBN-CTF-10-550, and (**d**) pBN-CTF-20-550.

Table 2. Surface area and porosity data from N_2 and CO_2 sorption studies.

CTF Product	S_{BET} [a] (m^2 g^{-1})	V_{tot} [b] (cm^3 g^{-1})	V_{micro} [c] (cm^3 g^{-1})	V_{micro}/V_{tot} [d]	$V_{1nm}(CO_2)$ [e] (cm^3 g^{-1})
pBN-CTF-10-400	809	0.51	0.25	0.50	0.015
pBN-CTF-20-400	348	0.19	0.15	0.79	0.009
pBN-CTF-10-550	1460	1.04	0.36	0.35	0.013
pBN-CTF-20-550	950	1.25	0.19	0.31	0.010

[a] Calculated BET surface area from N_2 adsorption at 77 K over a pressure range of P/P_0 = 0.01–0.07. [b] Total pore volume from N_2 adsorption isotherm at 77 K at P/P_0 = 0.95 for pores smaller than 40 nm. [c] Micropore volume from the NL-DFT method using the N_2 adsorption isotherm at 77 K at P/P_0 = 0.1 for pores with d $\leq$ 2 nm (20 Å). [d] Micropore volume/total pore volume. [e] Pore volume for pores with diameters smaller than 1 nm from CO_2 adsorption isotherms at 293 K and the CO_2 NL-DFT model.

In other CTF synthesis, e.g., with the tetra(4-cyanophenyl)ethylene monomer, $ZnCl_2$/monomer ratios of 10:1 and 20:1 were compared, with the former giving a more than two-fold higher surface area (2235 vs. 784 $m^2\ g^{-1}$) [37,44]. Thus, a ratio of 10:1 seems optimal for many ionothermal CTF syntheses. In the following, we will therefore only discuss the results for the 10:1 molar ratio; that is, the pBN-CTF-10 series. In agreement with other CTF works, the surface area of the sample synthesized at 400 °C is lower than that at 550 °C (Table 2, Figure 2) as generally the surface areas and total pore volumes for the resulting products increase with temperature [39]. The surface areas of the pBN-CTFs are comparable with other CTFs with longer linkers, e.g., terphenyl prepared by Kuhn et al. with a surface area of 975 $m^2\ g^{-1}$ [21], or even 2,8-dicyano-6H,12H-5,11-methanodibenzo [1,5]diazocine that was synthesized by Wang et al. with 612 $m^2\ g^{-1}$ [45].

Using NL-DFT calculations with a slit pore model on the N_2 adsorption isotherms, the pore widths and distribution as well as the total and micropore volume can be estimated (Figures 3 and S5, Table 2) [35]. We can note that for their amorphous nature, as evidenced by PXRD (Figure S3), the pBN-CTF-10-400, -20-400, and -10-550 materials feature a surprisingly narrow pore size distribution within 1–5 nm for 90% of the total pore volume (Figure 3a–c). The pore width distribution diagrams for the CTF-400s indicate pronounced maxima in the micropore region (<2 nm) and pore sizes larger than 2 nm up to 5 nm in a broad distribution. At 400 °C, the micropore volume encompasses more than 50% of the total pore volume; that is, the V_{micro}/V_{tot} values are above 0.50 (Table 2). At 550 °C, the total pore volume more than doubles in comparison to 400 °C, and the pore width distributions exhibit a broader contribution of mesopores between 2 and ~5 nm (Figure 3c) and beyond (Figure 3d), such that V_{micro}/V_{tot} drops below 35% (Table 1). Notably, the material with the highest surface area, namely pBN-CTF-10-550, has the lowest micropore volume fraction V_{micro}/V_{tot} among all the pBN-CTF materials listed in Table 2.

The pore size distribution (PSD) from N_2 sorption at 77 K is generally limited to pores between ~1 and ~40 nm. Macropores (>50 nm) are not accounted anymore by N_2 sorption. For pores smaller than 1 nm (10 Å), the size and distribution need to be obtained from CO_2 gas adsorption data, because for N_2 sorption at 77 K, the diffusion of the molecules into micropores smaller than 1 nm is very slow; hence, it requires very long N_2 adsorption measurements for equilibration of the adsorption isotherms, which cannot be assured. To avoid erroneous PSD results from the N_2 adsorption analysis, CO_2 adsorption analysis can be used (Figure 4a,b). The saturation pressure of CO_2 at 10 °C is ~4480 kPa (~33,450 Torr), so that a low relative pressure, which is necessary for the micropore analysis, is achieved in the range of moderate absolute pressures [46]. The micropore analysis with CO_2 at 283 K instead of N_2 at 77 K allows for a faster equilibration and access of even smaller pores as the kinetic diameter of CO_2 is only 3.30 Å versus 3.64 Å for N_2. The NL-DFT analysis of the CO_2 adsorption isotherms of the pBN-CTF-10s with the "CO_2 on carbon-based slit pore" model yield similar corrugated pore size distribution curves for the CTFs below 1 nm with pronounced maxima between 0.5 and 0.9 nm and at ~0.85 nm (Figure 2). The surface area was also calculated using the CO_2 adsorption at 195 K (values can be seen in Table 3 and isotherms in Figure S7a), which gave a smaller surface area than that of the N_2 counterpart, corresponding to the literature [37,47–50].

Volumetric CO_2 and CH_4 adsorption studies resulted in the isotherms depicted in Figure 4. At 283 K and 293 K, the pBN-CTF-10 materials show similar CO_2 sorption isotherm curvatures that did not level off much at 1 bar but still have a rather positive slope, which indicates that the uptake at 1 bar is far from saturated. At 195 K, the CO_2 uptake at 1 bar differentiates considerably for the pBN-CTF-10-400 and 10-550 material (Table 3, Figure S7), increasing nearly two-fold, from pBN-CTF-10-400 with 175 $cm^3\ g^{-1}$ to pBN-CTF-10-550 with 320 $cm^3\ g^{-1}$. As shown in Figures S9 and S10, this increase correlates

with the increase in surface area and pore volume from the 400 °C to the 550 °C material in Table 2.

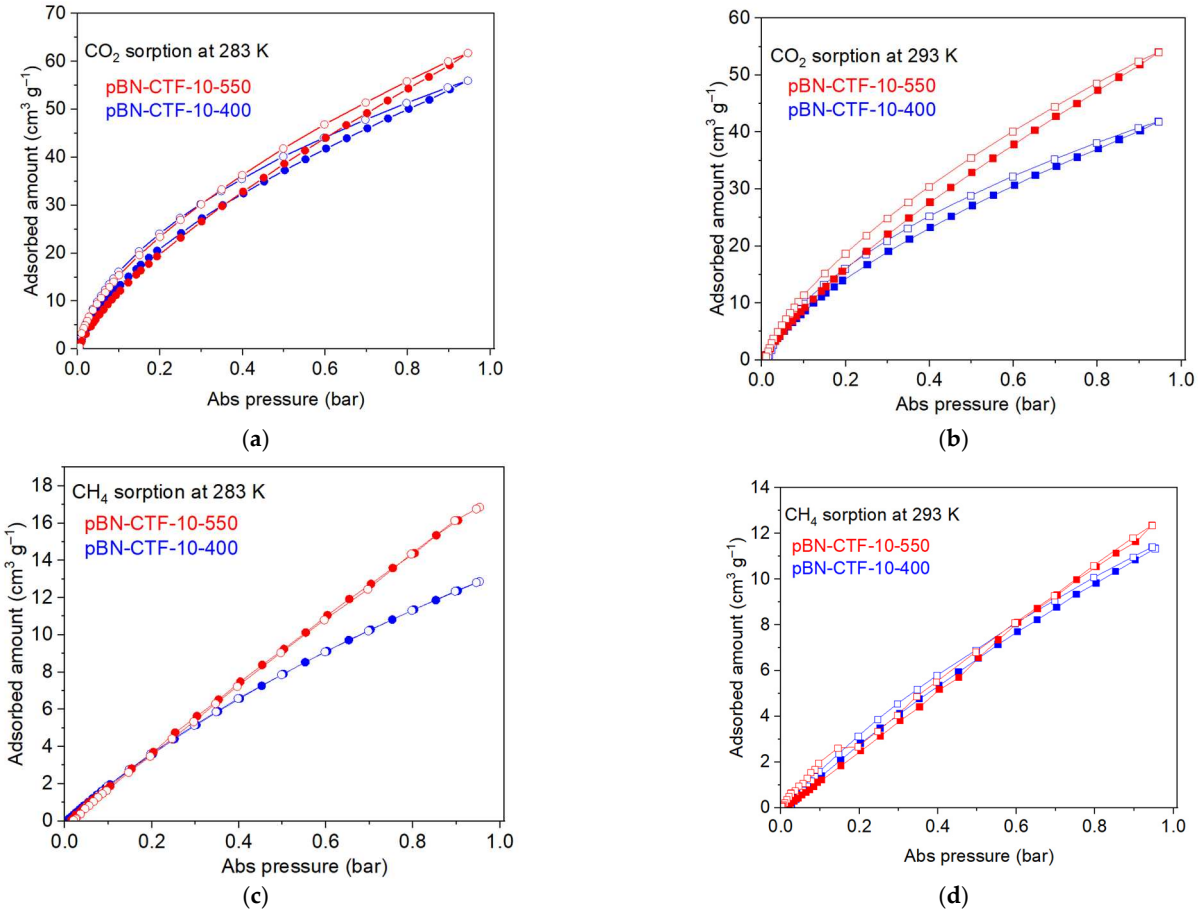

Figure 4. Adsorption and desorption isotherms of pBN-CTF-10-400 and pBN-CTF-10-550 for (**a**) CO_2 at 283 K, (**b**) CO_2 at 293 K, (**c**) CH_4 at 283 K, and (**d**) CH_4 at 293 K (filled symbols adsorption, empty symbols desorption). The CO_2 adsorption isotherms at 195 K are given in Figure S7a, and those for pBN-CTF-20-400 and -550 at 293 K are given in Figure S8.

Table 3. CO_2 and CH_4 adsorption results at 1 bar and heat of adsorption for CO_2 at zero coverage and CO_2:CH_4 selectivity.

CTF Product	S_{BET} (195 K) [(a)] (m^2 g^{-1})	CO_2 (cm^3 g^{-1})			CH_4 (cm^3 g^{-1})		CO_2 Q_{ads} [0 (b)] (kJ mol^{-1})	CH_4 Q_{ads} [0 (b)] (kJ mol^{-1})	IAST Selectivity for 50:50 CO_2:CH_4
		293 K	283 K	195 K	293 K	283 K			
pBN-CTF-10-400	524	42.8	55.9	175	11.3	12.9	79	36	22
pBN-CTF-10-550	746	54.0	61.7	320	12.3	16.9	60	39	- [(c)]

[(a)] BET surface area from CO_2 adsorption measured at 195 K in the range between 0.08 and 0.2 P/P_0. The difference in surface area between N_2 (77 K) and CO_2 (195 K) can be due to the kinetic energy difference at different temperatures and also the size of the molecules adsorbed. [(b)] Isosteric heat of adsorption of CO_2 or CH_4 towards zero loadings from the adsorption isotherms at 283 K and 293 K. [(c)] IAST selectivity for 50:50 mol:mol or equimolar fraction of CO_2 and CH_4 at 293 K and 1 bar. The linear CH_4 uptake of CTF-10-550 did not allow for a meaningful fit.

By comparing the pBN-CTFs from this work to other CTFs with linkers equal or longer than a biphenyl unit, it can be seen that the pBN-CTFs can compete very well in terms of CO_2 uptake (Figure 5, Table S4).

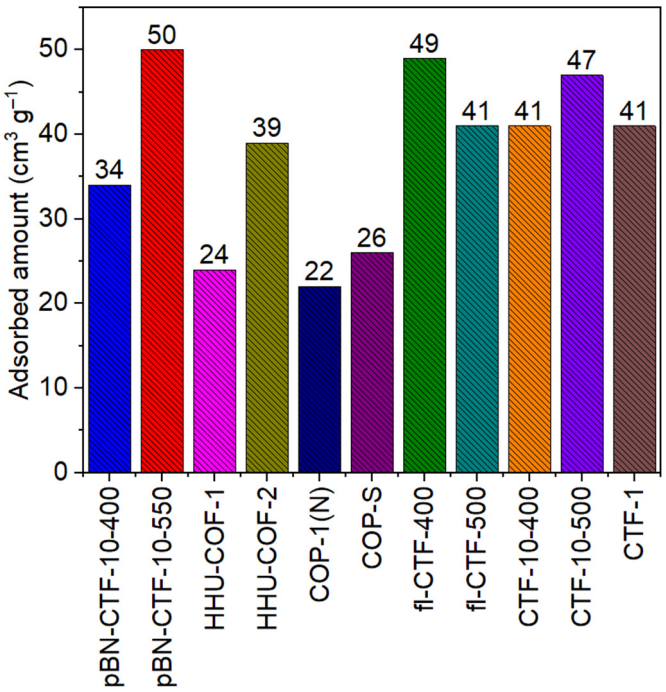

Figure 5. CO_2 uptake comparison at 298 K and 1 bar between the pBN-CTFs and selected CTFs with data from Table S4 [17,49,51–53]. The CTFs all have a linker with a length of at least a biphenyl unit, except for the reference of prototypical CTF-1. HHU-COF-1 is based on the monomer [1,1′-biphenyl]-4,4′-dicarbaldehyde, HHU-COF-2 on 2,2′,3,3′,5,5′,6,6′-octafluoro-[1,1′-biphenyl]-4,4′-dicarbaldehyde, condensed both with 1,3,5-tris-(4-aminophenyl)triazine [17]. COP-1(N) and COP-S are mixed linker CTFs from 2,4,6-trichloro-1,3,5-triazine with piperazine and 2,7-diazaspiro-[4,4]-nonane and [48], fl-CTF-400 and -500 are based on the 9H-fluorene-2,7-dicarbonitrile monomer [51], CTF-10-400 and -500 on 4,4′,4″,4‴-(1,4-phenylenebis(pyridine-4,2,6-triyl))tetrabenzonitrile [52], and CTF-1 on terephthalonitrile [53] (see Scheme S1 for the monomer structures). Table S7 summarizes the BET surface area, CO_2 uptake capacity, Q_{ads}, and CO_2/CH_4 IAST selectivity of the CTFs given here in Figure 5.

Covalent triazine frameworks are widely investigated for CO_2/N_2 and CO_2/CH_4 separation. The ideal adsorbed solution theory (IAST) can give an indication of the selectivity of different gas mixtures at a given pressure or for a given gas mixture at different pressures. The only criterion that IAST requires is that both gases should have an equal spreading pressure at the given temperature [54]. The IAST selectivity is derived from the single gas adsorption isotherms and was calculated here on the bases of fitting the adsorption isotherms with the Freundlich–Langmuir adsorption model, and the parameters that resulted from the isotherm fitting (Table S5) were used to calculate the selectivity (Table 3). For example, the sample pBN-CTF-10-400 at 293 K has a maximal loading of 7.8 mmol g^{-1} and 1.8 mmol g^{-1} for CO_2 and CH_4, respectively, and an affinity constant of 0.32 mmol g^{-1} bar^{-1} and 0.41 mmol g^{-1} bar^{-1} for CO_2 and CH_4, respectively, with an R^2 value of 0.999 for both fits (Table S5).

IAST underscores the selectivity for CO_2 over CH_4 for the pBN-CTF-10-400 material, as seen already in the higher uptake of CO_2 over CH_4 at the same temperature (Table 3). At 283 K, the slight pressure and composition dependent CO_2/CH_4 selectivity for pBN-CTF-10-440 varies between 7 and 22. It decreases with pressure and increases with an increasing CH_4 fraction (Figure S13). At 293 K, the CO_2/CH_4 selectivity for pBN-CTF-10-440 stays rather constant between 0.01 and 0.8 CH_4 molar fraction. The preference for CO_2 can be explained from the pore structure and the interaction strength between the gas molecules and the framework. pBN-CTF-10-400 has good microporosity and nitrogen

content. Micropores favor CO_2 adsorption due to its smaller kinetic diameter (3.3 Å) compared to CH_4 (3.8 Å), while nitrogen functionalities enhance CO_2 affinity through dipole-quadrupole interactions.

From the measurement of gas adsorption at two temperatures with ΔT = 10 to 20 °C, the enthalpy (ΔH) or heat of gas adsorption ($Q_{ads} = -\Delta H$) can be obtained [15,55]. Near zero coverage, the heat of adsorption for CO_2 is remarkably high in comparison to other CTFs, with 79 kJ mol^{-1} for pBN-CTF-10-400 (Table S6). In Figure 6, the isosteric heat of adsorption was plotted against the amount of CO_2 and CH_4 adsorbed by the frameworks. pBN-CTF-10-400 has a higher microporosity and higher nitrogen content than pBN-CTF-10-550. This relates to a higher affinity for CO_2 than for CH_4 because (as just noted) CO_2, with its smaller kinetic diameter (3.3 Å) compared to CH_4 (3.8 Å), can occupy smaller micropores, and the CO_2 quadrupole can interact with the dipole of nitrogen functionalities. Micropores generally allow for multi-site or "wall–guest–wall" interactions between guest molecules and the inner pore surface [56]. The large decrease in the isosteric heat of adsorption from a near zero adsorbed amount to ~0.5 mmol g^{-1} adsorbed amount seen in Figure 6 for both gases is due to the initial filling of the very small or ultra-micropores with a diameter in the dimension of the adsorbate molecule with wall-to-wall interactions and the occupation of the nitrogen atom sites, which also have higher adsorption energies. Notably, the CO_2 heat of adsorption values of pBN-CTF-10-550 drop below the liquefaction heat of CO_2 of 17 kJ mol^{-1} when the adsorbed amount surpasses 1.1 mmol g^{-1}, while the heat of adsorption of pBN-CTF-10-400 stays well above the liquefaction heat of CO_2. A drop below the heat of liquefaction of CO_2 indicates weaker adsorbate–surface interactions than adsorbate–adsorbate interactions in the liquid phase. This behavior is beneficial in pressure or temperature swing adsorption (PSA/TSA) applications as it facilitates easier desorption with a lower energy input.

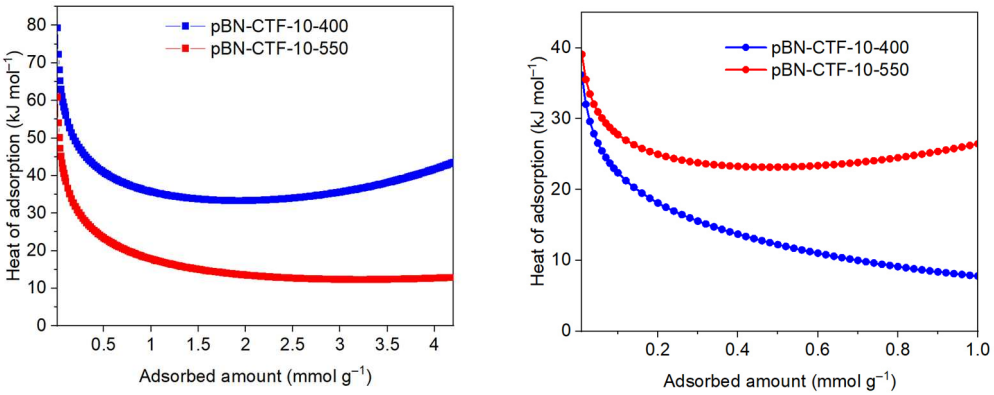

Figure 6. Isosteric heat of adsorption for (**a**) CO_2 and (**b**) CH_4 on pBN-CTF-10-400 and 550.

Conversely, pBN-CTF-10-550 exhibits a higher Q_{ads} for CH_4 over the whole uptake range compared to pBN-CTF-10-400 and also a higher heat of adsorption for CH_4 than for CO_2 once the adsorbed CO_2 amount exceeded ~0.4 mmol g^{-1} (compare Figure 6a,b). This can be explained by the more carbon-like non-polar nature of the pBN-CTF-10-550 material with less nitrogen content than pBN-CTF-10-400, which gives the former a relatively higher affinity to non-polar CH_4 [57,58]. As expected, the heat of adsorption near zero coverage is lower for CH_4 than for CO_2 for both CTFs (Table 3). A further comparison of the literature for CO_2 uptake and $Q_{ads}{}^0$ for CO_2 in CTFs can be found in Table S4 and Table S7, respectively, in the Supplementary Materials [14,18,25,26,59–69].

The thermogravimetric analysis showed that under air, all samples started decomposing (with weight loss) at ~400 °C, including the pBN-CTF, which was synthesized at 550 °C

(Figure S14). This mass loss of the pBN-CTF-10-400 sample is complete below 700 °C with a residual mass of ~2.5 wt%. The mass loss of pBN-CTF-10-550 continues to ~770 °C, leaving only ~0.2 wt%.

3. Materials and Methods

3.1. Instrumentation

Fourier transform infrared spectroscopic measurements were taken using a Bruker Tensor 37 (Bruker AXS, Karlsruhe, Germany) with KBr pellets in the range between 4000 and 500 cm^{-1}. For the N_2 sorption analysis, a Quantachrome Autosorb-IQ-MP (Quantachrome, Boynton Beach, FL, USA) was used. The samples were degassed for 24 h at 120 °C before connecting to the device. The measurement was taken at 77 K. The results were interpreted with the BET equation. The CO_2 sorption analysis was performed with a Quantachrome Autosorb-IQ-MP (Quantachrome, Boynton Beach, FL, USA). The measurement temperatures were 293, 283, and 195 K after activating (degassing) the samples under vacuum at 120 °C for 24 h. The temperature was held by virtue of a thermostated water bath (293 and 283 K) or with a cryodyne refrigerator model 8200 (195 K) (Janis, Woburn, MA, USA).

Thermogravimetric analysis was performed with a TG Tarsus 209 F3 (Netzsch, Selb, Germany). The samples were analyzed under synthetic air with a heating rate of 10 K/min from 25 to 900 °C. Powder X-ray diffraction patterns were recorded using a Bruker D2 phaser from Bruker (Bruker AXS, Karlsruhe, Germany) with Cu-Kα radiation, λ = 1.54182 Å at 300 W, 30 kV, 10 mA. Nuclear magnetic resonance (^{1}H-NMR) spectra were collected with a Bruker Avance III-600-I (Bruker, Karlsruhe, Germany). The chemical shifts are given in ppm and are referenced to the residual proton signal of the deuterated solvent (7.26 ppm for $CDCl_3$, 7.16 for C_6D_6).

3.2. Chemicals

Phenazine (99.86%) and 4-bromobenzonitrile (95%) were obtained from BLDpharm (Reinbek, Germany). Sodium dithionite (85%) was obtained from VWR chemicals (Darmstadt, Germany). Palladium acetate (99.9%) and tri-tert-butyl phosphine (99%) were purchased from Sigma-Aldrich (Darmstadt, Germany). All solvents were purchased from commercial suppliers with a minimum purity of 99.8%.

3.3. Synthesis of 5,10-Dihydrophenazine

Following the literature [70], a phenazine (2.5 g, 13.87 mmol) solution in ethanol (30 mL) and a sodium dithionite (24.1 g, 137 mmol) solution in water (125 mL) were placed into a round-bottom flask and heated to reflux at 95 °C for 3 h. Afterwards, the flask was cooled to room temperature and then the product was separated by filtration, washed three times with water (3 × 15 mL), dried under vacuum (10^{-3} mbar), and stored under nitrogen to avoid any oxidation. The yield was 2.10 g, 85%.

^{1}H NMR (600 MHz, $CDCl_3$) δ 8.27 (dd, J = 6.8, 3.5 Hz, 1H), 7.86 (dd, J = 6.8, 3.4 Hz, 1H), 6.12 (s, 2H), 1.57 (s, 3H).

3.4. Synthesis of 4,4′-(Phenazine-5,10-diyl)dibenzonitrile (pBN)

5,10-Dihydrophenazine (2 g, 11 mmoL), 4-bromobenzonitrile (4.38 g, 24 mmoL), and potassium carbonate (9.1 g, 65.8 mmoL) were combined in degassed toluene (80 mL) in a round-bottom flask under N_2 atmosphere according to the literature [70]. To this mixture, palladium acetate (0.141 g, 0.62 mmoL) and tri-tert-butyl phosphine (0.464 g, 2.30 mmoL) dissolved in 10 mL of toluene were added; the flask was then refluxed at 111 °C for 20 h. During cooling, water (30 mL) was added to the reaction mixture in order to stop the

reaction. The product was extracted from the water phase using chloroform (200 mL). The separated organic phase was washed with brine (saturated aqueous NaCl solution) three times (3 × 30 mL) and was dried over magnesium sulfate ($MgSO_4$) for 15 min. The organic phase was then filtered and concentrated via a rotary evaporator to ~50 mL; after that, 100 mL of n-hexane was added and cooled in an ice bath for 10 min. The separated product was filtered and dried in a vacuum oven (10^{-3} mbar) at 60 °C.

^{1}H NMR (600 MHz, C_6D_6) δ 6.96 (d, *J* = 8.2 Hz, 4H), 6.71 (d, *J* = 8.2 Hz, 4H), 6.41–6.37 (m, 4H), 5.69 (dt, *J* = 7.9, 3.9 Hz, 4H).

3.5. pBN-CTF Synthesis

Inside the glove box, a glass ampule with a Schlenk fitting was filled with (0.2 g, 0.5 mmol) pBN-2CN and 10 or 20 equivalents (0.680 g, 5 mmol or 1.3 g, 10 mmol) of anhydrous zinc chloride. Outside the glovebox, the ampule was evacuated and flame-sealed and heated for 48 h in a tube furnace at the chosen temperature of 350, 400, or 550 °C. The 350 and 400 °C reactions were carried out in a normal borosilicate glass (Pyrex); for 550 °C, a quartz glass ampule was used. After cooling the ampule to room temperature, the ampule was carefully opened with no sign of pressure built-up inside.

The reaction product was stirred in distilled water acidified with 0.5 mol/L of hydrochloric acid (HCl) to pH = 4 (50 mL) for three days. The stirring was vigorous to ensure the mechanical break-up of the black monolith to provide fine particles. After additional stirring for 72 h in distilled water, the product was filtered and washed with the organic solvents chloroform, acetone, and methanol (30 mL each) in this order. After the washing, the product was dried in a vacuum (10^{-3} mbar) oven at 60 °C for 24 h. The yields are listed in Table 1.

4. Conclusions

The molecule 4,4′-(phenazine-5,10-diyl)dibenzonitrile, with a long—about 12 Å—separation between the nitrile groups, can be successfully transformed by ionothermal synthesis into a porous covalent triazine framework (pBN-CTF). The surface area increases expectedly with the synthesis temperature and ranges from 809 to 1460 m^2 g^{-1} for the samples synthesized at 400 and 550 °C, respectively, with pores ranging between 1 and 4 nm. The pBN-CTF exhibited a good CO_2 uptake at 293 K, showing a similar performance to benchmark materials like CTF-1, due to the relatively high micropore fraction that ranged between 35% for the 550 °C and 50% for the 400° samples. The new material showed a significant difference and stark contrast to the adsorption of CO_2 over CH_4 for the potential separation, with a selectivity that reaches 22. For further work on pBN-CTFs and other CTFs in general, we plan to increase the nitrogen content of the formed framework through the addition of a nitrogen-rich compound such as melamine in order to introduce additional electron pair donors and thereby influence the adsorption properties. We will also check the elongation of the phenyl group in pBN with a biphenyl group, giving the monomer 4′,4‴-(phenazine-5,10-diyl)bis([1,1′-biphenyl]-4-carbonitrile)) that can be assumed to form CTFs with an even larger pore width of over 2 nm channel cross-sections to allow for faster mass transport; that is, diffusion through the then hierarchical micro-mesopores.

Supplementary Materials: The following supporting information can be downloaded at: https://www.mdpi.com/article/10.3390/molecules30153110/s1, Section S1. Scanning electron microscopy; Section S2. Fourier transform infrared spectroscopy and elemental analysis; Section S3. Powder X-ray diffraction; Section S4. Samples synthesized at 350 °C and their N_2 and CO_2 sorption studies; Section S5. CO_2 adsorption isotherms; Section S6. Calculations and fitting for the isosteric heat of adsorption and IAST selectivity of CO_2 and CH_4; Section S7. Thermogravimetric analysis (TGA); Section S8. Nuclear magnetic resonance spectrometry (NMR); Section S9. References.

Author Contributions: Conceptualization, H.O.; methodology, H.O., V.K., R.O., and M.N.A.F.; software, H.O.; validation, C.J. and H.O.; formal analysis, H.O.; investigation, H.O.; resources, C.J.; data curation, H.O.; writing—original draft preparation, H.O.; writing—review and editing, H.O. and C.J.; visualization, H.O.; supervision, C.J.; project administration, C.J. All authors have read and agreed to the published version of the manuscript.

Funding: This research received no external funding.

Institutional Review Board Statement: Not applicable.

Informed Consent Statement: Not applicable.

Data Availability Statement: The original contributions presented in this study are included in the article/Supplementary Materials. Further inquiries can be directed to the corresponding author.

Acknowledgments: Special thanks goes to Dietrich Püschel for his advice and supervision and to Birgit Tommes for her IR measurements.

Conflicts of Interest: The authors declare no conflicts of interest.

References

1. Thommes, M.; Kaneko, K.; Neimark, A.V.; Olivier, J.P.; Rodriguez-Reinoso, F.; Rouquerol, J.; Sing, K.S.W. Physisorption of gases, with special reference to the evaluation of surface area and pore size distribution (IUPAC Technical Report). *Pure Appl. Chem.* **2015**, *87*, 1051–1069. [CrossRef]
2. Cychosz, K.A.; Thommes, M. Progress in the Physisorption Characterization of Nanoporous Gas Storage Materials. *Engineering* **2018**, *4*, 559–566. [CrossRef]
3. Bojdys, M.J.; Jeromenok, J.; Thomas, A.; Antonietti, M. Rational Extension of the Family of Layered, Covalent, Triazine-Based Frameworks with Regular Porosity. *Adv. Mater.* **2010**, *22*, 2202–2205. [CrossRef] [PubMed]
4. Meier, C.B.; Clowes, R.; Berardo, B.E.; Jelfs, K.E.; Zwijnenburg, M.A.; Sprick, R.S.; Cooper, A.I. Structurally Diverse Covalent Triazine-Based Framework Materials for Photocatalytic Hydrogen Evolution from Water. *Chem. Mater.* **2019**, *31*, 8830–8838. [CrossRef] [PubMed]
5. Kuhn, P.; Forget, A.; Su, D.; Thomas, A.; Antonietti, M. From Microporous Regular Frameworks to Mesoporous Materials with Ultrahigh Surface Area: Dynamic Reorganization of Porous Polymer Networks. *J. Am. Chem. Soc.* **2008**, *130*, 13333–13337. [CrossRef] [PubMed]
6. Kuecken, S.; Acharjya, A.; Zhi, L.; Schwarze, M.; Schomäcker, R.; Thomas, A. Fast tuning of covalent triazine frameworks for photocatalytic hydrogen evolution. *Chem. Commun.* **2017**, *53*, 5854–5857. [CrossRef] [PubMed]
7. Liao, L.; Li, M.; Yin, Y.; Chen, J.; Zhong, Q.; Du, R.; Liu, S.; He, Y.; Fu, W.; Zeng, F. Advances in the Synthesis of Covalent Triazine Frameworks. *ACS Omega* **2023**, *8*, 4527–4542. [CrossRef] [PubMed]
8. Liu, M.; Guo, L.; Jin, S.; Tan, B. Covalent triazine frameworks: Synthesis and applications. *J. Mater. Chem. A* **2019**, *7*, 5153–5172. [CrossRef]
9. Lee, J.-S.M.; Cooper, A.I. Advances in Conjugated Microporous Polymers. *Chem. Rev.* **2020**, *120*, 2171–2214. [CrossRef] [PubMed]
10. Krishnaraj, C.; Jena, H.S.; Leus, K.; van der Voort, P. Covalent triazine frameworks—A sustainable perspective. *Green Chem.* **2020**, *22*, 1038–1071. [CrossRef]
11. Aggarwal, S.; Awasthi, S.K. Emerging trends in the development and applications of triazine-based covalent organic polymers: A comprehensive review. *Dalton Trans.* **2024**, *53*, 11601–11643. [CrossRef] [PubMed]
12. Bhunia, A.; Esquivel, D.; Dey, S.; Fernández-Terán, R.; Goto, Y.; Inagaki, S.; Van Der Voort, P.; Janiak, C. A photoluminescent covalent triazine framework: CO_2 adsorption, light-driven hydrogen evolution and sensing of nitroaromatics. *J. Mater. Chem. A* **2016**, *4*, 13450–13457. [CrossRef]
13. Gao, Q.; Li, X.; Ning, G.-H.; Leng, K.; Tian, B.; Liu, C.; Tang, W.; Xu, H.-S.; Loh, K.P. Highly photoluminescent two-dimensional imine-based covalent organic frameworks for chemical sensing. *Chem. Commun.* **2018**, *54*, 2349–2352. [CrossRef] [PubMed]
14. Dey, S.; Bhunia, A.; Esquivel, D.; Janiak, C. Covalent triazine-based frameworks (CTFs) from triptycene and fluorene motifs for CO_2 adsorption. *J. Mater. Chem. A* **2016**, *4*, 6259–6263. [CrossRef]
15. Wessely, I.D.; Schade, A.M.; Dey, S.; Bhunia, A.; Nuhnen, A.; Janiak, C.; Bräse, S. Covalent Triazine Frameworks Based on the First Pseudo-Octahedral Hexanitrile Monomer via Nitrile Trimerization: Synthesis, Porosity, and CO_2 Gas Sorption Properties. *Materials* **2021**, *14*, 3214. [CrossRef] [PubMed]
16. Wang, K.; Huang, H.; Liu, D.; Wang, C.; Li, J.; Zhong, C. Covalent Triazine-Based Frameworks with Ultramicropores and High Nitrogen Contents for Highly Selective CO_2 Capture. *Environ. Sci. Technol.* **2016**, *50*, 4869–4876. [CrossRef] [PubMed]

17. Bügel, S.; Hähnel, M.; Kunde, T.; de Sousa Amadeu, N.; Sun, Y.; Spieß, A.; Beglau, T.H.Y.; Schmidt, B.M.; Janiak, C. Synthesis and Characterization of a Crystalline Imine-Based Covalent Organic Framework with Triazine Node and Biphenyl Linker and Its Fluorinated Derivate for CO_2/CH_4 Separation. *Materials* **2022**, *15*, 2807. [CrossRef] [PubMed]
18. Dey, S.; Bügel, S.; Sorribas, S.; Nuhnen, A.; Bhunia, A.; Coronas, J.; Janiak, C. Synthesis and Characterization of Covalent Triazine Framework CTF-1@Polysulfone Mixed Matrix Membranes and Their Gas Separation Studies. *Front. Chem.* **2019**, *7*, 693. [CrossRef] [PubMed]
19. Bügel, S.; Spieß, A.; Janiak, C. Covalent triazine framework CTF-fluorene as porous filler material in mixed matrix membranes for CO_2/CH_4 separation. *Microporous Mesoporous Mater.* **2021**, *316*, 110941. [CrossRef]
20. Bügel, S.; Hoang, Q.-D.; Spieß, A.; Sun, Y.; Xing, S.; Janiak, C. Biphenyl-Based Covalent Triazine Framework/Matrimid® Mixed-Matrix Membranes for CO_2/CH_4 Separation. *Membranes* **2021**, *11*, 795. [CrossRef] [PubMed]
21. Kuhn, P.; Antonietti, M.; Thomas, A. Porous, Covalent Triazine-Based Frameworks Prepared by Ionothermal Synthesis. *Angew. Chem. Int. Ed.* **2008**, *47*, 3450–3453. [CrossRef] [PubMed]
22. Buyukcakir, O.; Je, S.H.; Talapaneni, S.N.; Kim, D.; Coskun, A. Charged Covalent Triazine Frameworks for CO_2 Capture and Conversion. *ACS Appl. Mater. Interfaces* **2017**, *9*, 7209–7216. [CrossRef] [PubMed]
23. Gu, C.; Liu, D.; Huang, W.; Liu, J.; Yang, R. Synthesis of covalent triazine-based frameworks with high CO_2 adsorption and selectivity. *Polym. Chem.* **2015**, *6*, 7410–7417. [CrossRef]
24. Mukhtar, A.; Mellon, N.B.; Bustam, M.A.; Saqib, S.; Lee, S.-P.; Kareem, F.A.A.; Ullah, S. Impact of amine functionality on the selective CO_2/CH_4 adsorption behavior of porous covalent triazine adsorbent. *J. Nat. Gas Eng.* **2020**, *83*, 103582. [CrossRef]
25. Wang, G.; Leus, K.; Jena, H.S.; Krishnaraj, C.; Zhao, S.; Depauw, H.; Tahir, N.; Liu, Y.-Y.; Van Der Voort, P. A fluorine-containing hydrophobic covalent triazine framework with excellent selective CO_2 capture performance. *J. Mater. Chem. A* **2018**, *6*, 6370–6375. [CrossRef]
26. Zhao, Y.; Yao, K.X.; Teng, B.; Zhang, T.; Han, Y. A perfluorinated covalent triazine-based framework for highly selective and water–tolerant CO_2 capture. *Energy Environ. Sci.* **2013**, *6*, 3684–3692. [CrossRef]
27. Dawson, R.; Cooper, A.I.; Adams, D.J. Chemical functionalization strategies for carbon dioxide capture in microporous organic polymers. *Polym. Int.* **2013**, *62*, 345–352. [CrossRef]
28. Flaig, R.W.; Osborn Popp, T.M.; Fracaroli, A.M.; Kapustin, E.A.; Kalmutzki, M.J.; Altamimi, R.M.; Fathieh, F.; Reimer, J.A.; Yaghi, O.M. The Chemistry of CO_2 Capture in an Amine-Functionalized Metal–Organic Framework under Dry and Humid Conditions. *J. Am. Chem. Soc.* **2017**, *139*, 12125–12128. [CrossRef] [PubMed]
29. Gunasekar, G.H.; Park, K.; Ganesan, V.; Lee, K.; Kim, N.-K.; Jung, K.-D.; Yoon, S. A Covalent Triazine Framework, Functionalized with Ir/N-Heterocyclic Carbene Sites, for the Efficient Hydrogenation of CO_2 to Formate. *Chem. Mater.* **2017**, *29*, 6740–6748. [CrossRef]
30. Jia, J.; Chen, Z.; Belmabkhout, Y.; Adil, K.; Bhatt, P.M.; Solovyeva, V.A.; Shekhah, O.; Eddaoudi, M. Carbonization of covalent triazine-based frameworks via ionic liquid induction. *J. Mater. Chem. A* **2018**, *6*, 15564–15568. [CrossRef]
31. Keskin, S.; van Heest, T.M.; Sholl, D.S. Can Metal–Organic Framework Materials Play a Useful Role in Large-Scale Carbon Dioxide Separations? *ChemSusChem* **2010**, *3*, 879–891. [CrossRef] [PubMed]
32. Zhang, Y.; Jin, S. Recent Advancements in the Synthesis of Covalent Triazine Frameworks for Energy and Environmental Applications. *Polymers* **2019**, *11*, 31. [CrossRef] [PubMed]
33. Zhang, L.; Li, X.; Antonietti, M. General, Metal-free Synthesis of Carbon Nanofiber Assemblies from Plant Oils. *Angew. Chem. Int. Ed.* **2021**, *60*, 24257–24265. [CrossRef] [PubMed]
34. Katekomol, P.; Roeser, J.; Bojdys, M.; Weber, J.; Thomas, A. Covalent Triazine Frameworks Prepared from 1,3,5-Tricyanobenzene. *Chem. Mater.* **2013**, *25*, 1542–1548. [CrossRef]
35. Kuecken, S.; Schmidt, J.; Zhi, L.; Thomas, A. Conversion of amorphous polymer networks to covalent organic frameworks under ionothermal conditions: A facile synthesis route for covalent triazine frameworks. *J. Mater. Chem. A* **2015**, *3*, 24422–24427. [CrossRef]
36. Ren, S.; Bojdys, M.J.; Dawson, R.; Laybourn, A.; Khimyak, Y.Z.; Adams, D.J.; Cooper, A.I. Porous, Fluorescent, Covalent Triazine-Based Frameworks Via Room-Temperature and Microwave-Assisted Synthesis. *Adv. Mater.* **2012**, *24*, 2357–2361. [CrossRef] [PubMed]
37. Bhunia, A.; Vasylyeva, V.; Janiak, C. From a Supramolecular Tetranitrile to a Porous Covalent Triazine-Based Framework with High Gas Uptake Capacities. *Chem. Commun.* **2013**, *49*, 3961–3963. [CrossRef] [PubMed]
38. Öztürk, S.; Xiao, Y.-X.; Dietrich, D.; Giesen, B.; Barthel, J.; Ying, J.; Yang, X.-Y.; Janiak, C. Nickel nanoparticles supported on a covalent triazine framework as electrocatalyst for oxygen evolution reaction and oxygen reduction reactions. *Beilstein J. Nanotechnol.* **2020**, *11*, 770–781. [CrossRef] [PubMed]
39. Dey, S.; Bhunia, A.; Breitzke, H.; Groszewicz, P.B.; Buntkowsky, G.; Janiak, C. Two linkers are better than one: Enhancing CO_2 capture and separation with porous covalent triazine-based frameworks from mixed nitrile linkers. *J. Mater. Chem. A* **2017**, *5*, 3609–3620. [CrossRef]

40. Oxley, J.C.; Smith, J.L.; Moran, J.S. Decomposition of Azo- and Hydrazo-Linked Bis Triazines. *J. Energy Mater.* **2009**, *27*, 63–93. [CrossRef]
41. Kuhn, P.; Thomas, A.; Antonietti, M. Toward Tailorable Porous Organic Polymer Networks: A High-Temperature Dynamic Polymerization Scheme Based on Aromatic Nitriles. *Macromolecules* **2009**, *42*, 319–326. [CrossRef]
42. Preis, E.; Dong, W.; Brunklaus, G.; Scherf, U. Microporous, tetraarylethylene-based polymer networks generated in a reductive polyolefination process. *J. Mater. Chem. C* **2015**, *3*, 1582–1587. [CrossRef]
43. Dey, S.; Bhunia, A.; Boldog, I.; Janiak, C. A mixed-linker approach towards improving covalent triazine-based frameworks for CO_2 capture and separation. *Microporous Mesoporous Mater.* **2017**, *241*, 303–315. [CrossRef]
44. Bhunia, A.; Boldog, I.; Möller, A.; Janiak, C. Highly stable nanoporous covalent triazine-based frameworks with an adamantane core for carbon dioxide sorption and separation. *J. Mater. Chem. A* **2013**, *1*, 14990–14999. [CrossRef]
45. Tao, L.; Niu, F.; Liu, J.; Wang, T.; Wang, Q. Troger's base functionalized covalent triazine frameworks for CO_2 capture. *RSC Adv.* **2016**, *6*, 94365–94372. [CrossRef]
46. Quantachrome Instruments (1900 Corporate Drive, Boynton Beach, FL 33426 USA) Powder Tech Note 35. Available online: https://wiki.anton-paar.com/en/gas-adsorption-for-surface-area-and-pore-size-analysis/ (accessed on 25 June 2025).
47. Lim, H.; Cha, M.C.; Chang, J.Y. Preparation of Microporous Polymers Based on 1,3,5-Triazine Units Showing High CO2 Adsorption Capacity. *Macromol. Chem. Phys.* **2012**, *213*, 1385–1390. [CrossRef]
48. Lu, Y.-C.; Yang, J.-P.; Yang, B.-T.; Chen, C.-C.; Lai, L.-L. Introduction of a spiro-linker in triazine-based polymers to enlarge void space and increase IPA adsorbing capacity to 164.7 mg/g at 1000 ppm. *J. Taiwan Inst. Chem. Eng.* **2022**, *140*, 104531. [CrossRef]
49. Wang, H.; Jiang, D.; Huang, D.; Zeng, G.; Xu, P.; Lai, C.; Chen, M.; Cheng, M.; Zhang, C.; Wang, Z. Covalent triazine frameworks for carbon dioxide capture. *J. Mater. Chem. A* **2019**, *7*, 22848–22870. [CrossRef]
50. Özdemir, J.; Mosleh, I.; Abolhassani, M.; Greenlee, L.F.; Beitle, R.R.; Beyzavi, M.H. Covalent Organic Frameworks for the Capture, Fixation, or Reduction of CO_2. *Front. Energy Res.* **2019**, *7*, 77. [CrossRef]
51. Hug, S.; Mesch, M.B.; Oh, H.; Popp, N.; Hirscher, M.; Senker, J.; Lotsch, B.V. A fluorene based covalent triazine framework with high CO_2 and H_2 capture and storage capacities. *J. Mater. Chem. A* **2014**, *2*, 5928–5936. [CrossRef]
52. Lee, Y.J.; Talapaneni, S.N.; Coskun, A. Chemically Activated Covalent Triazine Frameworks with Enhanced Textural Properties for High Capacity Gas Storage. *ACS Appl. Mater. Interfaces* **2017**, *9*, 30679–30685. [CrossRef] [PubMed]
53. Wang, G.; Leus, K.; Zhao, S.; Van Der Voort, P. Newly Designed Covalent Triazine Framework Based on Novel N-Heteroaromatic Building Blocks for Efficient CO_2 and H_2 Capture and Storage. *ACS Appl. Mater. Interfaces* **2018**, *10*, 1244–1249. [CrossRef] [PubMed]
54. Ismail, M.; Bustam, M.A.; Kari, N.E.; Yeong, Y.F. Ideal Adsorbed Solution Theory (IAST) of Carbon Dioxide and Methane Adsorption Using Magnesium Gallate Metal-Organic Framework (Mg-gallate). *Molecules* **2023**, *28*, 3016. [CrossRef] [PubMed]
55. Nuhnen, A.; Janiak, C. A practical guide to calculate the isosteric heat/enthalpy of adsorption via adsorption isotherms in metal–organic frameworks, MOFs. *Dalton Trans.* **2020**, *49*, 10295–10307. [CrossRef] [PubMed]
56. Zhao, H.; Jin, Z.; Su, H.; Zhang, J.; Yao, X.; Zhao, H.; Zhu, G. Target synthesis of a novel porous aromatic framework and its highly selective separation of CO_2/CH_4. *Chem. Commun.* **2013**, *49*, 2780–2782. [CrossRef] [PubMed]
57. Liu, D.; Zou, Z.; Cai, Y.; Qiu, Y.; Zhou, Y.; He, S. An updated study on CH_4 isothermal adsorption and isosteric adsorption heat behaviors of variable rank coals. *J. Nat. Gas Sci. Eng.* **2021**, *89*, 103899. [CrossRef]
58. Woschko, D.; Yilmaz, S.; Jansen, C.; Spieß, A.; Oestreich, R.; Matemb Ma Ntep, T.; Janiak, C. Enhanced sorption in an indium-macetylenedicarboxylate metal–organic framework with unexpected chains of cis-μ-OH-connected {InO6} octahedra. *Dalton Trans.* **2023**, *52*, 977–989. [CrossRef] [PubMed]
59. Tuci, G.; Iemhoff, A.; Ba, H.; Luconi, L.; Rossin, A.; Papaefthimiou, V.; Palkovits, R.; Artz, J.; Pham-Huu, C.; Giambastiani, G. Playing with covalent triazine framework tiles for improved CO_2 adsorption properties and catalytic performance. *Beilstein J. Nanotechnol.* **2019**, *10*, 1217–1227. [CrossRef] [PubMed]
60. Tuci, G.; Pilaski, M.; Ba, H.; Rossin, A.; Luconi, L.; Caporali, S.; Pham-Huu, C.; Palkovits, R.; Giambastiani, G. Unraveling Surface Basicity and Bulk Morphology Relationship on Covalent Triazine Frameworks with Unique Catalytic and Gas Adsorption Properties. *Adv. Funct. Mater.* **2017**, *27*, 1605672. [CrossRef]
61. Hug, S.; Stegbauer, L.; Oh, H.; Hirscher, M.; Lotsch, B.V. Nitrogen-Rich Covalent Triazine Frameworks as High-Performance Platforms for Selective Carbon Capture and Storage. *Chem. Mater.* **2015**, *27*, 8001–8010. [CrossRef]
62. Zhu, X.; Tian, C.; Veith, G.M.; Abney, C.W.; Dehaudt, J.; Dai, S. In Situ Doping Strategy for the Preparation of Conjugated Triazine Frameworks Displaying Efficient CO_2 Capture Performance. *J. Am. Chem. Soc.* **2016**, *138*, 11497–11500. [CrossRef] [PubMed]
63. Yuan, K.; Liu, C.; Zong, L.; Yu, G.; Cheng, S.; Wang, J.; Weng, Z.; Jian, X. Promoting and Tuning Porosity of Flexible Ether-Linked Phthalazinone-Based Covalent Triazine Frameworks Utilizing Substitution Effect for Effective CO_2 Capture. *ACS Appl. Mater. Interfaces* **2017**, *9*, 13201–13212. [CrossRef] [PubMed]
64. Park, K.; Lee, K.; Kim, H.; Ganesan, V.; Cho, K.; Jeong, S.K.; Yoon, S. Preparation of covalent triazine frameworks with imidazolium cations embedded in basic sites and their application for CO_2 capture. *J. Mater. Chem. A* **2017**, *5*, 8576–8582. [CrossRef]

65. Fu, Y.; Wang, Z.; Li, S.; He, X.; Pan, C.; Yan, J.; Yu, G. Functionalized Covalent Triazine Frameworks for Effective CO_2 and SO_2 Removal. *ACS Appl. Mater. Interfaces* **2018**, *10*, 36002–36009. [CrossRef] [PubMed]
66. Yuan, K.; Liu, C.; Liu, C.; Zhang, S.; Yu, G.; Yang, L.; Yang, F.; Jian, X. Construction of triphenylamine functional phthalazinone-based covalent triazine frameworks for effective CO_2 capture. *Polym. J.* **2018**, *151*, 65–74. [CrossRef]
67. Du, J.; Liu, Y.; Krishna, R.; Yu, Y.; Cui, Y.; Wang, S.; Liu, Y.; Song, X.; Liang, Z. Enhancing Gas Sorption and Separation Performance via Bisbenzimidazole Functionalization of Highly Porous Covalent Triazine Frameworks. *ACS Appl. Mater. Interfaces* **2018**, *10*, 26678–26686. [CrossRef] [PubMed]
68. Jena, H.S.; Krishnaraj, C.; Wang, G.; Leus, K.; Schmidt, J.; Chaoui, N.; Van Der Voort, P. Acetylacetone Covalent Triazine Framework: An Efficient Carbon Capture and Storage Material and a Highly Stable Heterogeneous Catalyst. *Chem. Mater.* **2018**, *30*, 4102–4111. [CrossRef]
69. Mukherjee, S.; Das, M.; Manna, A.; Krishna, R.; Das, S. Newly designed 1,2,3-triazole functionalized covalent triazine frameworks with exceptionally high uptake capacity for both CO_2 and H_2. *J. Mater. Chem. A* **2019**, *7*, 1055–1068. [CrossRef]
70. Sánchez, M.I.; Martínez-Costas, J.; Mascareñas, J.L.; Vázquez, M.E. MitoBlue: A Nontoxic and Photostable Blue-Emitting Dye That Selectively Labels Functional Mitochondria. *ACS Chem. Biol.* **2014**, *9*, 2742–2747. [CrossRef] [PubMed]

Supplementary Materials:

Synthesis and Characterization of Covalent Triazine Frameworks Based on 4,4‘-(Phenazine-5,10-diyl)dibenzonitrile and Its Application in CO_2/CH_4 Separation

Hanibal Othman, Robert Oestreich, Vivian Küll, Marcus N. A. Fetzer and Christoph Janiak *

Institut für Anorganische Chemie und Strukturchemie, Heinrich-Heine-Universität Düsseldorf, 40204 Düsseldorf, Germany; hanibal.othman@hhu.de (H.O.); robert.oestreich@hhu.de (R.O.); vivian.kuell@hhu.de (V.K.); marcus.fetzer@hhu.de (M.N.A.F.)
* Correspondence: janiak@uni-duesseldorf.de

Section S1. Scanning electron microscopy

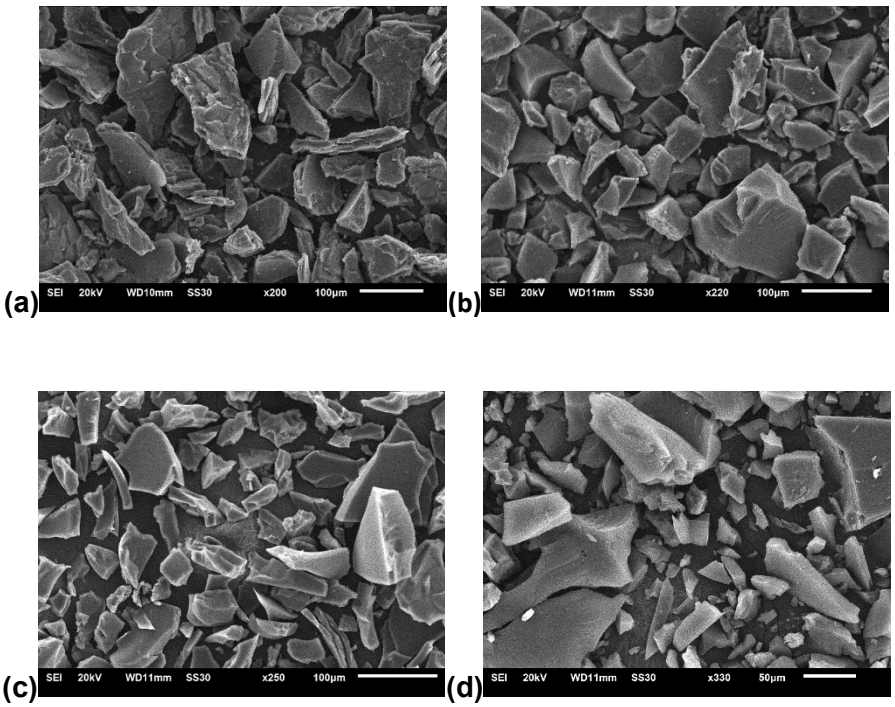

Figure S1. SEM images of (a) pBN CTF-10-400, (b) pBN -CTF-20-400, (c) pBN-CTF-10-550 and (d) pBN-CTF-20-550.

Section S2. Fourier transform infrared spectroscopy and elemental analysis

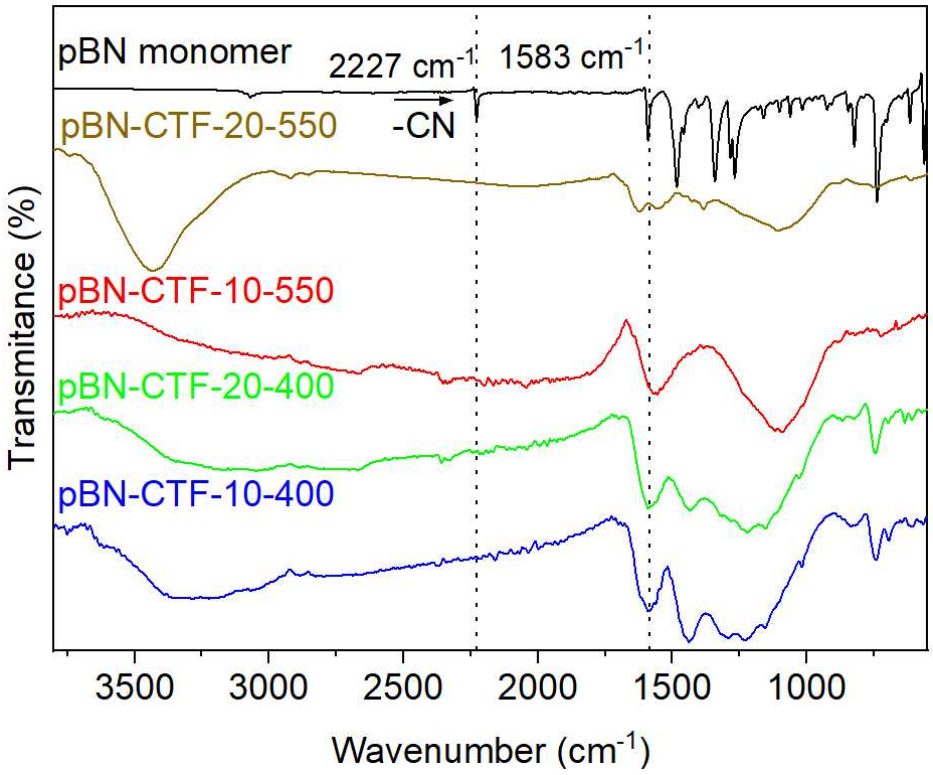

Figure S2. FT-IR spectra of the synthesized pBN-CTFs and the pBN monomer (in black).

Elemental analysis:

Table S1. Elemental analysis results.[(a)]

CTF product	C (wt%)	H (wt%)	N (wt%)	residual wt%	C/N mass ratio	C/H mass ratio
Theoretical CTF	81.2	4.2	14.6	0.00	5.5	19.4
pBN-CTF-10-350	68.5	4.2	7.9	19.4	8.6	16.3
pBN-CTF-10-400	68.3	3.5	6.5	21.7	10.5	19.5
pBN-CTF-10-550	60.7	3.3	5.2	30.8	11.6	18.4
pBN-CTF-20-400	69.3	3.4	6.4	20.9	10.6	20.4
pBN-CTF-20-550	61.6	3.2	5.0	30.2	12.3	19.3

[(a)] From combustion analysis.

CTF product	Zn (wt%) [(b)]	Cl (wt%) [(b)]	Sum Zn+Cl (wt%) [b]
pBN-CTF-10-350	4.3	9.8	14.1
pBN-CTF-10-400	4.7	8.6	13.3
pBN-CTF-10-550	4.5	9.5	14.0
pBN-CTF-20-400	4.4	8.1	12.5
pBN-CTF-20-550	4.2	7.0	11.2

[(b)] From SEM-EDX

Section S3. Powder X-ray diffraction

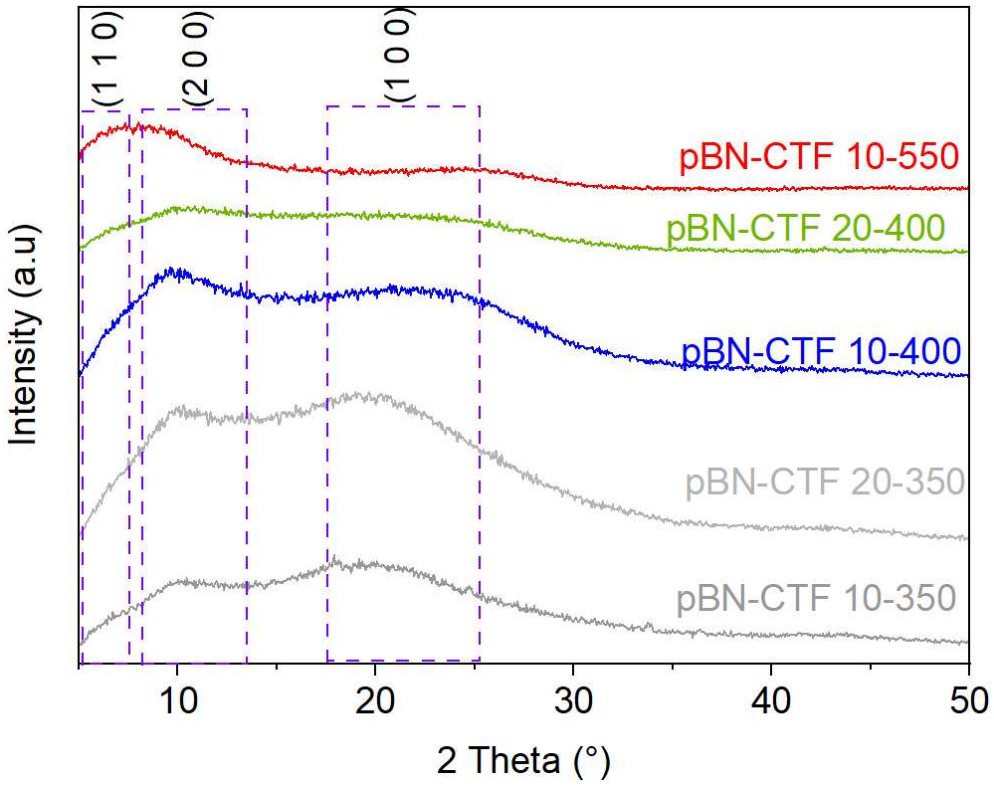

Figure S3. Powder X-ray diffraction patterns of pBN-CTFs. The regions for the (1 1 0), (2 0 0) and (1 0 0) reflections which are expected in more crystalline pBN-CTFs are indicated, based on the estimation from the hexagon edge and width lengths in Figure S4. 2Theta for the reflection from the hexagonal layers in eclipsed stacking with a separation of 3.5 Å (0 0 1 reflection) is 25.4°.

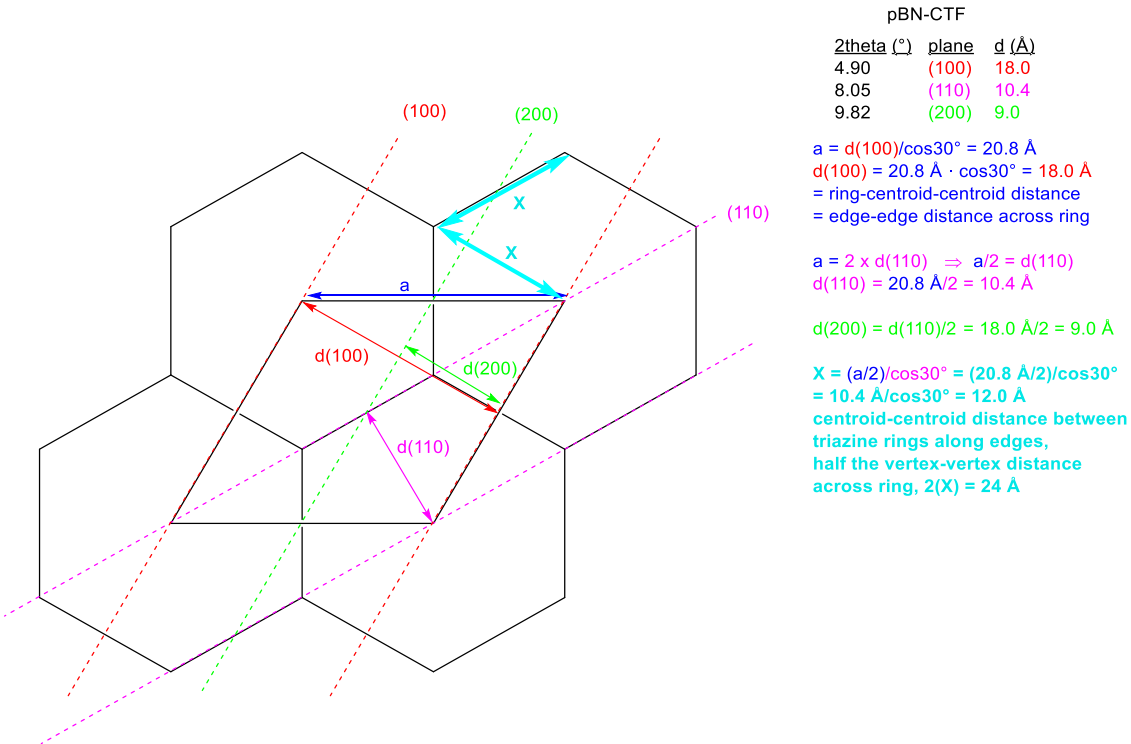

Figure S4. Correlation of the estimated edge length (X = 12.0 Å) and width (a = 20.8 Å) of the ideal hexagon (cf. Figure 1 in the main text) with the 2theta (2θ) values expected in the powder X-ray diffractograms in Figure S3 from the reflection planes and the d spacing according to the Bragg equation n λ = 2d sinθ or d = nλ /(2sinθ) with λ = 1.5406 Å and n = 1 [1].

Section S4. Samples synthesized at 350 °C and their N_2 and CO_2 sorption studies

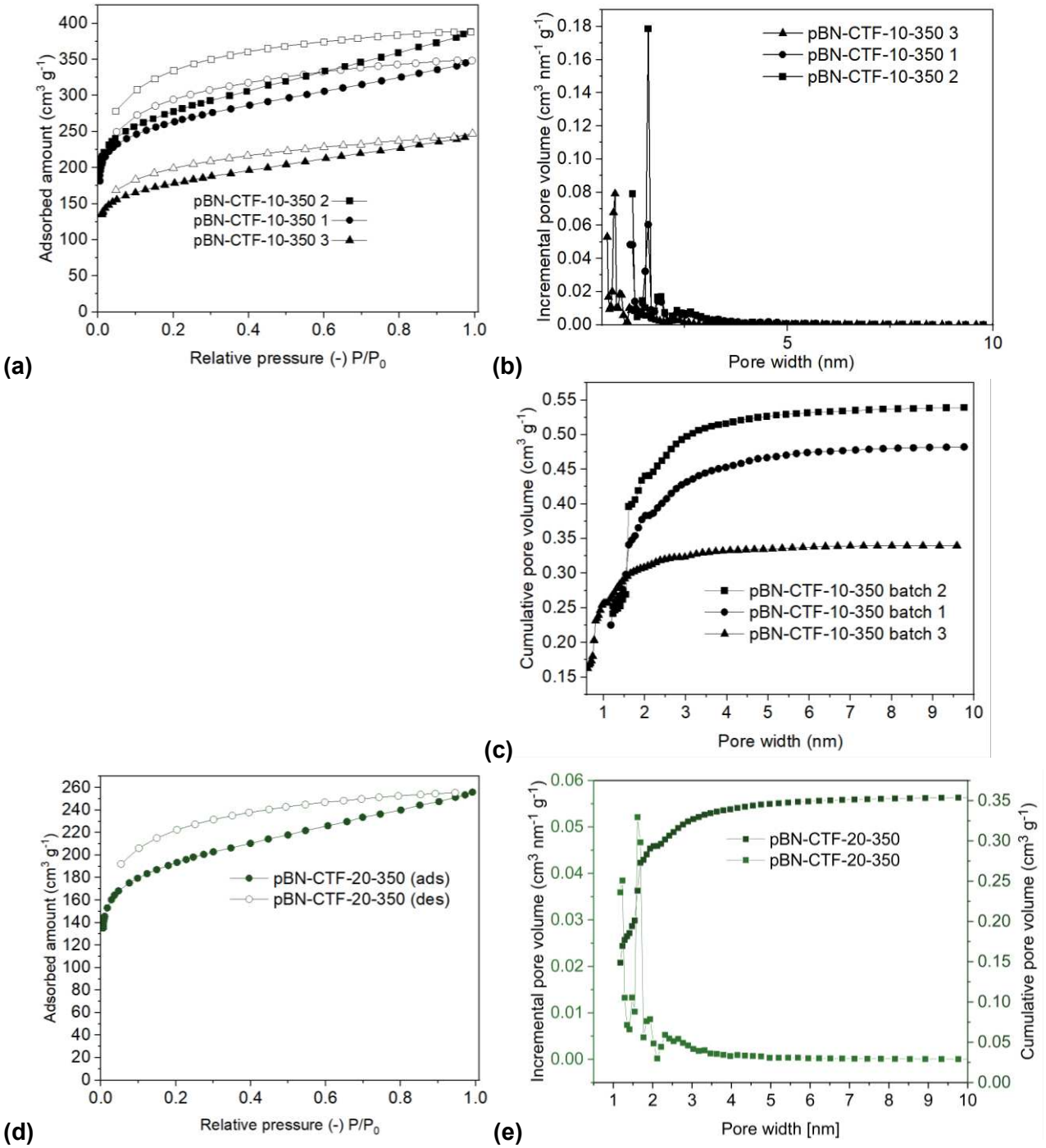

Figure S5. (**a**) N_2 sorption isotherms at 77 K of the samples synthesized with a 10:1 $ZnCl_2$:monomer ratio at 350 °C (filled symbols adsorption, empty symbols desorption). (**b**) Pore size distribution of the samples synthesized with 10:1 salt: monomer ratio at 350 °C from NL-DFT using the "N_2 on carbon 77 K (slit-pore, NLDFT equilibrium)" model. (**c**) Cumulative pore volume for the batches of of the samples synthesized with 10:1 salt: monomer ratio at 350 °C from NL-DFT using the "N_2 on carbon 77 K (slit-pore, NLDFT equilibrium)" model. (d) N_2 sorption isotherms at 77 K of the sample pBN-CTF-20-350 (**e**) Pore size distribution and the cumulative pore volume of the sample pBN-CTF-20-350 from NL-DFT using the "N_2 on carbon 77 K (slit-pore, NLDFT equilibrium)" model.

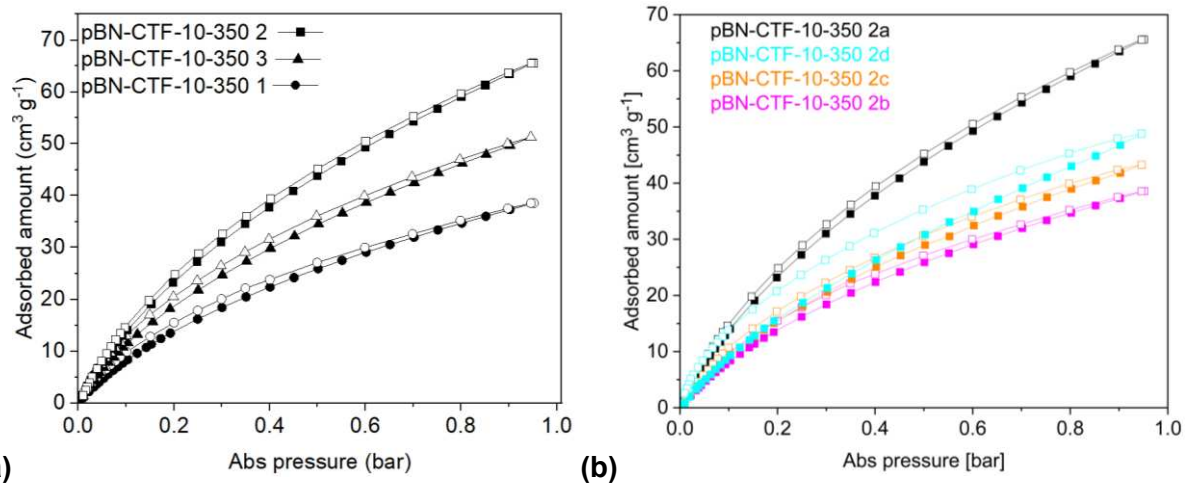

(a) **(b)**

Figure S6. (a) CO_2 sorption isotherms at 293 K of pBN-CTF-10-350 from three different batches (1, 2, 3). (b) CO_2 sorption isotherms at 293 K of four probes (a, b, c, d) from the same batch 2 of pBN-CTF-10-350 (filled symbols adsorption, empty symbols desorption). See Table S2 for the CO_2 uptake values at 1 bar.

Table S2. Surface area and porosity data from N_2 and CO_2 sorption studies of different pBN-CTF-10-350 samples showing inconsistencies in the sorption behavior.

CTF-10-350		S_{BET} [(a)] ($m^2\ g^{-1}$)	V_{tot} [(b)] ($cm^3\ g^{-1}$)	V_{micro} [(c)] ($cm^3\ g^{-1}$)	V_{micro}/V_{tot} [(d)]	CO_2 uptake 293 K, 1 bar ($cm^3\ g^{-1}$) [(e)]	$V_{1nm}(CO_2)$ [(f)] ($cm^3\ g^{-1}$)
Batch 1		980	0.538	0.377	70	38.5	0.010
Batch 2	**probe a**	1027	0.588	0.433	73	65.6	0.013
	probe b	-	-	-	-	38.5	0.009
	probe c	-	-	-	-	43.3	0.009
	probe d	-	-	-	-	48.8	0.008
Batch 3		660	0.37	0.30	81	51.3	0.012
CTF-20-350		717	0.38	0.29	76	59.6	0.013

[(a)] Calculated BET surface area from N_2 adsorption at 77 K over a pressure range of P/P_0 = 0.01-0.07. The standard deviation (1σ) for a BET surface area in the range of 1000 $m^2\ g^{-1}$ is usually on the order of 20 $m^2\ g^{-1}$.

[(b)] Total pore volume from N_2 adsorption isotherm at 77 K at P/P_0 =0.95 for pores smaller than 40 nm.

[(c)] Micropore volume from the NL-DFT method using the N_2 adsorption isotherm at 77 K at P/P_0 = 0.1 for pores with d ≤ 2 nm (20 Å).

[(d)] Micropore volume/total pore volume.

[(e)] A standard deviation (1σ) for gas uptake measurements should be at the most 5%.

[(f)] Pore volume for pores with diameters smaller than 1 nm from CO_2 adsorption isotherms at 293 K and the CO_2 NL-DFT model.

Section S5. CO_2 adsorption isotherms.

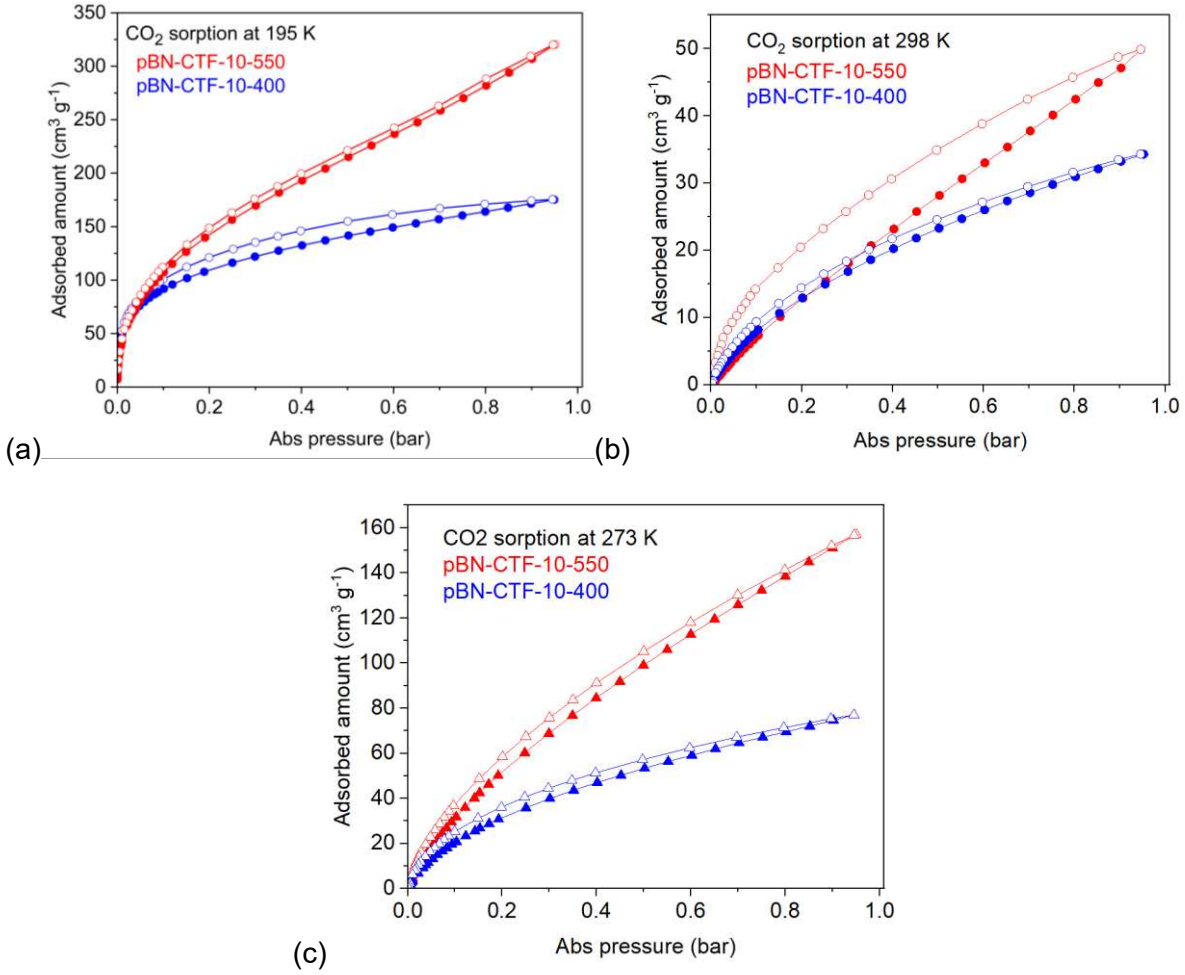

Figure S7. CO_2 adsorption isotherms of pBN-CTF-10s at (a)195 K, (b) 298 K and (c) 273 K.

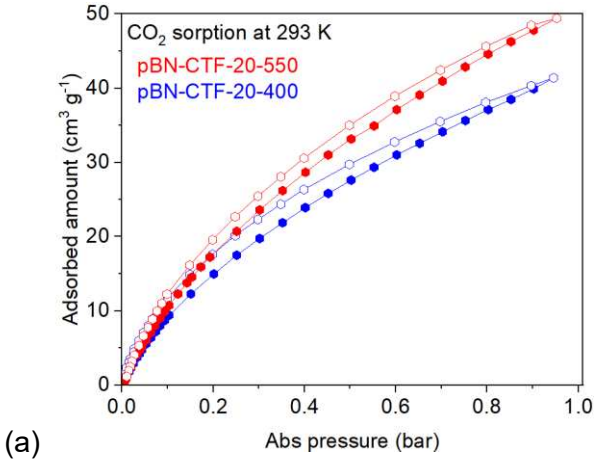

Figure S8. CO_2 adsorption isotherms of pBN-CTF-20-400 and pBN-CTF-20-550 at 293 K.

Table S3. CO_2 uptake results for pBN-CTF-20-400, 550.

Sample	Temp. CO_2 ads. (K)	CO_2 uptake at 1 bar (mmol g^{-1})	CO_2 uptake at 1 bar (cm^3 g^{-1}) [(a)]
pBN-CTF-20-400	293	1.7	41.3
pBN-CTF-20-550	293	2.0	49.5

[(a)] Conversion between uptake in cm^3 g^{-1} and uptake in mmol g^{-1} at 293 K:
cm^3 g^{-1} = mmol g^{-1} × 24.360 cm^3 $mmol^{-1}$ (i.e. 24.360 L mol^{-1} for an ideal gas at 1 bar and 293 K).

In the main text we had noted that the increase in CO_2 uptake correlates with the increase in BET surface area from N_2 sorption. The CO_2 uptake was measured at the temperatures of 298 K, 293 K, 283 K, 273 K and 195 K (Table 3, Table S4) for the two materials pBN-CTF-10-400 and pBN-CTF-10-550. As we have only two data points for the BET surface area for the all these CO_2 uptake measurements a correlation coefficient for a line through two data points is not meaningful. But we can note that the five lines have all positive slopes and show the increasing CO_2 uptake with BET surface area (Figure S9). Although for the three highest temperatures 283 K, 293 K and 298 K the increase is rather small. A sizable increase is, however, seen at 195 K and 273 K.

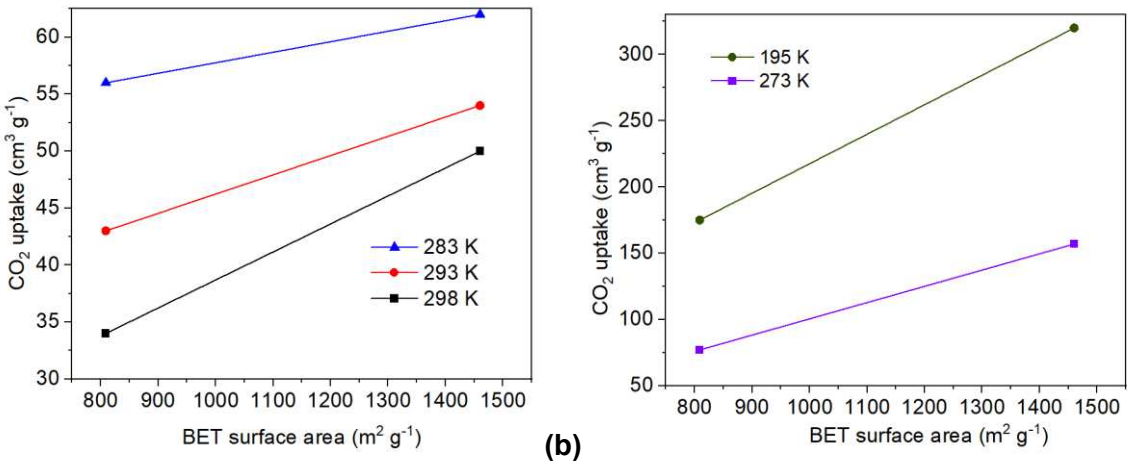

Figure S9. Scatter plot for the correlation of CO_2 uptake at (**a**) 283 K, 293 K, 298 K, (**b**) 195 K and 273 K and the BET surface area from N_2 sorption for pBN-CTF-10-400 (S_{BET} = 809 m^2 g^{-1}) and pBN-CTF-10-550 (S_{BET} = 1460 m^2 g^{-1}) (Table 2).

If we combine the pBN-CTF-20-400 and -20-550 materials (Table S3) with pBN-CTF-10-400 and pBN-CTF-10-550 for the CO_2 uptake data measured at 293 K (Table S4), then we can correlate the CO_2 uptake over four BET surface areas (Figure S10).

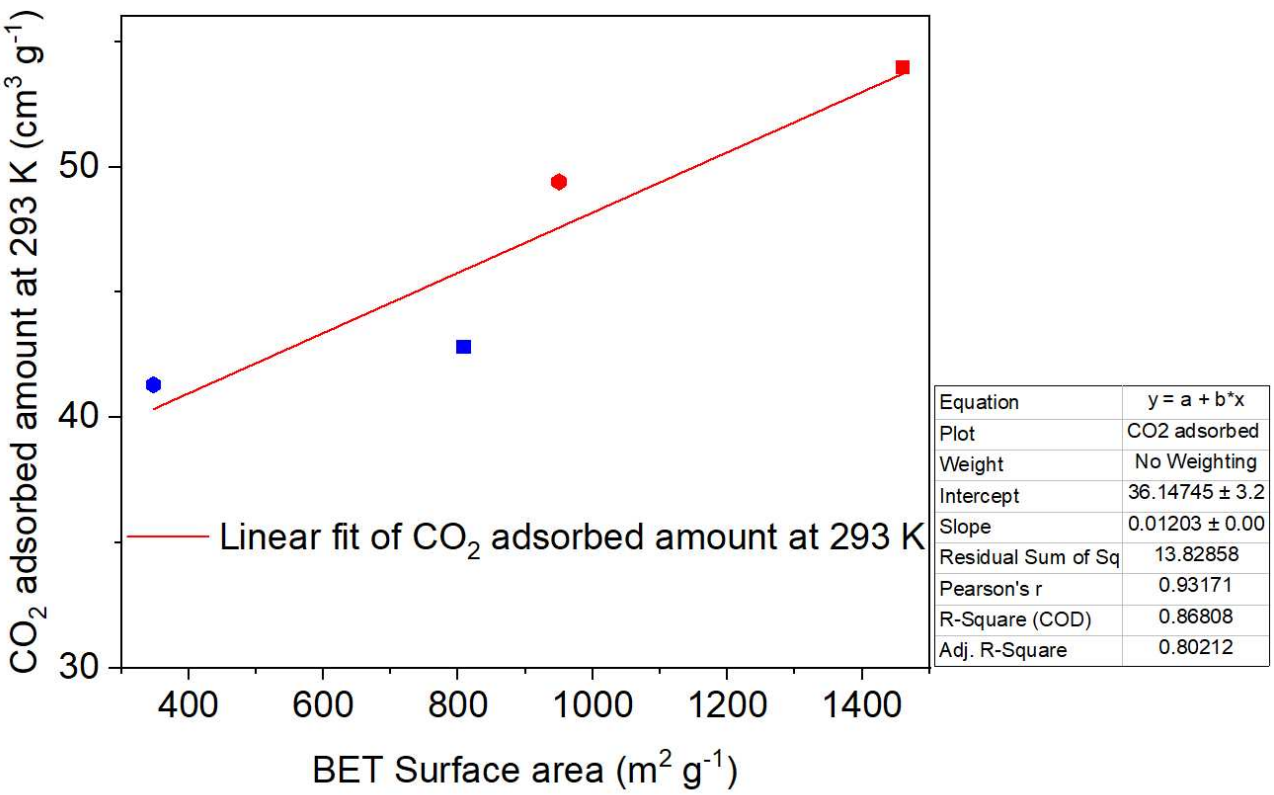

Figure S10. Scatter plot for the correlation of CO_2 uptake at 293 K and the BET surface area from N_2 sorption for pBN-CTF-20-400 (S_{BET} = 348 m^2 g^{-1}), pBN-CTF-10-400 (S_{BET} = 809 m^2 g^{-1}), pBN-CTF-20-550 (S_{BET} = 950 m^2 g^{-1}) and pBN-CTF-10-550 (S_{BET} = 1460 m^2 g^{-1}) (Table 2).

Table S4. Literature CO_2 uptake results.

Sample	Temp. CO_2 ads. (K)	CO_2 uptake at 1 bar (mmol g^{-1})	CO_2 uptake at 1 bar (cm^3 g^{-1}) [(a)]	CTF synthesis temperature (°C)	Ref.
pBN-CTF-10-400	273	3.1	77.0	400	This work
pBN-CTF-10-550	273	6.4	157.0	550	This work
pBN-CTF-10-400	293	1.91	42.8	400	This work
pBN-CTF-10-550	293	2.41	54.0	550	This work
pBN-CTF-10-400	298	1.37	34.2	400	This work
pBN-CTF-10-550	298	2.01	49.9	600	This work
DCBP-CTF-1	298	2.07	51.3	400	3
DCBP-CTF-2	298	1.84	45.6	400	3
F-DCBP-CTF-1	298	3.82	94.7	400	3
F-DCBP-CTF-2	298	3.02	74.7	400	3
F-CTF-1	298	3.21	79.5	400	4
F-CTF-1-600	298	3.41	84.5	600	4
CTF-DCN-400	298	1.2	29.7	400	5
CTF-DCN-500	298	1.59	39.4	500	5
CTF-FUM-350	298	2.38	59.0	350	5
CTF-FUM-400	298	1.84	45.6	400	5
CTF-FUM-500	298	1.55	38.4	500	5
CTF-1	298	1.41	34.9	400	6
CTF-1-600	298	2.24	55.5	600	6
cCTF-400	298	1.89	46.8	400	6
cCTF-450	298	1.41	34.9	450	6
cCTF-500	298	1.81	44.8	500	6
CTF1	298	3.32	82.3	400/600 (10 h/ 10 h)	7
CTF2	298	2.14	53.0	400/600 (10 h/ 10 h)	7
CTF3	298	2.03	50.3	400/600 (10 h/ 10 h)	7
CTF4	298	3.83	94.9	400/600 (10 h/ 10 h)	7
CTF5	298	3.12	77.3	400/600 (10 h/ 10 h)	7
CTF-ph	298	3.05	75.6	400/600	8
CTF-phHT	298	2.69	66.6	400/800	8
CTF-py	298	3.79	93.9	400/600	8
CTF-pyHT	298	4.22	104.6	400/800	8
bipy-CTF500	298	3.07	76.1	500	9
bipy-CTF600	298	2.95	73.1	600	9
Pym-CTF500	298	1.77	43.8	500	9
Pym-CTF600	298	2.15	53.3	600	9
fl-CTF300	298	0.71	17.6	300	10
fl-CTF350	298	2.29	56.7	350	10
fl-CTF400	298	1.97	48.8	400	10
fl-CTF500	298	1.65	40.9	500	10
fl-CTF600	298	1.80	44.6	600	10
HAT-CTF-450/600	298	4.8	118.9	450/600 (20 h/ 20 h)	11
CTF-1	298	1.65	40.9	400	12
caCTF-1-700	298	3.55	88.0	700	12
PHCTF-4	298	1.57	38.9	250, 300, 350 (10 h), 400 (20 h)	13
PHCTF-5	298	1.34	33.2	250, 300, 350 (10 h), 400 (20 h)	13
CTF-10-400	298	1.68	41.1	400	14
CTF-20-400	298	2.09	51.8	400	14
CTF-5-500	298	1.91	47.3	500	14
CTF-10-500	298	1.90	44.5	500	14
bpim-CTF400	298	2.46	60.9	400	15
bpim-CTF500	298	2.77	68.6	500	15
CTF-CSU41	298	1.80	44.6	250, 300, 350 (10 h), 400 (20 h)	16

PHCTF-8(650)	298	2.54	62.9	650	17
CTF-BIB-1	298	2.32	57.5	500	18
CTF-BIB-2	298	2.27	56.2	550	18
CTF-BIB-3	298	1.98	49.1	600	18
acac-CTF-5-500	298	1.97	48.8	500	19
acac-CTF-10-500	298	1.91	47.3	500	19
df-TzCTF600	298	4.6	114.0	600	20

[(a)] Conversion between uptake in $cm^3\ g^{-1}$ and uptake in $mmol\ g^{-1}$

at 293 K:

$cm^3\ g^{-1} = mmol\ g^{-1} \times 24.360\ cm^3\ mmol^{-1}$ (i.e. 24.360 L mol^{-1} for an ideal gas at 1 bar and 293 K).

at 298 K:

$cm^3\ g^{-1} = mmol\ g^{-1} \times 24.791\ cm^3\ mmol^{-1}$ (i.e. 24.791 L mol^{-1} for an ideal gas at 1 bar and 298 K).

at 273 K:

$cm^3\ g^{-1} = mmol\ g^{-1} \times 24.414\ cm^3\ mmol^{-1}$ (i.e. 24.791 L mol^{-1} for an ideal gas at 1 bar and 298 K).

Section S6. Calculations and fitting for the isosteric heat of adsorption and IAST selectivity of CO_2 and CH_4

The adsorption isotherms were fitted using the 3PSim software, this software is used in order to calculate and fit adsorption data using different fitting models such as Toth, Henry, Freundlich-Langmuir, multi component Sips and many others. After trying different methods of fitting the best one was Freundlich-Langmuir model using the following equation (1):

$$Q = Q_{max} \cdot kC^c/1+kc^c \qquad (1)$$

where
Q: amount adsorbed [mmol g^{-1}]
Q_{max}: maximal loading [mmol g^{-1}]
C: pressure [bar]
k: affinity constant
c: heterogeneity exponent

The isosteric heat of adsorption was calculated after fitting the adsorption isotherms via the Freundlich-Langmuir fit using the following equation [21].

$$n = a \cdot b \cdot p^c/1+b \cdot p^c \qquad (2)$$

Where n: the adsorbed amount (mmol g^{-1}).
a: the maximal loading (mmol g^{-1})
b: the affinity constant
c: the heterogeneity exponent
the pressure at the giving adsorbed amount can be calculated when rearranging the Freundlich-Langmuir equation to the following form.

$$P(n) = c \cdot \sqrt{(n/a \cdot b - n \cdot b)} \qquad (3)$$

The parameters a, b and c were taken from the fitting equation.
The isosteric heat of adsorption was then calculated via the Clausius-Clapeyron equation:

$$\Delta H_{(ads)} \cdot n = -R \cdot \ln(p_2/p_1) \cdot (T_1 \cdot T_2)/(T_2-T_1) \qquad (4)$$

Where $\Delta H_{(ads)}$: the isosteric enthalpy of adsorption in kJ mol^{-1}
T_1: absolute Temperature K (283)
T_2: absolute Temperature K (293)
R: the universal gas constant with the value 8.3145 J K^{-1} mol^{-1}.

According to ref [22], when interpolating the loading n, the enthalpy of adsorption is obtained as a function of a loading.

$$\Delta H_{(ads)} \cdot = -R \cdot m' \qquad (5)$$

$$m' = \ln(p_2/p_1) \cdot (T_1 \cdot T_2)/(T_2-T_1) \qquad (6)$$

$$-\Delta H_{(ads)} = Q_{st} \qquad (7)$$

The IAST (ideal adsorbed solution theory) selectivity calculations were done with the "IAST Sips" isotherm model with two components, the parameters of which were taken from the Freundlich-Langmuir fit done with the 3PSim software and used as input. The molar fraction was set to 0.5 for CO_2 and 0.5 for CH_4. The IAST selectivity was calculated after adjusting the settings to a constant pressure and variable molar fraction of both components. Afterwards the CO_2 selectivity values were plotted against the molar fraction of CH_4. IAST selectivity was calculated using the following formula (8):

$$S = (X_1/X_2)/(Y_1/Y_2) \quad (8)$$

Where
X_1: absorbed fractions of CO_2
X_2: absorbed fractions of CH_4
Y_1: molar fraction of CO_2
Y_2: molar fraction of CO_2

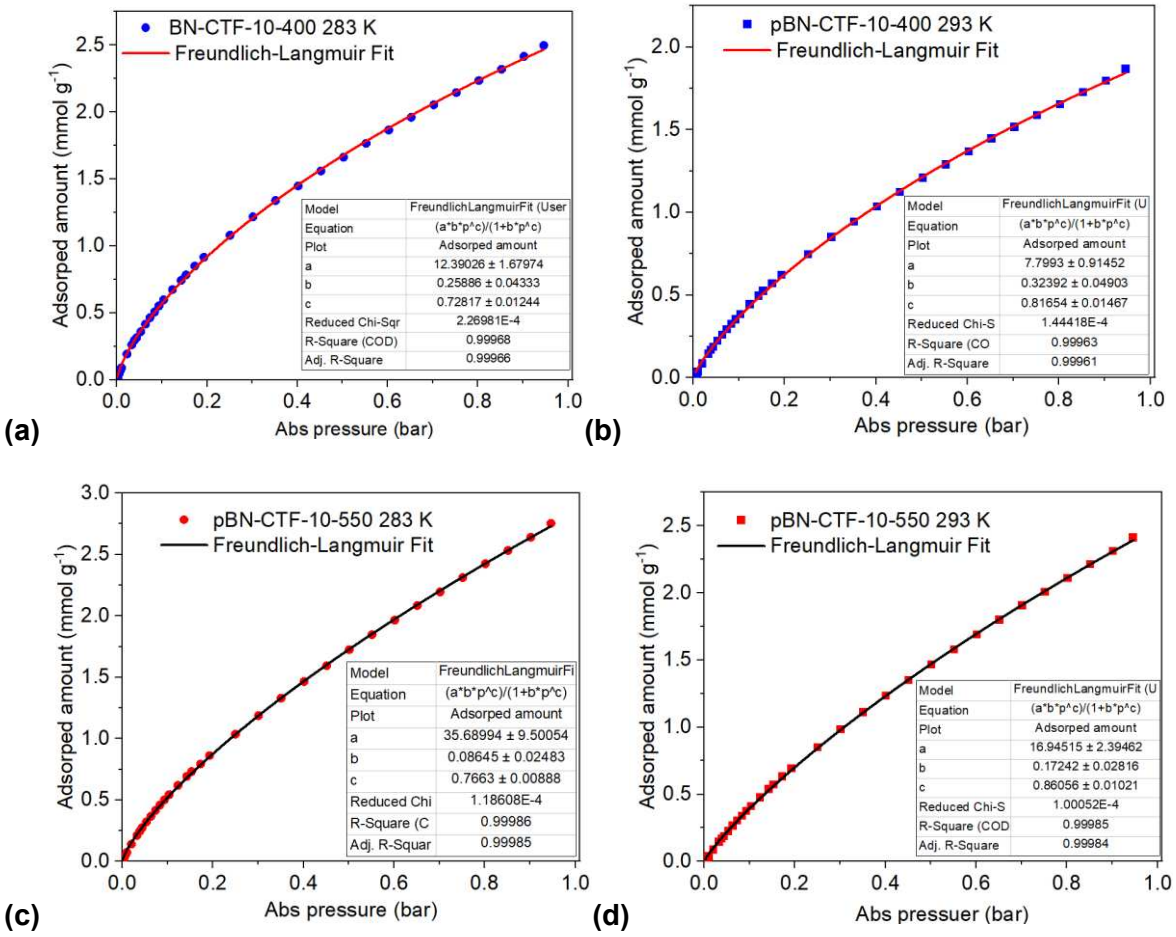

Figure S11. Experimental CO_2 adsorption isotherms of (**a**) pBN-CTF 10-400 at 283 K, (**b**) pBN-CTF 10-400 at 293 K, (**c**) pBN-CTF 10-550 at 283 K and (**d**) pBN-CTF 10-550 at 293 K with their corresponding Freundlich-Langmuir model fits and parameters.

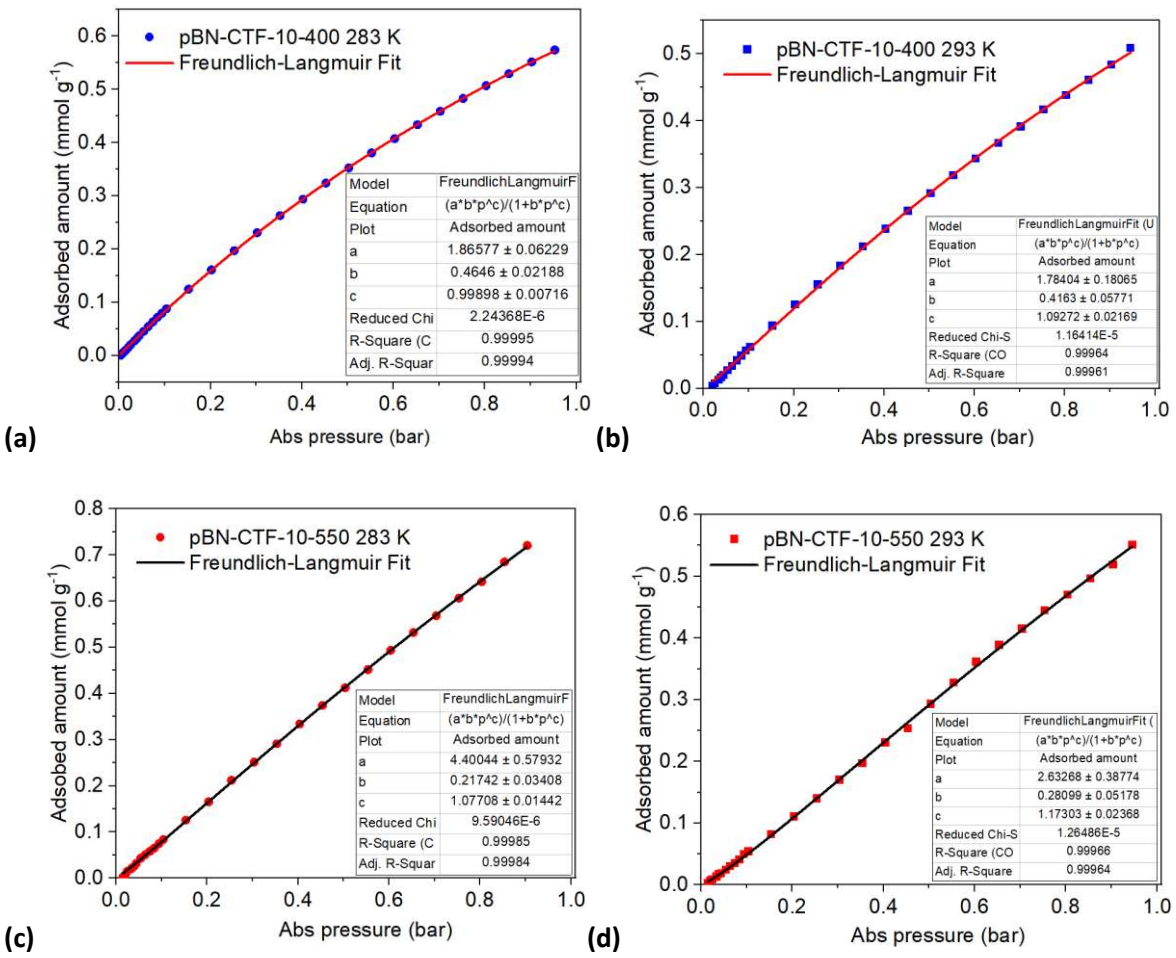

Figure S12. Experimental CH_4 adsorption isotherms of (a) pBN-CTF-10-400 at 283 K, (b) pBN-CTF 10-400 at 293 K, (c) pBN-CTF 10-550 at 283 K, (d) pBN-CTF 10-550 at 293 K, corresponding Freundlich-Langmuir model fits and parameters. The linear CH_4 uptake of pBN-CTF-10-550 did not allow for a meaningful fit.

Table S5. Freundlich-Langmuir adsorption isotherm model fitting parameters for the pBN-CTF-10-400 [(a)]

Sample	R^2	CO_2 Affinity constant (mmol $g^{-1}bar^{-1}$)	Maximal CO_2 loading (mmol g^{-1})	CH_4 Affinity constant (mmol g^{-1} bar^{-1})	Maximal CH_4 loading (mmol g^{-1})
pBN-CTF-10-400 293 K	0.999	0.323	7.799	0.416	1.784
pBN-CTF-10-400 283 K	0.999	0.258	12.390	0.464	1.8657

[(a)] The linear CH_4 uptake of CTF-10-550 did not allow for a meaningful fit.

Table S6. Comparison between the pBN-CTFs and CTFs from literature for the isosteric heat of adsorption of CO_2 near zero loading (Q_{ads}^0) and the IAST selectivity of CO_2 over CH_4.

Sample	CO_2 Q_{ads}^0 (kJ mol^{-1})	IAST selectivity CO_2/CH_4 (50:50) at 298 K and 1 bar	Ref.
pBN-CTF-10-400	79	22	This work
pBN-CTF-10-550	60	-	This work
CTF-DCN-400	47	8	5
CTF-DCN-500	60	10	5
CTF-Fum-350	58	20	5
CTF-Fum-400	64	20	5
CTF-Fum-500	58	14	5
CTF-1	27	-	6
CTF-1-600	30	-	6
cCTF-400	49	-	6
cCTF-450	46	-	6
cCTF-500	43	-	6
CTF1	43	-	7
CTF2	23.8	-	7
CTF3	25.8	-	7
CTF4	21.5	-	7
CTF5	24.9	-	7
CTF-ph	33.2	-	8
CTF-phHT	25.4	-	8
CTF-py	35.1	-	8
CTF-pyHT	27.1	--	8
Pym-CTF500	39	-	9
Pym-CTF600	30	-	9
fl-CTF300	43	-	10
fl-CTF350	32	-	10
fl-CTF400	30	-	10
fl-CTF500	31	-	10
fl-CTF600	32	-	10
HAT-CTF-450/600	27	-	11
CTF-1	39.6	-	12
CaCTF-1-700	30.6	-	12
PHCTF-4	24.3	9	13

PHCTF-5	23	8	13
CTF-20-400	22	-	14
CTF-5-500	25	-	14
bpim-CTF400	31	-	15
bpim-CTF500	28	-	15
CTF-CSU41	44	44.6	16
PHCTF-8(650)	28	7	17
CTF-BIB-1	20.5	6.9	18
CTF-BIB-2	20.4	6.9	18
CTF-BIB-3	17.4	4.6	18
acac-CTF-10-500	23.6	-	19
df-TzCTF600	34	30	20

Table S7. BET surface area, CO_2 uptake capacity, Q_{ads}, and CO_2/CH_4 IAST selectivity of the CTFs given in Figure 5 in the main text.

Sample	S_{BET} [$m^2\ g^{-1}$]	CO_2 uptake [$cm^3\ g^{-1}$] [a]	CO_2 Q_{ads}^0 [kJ mol^{-1}]	IAST CO_2/CH_4	Ref
pBN-CTF-10-400	809	34	79	22	This work
pBN-CTF-10-550	1460	50	60	- [b]	This work
HHU-COF-1	2351	24	- [b]	2	18
HHU-COF-2	1346	39	- [b]	2.5	18
COP-1(N)	105	22	35	- [b]	53
COP-S	253	26	26	- [b]	53
fl-CTF-400	2862	49	30	- [b]	59
fl-CTF-500	2322	41	31	- [b]	59
CTF-10-400	1033	41	28	- [b]	62
CTF-10-500	1251	47	26	- [b]	62
CTF-1	1034	41	40	- [b]	64

[a] At 298 K. [b] Data not given in reference.

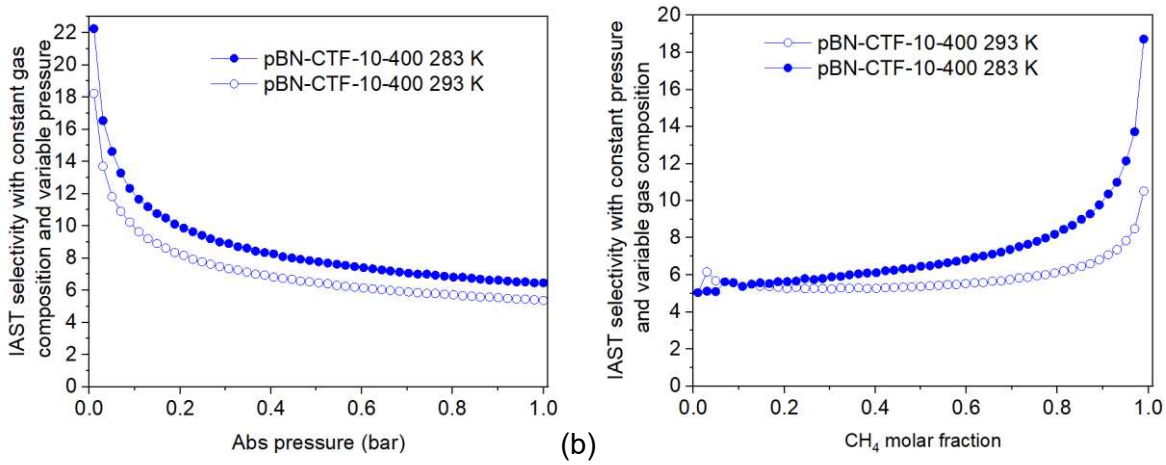

Figure S13. (a) IAST selectivity for pBN-CTF10-400for CO_2 versus CH_4 at a constant gas composition of 0.5:0.5 (mol:mol) and variable pressure at 283 and 293 K. (b) IAST selectivity for pBN-CTF10-400 for CO_2 versus CH_4 at constant gas pressure of 1 bar? and variable gas composition at 283 and 293 K .

Section S7. Thermogravimetric analysis (TGA)

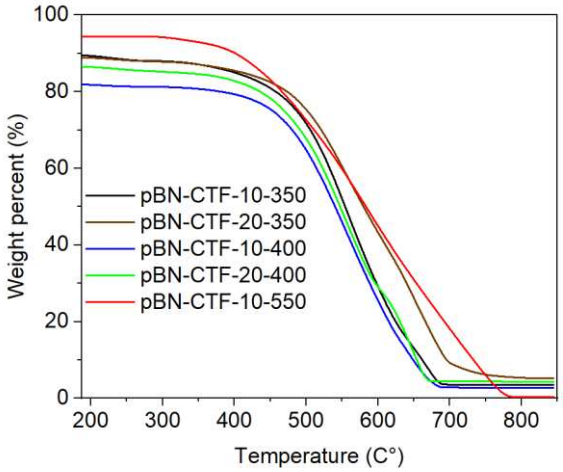

Figure S14. Thermogravimetric analysis of the synthesized pBN-CTFs with a 10 K min^{-1} heating rate under air. An initial loss up to 200 °C is due to adsorbed solvent or moisture.

Section S8. Nuclear magnetic resonance spectrometry (NMR)

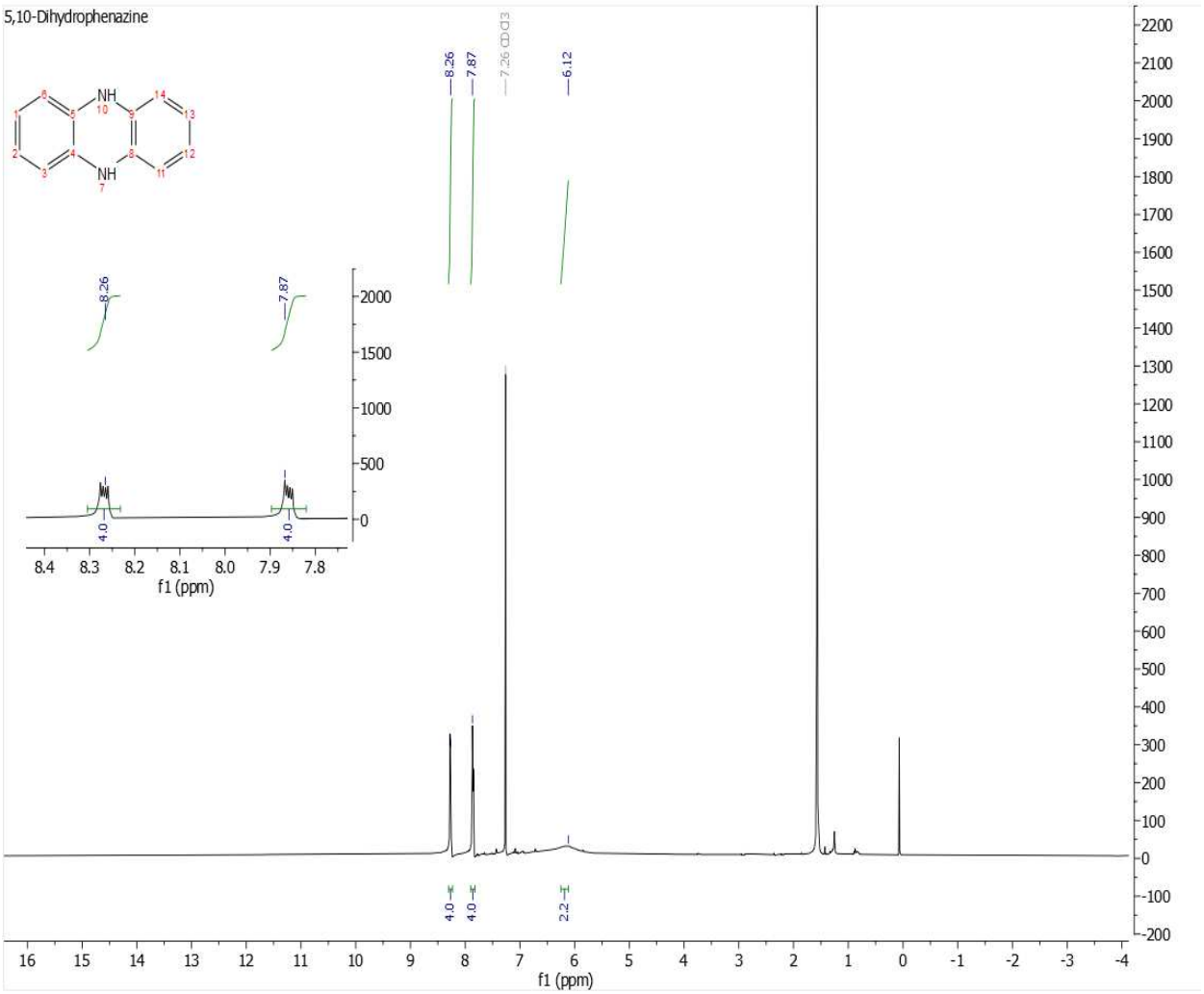

Figure S15. ^{1}H NMR spectrum (600 MHz) of 5,10-dihydrophenazine in $CDCl_3$.

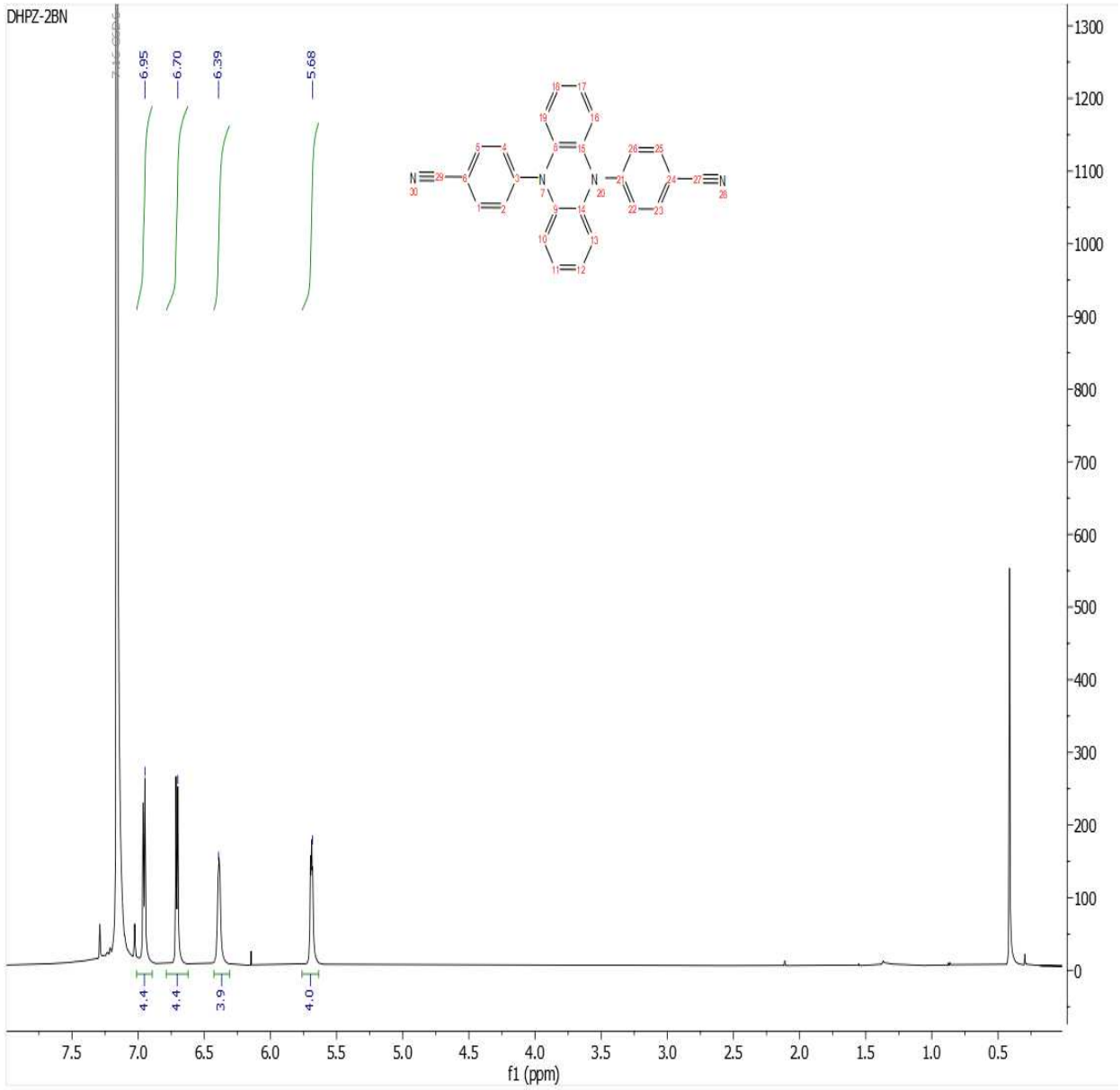

Figure S16. ^{1}H NMR spectrum (600 MHz) of 4,4'-(phenazine-5,10-diyl)dibenzonitrile in C_6D_6.

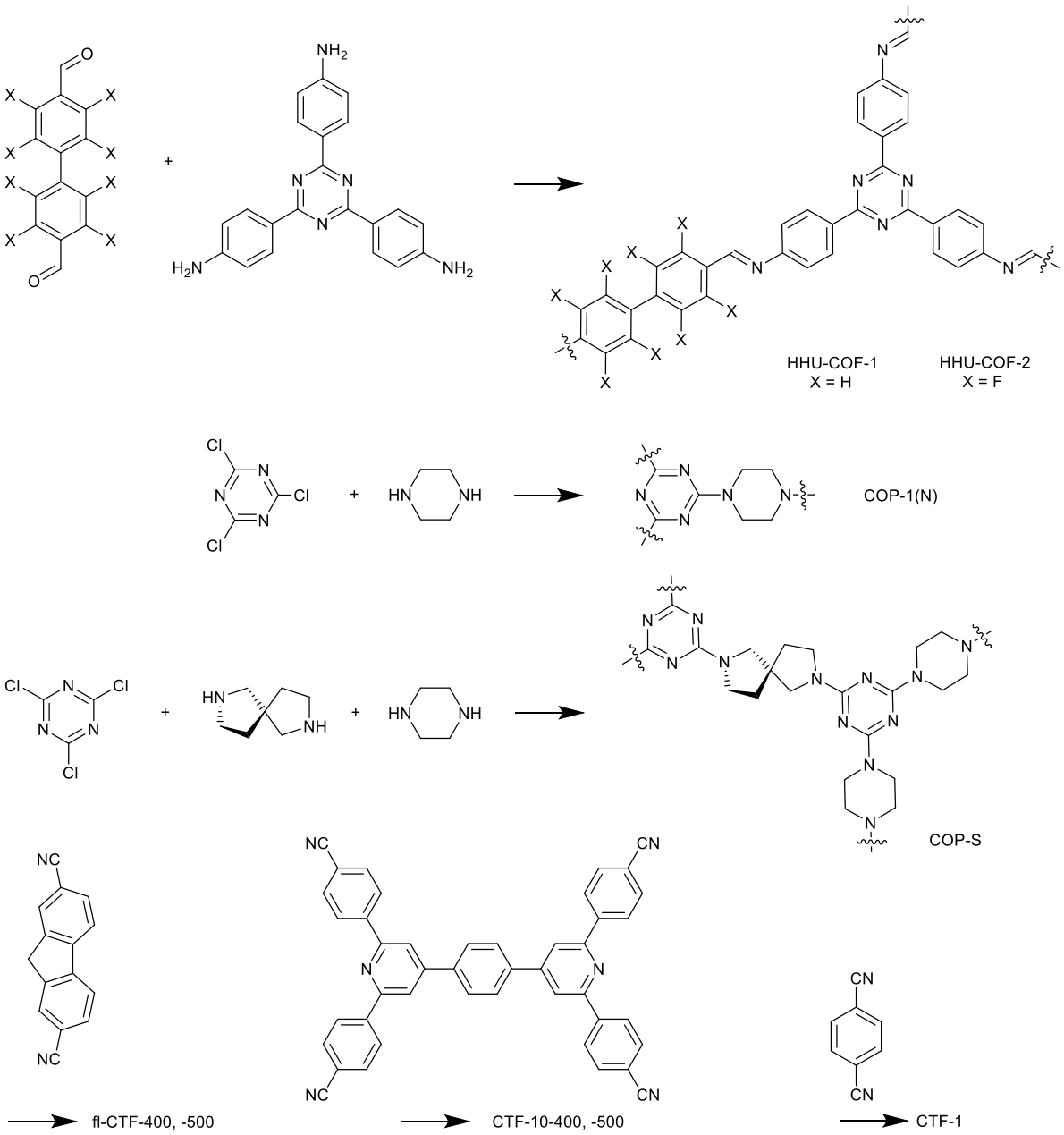

Scheme S1: A graphical presentation of the monomers used for the CTFs in Figure 5.

Section S9. References

1- Bügel, S.; Hähnel, M.; Kunde, T.; de Sousa Amadeu, N.; Sun, Y.; Spieß, A.; Beglau, T.H.Y.; Schmidt, B.M.; Janiak, C. Synthesis and Characterization of a Crystalline Imine-Based Covalent Organic Framework with Triazine Node and Biphenyl Linker and Its Fluorinated Derivate for CO_2/CH_4 Separation. *Materials* **2022**, *15(8)*, 2807.doi: 10.3390/ma15082807

2- Dey, S.; Bhunia, A.; Esquivel, D.; Janiak, C. Covalent triazine-based frameworks (CTFs) from triptycene and fluorene motifs for CO_2 adsorption. *J. Mater. Chem. A* **2016**, *4*, 6259-6263. doi:10.1039/C6TA00638H.

3- Wang, G.; Leus, K.; Jena, H.S.; Krishnaraj, C.; Zhao, S.; Depauw, H.; Tahir, N.; Liu, Y.-Y.; Van Der Voort, P. A fluorine-containing hydrophobic covalent triazine framework with excellent

selective CO_2 capture performance. *J. Mater. Chem. A* **2018**, *6*, 6370-6375, doi:10.1039/C7TA08913A.

4- Zhao, Y.; Yao, K.X.; Teng, B.; Zhang, T.; Han, Y. A perfluorinated covalent triazine-based framework for highly selective and water–tolerant CO_2 capture. *Energy Environ. Sci.* **2013**, *6*, 3684-3692. doi:10.1039/C3EE42548G.

5- Wang, H.; Jiang, D.; Huang, D.; Zeng, G.; Xu, P.; Lai, C.; Chen, M.; Cheng, M.; Zhang, C.; Wang, Z. Covalent triazine frameworks for carbon dioxide capture. *J. Mater. Chem. A* **2019**, *7*, 22848-22870. doi:10.1039/C9TA06847C.

6- Özdemir, J.; Mosleh, I.; Abolhassani, M.; Greenlee, L.F.; Beitle, R.R.; Beyzavi, M.H. Covalent Organic Frameworks for the Capture, Fixation, or Reduction of CO_2. *Front. Energy Res.* **2019**, *7.* doi:10.3389/fenrg.2019.00077.

7- Tuci, G.; Iemhoff, A.; Ba, H.; Luconi, L.; Rossin, A.; Papaefthimiou, V.; Palkovits, R.; Artz, J.; Pham-Huu, C.; Giambastiani, G. Playing with covalent triazine framework tiles for improved CO_2 adsorption properties and catalytic performance. *Beilstein J. Nanotechnol.* **2019**, *10*, 1217-1227. doi:10.3762/bjnano.10.121.

8- Tuci, G.; Pilaski, M.; Ba, H.; Rossin, A.; Luconi, L.; Caporali, S.; Pham-Huu, C.; Palkovits, R.; Giambastiani, G. Unraveling Surface Basicity and Bulk Morphology Relationship on Covalent Triazine Frameworks with Unique Catalytic and Gas Adsorption Properties. *Adv. Funct. Mater*. **2017**, *27*, 1605672. https://doi.org/10.1002/adfm.201605672.

9- Hug, S.; Stegbauer, L.; Oh, H.; Hirscher, M.; Lotsch, B.V. Nitrogen-Rich Covalent Triazine Frameworks as High-Performance Platforms for Selective Carbon Capture and Storage. *Chem. Mater*. **2015**, *27*, 8001-8010. doi:10.1021/acs.chemmater.5b03330.

10- Hug, S.; Mesch, M.B.; Oh, H.; Popp, N.; Hirscher, M.; Senker, J.; Lotsch, B.V. A fluorene based covalent triazine framework with high CO_2 and H_2 capture and storage capacities. *J. Mater. Chem. A* **2014**, *2*, 5928-5936. doi:10.1039/C3TA15417C.

11- Zhu, X.; Tian, C.; Veith, G.M.; Abney, C.W.; Dehaudt, J.; Dai, S. In Situ Doping Strategy for the Preparation of Conjugated Triazine Frameworks Displaying Efficient CO_2 Capture Performance. *J. Am. Chem. Soc*. **2016**, *138*, 11497-11500. doi:10.1021/jacs.6b07644.

12- Lee, Y.J.; Talapaneni, S.N.; Coskun, A. Chemically Activated Covalent Triazine Frameworks with Enhanced Textural Properties for High Capacity Gas Storage. *ACS. Appl. Mater. Interfaces* **2017**, *9*, 30679-30685. doi:10.1021/acsami.7b08930.

13- Yuan, K.; Liu, C.; Zong, L.; Yu, G.; Cheng, S.; Wang, J.; Weng, Z.; Jian, X. Promoting and Tuning Porosity of Flexible Ether-Linked Phthalazinone-Based Covalent Triazine Frameworks Utilizing Substitution Effect for Effective CO_2 Capture. *ACS. Appl. Mater. Interfaces* **2017**, *9*, 13201-13212. doi:10.1021/acsami.7b01783.

14- Wang, G.; Leus, K.; Zhao, S.; Van Der Voort, P. Newly Designed Covalent Triazine Framework Based on Novel N-Heteroaromatic Building Blocks for Efficient CO_2 and H_2 Capture and Storage. *ACS. Appl. Mater. Interfaces* **2018**, *10*, 1244-1249. doi:10.1021/acsami.7b16239.

15- Park, K.; Lee, K.; Kim, H.; Ganesan, V.; Cho, K.; Jeong, S.K.; Yoon, S. Preparation of covalent triazine frameworks with imidazolium cations embedded in basic sites and their application for CO_2 capture. *J. Mater. Chem. A* **2017**, *5*, 8576-8582. doi:10.1039/C6TA11226A.

16- Fu, Y.; Wang, Z.; Li, S.; He, X.; Pan, C.; Yan, J.; Yu, G. Functionalized Covalent Triazine Frameworks for Effective CO_2 and SO_2 Removal. *ACS. Appl. Mater. Interfaces* **2018**, *10*, 36002-36009. doi:10.1021/acsami.8b13417.

17- Yuan, K.; Liu, C.; Liu, C.; Zhang, S.; Yu, G.; Yang, L.; Yang, F.; Jian, X. Construction of triphenylamine functional phthalazinone-based covalent triazine frameworks for effective CO_2 capture. *Polym. J* **2018**, *151*, 65-74. doi: 10.1016/j.polymer.2018.07.061.

18- Du, J.; Liu, Y.; Krishna, R.; Yu, Y.; Cui, Y.; Wang, S.; Liu, Y.; Song, X.; Liang, Z. Enhancing Gas Sorption and Separation Performance via Bisbenzimidazole Functionalization of Highly Porous Covalent Triazine Frameworks. *ACS. Appl. Mater. Interfaces* **2018**, *10*, 26678-26686. doi:10.1021/acsami.8b08625.

19- Jena, H.S.; Krishnaraj, C.; Wang, G.; Leus, K.; Schmidt, J.; Chaoui, N.; Van Der Voort, P. Acetylacetone Covalent Triazine Framework: An Efficient Carbon Capture and Storage Material and a Highly Stable Heterogeneous Catalyst. *Chem. Mater*. **2018,** *30*, 4102-4111. doi:10.1021/acs.chemmater.8b01409.

20- Mukherjee, S.; Das, M.; Manna, A.; Krishna, R.; Das, S. Newly designed 1,2,3-triazole functionalized covalent triazine frameworks with exceptionally high uptake capacity for both CO_2 and H_2. *J. Mater. Chem. A* **2019**, *7*, 1055-1068. doi:10.1039/C8TA08185A.

21- Nuhnen, A.; Janiak, C. A practical guide to calculate the isosteric heat/enthalpy of adsorption via adsorption isotherms in metal–organic frameworks, MOFs. *Dalton Trans.* **2020**, *49*, 10295-1030. doi:10.1039/D0DT01784A.

3.3 Contribution in other publication:

In this chapter, all publications published up to this point in the role of co-author are presented. The co-authorships were carried out in the context of N_2 adsorption service measurements.

The publications are presented in chronological order, starting with the most recent ones. For this purpose, the short summaries are written, and the individual contribution to each publication has been highlighted once again.

"Synthesis and characterization of lignin-modified geopolymer composites for aqueous phase sequestration of methyl orange dye in a fixed-bed column"

Idriss Kamdem Taquieteu, Hermann Dzoujo Tamaguelon, Victor Shikuku, Sylvain Tome, Donald Kamdem Njouond, Manelle Fouetfack Dongmo, Hanibal Othman, Annette Vollrath, Abdulrahman Mohabbat, Christoph Janiak, Charles Banenzouéa and David Joh Daniel Dina, *Mater. Adv*., **2025**, DOI: 10.1039/D5MA00248F

The present work evaluated the performance of pozzolan and sawdust derived geopolymer–lignin composites in the sequestration of methyl orange (MO) in a fixed bed as an auspicious strategy for valorization of waste sawdust. GP_0, GP-CL_5 and GP-CL10 composites were prepared via alkalination, replacing pozzolan with 0,5 and 10% lignin (CL) extracted from sawdust, respectively. The composites were characterized using standard methods, namely X-ray diffraction (XRD), Fourier transform infrared (FTIR) spectroscopy, thermogravimetric analysis (TGA), Brunauer–Emmett–Teller (BET) surface analysis and scanning electron microscopy (SEM). The specific surface areas were decreased by the addition and increase in CL fraction from 53.4 to 24.9 $m^2\ g^{-1}$ for GP_0 and GP-CL10, respectively. Incorporation of CL resulted into a poly(ferro-lignino-sialate) single-network. Addition of CL increased the breakthrough time and the operating time of the column. The Thomas model best described the breakthrough curves. MO sequestration performance (Q_0) was three times better on GP-CL_{10} than GP_0 when the feed rate was increased. The MO fixation mechanism mainly includes external and internal diffusion and electrostatic interactions. The adsorption is driven by the surface chemistry rather than textural characteristics of the adsorbent. These results indicate that geopolymer–lignin composites are potential eco-adsorbents for the removal of azo dyes in a continuous adsorption system and presents a plausible way for recycling sawdust.

Type of contribution to the publication:

N_2 adsorption measurement of the samples.

“**Novel Superadsorbent from Pozzolan-Charcoal based Geopolymer Composite for the Efficient Removal of Aqueous Crystal Violet”**

Jacques Madiba Mboka, Hermann Dzoujo Tamaguelon, Victor Shikuku, Sylvain Tome, Valery Franck Deugueu, Hanibal Othman, Christoph Janiak, Marchand Manga Dika, Marie Annie Etoh & David Joh Daniel Dina, *Water Air Soil Pollut*. **2024**, DOI: 10.1007/s11270-024-07257-4

In this study, geopolymer composites, GP_0, $GPC_{2.5}$, GPC_5, $GPC_{7.5}$ and GPC_{10} were synthesized from pozzolan, a naturally occurring, abundant and inexpensive precursor, substituted with varying proportions of 0, 2.5, 5, 7.5, and 10% content by weight of charcoal powder (CP), an industrial waste product, respectively. The geocomposites were characterized by Fourier Transformed Infrared Spectroscopy (FTIR), BET (Bruamer Emmet Teller) method, scanning electron microscopy (SEM), thermogravimetric analysis (TGA), methylene blue and iodine indices. The adsorption performances for the removal of crystal violet, a toxic dye, from water in batch mode were evaluated. Incorporation of charcoal powder improved the functional group density, the microporous structure and the specific surface areas (SSA) of the pozzolan-based geopolymers resulting in increased adsorption efficacy. Langmuir, Freundlich, Temkin, Dubin-Radushkevich-Kaganer and Flory Huggins isotherms were applied to model the equilibrium data. The $GPC_{7.5}$ composite (7.5% wt CP), with SSA 15.93 $m^2\ g^{-1}$, exhibited an unprecedented ultrahigh maximum monolayer adsorption density of 2803 mg g^{-1}, a new benchmark value for adsorption of crystal violet. The adsorption rate was best described by the pseudo-first order kinetic model with an invariable adsorption rate constant (k1). The Gibbs free energy ($\Delta G < 0$) signify a spontaneous and feasible adsorption process while the magnitude of the adsorption energies corresponded to a physisorption mechanism. The $GPC_{7.5}$ composite is a novel inexpensive superadsorbent for the abatement of crystal violet dye in aqueous media with about 1000 mg g^{-1} higher adsorption capacity than pristine pozzolan-based geopolymer (GP_0). The synthesis adopted minimal and abundant precursors producing a material that is techno-economical and reproducible in many countries, especially emerging economies.

Type of contribution to the publication:

N_2 adsorption measurement of the samples.

3.4. Unpublished works:

3.4.1 Manganese induced phosphorescence in the metal-organic framework Mg-CPO-27: application and effect.

Hanibal Othman, Julia Michalski, Markus N.A. Fetzer, Christoph Janiak.

The metal-organic framework Mg-CPO-27 ($Mg_2(dhtp)(H_2O)_2$]), was synthesized via solvothermal methods, with different amounts of manganese ions incorporated in situ. The structural integrity and crystallinity of the modified MOFs were confirmed by powder X-ray diffraction (PXRD), and nitrogen adsorption measurements were conducted to assess the surface area. A key finding of this study was the discovery of Mn-induced luminescence with just 1 wt% Mn addition, a phenomenon not observed in other MOFs when adding other paramagnetic metals such as iron (Fe), nickel (Ni), or cobalt (Co). Photoluminescence studies revealed distinct changes in the absorption and emission spectra, demonstrating the emergence of a new luminescence band in Mg-CPO-27 at 720 nm upon Mn incorporation. Time-resolved measurements provided further insight into the luminescent lifetime, reinforcing the unique photophysical behaviour of Mn-modified Mg-CPO-27. Additionally, we investigated the thermal dependence of the luminescence, observing significant variations in intensity and lifetime with temperature changes ranging between 2 and 9 µs and a thermal quenching efficiency of 100 % at room temperature. These findings highlight the potential of Mn addition for tuning the optical properties of Mg-CPO-27, making it a promising candidate for applications in sensing and optoelectronics.

Contribution to the work:

Hanibal Othman: Synthesis and characterization of the samples, assessment and interpretation of the results, writing and revision of the manuscripts.

Julia Michalski: X-ray photoelectron spectroscopy (XPS) analysis and interpretation, writing.

Markus N.A. Fetzer: Energy-dispersive X-ray spectroscopy measurements analysis and scanning electron microscopy photos.

Christoph Janiak: Idea and conceptualization, assessment and interpretation of the results writing and revision of the manuscripts.

Manganese induced phosphorescence in the metal-organic framework Mg-CPO-27: application and effect.

Hanibal Othman[1], Julia Michalski[1], Markus N.A. Fetzer[1], Christoph Janiak[1]*.

[1] Institut für Anorganische Chemie und Strukturchemie, Heinrich-Heine-Universität Düsseldorf, D-40204 Düsseldorf, Germany; hanibal.othman@hhu.de (H.O.); julia.michalski@hhu.de (J.M.); markus.fetzer@hhu.de (M.F.); janiak@uni-duesseldorf.de (C.J.)

Abstract:

The metal-organic framework Mg-CPO-27 ($Mg_2(dhtp)(H_2O)_2$]), was synthesized via solvothermal methods, with different amounts of manganese ions incorporated in situ. The structural integrity and crystallinity of the modified MOFs were confirmed by powder X-ray diffraction (PXRD), and nitrogen adsorption measurements were conducted to assess the surface area. A key finding of this study was the discovery of Mn-induced luminescence with just 1 wt% Mn addition, a phenomenon not observed in other MOFs when adding other paramagnetic metals such as iron (Fe), nickel (Ni), or cobalt (Co). Photoluminescence studies revealed distinct changes in the absorption and emission spectra, demonstrating the emergence of a new luminescence band in Mg-CPO-27 at 720 nm upon Mn incorporation. Time-resolved measurements provided further insight into the luminescent lifetime, reinforcing the unique photophysical behaviour of Mn-modified Mg-CPO-27. Additionally, we investigated the thermal dependence of the luminescence, observing significant variations in intensity and lifetime with temperature changes ranging between 2 and 9 µs and a thermal quenching efficiency of 100 % at room temperature. These findings highlight the potential of Mn addition for tuning the optical properties of Mg-CPO-27, making it a promising candidate for applications in sensing and optoelectronics.

Introduction:

MOFs are crystalline metal-coordination frameworks with potential porosity. MOFs consist of organic linkers and metal atoms, the latte rare also called secondary building units or SBUs. SBUs normally are metal atoms or metal oxido clusters together with the donor atoms of the organic linker that coordinate to the metal atoms. The tunability of the structure and a high surface area drive the interest in MOFs being used

in a range of potential applications, including catalysis, sorption, and sensing technologies. [1-8]

MOFs can exhibit various forms of luminescence, originating from linker, metal, guest species or a combination thereof. [9-12] Significant metal-based luminescence (not only in MOFs) is typically restricted to lanthanides (Ln), especially to europium (Eu), erbium (Er), and ytterbium (Yb). [13-16].

Mn^{2+} (d^5, high-spin) exhibits characteristic luminescence arising from the spin-forbidden $^4T_1 \rightarrow {}^6A_1$ transition in octahedral coordination. Due to its spin- and parity-forbidden nature, this transition results in long-lived emission (μs-ms range) and weak absorption. The emission wavelength is strongly ligand-field so in the case of strong fields, this stabilize the $^4T_1$ state, leading to red-shifted emission (610–660 nm). Although forbidden, the $^4T_1 \rightarrow {}^6A_1$ transition becomes partially allowed via vibronic coupling or local asymmetry. These properties make Mn^{2+} a useful dopant in phosphors for LEDs, bioimaging, and optical communication [17-18]. Charge transfer within MOFs can occur in two principal ways, each imparting distinctive optical property. The first and more common process is ligand-to-metal charge transfer (LMCT), where an excited linker transfers charge to the metal center, thus exciting it and subsequently returning to a relaxed state.[19-20] In the case of Manganese, manganese is an insufficient center to excite [21-22] so it becomes easier to excite a ligand that is in the vicinity of Mn and to transfer the energy absorbed to the triblet energy state of Mn(II) via intersystem crossing thus inducing the $^4T_1$ to $^6S_1$ radiative transition to generate the observed phosphorescence [23].

This charge transfer capability not only enhances the luminescent properties but also broadens the range of possible applications, as LMCT can be harnessed for specific functional purposes. A practical method to induce or enhance luminescence in MOFs is through metal doping, where luminescent elements or molecules are incorporated into the framework to emit light upon excitation at specific wavelengths. Metal doping is frequently employed to induce such properties, as well as to introduce other functionalities like photocatalytic activity and gas adsorption capacity. [10,22-24] and several transition metals, including manganese (Mn), iron (Fe), cobalt (Co), and copper (Cu), are among the metals commonly used for doping. Each metal brings its unique properties, enabling MOFs to be optimized for targeted applications. Figure 1 illustrates LMCT process, highlighting the mechanisms of charge transfer and their significance in tuning the photophysical properties of MOFs. [10,25,26]

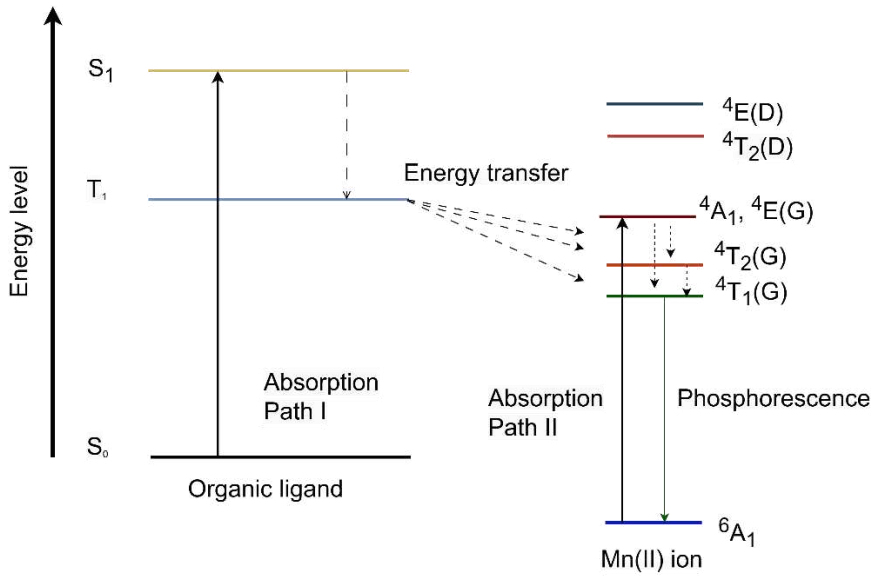

Figure 1: Schematic diagram showing the emission mechanism of phosphorescent manganese(II) "complexes. Adv. Optical Mater. 2020, 8, 2000985" [23]

In this study, we present the successful modification of two distinct metal-organic frameworks, namely, MOF-5 and Mg-CPO-27, using manganese ions (Mn^{2+}). The Mn^{2+} ions, characterized by a d^5 electronic configuration, allow us to track the luminescent behaviour with precision using Tanabe-Sugano diagrams, a valuable tool for understanding the electronic transitions of transition metal complexes. Upon adding, manganese atoms are incorporated into the MOF frameworks, with some atoms statistically residing within the pores of the structure while others become integrated into the secondary building units (SBUs) of the frameworks [14].

This integration enables a unique interaction between the manganese ions and the organic linkers that form the backbone of the MOFs. Specifically, the linkers sensitize the embedded manganese ions via a ligand-to-metal charge transfer (LMCT) process, resulting in a distinctive phosphorescence effect that is most pronounced at 77 K. This observed phosphorescence is significant, as it reveals the ability of the modified MOFs to emit light over prolonged periods, a characteristic that opens potential applications in optical materials and sensors.

Additionally, the luminescent properties of the Mn@MOFs were monitored across a range of temperatures. This allowed us to explore their potential utility in thermometric applications, where temperature-dependent luminescence can serve as an indicator of environmental changes. Our findings suggest that the Mn@MOFs exhibit a luminescent response that is sensitive to temperature variations, offering a promising platform for the development of materials that react dynamically to thermal shifts.

Such temperature-responsive behaviour could be harnessed in fields such as temperature sensing and thermometry, where responsive materials are in high demand for both industrial and scientific applications.

Experimental section:

The synthesis of Mg-CPO-27 and Mn@Mg-CPO-27. [27]

In a synthesis vessel, (0.2 mmol, 0.037g) of 2,5- dihydroxyterephthalic acid (H_4dhtp) was dissolved in 15 mL of dry dimethylformamide (DMF), In the same flask a solution of (0.6 mmol, 0.153 g) of magnesium nitrate hexahydrate in 15 mL of DMF was added with an extra addition of a 2 mL mixture of (1:1) ethanol and water. After 5 min of sonication, the mixture was placed in an oven for 24 h at 120°C with a 5 h heating ramp and 5 h cooling ramp. The product was washed with fresh absolute ethanol and allowed to be shaken on a shaking plate in the EtOH for 24 h, then the EtOH was removed by centrifugation. This washing procedure was repeated twice before drying of the separated solid at 60 °C in a drying-oven. Yield 40 mg, 70 %

To synthesize the Mn modified version of Mg-CPO-27 the same steps were done as the previous synthesis but with an addition of (0.015 mg, 5 mol%) of manganese (II) nitrate tetrahydrate. The yield of the reaction was significantly lower than that of the pristine MOF with only 45 mg, 70%

Results:

The addition of Mn to the cubic MOF-5 crystals was achieved through a post-synthetic modification by gently agitating the crystals in a manganese nitrate tetrahydrate solution for 48–72 hours. MOF-5 poses a lot of problems and is not practical for the purpose of the article, it was decided that the characterization is summarized in the SI. In contrast, Mg-CPO-27 was modified in situ, where manganese could have played an active role in the framework formation during synthesis.

AAS analysis reveals that the Mg-CPO-27 sample modified *in-Situ* reached the highest manganese content, achieving 1% Mn. Thus, the sample will be labelled as 1% Mn@Mg-CPO-27. Scanning electron microscopy (SEM) integrated with energy-dispersive X-ray (EDX) mapping confirms the incorporation of manganese atoms within the structures and pores of Mg-CPO-27. The EDX spectrum further indicates manganese presence in these samples. Fourier-transform infrared (FTIR) spectroscopy was employed to identify the functional groups in the frameworks Figure 2, Figure S1(a).

Notably. These changes, including the observed peaks at 700, 1650 cm^{-1}, are present in 1% Mn@Mg-CPO-27.It is important to note that these signals may not always be prominent due to the low concentration of Mn within the framework. Furthermore, Mn may reside within the MOF's pores as manganese nitrate, where it does not interact directly with the framework structure, potentially reducing observable bonding signals.

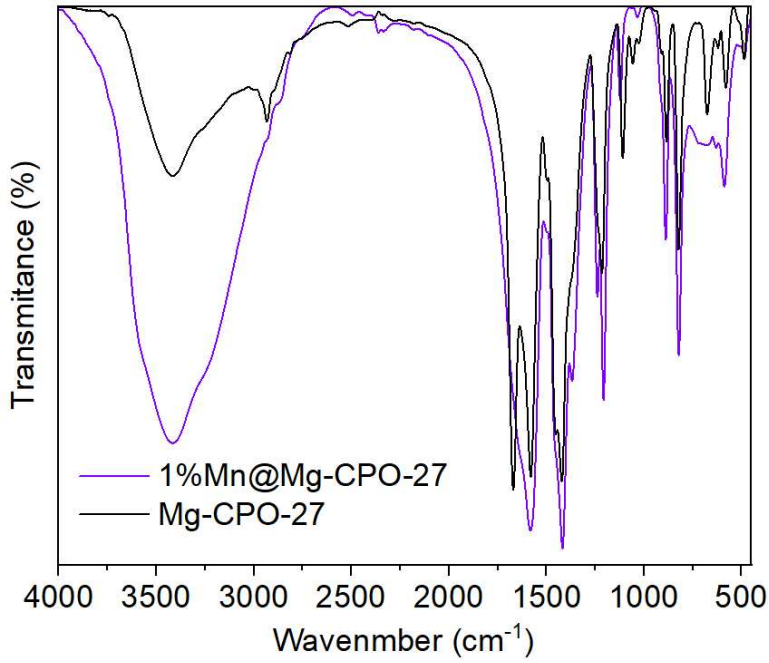

Figure 2: FTIR spectra comparison between pristine Mg-CPO-27 (black) and 1%Mn@Mg-CPo-27 (purble).

Powder X-ray diffraction (PXRD) was used to assess the crystallinity of the samples.

In the 1% Mn@Mg-CPO-27 sample, likely due to the low Mn concentration in this material the change is minimal thus the effect of Mn has minimized the structural perturbation. N_2 adsorption was recorded to study the porosity of the MOFs, resulting in a surface area that as lower than other M-CPO-27 in literature. Both MOFs had a type II isotherms that is non and microporous materials with a hysteresis loop of type H2(b) which can associate with pore blocking indicating that the size of the neck is not proportional to the pore size. Pristine Mg-CPO-27 demonstrated a surface area (1111 $m^2\ g^{-1}$) lower than reported in literature, while 1% Mn@Mg-CPO-27 showed a very small surface area 331 $m^2\ g^{-1}$.

X-ray photoelectron spectroscopy (XPS):

XPS measurements were conducted to determine the oxidation state and bonding environment of the nonmetal ions (C, N, O and Cl), the metal Mn and the alkaline earth metal Mg in the CPO-27. The XPS survey spectrum CPO-27 confirmed the presence

of the elements C, O, N and Mg of the synthesized material. The survey spectra are shown in Figure 3(a), and the high-resolution spectra are in Figure S3. The high-resolution carbon *1s* spectrum (C *1s*) can be fitted into 4 peaks with binding energies of 284.6 eV, 284.8 eV, 286.4 eV, and 288.8 eV, which indicate the presence of (C = C), (C-C), (C-N), and (C=O).[28] The position of each peak is assigned in **Table S1**. The oxygen spectrum (O *1s*) can be deconvoluted into three peaks positioned at 530.5 eV, 531.9 eV and 532.3 eV, which are related to metal-oxides, (C=O) and (C-O). [29] The positions of these peaks are provided in **Table S2**. The nitrogen 1s (N *1s*) survey scan shows a small peak. The nitrogen *1s* (N *1s*) high resolution spectrum shows one peak at a binding energy of 400.0 eV, corresponding to ($C\text{-}NH_2$).[30-31] The binding energy value of N *1s* is summarized in **Table S3**. The manganese $2p_{1/2}$ (Mn $2p_{1/2}$) spectrum shows a Mn $2p_{3/2}$ peak at 640.3 eV with a satellite feature at 643.6 eV and 656.8 eV characteristic for Mn^{2+} in MnO. [32-33] The Mn *2p* binding energy values are summarized in Table S4. The magnesium *2s* (Mg *2s*) signal shows two peaks at binding energies of 89.5 eV and 90.4 eV, which are consistent with the presence of Mg^{2+} species. These binding energies indicate magnesium in an oxidized state, which could indicate the presence of MgO.[34] The Mg *2s* binding energy values are summarized in Table S5. The magnesium *2p* (Mg *2p*) signal displays three peaks at binding energies of 350.3 eV, 352.0 eV and 353.9 eV, which correspond to metallic Mg, MgO and $Mg(OH)_2$. The Mg *2p* binding energy values are summarized in **Table S4**, **Table S6**.

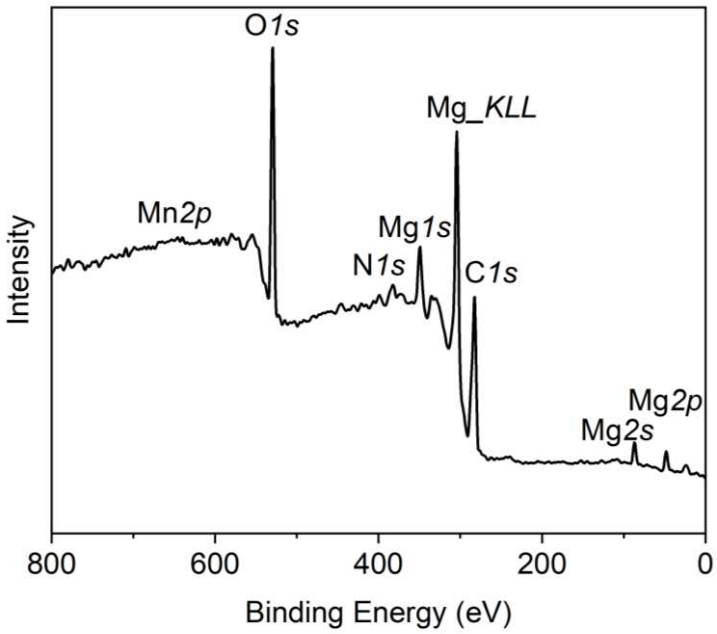

(a)

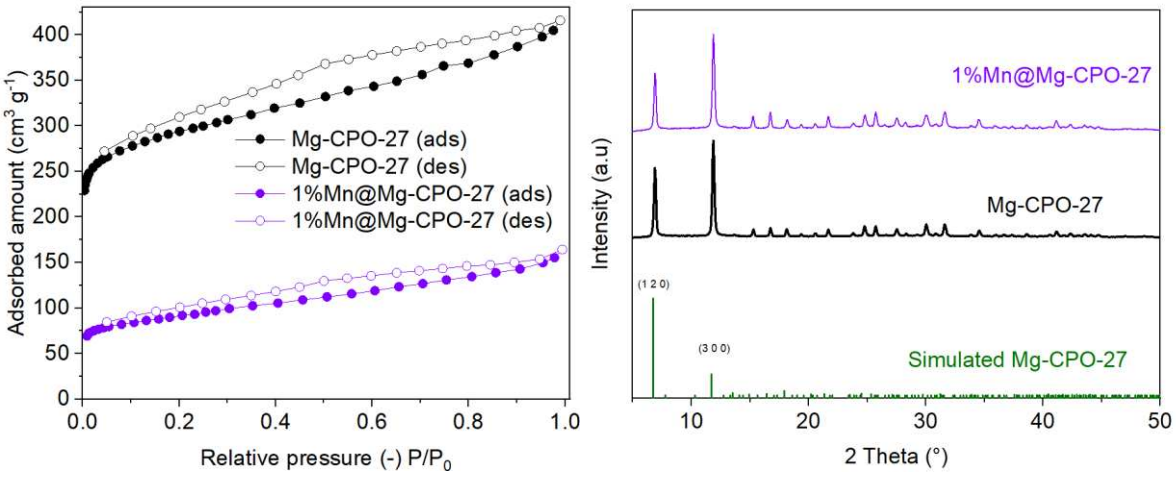

(b) **(c)**

Figure 3: (a) XPS spectrum of the 1%Mn@Mg-CPO-27 sample, (b) N_2 adsorption isotherms of eh samples Mg-CPO-27 and 1%Mn@Mg-CPO-27. (c) PXRD comparison between the samples Mg-CPO-27 and 1%Mn@Mg-CPO-27.

Luminescence studies in pristine and modified MOFs:

The optical properties of both pristine and 1%Mn@Mg-CPO-27s were analysed by recording their emission and absorption spectra. In the 1%Mn@Mg-CPO-27, the presence of manganese was evident in the emission spectrum Figure 5, where a broad band spanning 650–800 nm was observed, with a maximum at approximately 720 nm. This feature was completely absent in the emission spectrum of pristine Mg-CPO-27. Interestingly, this band is red-shifted compared to the emission peaks typically observed for octahedral Mn^{2+} complexes, which are usually centred around 600 nm and are characteristic of orange luminescence. The disappearance of this band when measurements were conducted at room temperature strongly suggests that this transition corresponds to phosphorescence rather than fluorescence. [35-38] The mechanisms behind the quenching effect associated with this emission will be discussed in detail in the Discussion section of this paper.

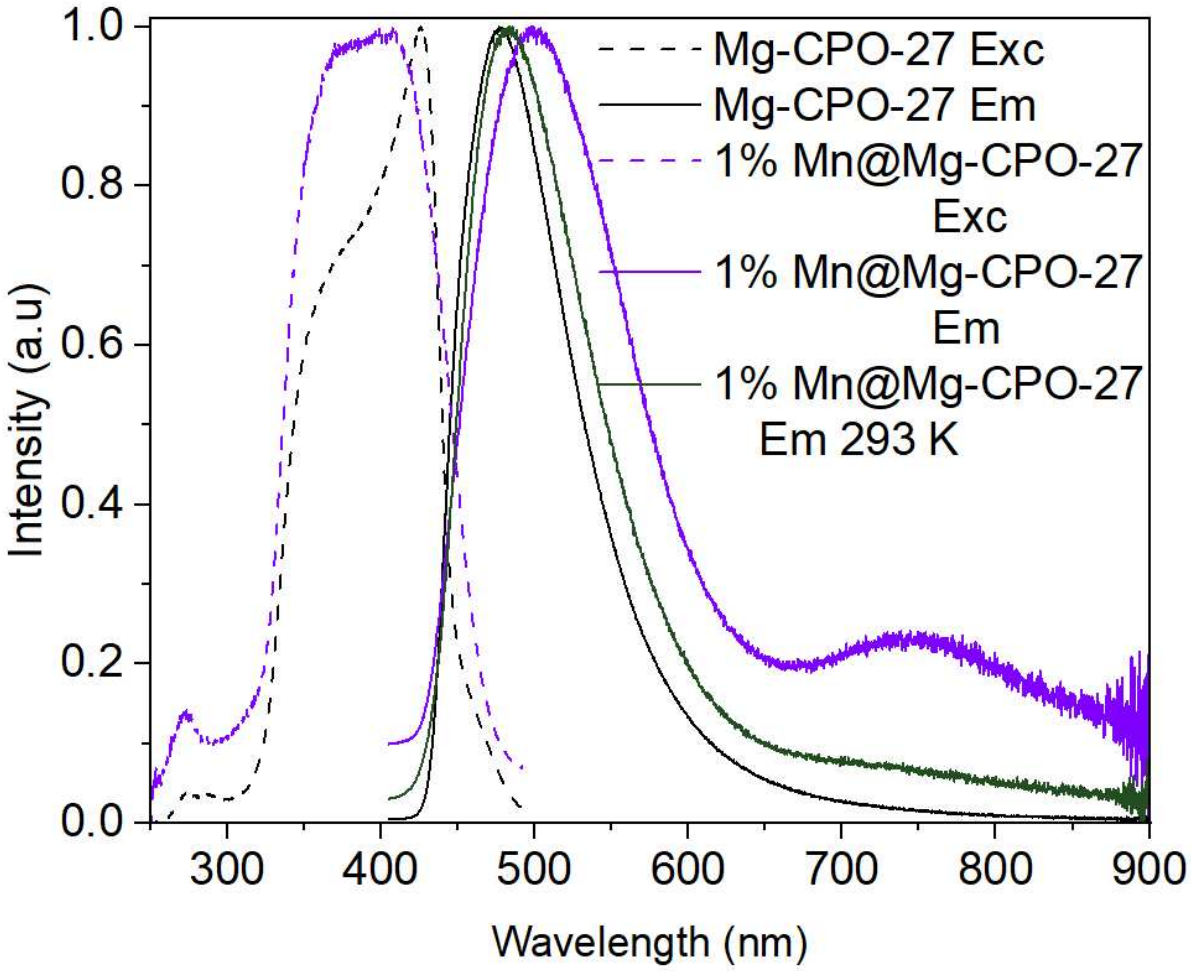

Figure 4: Excitation and emission spectra of the samples Mg-CPO-27 and 1%Mn@Mg-CPO-27 at 77 K and 293 K where the λ_{Em} = 505 nm and λ_{Exc} = 390 nm

In addition to the broad emission band, the fluorescence region of the modified MOF spectra, spanning 370–525 nm, exhibited a slight red shift of approximately 10 nm relative to the pristine samples. This shift is likely attributed to alterations in the electronic environment of the MOF framework caused by the incorporation of manganese. To further investigate the nature of this transition, decay time measurements were performed. The measured decay time for the broad emission band was relatively long, with an average life time of 9 µs at 77 K, providing additional evidence to support the hypothesis of phosphorescence. This prolonged decay time is indicative of an electron transition from a triplet state to the ground state and is significantly longer than the fluorescence decay time. A similar broad emission peak between 650–800 nm was also detected in the 1% Mn@Mg-CPO-27 sample, which was absent in the spectrum of pristine Mg-CPO-27, further confirming that the observed feature originates from manganese. Additionally, this broad peak disappeared at room temperature, indicating a thermal quenching effect. The luminescence intensity of this band was plotted as a function of its decay time to extract the average relaxation time,

which is depicted in Figure 5. The mean relaxation time for 1% Mn@Mg-CPO-27 was in microcescond range, which is again significantly longer than the typical decay times associated with fluorescence transitions (10^{-7}–10^{-9} s). These observations collectively highlight the unique optical behaviour introduced by manganese addition in these MOF systems. The table with the summary of the average decay time can be found in Table S7.

The influence of manganese concentration on the optical properties of the MOFs was further explored by synthesizing a sample with nearly double the Mn content compared to the original modified sample. This sample was analysed under identical experimental conditions to ensure comparability. A significant increase in the intensity of the emission band was observed, demonstrating a direct correlation between the manganese concentration and the luminescence intensity. This finding suggests that higher Mn content enhances the optical response of the material, likely due to increased active sites contributing to the emission process Figure S5(b).

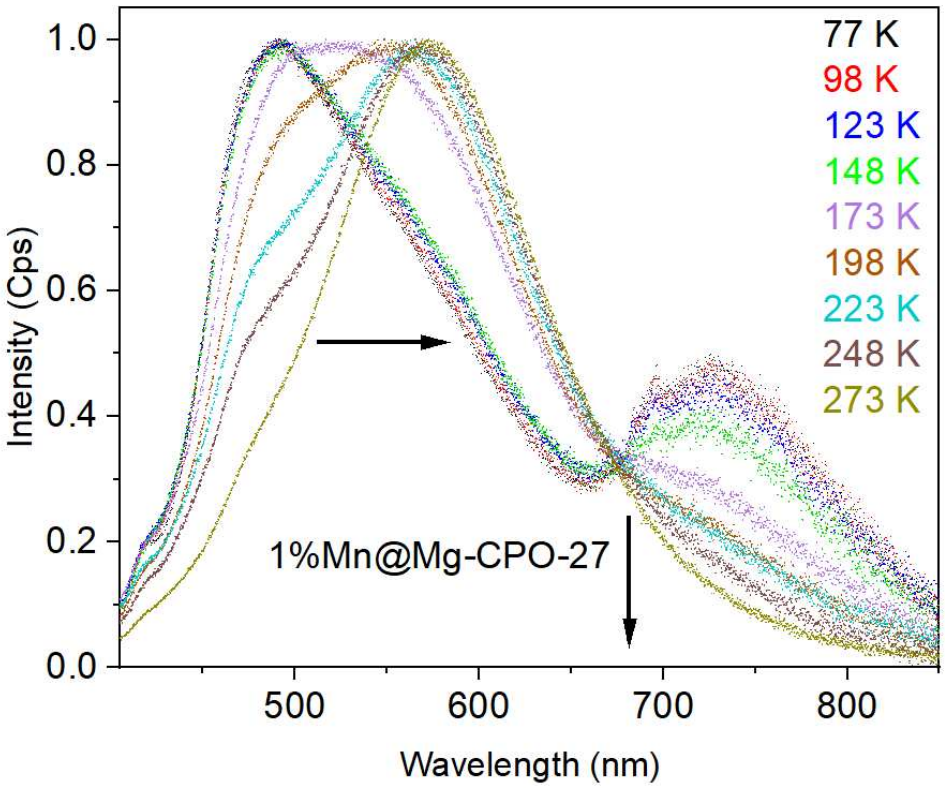

(a)

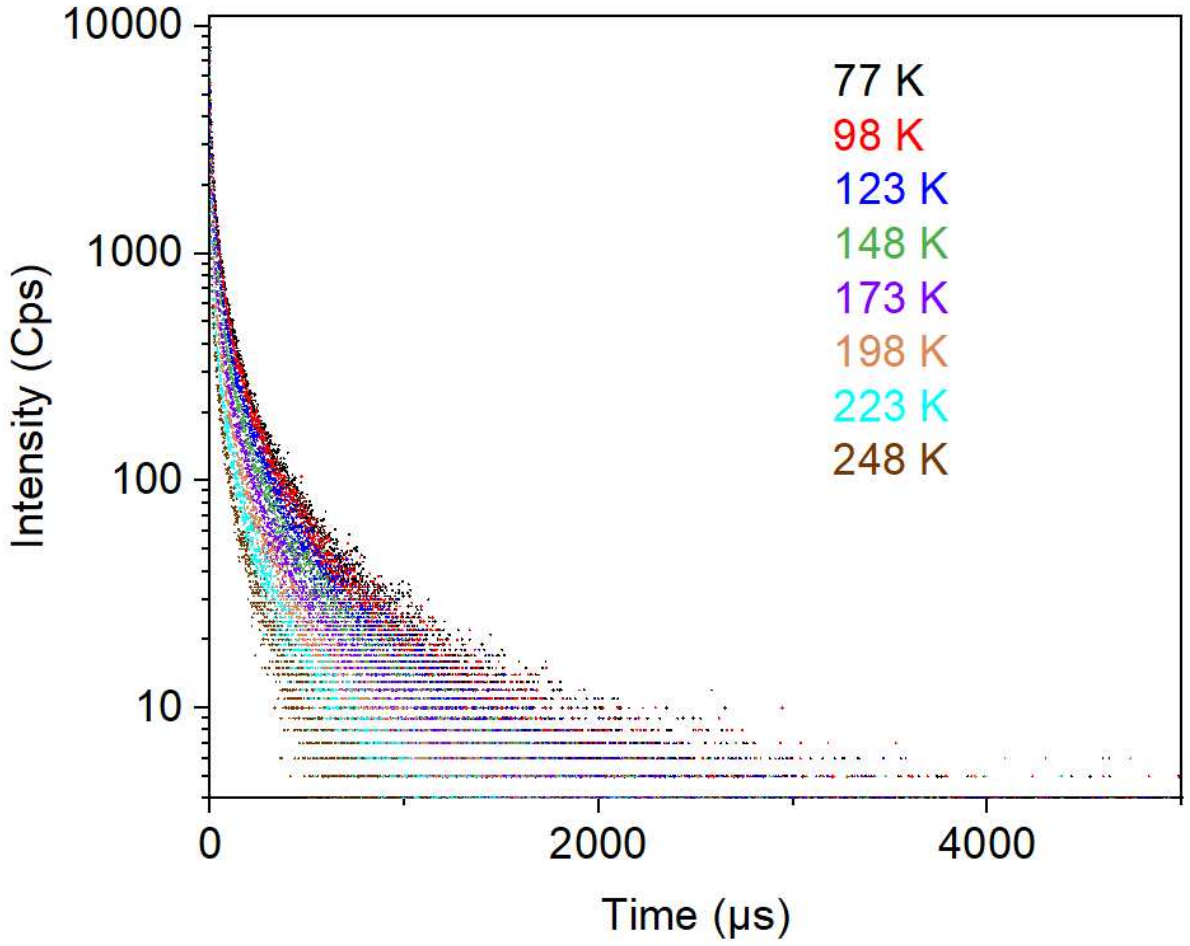

(b)

Figure 5: (a) Temperature dependence of the phosphorescence recorded at different temperatures increasing in a 25 K steps with a λ_{Exc} = 390 nm, (b) time-resolved laser-induced luminescence/phosphorescence (LLP) decay curve of 1%Mn@Mg-CPO-27 with a micro flashlamp λ_{Exc} = 390 nm.

Phosphorescence in the Mn@MOF samples was suspected to result from the paramagnetic effect, a phenomenon first observed by Yuster and Weismann in the 1940s. [38] This effect occurs when a paramagnetic atom facilitates and enhances interactions between singlet and triplet states, promoting phosphorescence through intersystem crossing (ISC). [39-40] To investigate this, a series of MOF-5 samples were post-synthetically modified with other paramagnetic atoms, including Fe, Co, and Ni. Emission spectra of these samples were recorded under the same conditions as those of the 1%Mn@Mg-CPO-27 samples. Interestingly, none of these samples displayed phosphorescent behaviour, nor did they show the characteristic band observed in the Mn@MOF samples. Figure S8 illustrates the emission spectra for these paramagnetically doped samples. This effect describes the ability of a paramagnetic atom to enhance the interaction between singlet and triplet states, thereby facilitating

phosphorescence through an intersystem crossing (ISC) mechanism. [40] Interestingly, none of the Fe, Co, or Ni doped samples exhibited phosphorescent behaviour, nor did they display the characteristic broad emission band observed in the 1%Mn@Mg-CPO-27. These results suggest that the phosphorescence observed in Mn@MOF samples cannot be generalized to other paramagnetic atoms and may involve unique properties or interactions specific to manganese. Luminescence thermal dependence was observed Figure 6 and Figure S5, while increasing the temperature of the sample gradually. The peak that is situated between 700-850 nm was influenced greatly with temperature change further pushing the idea that this band resulted from the $^4T_1$ to $^6A_1$ transition of the Mn. Two conditions of the Mg-CPO-27 and the 1% Mn@Mg-CPO-27 were tested, one was dry samples, and the other was slightly wet sample (DMF) to investigate the effect of the solvent on the special peak and the general luminescence of the MOF. MOF-5 was not considered for this experiment due to stability difficulties that leads to rapid decomposition of the structure when introduced to moisture (ambient atmosphere). The wet samples (1% Mn@Mg-CPO-27) showed a very predictable quenching of the suspected band at higher temperatures which is known in phosphorescent material. [41] While the main fluorescence of the MOF displayed a bathochromic shift that is a result of presence of the solvent. The effect begins at 177 K and at 273 K the peak of the fluorescence is completely shifted from 490 nm to 573 nm. In the dry sample the band at 750 nm is much more intense and pronounced than that of the wet sample. It clear that the sample shows sensitivity toward the increase in temperature of the medium with a quenching efficiency that reached 58 % at 252 K where the quenching efficiency was calculated using the following equation,

$QE = 1- I_t/I_0 \times 100$

Where (1)

QE is quenching efficiency

I_t is the intensity of the emission at a given temperature

I_0 is the intensity of the emission at the lowest temperature in this case is 77 K

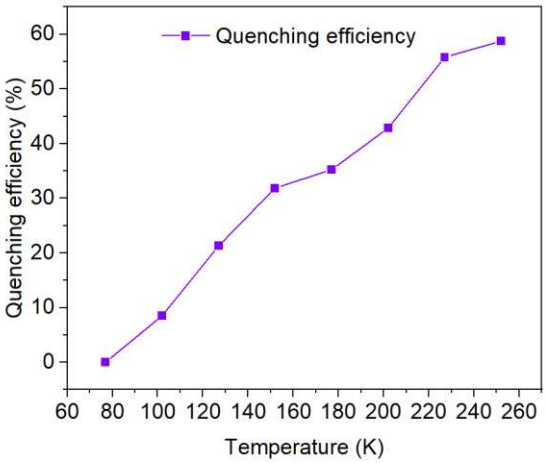

Figure 6: Quenching efficiency of temperature in the sample 1%Mn@Mg-CPO-27.

Discussion:

The addition of Mn^{2+} to the MOF affects primarily the luminescence properties, while the overall crystal structure remains intact, with only moderate changes in surface area and thermal stability. The incorporation of manganese into the secondary building units or pores introduces new electronic transitions absent in the pure Mg-based MOF. This effect is Mn-induced and can be understood from the Tanabe–Sugano diagram for a d^5 ion, where the observed luminescence corresponds to the $^4T_1 \rightarrow {}^6A_1$ transition.

The broad emission band between 650 – 850 nm suggests a charge transfer process from the linker (2,5-dihydroxyterephthalic acid) to the Mn^{2+} centers, leading to the formation of a broadband temperature-sensitive emitter. At higher temperatures, this emission is quenched due to increased mixing of singlet and triplet states, which enhances non-radiative decay pathways. Such broadband emitters are characterized by a large Huang–Rhys factor (S), which describes the strong electron–phonon coupling and the large Stokes shift. The displacement of potential energy surfaces between ground and excited states can be represented using the Morse interionic potential.

The thermal quenching arises from multiple non-radiative transitions. In configurational coordinate diagrams, the crossover point between the excited and ground-state potential surfaces lies at an energy lower than the vibrational states of the excited state, facilitating internal conversion. In addition, excitation energy can be transferred to vibrational modes of residual guest molecules (DMF, H_2O) or functional groups of the

linker itself (C–H stretching, O–H bending), which further contributes to quenching at elevated temperatures. This is schematically represented in Figure 7 [41].

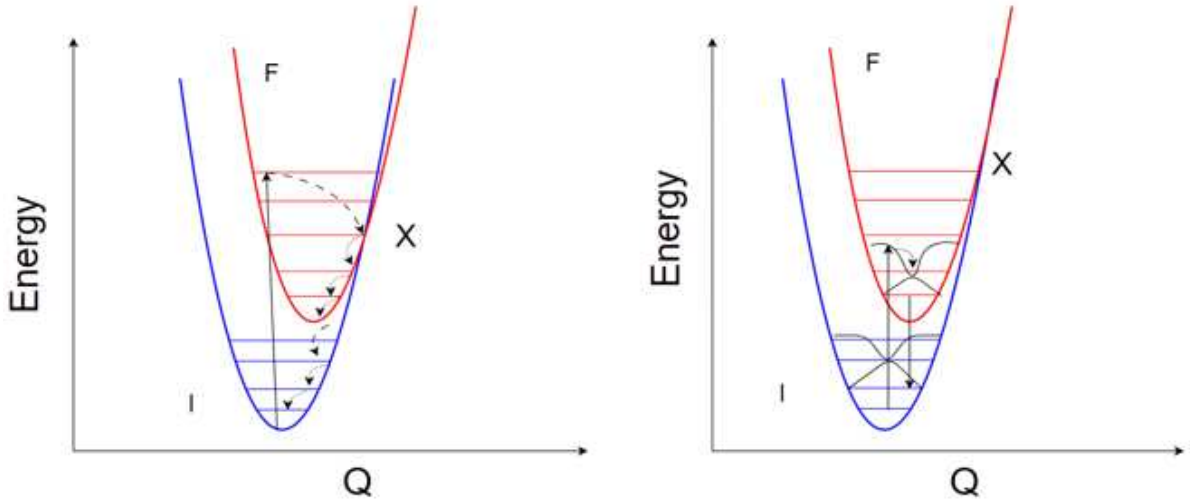

Figure 7: Configurational coordinate diagrams to explain the crossover point and the broadband emission (a) The crossover effect at higher temperatures, (b) the broad band emitter at deep temperatures.

Conclusions:

In conclusion, two metal-organic frameworks were synthesised, modified and successfully characterised. The proper modification techniques did not compromise the crystal structure and its stability. The modification process had a significant effect on the luminescent properties of the MOFs, where the induced LMCT, promoting phosphorescence as the result of $^4T_1$ to $^6S_1$ transition. The intensity of this transition was hugely affected by the concentration of Mn inside the grid of the MOF. 1%Mn@Mg_2CPO-27 had a surface area of 331 m^2g^{-1} and a phosphorescence life-time ranging between 2 and 9 µs at different temperatures. The quenching efficiency of temperature was measured to be 100 % at room temperature and 70 % at 248 K. MOF-5 showed a new transition at 488 % when 10 %wt Mn was added to the structure. It is worth mentioning that the appearance of phosphorescence is shown to be limited to Mn as a paramagnetic metal, as other para-magnetic metals such as Fe, Ni and Co did not promote such transitions.

Refs:

1. V. F. Yusuf, N. I. Malek, S. K. Kailasa, *ACS. Omega* **2022**, *7*, 44507–44531, DOI: 10.1021/acsomega.2c05310.
2. A. Bavykina, N. Kolobov, I. S. Khan, J. A. Bau, A. Ramirez, J. Gascon, *Chem. Rev.* **2020**, *120*, 8468–8535, DOI: 10.1021/acs.chemrev.9b00685.
3. P. García-García, M. Müller, A. Corma, *Chem. Sci.* **2014**, *5*, 2979–3007, DOI: https://doi.org/10.1039/C4SC00265B
4. J. Wales, D. Hughes, E. Marshall, P. Chambers, *Ind. Eng. Chem. Res.* **2022**, *61*, 9529–9543, DOI: 10.1021/acs.iecr.2c00222.
5. C. Jiang, X. Wang, Y. Ouyang, K. Lu, W. Jiang, H. Xu, X. Wei, Z. Wang, F. Dai, D. Sun, *Nanoscale Adv.* **2022**, *4*, 2077–2089, DOI: https://doi.org/10.1039/D2NA00061J.
6. H. Y. Li, S. N. Zhao, S. Q. Zang, J. Li, *Chem. Soc. Rev.* **2020**, *49*, 6364–6401, DOI: https://doi.org/10.1039/C9CS00778D.
7. H. Sohrabi, S. Ghasemzadeh, S. Shakib, M. R. Majidi, A. Razmjou, Y. Yoon, A. Khataee, *Ind. Eng. Chem. Res.* **2023**, *62*, 4611–4627, DOI: https://doi.org/10.1021/acs.iecr.2c03011.
8. T. Wu, X. J. Gao, F. Ge, H. G. Zheng, *Cryst. Eng. Comm.* **2022**, *46*, DOI 10.1039/d2ce01159j.
9. S. Xing, C. Janiak, *Chemical Communications* **2020**, *56*, 12290–12306.
10. Q. B. Bo, G.X. Sun, D. L. Geng, *Inorg. Chem.* **2010,** *49***,** 2**,** 561–571, DOI 10.1021/ic901730f.
11. C. Kittipong, P. Khemthong, F. Kielar, Y. Zhou, *Acta. Crystallogr. E Crystallogr. Commun.* **2016**, *72*,87-91, DOI: 10.1107/S205698901502397X.
12. A. Kumar, A. R. Chowdhuri, A. Kumari, S. K. Sahu, *Mater. Sci. Eng. C* **2018**, *92, 913-921,* DOI: 10.1016/j.msec.2018.07.039.
13. M. Dramićanin, in *Luminescence Thermometry*, **2018**.
14. F. Luo, S. R. Batten, *Dalton Trans.* **2010**, *39*, 4485-4488, DOI: 10.1039/c002822n.
15. X. Wei, G. Zhao, P. Feng, Y. Kou, Y. Tang, *ACS. Appl. Nano Mater.* **2022**, *5*, 1161-1168, DOI: 10.1021/acsanm.1c03751.
16. Y. G. Sun, X. F. Gu, F. Ding, P. F. Smet, E. J. Gao, D. Poelman, F. Verpoort, *Cryst. Growth Des.* 2010, *10*, 1059–1067, DOI 10.1021/cg900299v.
17. Q. Zhou, L. Dolgov, A. M. Srivastava, L. Zhou, Z. Wang, J. Shi, M. D. Dramićanin, M. G. Brik, M. Wu, *J. Mater. Chem. C* 2018, *6*, 2652–2671, DOI: **https://doi.org/10.1039/C8TC00251G.**
18. A. V. Artemev, M. P. Davydova, A. S. Berezin, V. K. Brel, V. P. Morgalyuk, I. Y. Bagryanskaya, D. G. Samsonenko, *Dalton Trans.* **2019**, *48*, 16448–16456.
19. R. Haldar, A. Ghosh, T. K. Maji, *Chemical Communications* 2023, *59*, 1569–1588.
20. F. Juliá, *Chem. Cat. Chem.* **2022**, *14*, DOI 10.1002/cctc.202200916, DOI: **https://doi.org/10.1039/C9DT03283E**
21. F. A. Cotton, D. M. L. Goodgame, M. Goodgame, *J. Am. Chem. Soc.* **1962**, *84*, 167-172, DOI 10.1021/ja00861a008.
22. M. Wrighton, D. Ginley, *Chem. Phys.* 1974, *4*, 295-299, DOI: 10.1016/0301-0104(74)80097-2.
23. P. Tao, S. J. Liu, W. Y. Wong, *Adv. Opt. Mater.* 2020, *8*, DOI: 10.1002/adom.202000985.
24. F. Zhang, H. Yao, T. Chu, G. Zhang, Y. Wang, Y. Yang, *Chem. Eur. J.* **2017**, *23*, 10293-10300, DOI: 10.1002/chem.201701852.
25. S. Dai, Y. Liu, Y. Mei, J. Hu, K. Wang, Y. Li, N. Jin, X. Wang, H. Luo, W. Li, *Dalton Trans.* **2022**, *51*, 15446-15457, DOI: 10.1039/d2dt01837c.
26. S. W. Lv, J. M. Liu, N. Zhao, C. Y. Li, Z. H. Wang, S. Wang, *New J. Chem.* **2020**, *44*, 1245-1252, DOI: 10.1039/c9nj05503g.
27. L. Zhang, X. Xin, Y. Lu, D. Sun, *Chem. Res. Chin. Univ.* **2018**, *34*, 175-179 DOI 10.1007/s40242-018-7248-5.
28. M. C. Biesingera, B. P. Payne, A. P. Grosvenord, L. W. M. Lau, A. R. Gerson and R. S. C. Smart, *Appl. Surf. Sci*. **2011**, 257, 2717-2730, DOI: 10.1016/j.apsusc.2010.10.051

29. H. Nohira, W.Tsai, W. Besling, E. Young, J. Petry, T. Conrad, W. Vandervorst, S. De Gendt, M. Heyns, J. Maes, M. Tuominen, *J. Non-Cryst. Solids*, **2002**, 303, 83–87, DOI: 10.1016/S0022-3093(02)00970-5.
30. C.D. Wagner, A.V. Naumkin, A. Kraut-Vass, J.W. Allison, C.J. Powell, J.R.Jr. Rumble, NIST Standard Reference Database 20, Version 3.4.
31. A. Trenczek-Zajac, M. Radecka, K. Zakrzewska, A. Brudnik, E. Kusior, S. Bourgeois, M. C. M. De Lucas, L. Imhoff, *J. Power Sources* **2009**, *194*, 93–103, DOI: https://doi.org/10.1016/j.jpowsour.2008.12.112.
32. Y. Cheng, T. Huang, C. Liu, S. Zhang, *Chem. Eng. Sci*. **2019**, 371, 88-95, DOI: https://doi.org/10.1016/j.cej.2019.03.252.
33. S. Luo, L. Duan, B. Sun, M. Wei, X. Li, A. Xu, *Appl. Catal*. **2015**, 164, 92-99, DOI: https://doi.org/10.1016/j.apcatb.2014.09.008.
34. P.P.K. Agarwal, D. Jensen, C. Chen, R.M. Rioux, T. Matsoukas, *Appl. Energy Mater.* **2022**, 5, 6716-6723, DOI: https://doi.org/10.1021/acsaem.2c00312.
35. Zhang, M.-L.; Zhai, Z.-M.; Yang, X.-G.; Huang, Y.-D.; Zheng, Y.-J.; Ma, L.-F, *Front.* **2020**, *8*, DOI: 10.3389/fchem.2020.593948.
36. Yuster, P.; Weissman, S. I, *J. Chem. Phys.* **2004**, *17* (12), 1182-1188. DOI: 10.1063/1.1747140.
37. Liu, S.; Fang, X.; Lu, B.; Yan, D.. *Nat. Commun.* **2020**, *11* (1), 4649, DOI: 10.1038/s41467-020-18482-w.
38. Tobita, S.; Arakawa, M.; Tanaka, I, *J. Phys. Chem.* **1985**, *89* (26), 5649-5654, DOI: 10.1021/j100272a015.
39. Boustead, I, *Eur. Polym. J.* **1970**, *6* (5), 731-741, DOI: https://doi.org/10.1016/0014-3057(70)90023-6.
40. Huang, H.; Bu, Y, *J. Phys. Chem. C* **2019**, *123* (46), 28327-28335, DOI:10.1021/acs.jpcc.9b05453.
41. in An Introduction to the Optical Spectroscopy of Inorganic Solids, **2005**, pp. 151-197.
42. Yang, X.; Yan, D, *J. Mater. Chem. C* **2017**, *5* (31), 7898-7903, DOI: 10.1039/C7TC02493B.
43. V. Villemot, M. Hamel, R. B. Pansu, I. Leray, G. H. V. Bertrand, *RSC. Adv.* **2020**, *10*, 18418–18422, DOI: **https://doi.org/10.1039/D0RA02509G**.

Supporting Information:

Synthesis of isoretecular Metal-organic Framework-5 (MOF-5): [43]

Using the procedure developed by Villemot, Zinc nitrate hexahydrate (0.68 g, 2.3 mmol) and 1,4-Benzenedicarboxylic acid (100 mg, 0.6 mmol) were each dissolved in 5ml Diethylformamide (DEF). After the combination of solutions, an extra 5 ml of DEF were added to reach a final 15 ml volume. The mixture was sealed in a tube and allowed to sonicate for 10 min until completely dissolved. With slow heating and cooling ramps, the tube was then heated at 75°C in a convection oven for 168 h. The resulting crystals were collected and washed with dry Dimethylformamide (DMF) for 3 days changing the DMF every 24 h. The crystals were stored in DMF until the day of measurement and then dried supercriticaly.

IR: 1575 (v C=O Stretching (MOF ligand),1690 (v C=O Stretching (free Ligand), 3436 (v O-H stretching)

The synthesis of Mnmodified Isoreticular metal-organic framework-5 (MOF-5):

Zinc nitrate hexahydrate (2.3 mmol, 0.68 mg) and 1,4-Benzenedicarboxylic acid (0.6 mmol, 100 mg) were each dissolved in 5ml Diethylformamide (DEF). After the combination of the solutions, an extra 5 ml of DEF were added to reach a final 15 ml volume. The mixture was sealed in a tube and allowed to sonicate for 10 min until completely dissolved. With slow heating and cooling ramps (5h each), the tube was then heated at 75°C in a convection oven for 168 h. The resulting crystals were collected and shaken in a concentrated solution of Mn(NO3)2·4H2O (the crystals and the solution should be protected from light with an Aluminium foil). After two days the crystals were washed with dry DMF 3 times and dried super-critically before measurement. IR: 671 (v Mn-O), 1575 (v C=O Stretching (MOF ligand),1690 (v C=O Stretching (free Ligand), 3436 (v O-H stretching)

Fourier transform infrared spectroscopy and X-ray diffraction:

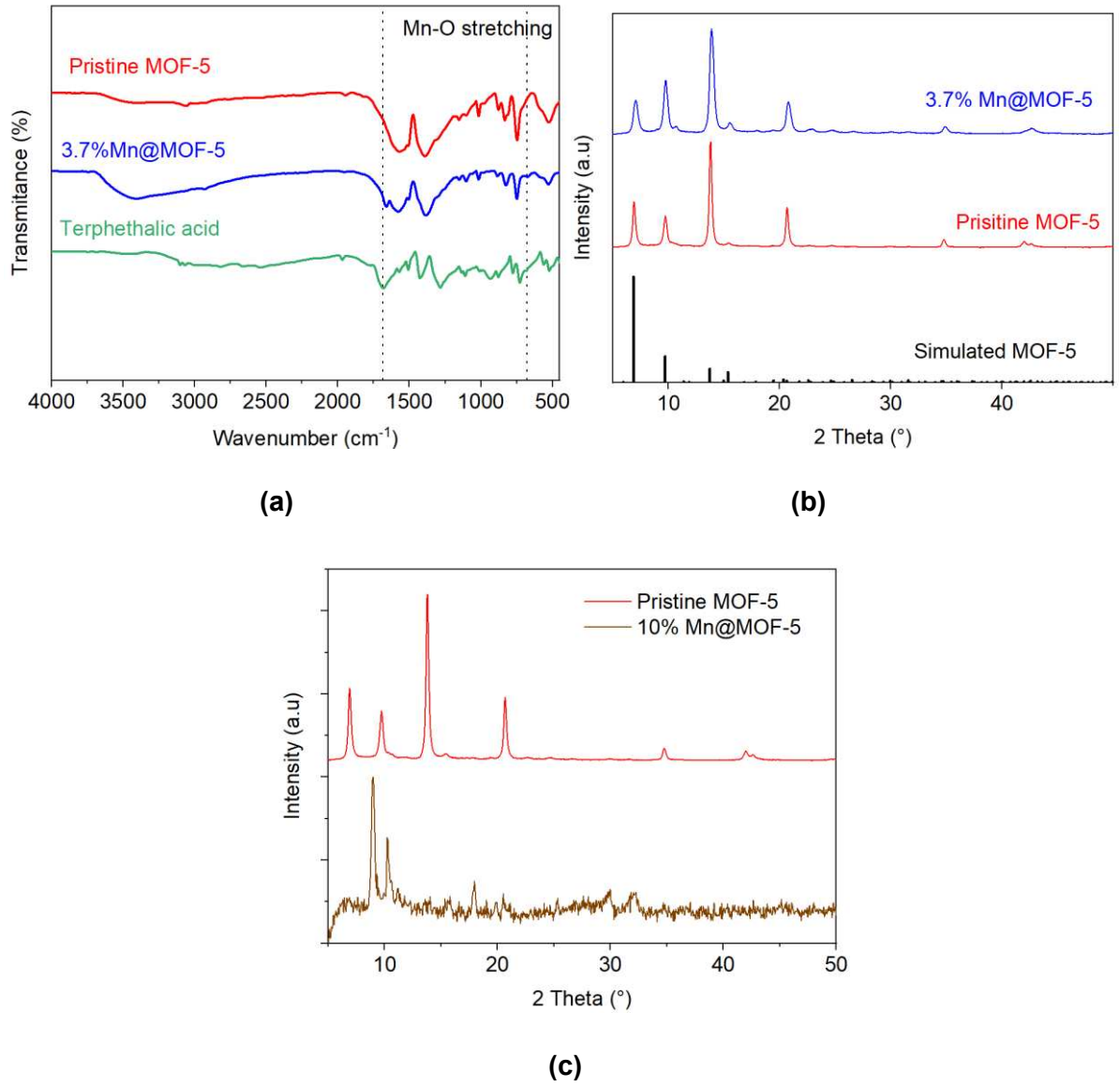

Figure S1: (a) IR spectrums of pristine MOF-5 and the modified sample, (b) PXRD pattern of the pristine MOF-5 and the modified samples, (c) comparison between pristine MOf-5 and the heavily modified MOF-5.

A new band appears at 675 cm^{-1} in Mn@MOF-5, which correlates with the Mn–O bond stretch. Additionally, a shift in the C=O stretching vibration in terephthalic acid from 1685 cm^{-1} to 1571 cm^{-1} aligns with the coordination within the MOF framework. For the 3.7% Mn@MOF-5 sample, most diffraction peaks align with those of the simulated pattern. However, the (4 0 0) reflection at 2θ =14° shows a slight shift, suggesting a lattice change. This shift is likely due to minor strain in the crystal structure caused by differences in the ionic radii of the metals incorporated into the MOF. Additionally, defect formation may contribute to these lattice shifts by locally distorting the crystal structure.

Thermogravimetric analysis:

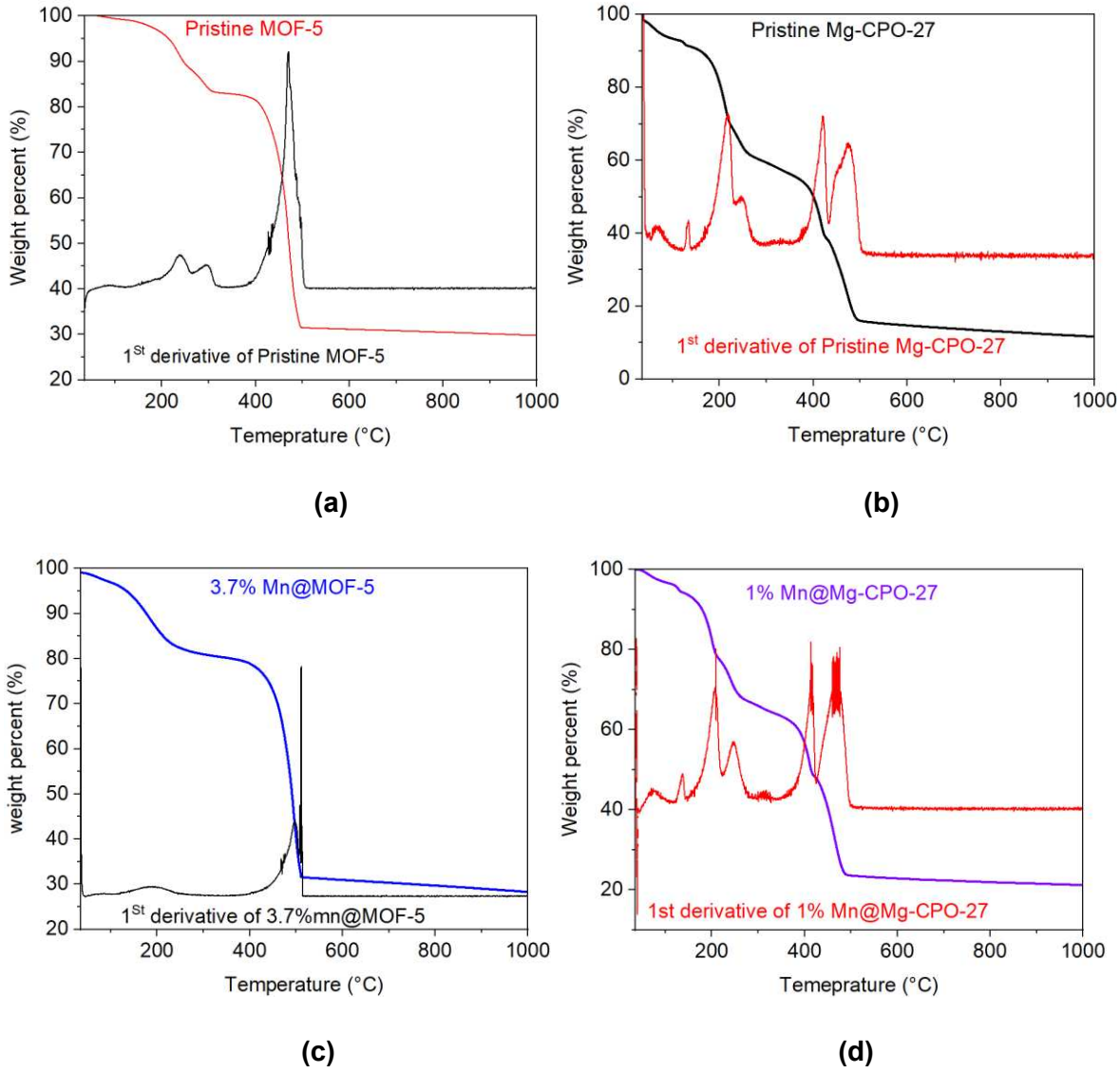

Figure S2: TGA diagrams of (a): pristine MOF-5, (b): pristine Mg-CPO-27, (c): 3.7%Mn@MOF-5, (d): 1%Mn@Mg-CPO-27.

X-ray photoelectron spectroscopy:

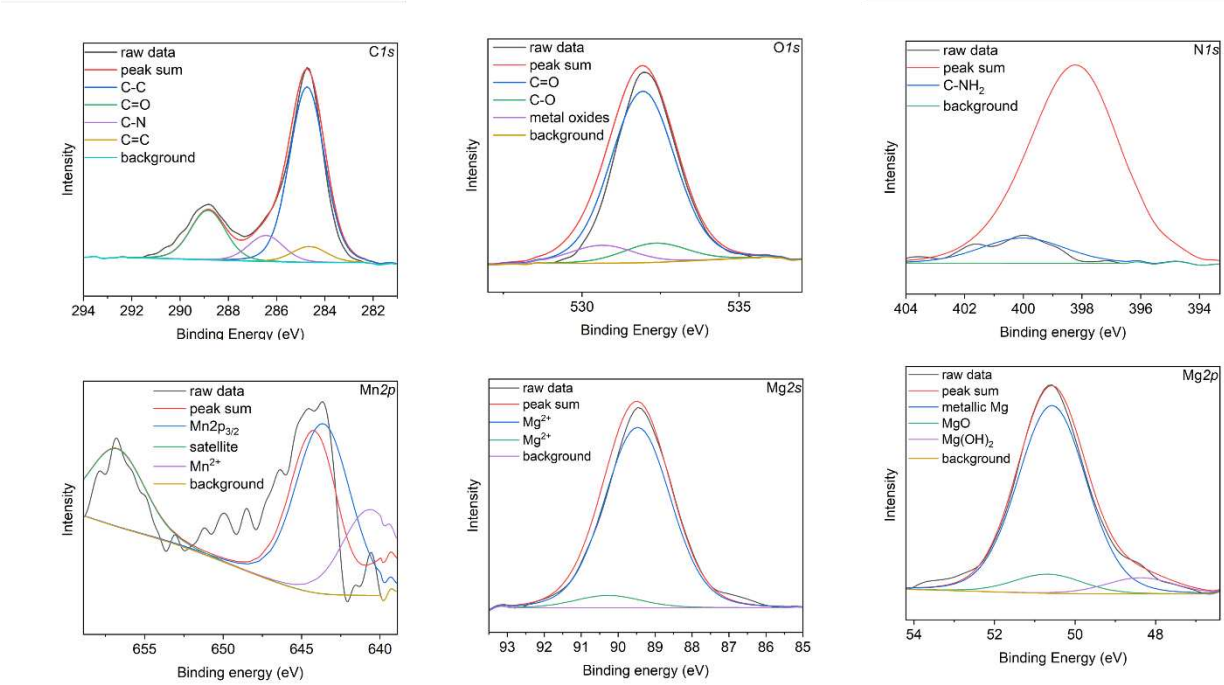

Figure S3: High resolution X-ray photoelectron spectra of C 1s, O 1s N 1s, Mn 2p, Mg 2sand Mg 2p of CPO-27.

Table S1: XPS peak types and corresponding binding energies of carbon in CPO-27.

Element	Characteristic peak	C=C (eV)	C-C (eV)	C-N (eV)	C=O (eV)
C	C *1s*	284.6	284.8	286.4	288.8

Table S2: XPS peak types and corresponding binding energies of oxygen in CPO-27.

Element	Characteristic peak	Metal oxides (eV)	C=O (eV)	C-O (eV)
O	O *1s*	530.5	531.9	532.3

Table S3: XPS peak types and corresponding binding energy of nitrogen in CPO-27.

Element	Characteristic peak	$C\text{-}NH_2$ (eV)
N	N *1s*	400.0

Table S4: XPS peak types and corresponding binding energies of manganese in CPO-27.

Element	Characteristic peak	$Mn2p_{3/2}$(eV)	Satellite peak(eV)	Mn^{2+} (eV)
Mn	Mn *2p*	640.6	656.8	643.6

Table S5: XPS peak types and corresponding binding energies of magnesium in CPO-27.

Element	Characteristic peak	Mg^{2+} (eV)	Mg^{2+} (eV)
Mg	Mg *2s*	89.5	90.4

Table S6: XPS peak types and corresponding binding energies of magnesium in CPO-27.

Element	Characteristic peak	Metallic Mg(eV)	MgO (eV)	$Mg(OH)_2$ (eV)
Mg	Mg *2p*	350.3	352.0	353.9

N_2 adsorption analysis:

The Brunauer-Emmett-Teller (BET) surface area was measured via N_2 adsorption. Pristine MOF-5 exhibits a type I isotherm, indicative of a microporous structure consistent with literature. In the 3.7% Mn@MOF-5, the isotherm also displays type I characteristics but with increased adsorption at higher relative pressures. Notably, a H2(a)-type hysteresis loop appears in the Modified sample, suggesting a wider cavity size distribution than neck size. Surface area measurements align with expectations, with pristine MOF-5 showing a significantly higher surface area (4169 $m^2 g^{-1}$) and total pore volume of 1.47 $cm^3 g^{-1}$, while the Mn@MOF displays a reduced surface area of 662 $m^2 g^{-1}$ and pore volume of 0.45 $cm^3 g^{-1}$.

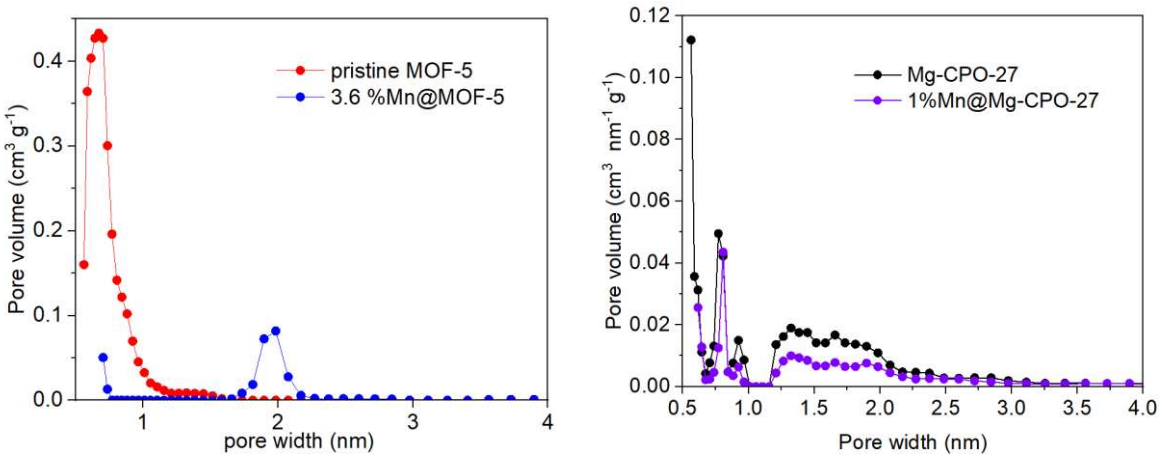

(a) (b)

Figure S4: Pore size distribution of the samples pristine vs modified (a) MOF-5, (b) Mg-CPO-27.

Excitation and emission spectra:

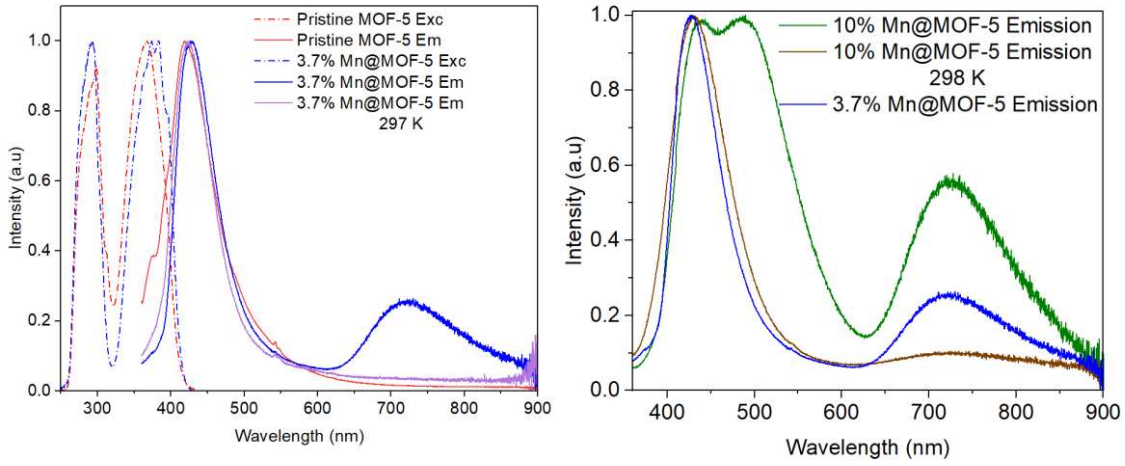

(a) **(b)**

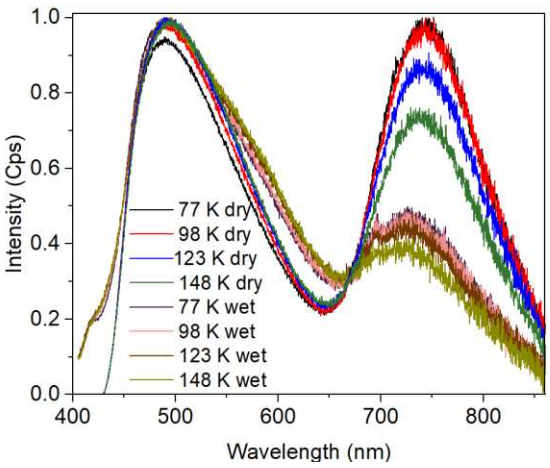

(c)

Figure S5: (a) Pristine MOF-5 and 3.7%Mn@MOF-5 emission and excitation comparison at 77 K and at 297 K with Λ_{Exc} = 345 nm, Λ_{Em} =445 nm, (b) emission and excitation comparison at 77 K and at 297 K between 10%Mn@MOF-5 and 3.7%Mn@MOF-5, (c) emission comparison between different temperatures.

the spectrum of this higher Mn wt% sample revealed the emergence of a new band at approximately 488 nm, which was entirely absent in all previously studied samples. The appearance of this band indicates that higher Mn levels may introduce new electronic transitions or interactions within the framework, potentially altering the photophysical properties of the material.

The comparison between the activated and not activated samples show a stark difference in the intensity of the $^4T_1$ to $^6S_1$ transition, showing the effect of the solvent molecules trapped inside the grid of the MOF, leading to a connection between surface area and the intensity of the emission.

Life times decay plots and the fitting:

This fitting and the parametrs resulting from which can lead us to the estimate the duration of the emission in question.

The estimation of the average life time if the emission is done using the equation :

$$(A_1*t_1 + A_2*t_2 + A_3*t_3)/(A_1+ A_2 + A_3) \quad (2)$$

The parameters A_1,A_2,A_3,t_1,t_2 and t_3 are taken respectively from fits below and plugged into the eqution..The best model that was found was the Kohlrasuch-Williams-Watt model following the equation:

$$Y = A_1*\exp(-x/t_1) + A_2*\exp(-x/t_2) + A_3*\exp(-(x/t_3)^b) \quad (3)$$

Where:

A_1, A_2 and A_3 are the amplitudes of the components

t_1,t_2 and t_3 are the times of comonents

and b is the exponential stretching constant.

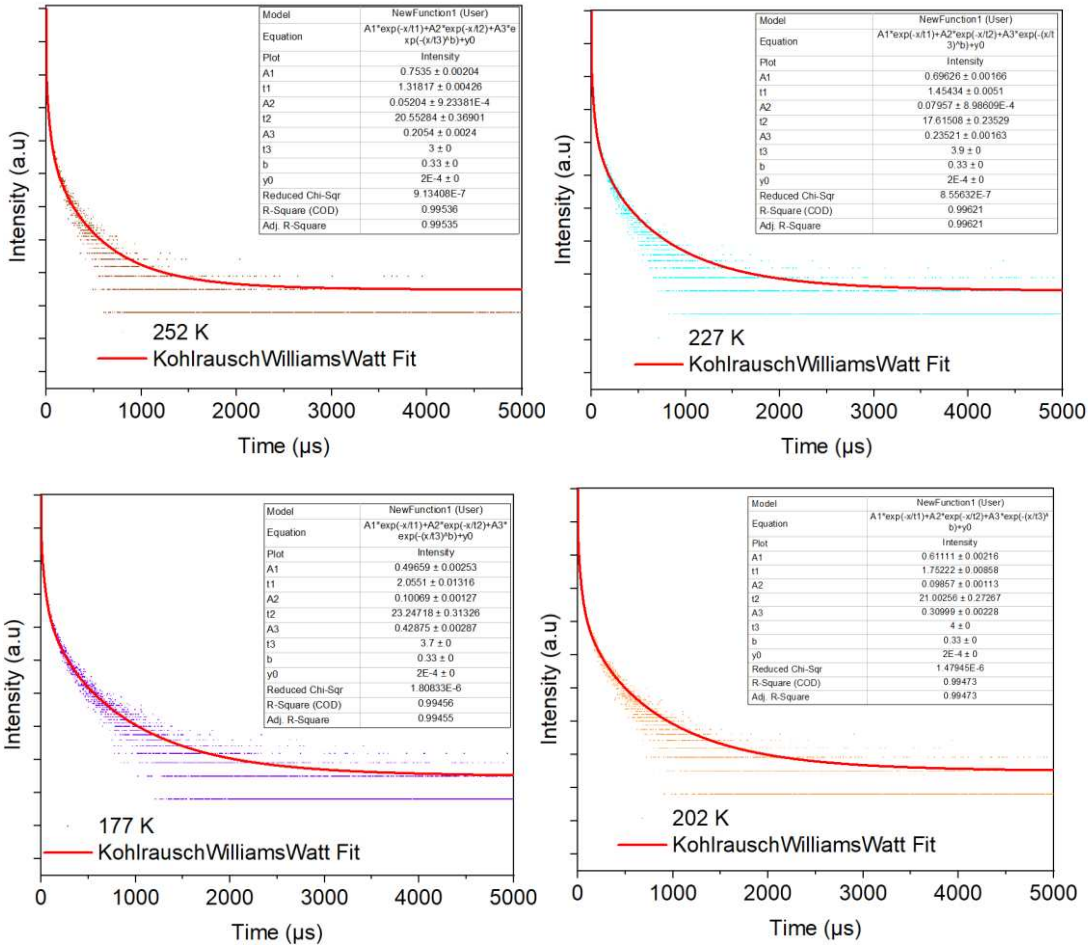

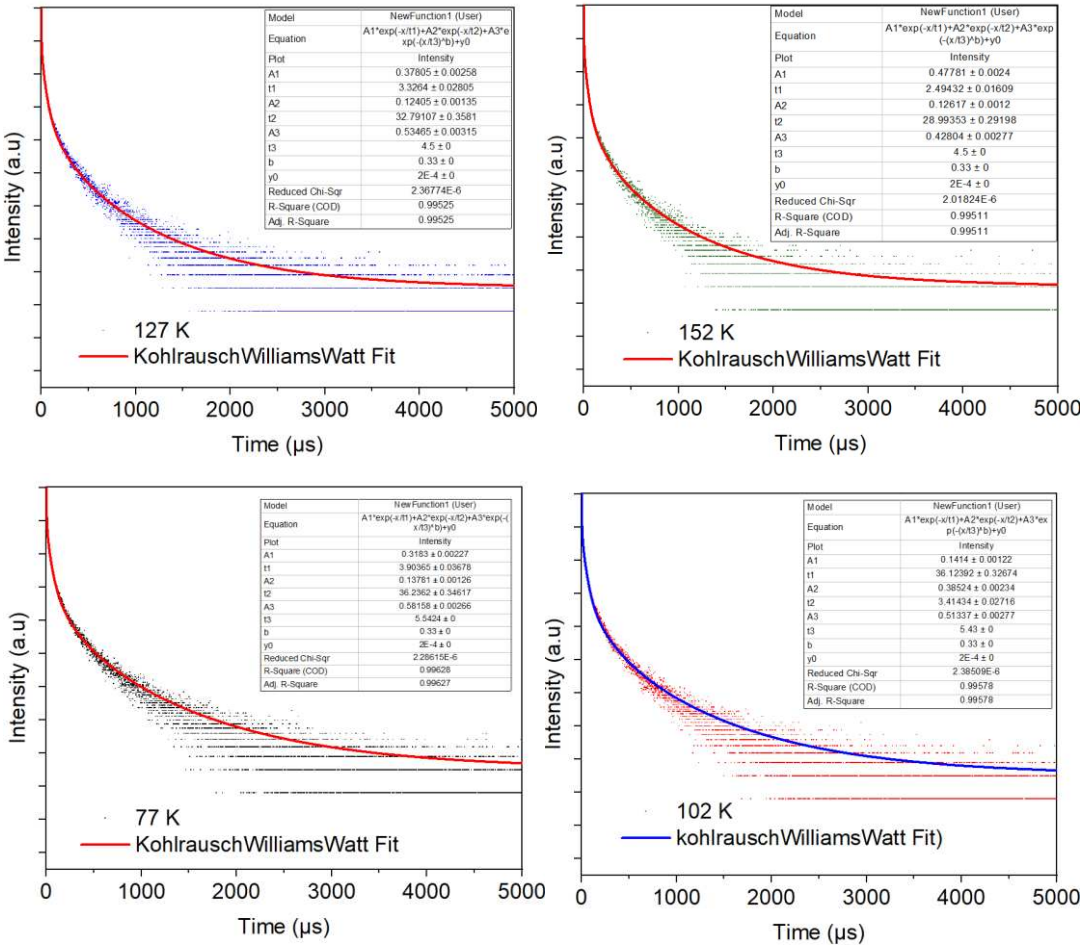

Figure S6: Life-time parameters using Kohlrausch-Williams-Watt fitting model at increasing temperature.

Table S7: Summary of lifetimes of sample 1%Mn@Mg-CPO-27 at different temperatures:

Temperature [K]	Average life time [μs]
77	9.116
102	8.856
127	7.457
152	6.565
177	4.822
202	4.296
227	3.295
252	2.650

Adding paramagnetic metals to MOF-5:

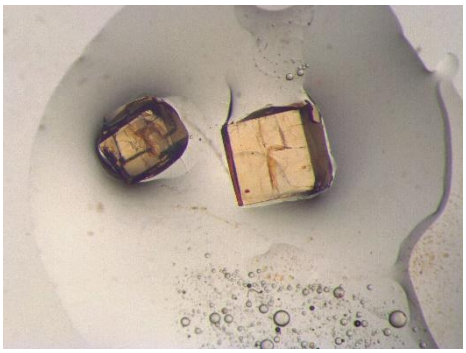

(a)

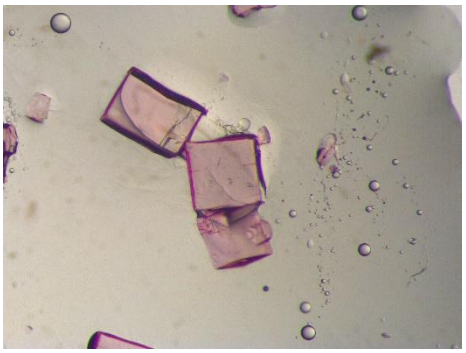

(b)

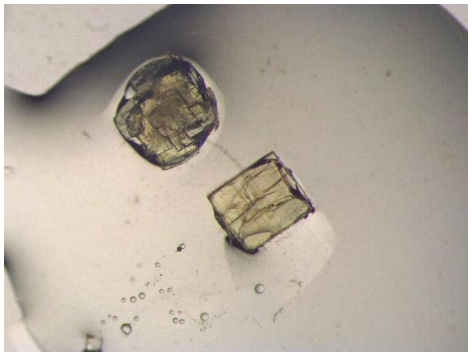

(c)

Figure S7: Image above (a) Iron, image above (b) Cobalt and image under (c) Nickel.

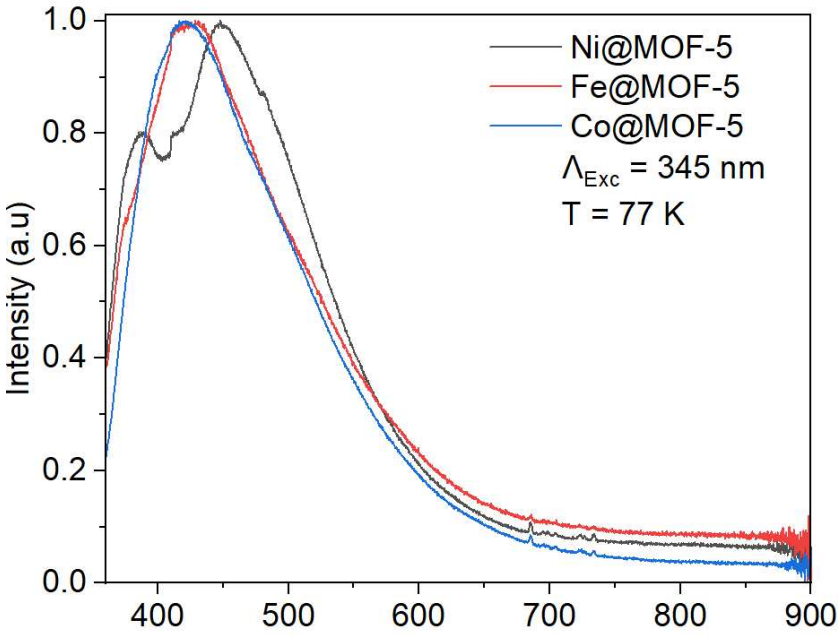

Figure S8: emission spectra of MOF-5 modified with Ni, Fe and Co at 77 K with Λ_{Exc} = 345 nm.

Scanning electron microscopy (SEM) and The Energy Dispersive X-ray mapping (EDX):

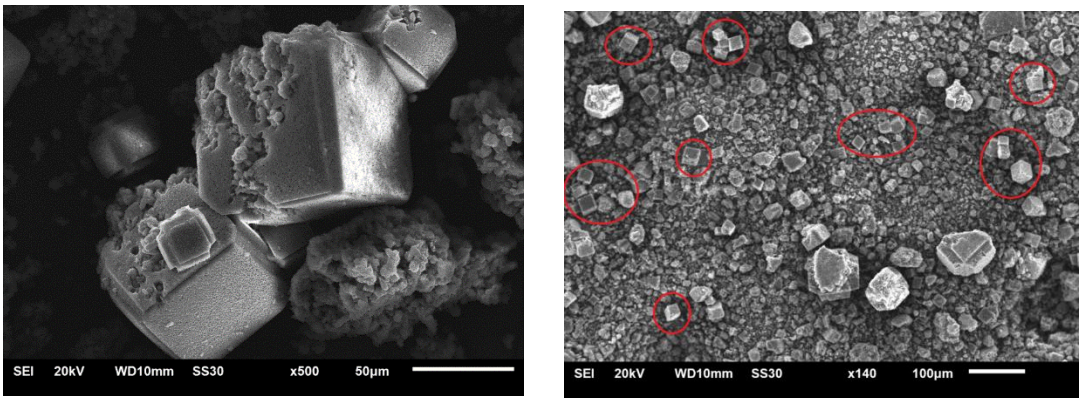

(a) (b)

Figure S9: (a) Mg-CPO-27, (b) 1%Mn@Mg-CPO-27

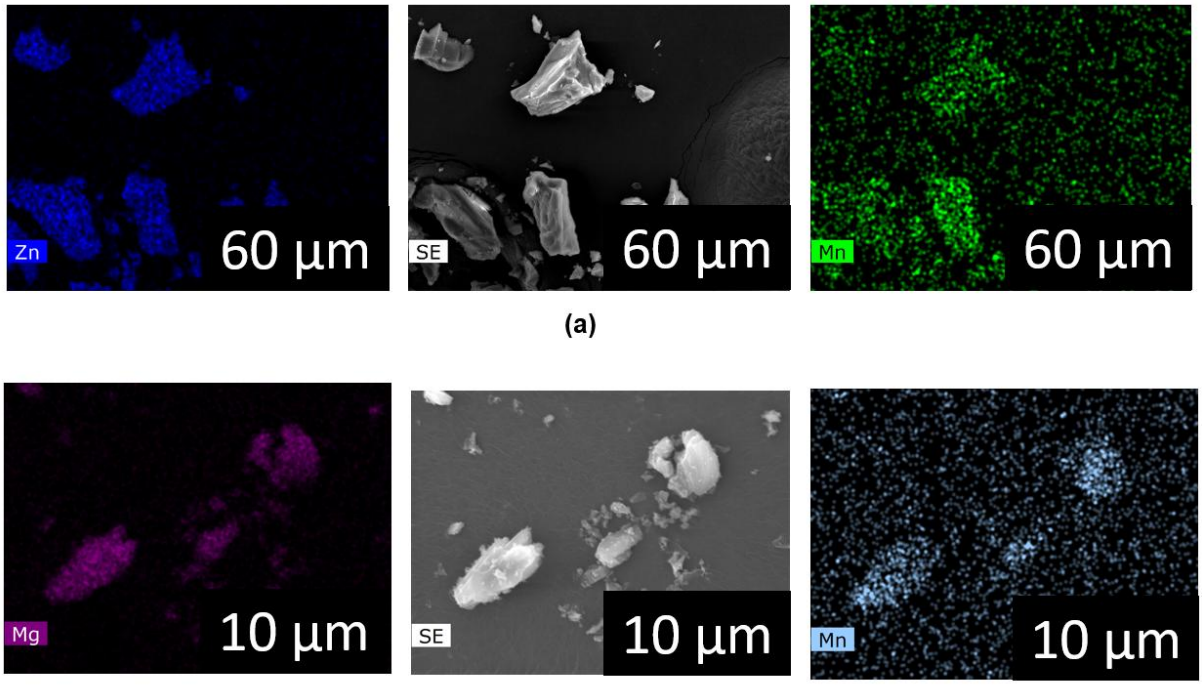

(a)

(b)

Figure S10: (a) EDX mapping of the sample 3.7% Mn@MOF-5, (b) 1%Mn@Mg-CPO-27

4. Conclusion:

This dissertation has explored the synthesis, structural design, and photophysical behavior of luminescent porous materials—specifically metal–organic frameworks (MOFs) and covalent triazine frameworks (CTFs)—with an emphasis on their potential in sensing and functional applications. Through the integration of luminescent chromophores and strategic framework engineering, this work provides deeper insight into the interplay between porosity, structure, and optical performance. The aluminum-based MOF Al-BP-Naph was successfully synthesized and characterized as a luminescent sensor for Fe^{3+} ions. Its naphthylamino-functionalized linker endowed the material with strong intrinsic photoluminescence, high surface area, and excellent selectivity toward Fe^{3+} through a rapid fluorescence quenching mechanism. The quenching effect was attributed to a competitive absorption process rather than static or dynamic quenching, enabling sensitive detection down to micromolar concentrations. The low detection limit and short response time highlight Al-BP-Naph as a highly efficient and practical luminescent probe for iron sensing in liquid media. Furthermore, the incorporation of thermally activated delayed fluorescence (TADF) emitters into covalent triazine frameworks demonstrated the capacity of CTFs to act as robust, porous hosts for advanced adsorptive behaviour. Their high surface area, tunable porosity, and stability enabled the investigation of structure–property relationships in CO_2/CH_4 adsorption and separation. The study of isosteric heats of adsorption and IAST selectivity provided valuable insight into the adsorption behavior of these frameworks, confirming their versatility for both photophysical and gas sorption applications. Although preliminary, the exploration of Mn-doped Mg-CPO-27 revealed the potential of transition-metal modification to induce phosphorescence in MOFs. The observed temperature-dependent emission intensity and lifetime variations suggest that these systems may serve as promising candidates for luminescent thermometry upon further optimization.

Collectively, these findings underscore the importance of structural tunability in governing the optical and functional properties of porous materials. By coupling luminescent linkers, framework rigidity, and controlled porosity, it is possible to design materials that exhibit high selectivity, stability, and sensitivity across multiple application domains—from chemical sensing and environmental monitoring to energy conversion and optical devices. Future work should focus on enhancing the crystallinity of CTFs, exploring multivariate MOF systems for ratiometric sensing, and extending phosphorescence-based studies toward hybrid organic–inorganic materials with prolonged afterglow emission. The continued convergence of framework chemistry and photophysics will undoubtedly lead to the next generation of multifunctional porous materials, bridging the gap between fundamental design principles and real-world applications.

5. References:

[1] I. Khan, A. Altaf, S. Sadiq, S. Khan, A. Khan, S. Khan, M. Humayun, A. Khan, R. A. Abumousa, M. Bououdina, “Towards sustainable solutions: Comprehensive review of advanced porous materials for CO_2 capture, hydrogen generation, pollutant degradation, and energy application” *Chemical Engineering Journal Advances* **2025**, *21*, 100691.

[2] V. Sharma, A. Agrawal, O. Singh, R. Goyal, B. Sarkar, N. Gopinathan, S. P. Gumfekar, “A comprehensive review on the synthesis techniques of porous materials for gas separation and catalysis” *Can J Chem Eng* **2022**, *100*, 2653–2681.

[3] M. Thommes, K. Kaneko, A. V. Neimark, J. P. Olivier, F. Rodriguez-Reinoso, J. Rouquerol, K. S. W. Sing, “Physisorption of gases, with special reference to the evaluation of surface area and pore size distribution (IUPAC Technical Report)” *Pure and Applied Chemistry* **2015**, *87*, 1051–1069.

[4] A. Rabbani, A. M. Fernando, R. Shams, A. Singh, P. Mostaghimi, M. Babaei, “Review of Data Science Trends and Issues in Porous Media Research With a Focus on Image-Based Techniques” *Water Resour Res* **2021**, *57*, DOI 10.1029/2020WR029472.

[5] S. Hou, S. Jin, B. Tan, “Fine-tuning structural porosity and methane storage capacity of hyper-cross-linked polymers via aromatic external cross-linkers” *Sep Purif Technol* **2025**, *363*, 132168.

[6] S. Sun, H. Sun, P. T. Williams, C. Wu, “Recent advances in integrated CO_2 capture and utilization: a review” *Sustain Energy Fuels* **2021**, *5*, 4546–4559.

[7] A. Memetova, I. Tyagi, R. R. Karri, V. Kumar, K. Tyagi, Suhas, N. Memetov, A. Zelenin, T. Pasko, A. Gerasimova, D. Tarov, M. H. Dehghani, K. Singh, “Porous carbon-based material as a sustainable alternative for the storage of natural gas (methane) and biogas (biomethane): A review” *Chemical Engineering Journal* **2022**, *446*, 137373.

[8] P. Ndlovu, S. Babaee, P. Naidoo, “Review on CH4-CO2 replacement for CO2 sequestration and CH4/CO2 hydrate formation in porous media” *Fuel* **2022**, *320*, 123795.

[9] S. S. Hoseini, A. Seyedkanani, G. Najafi, A. P. Sasmito, A. Akbarzadeh, “Multiscale architected porous materials for renewable energy conversion and storage” *Energy Storage Mater* **2023**, *59*, 102768.

[10] M. Wang, W. Ou, Z. Yu, “Porous Silicon-Supported Catalytic Materials for Energy Conversion and Storage” *ChemSusChem* **2025**, *18*, DOI 10.1002/cssc.202401459.

[11] D. Dimbo, M. Abewaa, E. Adino, A. Mengistu, T. Takele, A. Oro, M. Rangaraju, “Methylene blue adsorption from aqueous solution using activated carbon of spathodea campanulata” *Results in Engineering* **2024**, *21*, 101910.

[12] N. Hoc Thang, D. Sy Khang, T. Duy Hai, D. Thi Nga, P. Dinh Tuan, “Methylene blue adsorption mechanism of activated carbon synthesised from cashew nut shells” *RSC Adv* **2021**, *11*, 26563–26570.

[13] Y. Ettahiri, A. Bouddouch, B. Akhsassi, A. Khali, L. Bouna, A. Benlhachemi, L. Pérez-Villarejo, “Optimized porous alkali-activated material for superior dye removal: synthesis and performance analysis” *Mater Adv* **2025**, *6*, 2435–2447.

[14] C.-P. Hou, Q. Wang, Q. Liu, Z.-G. Li, C.-L. Ke, X.-F. Wang, K. Huang, “Review: Development and application of porous materials to antibiotic drug adsorption and removal” *Journal of Water Process Engineering* **2025**, *69*, 106583.

[15] J. Letwaba, U. O. Uyor, M. L. Mavhungu, N. O. Achuka, P. A. Popoola, “A review on MOFs synthesis and effect of their structural characteristics for hydrogen adsorption” *RSC Adv* **2024**, *14*, 14233–14253.

[16] E. R. Engel, J. L. Scott, “Advances in the green chemistry of coordination polymer materials” *Green Chemistry* **2020**, *22*, 3693–3715.

[17] S. Liu, P. Zhang, J. Fu, C. Wei, G. Cai, “A Mini-Review: Pyridyl-Based Coordination Polymers for Energy Efficient Electrochromic Application” *Front Energy Res* **2021**, *9*, DOI 10.3389/fenrg.2021.620203.

[18] T. Fu, H. Liu, X. Wang, Y. Liu, “Fine tuning of pore size in metal–organic frameworks for superior removal of U(<scp>vi</scp>) from aqueous solution” *New Journal of Chemistry* **2024**, *48*, 6211–6220.

[19] W. Fan, X. Wang, X. Zhang, X. Liu, Y. Wang, Z. Kang, F. Dai, B. Xu, R. Wang, D. Sun, “Fine-Tuning the Pore Environment of the Microporous Cu-MOF for High Propylene Storage and Efficient Separation of Light Hydrocarbons” *ACS Cent Sci* **2019**, *5*, 1261–1268.

[20] A. K. Yadav, A. Gładysiak, A.-Y. Song, L. Gan, C. R. Simons, N. M. Alghoraibi, A. H. Alahmed, M. Younes, J. A. Reimer, H. Huang, J. G. Planas, K. C. Stylianou, “Sequential Pore Functionalization in MOFs for Enhanced Carbon Dioxide Capture” *JACS Au* **2024**, *4*, 4833–4843.

[21] Y. Li, G. Wen, J. Li, Q. Li, H. Zhang, B. Tao, J. Zhang, “Synthesis and shaping of metal–organic frameworks: a review” *Chemical Communications* **2022**, *58*, 11488–11506.

[22] S. Ma, H.-C. Zhou, “Gas storage in porous metal–organic frameworks for clean energy applications” *Chem. Commun.* **2010**, *46*, 44–53.

[23] H. Furukawa, K. E. Cordova, M. O’Keeffe, O. M. Yaghi, “The Chemistry and Applications of Metal-Organic Frameworks” *Science (1979)* **2013**, *341*, DOI 10.1126/science.1230444.

[24] B. Han, A. Chakraborty, “Ligand extension of aluminum fumarate metal-organic framework in transferring higher water for adsorption desalination” *Desalination* **2024**, *592*, 118135.

[25] S. K. Das, K. Bhunia, A. Mallick, A. Pradhan, D. Pradhan, A. Bhaumik, “A new electrochemically responsive 2D π-conjugated covalent organic framework as a high performance supercapacitor” *Microporous and Mesoporous Materials* **2018**, *266*, 109–116.

[26] Z. Mai, D. Liu, “Synthesis and Applications of Isoreticular Metal–Organic Frameworks IRMOFs-*n* (*n* = 1, 3, 6, 8)” *Cryst Growth Des* **2019**, *19*, 7439–7462.

[27] H. Li, M. Eddaoudi, M. O’Keeffe, O. M. Yaghi, “Design and synthesis of an exceptionally stable and highly porous metal-organic framework” *Nature* **1999**, *402*, 276–279.

[28] Z. Li, D. Zhan, A. Saeed, N. Zhao, J. Wang, W. Xu, J. Liu, “Fluoride sensing performance of fluorescent NH_2-MIL-53(Al): 2D nanosheets *vs.* 3D bulk” *Dalton Transactions* **2021**, *50*, 8540–8548.

[29] L. Zhang, J. Wang, T. Du, W. Zhang, W. Zhu, C. Yang, T. Yue, J. Sun, T. Li, J. Wang, “NH_2-MIL-53(Al) Metal–Organic Framework as the Smart Platform for Simultaneous High-Performance Detection and Removal of Hg^{2+}” *Inorg Chem* **2019**, *58*, 12573–12581.

[30] W. Fan, K.-Y. Wang, C. Welton, L. Feng, X. Wang, X. Liu, Y. Li, Z. Kang, H.-C. Zhou, R. Wang, D. Sun, “Aluminum metal–organic frameworks: From structures to applications” *Coord Chem Rev* **2023**, *489*, 215175.

[31] E. Pérez-Botella, S. Valencia, F. Rey, “Zeolites in Adsorption Processes: State of the Art and Future Prospects” *Chem Rev* **2022**, *122*, 17647–17695.

[32] R. Kumar Mishra, B. Singh, B. Acharya, “A comprehensive review on activated carbon from pyrolysis of lignocellulosic biomass: An application for energy and the environment” *Carbon Resources Conversion* **2024**, *7*, 100228.

[33] R. Fatima, P. Katiyar, K. Kushwaha, “Recent advances in mesoporous silica nanoparticle: synthesis, drug loading, release mechanisms, and diverse applications” *Frontiers in Nanotechnology* **2025**, *7*, DOI 10.3389/fnano.2025.1564188.

[34] J. C. Védrine, “Metal Oxides in Heterogeneous Oxidation Catalysis: State of the Art and Challenges for a More Sustainable World” *ChemSusChem* **2019**, *12*, 577–588.

[35] H. Zhang, I. bin Samsudin, S. Jaenicke, G.-K. Chuah, “Zeolites in catalysis: sustainable synthesis and its impact on properties and applications” *Catal Sci Technol* **2022**, *12*, 6024–6039.

[36] J. L. A. Reed, A. James, T. Carey, N. Fitzgerald, S. Kellet, A. Nearchou, A. L. Farrelly, H. A. H. Fell, P. K. Allan, J. A. Hriljac, “Engineered species-selective ion-exchange in tuneable dual-phase zeolite composites” *Chem Sci* **2024**, *15*, 13699–13711.

[37] C. C. H. Lin, K. A. Dambrowitz, S. M. Kuznicki, “Evolving applications of zeolite molecular sieves” *Can J Chem Eng* **2012**, *90*, 207–216.

[38] M. Sultana, M. H. Rownok, M. Sabrin, M. H. Rahaman, S. M. N. Alam, “A review on experimental chemically modified activated carbon to enhance dye and heavy metals adsorption” *Clean Eng Technol* **2022**, *6*, 100382.

[39] T. Linhares, M. T. Pessoa de Amorim, L. Durães, “Silica aerogel composites with embedded fibres: a review on their preparation, properties and applications” *J Mater Chem A Mater* **2019**, *7*, 22768–22802.

[40] S. S. Tripathy, J.-L. Bersillon, K. Gopal, “Removal of fluoride from drinking water by adsorption onto alum-impregnated activated alumina” *Sep Purif Technol* **2006**, *50*, 310–317.

[41] G. Férey, “Hybrid porous solids: past, present, future” *Chem. Soc. Rev.* **2008**, *37*, 191–214.

[42] H.-C. “Joe” Zhou, S. Kitagawa, “Metal–Organic Frameworks (MOFs)” *Chem. Soc. Rev.* **2014**, *43*, 5415–5418.

[43] D. Fröhlich, E. Pantatosaki, P. D. Kolokathis, K. Markey, H. Reinsch, M. Baumgartner, M. A. van der Veen, D. E. De Vos, N. Stock, G. K. Papadopoulos, S. K. Henninger, C. Janiak, “Water adsorption behaviour of CAU-10-H: a thorough investigation of its structure–property relationships” *J Mater Chem A Mater* **2016**, *4*, 11859–11869.

[44] M. E. Davis, “Ordered porous materials for emerging applications” *Nature* **2002**, *417*, 813–821.

[45] F. Jeremias, D. Fröhlich, C. Janiak, S. K. Henninger, “Water and methanol adsorption on MOFs for cycling heat transformation processes” *New J. Chem.* **2014**, *38*, 1846–1852.

[46] X.-Y. Yang, L.-H. Chen, Y. Li, J. C. Rooke, C. Sanchez, B.-L. Su, “Hierarchically porous materials: synthesis strategies and structure design” *Chem Soc Rev* **2017**, *46*, 481–558.

[47] K. Sumida, D. L. Rogow, J. A. Mason, T. M. McDonald, E. D. Bloch, Z. R. Herm, T.-H. Bae, J. R. Long, “Carbon Dioxide Capture in Metal–Organic Frameworks” *Chem Rev* **2012**, *112*, 724–781.

[48] C. Jansen, N. Assahub, A. Spieß, J. Liang, A. Schmitz, S. Xing, S. Gökpinar, C. Janiak, “The Complexity of Comparative Adsorption of C6 Hydrocarbons (Benzene, Cyclohexane, n-Hexane) at Metal–Organic Frameworks” *Nanomaterials* **2022**, *12*, 3614.

[49] M. Şevik, S. M. Sezdi, E. Kavak, T. A. Arici, M. Arici, “Stable Two-Fold Interpenetrated Cd(II)-MOF for Selective Dye Adsorption and Luminescence Detection of Hydroxyl-Substituted Nitroaromatic Compounds” *Cryst Growth Des* **2023**, *23*, 5163–5172.

[50] Ü. Kökçam-Demir, N. Tannert, M. Bengsch, A. Spieß, C. Schlüsener, S. Nießing, C. Janiak, “Improving porosity and water uptake of aluminum metal-organic frameworks (Al-MOFs) as graphite oxide (GO) composites” *Microporous and Mesoporous Materials* **2021**, *326*, 111352.

[51] L. Shi, K. O. Kirlikovali, Z. Chen, O. K. Farha, “Metal-organic frameworks for water vapor adsorption” *Chem* **2024**, *10*, 484–503.

[52] E. Rahmani, M. Rahmani, “Al-Based MIL-53 Metal Organic Framework (MOF) as the New Catalyst for Friedel–Crafts Alkylation of Benzene” *Ind Eng Chem Res* **2018**, *57*, 169–178.

[53] S. Dai, E. Montero-Lanzuela, A. Tissot, H. G. Baldoví, H. García, S. Navalón, C. Serre, “Room temperature design of Ce(<scp>iv</scp>)-MOFs: from photocatalytic HER and OER to overall water splitting under simulated sunlight irradiation” *Chem Sci* **2023**, *14*, 3451–3461.

[54] Z. Xu, S. Chen, B. Yang, H. Zhou, L. Wang, B. E. Keshta, W. Zhu, Y. Zhang, “Breakthrough developments in Metal-Organic frameworks (MOFs) for efficient C4 hydrocarbon separation” *Chemical Engineering Journal* **2025**, *508*, 160992.

[55] Y. He, W. Zhou, G. Qian, B. Chen, “Methane storage in metal–organic frameworks” *Chem. Soc. Rev.* **2014**, *43*, 5657–5678.

[56] L. Jimenez-Lopez, R. Morales Ospino, L. G. de Araujo, A. Celzard, V. Fierro, “Latest developments in the synthesis of metal–organic frameworks and their hybrids for hydrogen storage” *Nanoscale* **2025**, *17*, 6390–6413.

[57] A. L. Sutton, J. I. Mardel, M. R. Hill, “Metal-Organic Frameworks (MOFs) As Hydrogen Storage Materials At Near-Ambient Temperature” *Chemistry – A European Journal* **2024**, *30*, DOI 10.1002/chem.202400717.

[58] Z. A. Sandhu, M. A. Raza, N. S. Awwad, H. A. Ibrahium, U. Farwa, S. Ashraf, A. Dildar, E. Fatima, S. Ashraf, F. Ali, “Metal–organic frameworks for next-generation energy storage devices; a systematic review” *Mater Adv* **2024**, *5*, 30–50.

[59] W. Wang, D. Chen, F. Li, X. Xiao, Q. Xu, “Metal-organic-framework-based materials as platforms for energy applications” *Chem* **2024**, *10*, 86–133.

[60] W. Ma, Q. Zhang, D. Xiang, K. Mao, J. Xue, Z. Chen, Z. Chen, W. Du, K. Zhai, H. Zhang, “Metal-Organic Framework (MOF)-Based Sensors for Mercury (Hg) Detection: Design Strategies and Recent Progress” *Chemistry – A European Journal* **2025**, *31*, DOI 10.1002/chem.202403760.

[61] L. Liang, Y.-K. Ding, Y. Yin, F.-F. Yang, J. Yang, “Synthesis of an ammelide-based ultra-microporous Cd-MOF for sensitive detection of dichromate ions” *Chemical Communications* **2025**, *61*, 1834–1837.

[62] S. G. Guillen, J. Parres-Gold, A. Ruiz, E. Lucsik, B. Dao, T. K. L. Hang, M. Chang, A. O. Garcia, Y. Wang, F. Tian, “pH-Responsive Metal–Organic Framework Thin Film for Drug Delivery” *Langmuir* **2022**, *38*, 16014–16023.

[63] K. Wu, T. Fei, T. Zhang, “Humidity Sensors Based on Metal–Organic Frameworks” *Nanomaterials* **2022**, *12*, 4208.

[64] M. D. Allendorf, C. A. Bauer, R. K. Bhakta, R. J. T. Houk, “Luminescent metal-organic frameworks” *Chem Soc Rev* **2009**, *38*, 1330–1352.

[65] Q.-Q. Xia, X.-H. Wang, J.-L. Yu, Z.-Y. Xue, J. Chai, M.-X. Wu, X. Liu, “Tunable fluorescence emission based on multi-layered MOF-on-MOF” *Dalton Transactions* **2022**, *51*, 9397–9403.

[66] K. Müller-Buschbaum, F. Beuerle, C. Feldmann, “MOF based luminescence tuning and chemical/physical sensing” *Microporous and Mesoporous Materials* **2015**, *216*, 171–199.

[67] R. Sola-Llano, V. Martínez-Martínez, S. Furukawa, Y. Takashima, I. López-Arbeloa, “Tuning Light Emission towards White Light from a Naphthalenediimide-Based Entangled Metal-Organic Framework by Mixing Aromatic Guest Molecules” *Polymers (Basel)* **2018**, *10*, 188.

[68] Y. Cui, Y. Yue, G. Qian, B. Chen, “Luminescent Functional Metal–Organic Frameworks” *Chem Rev* **2012**, *112*, 1126–1162.

[69] A. J. Calahorro, E. San Sebastián, A. Salinas-Castillo, J. M. Seco, C. Mendicute-Fierro, B. Fernández, A. Rodríguez-Diéguez, “Effect of π–π stacking interactions on the emission properties of cadmium metal–organic frameworks based on 1,4-bis(4-pyridyl)-2,3-diaza-1,3-butadiene” *CrystEngComm* **2015**, *17*, 3659–3666.

[70] K. J. Stawiasz, J. I. Deneff, R. A. Reyes, T. J. Woods, L. E. S. Rohwer, N. Valdez, M. A. Rodriguez, A. Lawal, J. S. Moore, D. F. Sava Gallis, “Improved quantum yield in geometrically constrained tetraphenylethylene-based metal–organic frameworks” *CrystEngComm* **2023**, *25*, 2701–2705.

[71] D. Püschel, S. Hédé, I. Maisuls, S.-P. Höfert, D. Woschko, R. Kühnemuth, S. Felekyan, C. A. M. Seidel, C. Czekelius, O. Weingart, C. A. Strassert, C. Janiak, “Enhanced Solid-State Fluorescence of Flavin Derivatives by Incorporation in the Metal-Organic Frameworks MIL-53(Al) and MOF-5” *Molecules* **2023**, *28*, 2877.

[72] Y. Gao, H. Liu, S. Zhang, Q. Gu, Y. Shen, Y. Ge, B. Yang, “Excimer formation and evolution of excited state properties in discrete dimeric stacking of an anthracene derivative: a computational investigation” *Physical Chemistry Chemical Physics* **2018**, *20*, 12129–12137.

[73] E. V. Fedorenko, N. A. Lyubykh, A. A. Khrebtov, A. Yu. Beloliptsev, A. G. Mirochnik, “Exciplex luminescence of difluoroboron meta- and para-Nitrodibenzoylmethanates in solutions and polymer matrix” *Spectrochim Acta A Mol Biomol Spectrosc* **2023**, *303*, 123193.

[74] K. Nakashima, R. Suizu, S. Morishita, N. Tsurumachi, M. Funahashi, H. Masu, R. Ozawa, K. Nakamura, K. Awaga, “Enhanced Circularly Polarized Luminescence by a Homochiral Guest–Host Interaction in Gyroidal MOFs, [Ru(bpy) $_3$] [M $_2$ (ox) $_3$] (bpy = 2,2′-Bipyridyl, ox = Oxalate, M = Zn, Mn)” *ACS Materials Au* **2023**, *3*, 201–205.

[75] Z.-C. Zhang, Z.-G. Gu, J. Zhang, “Host–Guest Metal–Organic Frameworks-Based Long-Afterglow Luminescence Materials” *Molecules* **2024**, *29*, 2989.

The Al-BP-Naph paper

[77] H. A. Schwartz, M. Atar, M. Spilles, M. Fill, M. Ott, F. R. S. Purtscher, J. M. Gallmetzer, B. Öcal, S. Olthof, A. Griesbeck, K. Meerholz, T. S. Hofer, U. Ruschewitz, “Polarity profiling of porous architectures: solvatochromic dye encapsulation in metal–organic frameworks” *J Mater Chem C Mater* **2024**, *12*, 8759–8776.

[78] Q. Liu, S. Tian, X. Zhao, G. Sankar, “An enhanced fluorescent ZIF-8 film by capturing guest molecules for light-emitting applications” *J Mater Chem C Mater* **2021**, *9*, 5819–5826.

[79] S. Ghosh, A. Das, S. Biswas, “A functionalized UiO-66 MOF acting as a luminescent chemosensor for selective and sensitive turn-on detection of superoxide and acetylacetone” *Microporous and Mesoporous Materials* **2021**, *323*, 111251.

[80] Z. Xiang, C. Fang, S. Leng, D. Cao, “An amino group functionalized metal–organic framework as a luminescent probe for highly selective sensing of Fe3+ ions” *J Mater Chem A Mater* **2014**, *2*, 7662.

[81] S. Kumar, M. Thakur, S. Kumari, S. Sharma, S. S. Kanwar, “Chromium-functionalized metal-organic frameworks as highly sensitive, dual-mode sensors for real time and rapid detection of dopamine” *Talanta* **2025**, *289*, 127771.

[82] J. Chen, T. Guo, H. Gao, H. Meng, Z. Zhang, J. Li, Z. Song, X. Pei, S. Boonyuen, X. Zhang, Y. Jiang, J. Tao, “Mixed-linker Zr-based metal-organic framework as a highly sensitive probe for ultrafast and selective detection of fluoride ions” *Environ Res* **2025**, *276*, 121469.

[83] Z.-X. Lai, A. M. G. Muchlis, R. K. Devi, C.-L. Chiang, Y.-T. Syu, Y.-T. Tsai, C.-C. Lee, C. C. Lin, “Defect Engineering Strategy for Superior Integration of Metal–Organic Framework and Halide Perovskite as a Fluorescence Sensing Material” *ACS Appl Mater Interfaces* **2024**, *16*, 31023–31035.

[84] J. Hu, S. Chen, Z. Liu, J.-R. Li, J.-H. Huang, Z. Jiang, W. Ou, W.-M. Liao, J. Lu, J. He, “MOF-based colorimetric sensor for rapid and visual readout of trace acetylene” *J Mater Chem A Mater* **2023**, *11*, 10577–10583.

[85] Y. Yu, J.-P. Ma, C.-W. Zhao, J. Yang, X.-M. Zhang, Q.-K. Liu, Y.-B. Dong, “Copper(I) Metal–Organic Framework: Visual Sensor for Detecting Small Polar Aliphatic Volatile Organic Compounds” *Inorg Chem* **2015**, *54*, 11590–11592.

[86] G. Nickerl, I. Senkovska, S. Kaskel, “Tetrazine functionalized zirconium MOF as an optical sensor for oxidizing gases” *Chemical Communications* **2015**, *51*, 2280–2282.

[87] J. Zhou, S. H. H. Shokouh, L. Cui, T. Järvinen, O. Pitkänen, Z.-P. Lv, K. Kordas, “An ultra-sensitive NH_3 gas sensor enabled by an ion-in-conjugated polycroconaine/$Ti_3C_2T_x$ core–shell composite” *Nanoscale Horiz* **2023**, *8*, 794–802.

[88] H. C. Wentz, G. Skorupskii, A. B. Bonfim, J. L. Mancuso, C. H. Hendon, E. H. Oriel, G. T. Sazama, M. G. Campbell, “Switchable electrical conductivity in a three-dimensional metal–organic framework *via* reversible ligand n-doping” *Chem Sci* **2020**, *11*, 1342–1346.

[89] L. Zeng, T. Liu, C. He, D. Shi, F. Zhang, C. Duan, “Organized Aggregation Makes Insoluble Perylene Diimide Efficient for the Reduction of Aryl Halides via Consecutive Visible Light-Induced Electron-Transfer Processes” *J Am Chem Soc* **2016**, *138*, 3958–3961.

[90] S. A. A. Razavi, W. Chen, H.-C. Zhou, A. Morsali, “Tuning redox activity in metal–organic frameworks: From structure to application” *Coord Chem Rev* **2024**, *517*, 216004.

[91] M. C. de Koning, G. W. Peterson, M. van Grol, I. Iordanov, M. McEntee, “Degradation and Detection of the Nerve Agent VX by a Chromophore-Functionalized Zirconium MOF” *Chemistry of Materials* **2019**, *31*, 7417–7424.

[92] H. Yu, Q. Liu, M. Fan, J. Sun, Z.-M. Su, X. Li, X. Wang, “Novel Eu-MOF-based mixed matrix membranes and 1D Eu-MOF-based ratiometric fluorescent sensor for the detection of metronidazole and PA in water” *Dyes and Pigments* **2022**, *197*, 109812.

[93] Y.-J. Tong, L.-D. Yu, J. Zheng, G. Liu, Y. Ye, S. Huang, G. Chen, H. Yang, C. Wen, S. Wei, J. Xu, F. Zhu, J. Pawliszyn, G. Ouyang, “Graphene Oxide-Supported Lanthanide Metal–Organic Frameworks with Boosted Stabilities and Detection Sensitivities” *Anal Chem* **2020**, *92*, 15550–15557.

[94] K. Zheng, Z.-Q. Liu, Y. Huang, F. Chen, C.-H. Zeng, S. Zhong, S. W. Ng, “Highly luminescent Ln-MOFs based on 1,3-adamantanediacetic acid as bifunctional sensor” *Sens Actuators B Chem* **2018**, *257*, 705–713.

[95] Y. Du, H. Yang, R. Liu, C. Shao, L. Yang, “A multi-responsive chemosensor for highly sensitive and selective detection of Fe^{3+}, Cu^{2+}, $Cr_2O_7^{2-}$ and nitrobenzene based on a luminescent lanthanide metal–organic framework” *Dalton Transactions* **2020**, *49*, 13003–13016.

[96] M.-T. Chen, X.-D. Xie, J.-X. Meng, Y.-C. Ou, J.-Z. Wu, M.-L. Tong, “Tunable photoluminescence in flexible carboxylate ligand-based coordination polymers with interesting topologies and Fe^{3+} sensitivity” *CrystEngComm* **2020**, *22*, 6713–6719.

[97] A. Legrand, A. Pastushenko, V. Lysenko, A. Geloen, E. A. Quadrelli, J. Canivet, D. Farrusseng, “Cover Picture: Enhanced Ligand-Based Luminescence in Metal–Organic Framework Sensor (ChemNanoMat 9/2016)” *ChemNanoMat* **2016**, *2*, 841–841.

[98] T. Zhang, Y. Yin, X. Yang, N. Li, W. Wang, Y. Yang, W. Tian, F. Bai, B. Zou, “Space-confined charge transfer turns on multicolor emission in metal-organic frameworks via pressure treatment” *Nat Commun* **2025**, *16*, 4166.

[99] X. Xu, M. Ma, T. Sun, X. Zhao, L. Zhang, “Luminescent Guests Encapsulated in Metal–Organic Frameworks for Portable Fluorescence Sensor and Visual Detection Applications: A Review” *Biosensors (Basel)* **2023**, *13*, 435.

[100] Y. Shen, A. Tissot, C. Serre, **2022**, Royal Society of Chemistry preprint, DOI: 10.1039/d2sc04314a.

[101] Z. Wu, J. Nitsch, T. B. Marder, “Persistent Room-Temperature Phosphorescence from Purely Organic Molecules and Multi-Component Systems” *Adv Opt Mater* **2021**, *9*, DOI 10.1002/adom.202100411.

[102] M. A. El-Sayed, “Spin—Orbit Coupling and the Radiationless Processes in Nitrogen Heterocyclics” *J Chem Phys* **1963**, *38*, 2834–2838.

[103] M. Pamei, A. Puzari, “Luminescent transition metal–organic frameworks: An emerging sensor for detecting biologically essential metal ions” *Nano-Structures & Nano-Objects* **2019**, *19*, 100364.

[104] G. Xiao, B. Zhou, X. Fang, D. Yan, “Room-Temperature Phosphorescent Organic-Doped Inorganic Frameworks Showing Wide-Range and Multicolor Long-Persistent Luminescence” *Research* **2021**, *2021*, DOI 10.34133/2021/9862327.

[105] P. Tao, S. Liu, W. Wong, “Phosphorescent Manganese(II) Complexes and Their Emerging Applications” *Adv Opt Mater* **2020**, *8*, DOI 10.1002/adom.202000985.

[106] W. Li, S. Wu, J. Ren, P. Xiong, “Defects in Inorganic Mechanoluminescent Phosphors: Insights and Impacts” *Adv Funct Mater* **2025**, DOI 10.1002/adfm.202506198.

[107] M. Liu, L. Guo, S. Jin, B. Tan, “Covalent triazine frameworks: synthesis and applications” *J Mater Chem A Mater* **2019**, *7*, 5153–5172.

[108] S. Pourebrahimi, M. Pirooz, “Functionalized covalent triazine frameworks as promising platforms for environmental remediation: A review” *Cleaner Chemical Engineering* **2022**, *2*, 100012.

[109] H. Faraji, “Recent developments in the application of covalent triazine framework-based sorbents for analytical sample preparation” *Coord Chem Rev* **2024**, *505*, 215700.

[110] H. Othman, R. Oestreich, V. Küll, M. N. A. Fetzer, C. Janiak, “Synthesis and Characterization of Covalent Triazine Frameworks Based on 4,4′-(Phenazine-5,10-diyl)dibenzonitrile and Its Application in CO2/CH4 Separation” *Molecules* **2025**, *30*, 3110.

[111] S. Hug, L. Stegbauer, H. Oh, M. Hirscher, B. V. Lotsch, “Nitrogen-Rich Covalent Triazine Frameworks as High-Performance Platforms for Selective Carbon Capture and Storage” *Chemistry of Materials* **2015**, *27*, 8001–8010.

[112] L. Liao, M. Li, Y. Yin, J. Chen, Q. Zhong, R. Du, S. Liu, Y. He, W. Fu, F. Zeng, **2023**, American Chemical Society preprint, DOI: 10.1021/acsomega.2c06961.

[113] G. Wang, K. Leus, H. S. Jena, C. Krishnaraj, S. Zhao, H. Depauw, N. Tahir, Y. Y. Liu, P. Van Der Voort, “A fluorine-containing hydrophobic covalent triazine framework with excellent selective CO2 capture performance” *J Mater Chem A Mater* **2018**, *6*, 6370–6375.

[114] R. Sun, B. Tan, “Covalent Triazine Frameworks (CTFs): Synthesis, Crystallization, and Photocatalytic Water Splitting” *Chemistry – A European Journal* **2023**, *29*, DOI 10.1002/chem.202203077.

[115] R. Kishan, P. Rani, G. Singh, C. M. Nagaraja, “Functionalized Covalent Triazine Framework (CTF) for Catalytic CO_2 Fixation and Synthesis of Value-Added Chemicals” *Cryst Growth Des* **2024**, *24*, 7878–7887.

[116] A. Hayat, H. Ali, Z. Ajmal, A. Alshammari, M. M. Alghamdi, A. A. El-Zahhar, N. Almuqati, M. Sohail, A. M. Abu-Dief, S. Khan, Y. Al-Hadeethi, M. Z. Ansari, Y. Orooji, “Emerging breakthroughs in covalent triazine frameworks: From fundamentals towards photocatalytic water splitting and challenges” *Prog Mater Sci* **2025**, *147*, 101352.

[117] P. Puthiaraj, Y.-R. Lee, S. Zhang, W.-S. Ahn, “Triazine-based covalent organic polymers: design, synthesis and applications in heterogeneous catalysis” *J Mater Chem A Mater* **2016**, *4*, 16288–16311.

[118] E. Saputra, B. A. Prawiranegara, H. Sugesti, M. W. Nugraha, P. S. Utama, “Covalent triazine framework: Water treatment application” *Journal of Water Process Engineering* **2022**, *48*, 102874.

[119] D.-Y. Wang, W.-J. Wang, R. Wang, S.-C. Xi, B. Dong, “A fluorescent covalent triazine framework consisting of donor–acceptor structure for selective and sensitive sensing of Fe3+” *Eur Polym J* **2021**, *147*, 110297.

[120] A. M. Joy, S. T. Prasad, K. Ramakrishnan, “A Benzimidazole Linked Covalent Triazine Framework as a Fluorescent Probe for Selective Multiplatform Detection of Trinitrophenol” *Luminescence* **2025**, *40*, DOI 10.1002/bio.70256.

[121] S. Bügel, A. Spieß, C. Janiak, “Covalent triazine framework CTF-fluorene as porous filler material in mixed matrix membranes for CO2/CH4 separation” *Microporous and Mesoporous Materials* **2021**, *316*, DOI 10.1016/j.micromeso.2021.110941.

[122] C. Gu, D. Liu, W. Huang, J. Liu, R. Yang, “Synthesis of covalent triazine-based frameworks with high CO_2 adsorption and selectivity” *Polym Chem* **2015**, *6*, 7410–7417.

[123] K. Yuan, C. Liu, J. Han, G. Yu, J. Wang, H. Duan, Z. Wang, X. Jian, “Phthalazinone structure-based covalent triazine frameworks and their gas adsorption and separation properties” *RSC Adv* **2016**, *6*, 12009–12020.

[124] S. Ren, M. J. Bojdys, R. Dawson, A. Laybourn, Y. Z. Khimyak, D. J. Adams, A. I. Cooper, “Porous, Fluorescent, Covalent Triazine-Based Frameworks Via Room-Temperature and Microwave-Assisted Synthesis” *Advanced Materials* **2012**, *24*, 2357–2361.

[125] S. Yu, J. Mahmood, H. Noh, J. Seo, S. Jung, S. Shin, Y. Im, I. Jeon, J. Baek, “Direct Synthesis of a Covalent Triazine-Based Framework from Aromatic Amides” *Angewandte Chemie International Edition* **2018**, *57*, 8438–8442.

[126] L. Su, J. Xu, Z. Zhang, Y. Xiong, “One-step microwave-assisted ionothermal synthesis of AuNPs/CTF for sensitive surface-enhanced Raman spectroscopy detection” *Next Materials* **2025**, *8*, 100755.

[127] T. Chen, W.-Q. Li, W.-B. Hu, W.-J. Hu, Y. A. Liu, H. Yang, K. Wen, “Direct synthesis of covalent triazine-based frameworks (CTFs) through aromatic nucleophilic substitution reactions” *RSC Adv* **2019**, *9*, 18008–18012.

[128] L. Zhang, T. Sun, Z. Zhang, Z. Zhang, Y. Xu, “Rapid and Scalable Preparation of High-Crystalline Carboxyl-Functionalized Covalent Triazine Frameworks via Friedel-Crafts Reaction” *Angewandte Chemie International Edition* **2025**, *64*, DOI 10.1002/anie.202421251.

[129] S. Ren, R. Dawson, A. Laybourn, J. Jiang, Y. Khimyak, D. J. Adams, A. I. Cooper, “Functional conjugated microporous polymers: from 1,3,5-benzene to 1,3,5-triazine” *Polym Chem* **2012**, *3*, 928.

[130] C. B. Meier, R. S. Sprick, A. Monti, P. Guiglion, J. S. M. Lee, M. A. Zwijnenburg, A. I. Cooper, “Structure-property relationships for covalent triazine-based frameworks: The effect of spacer length on photocatalytic hydrogen evolution from water” *Polymer (Guildf)* **2017**, *126*, 283–290.

[131] K. Wang, L. Yang, X. Wang, L. Guo, G. Cheng, C. Zhang, S. Jin, B. Tan, A. Cooper, “Covalent Triazine Frameworks via a Low-Temperature Polycondensation Approach” *Angewandte Chemie International Edition* **2017**, *56*, 14149–14153.